AD-E 800 784

SYMPOSIUM PROCEEDINGS

THE INTERACTION OF NON-NUCLEAR MUNITIONS WITH STRUCTURES

U.S. AIR FORCE ACADEMY, COLORADO
MAY 10-13, 1983

DTIC
ELECTE
SEP 1 1983
S
D
B

83 08 19 093

COMPONENT PART NOTICE

THIS PAPER IS A COMPONENT PART OF THE FOLLOWING COMPILATION REPORT:

(TITLE): The Interaction of Non-Nuclear Munitions with Structures: Symposium Proceedings

Held at U.S. Air Force Academy, Colorado on May 10-13 1983, Part 1,

(SOURCE): Florida Univ., Eglin AFB. Graduate Engineering Center,

To ORDER THE COMPLETE COMPILATION REPORT USE ___AD-A132 115___.

THE COMPONENT PART IS PROVIDED HERE TO ALLOW USERS ACCESS TO INDIVIDUALLY AUTHORED SECTIONS OF PROCEEDINGS, ANNALS, SYMPOSIA, ETC. HOWEVER, THE COMPONENT SHOULD BE CONSIDERED WITHIN THE CONTEXT OF THE OVERALL COMPILATION REPORT AND NOT AS A STAND-ALONE TECHNICAL REPORT.

THE FOLLOWING COMPONENT PART NUMBERS COMPRISE THE COMPILATION REPORT:

AD#:	TITLE.
AD-P001 706	Ground Shock from Penetrating Conventional Weapons.
AD-P001 707	Calculational Evaluation of the Inclusion Effects on Stress Gage Measurements in Rock and Soil.
AD-P001 708	Free-Field Ground Shock Pressures from Buried Detonations in Saturated and Unsaturated Soils.
AD-P001 709	High Velocity Penetration into Fibre-Reinforced Concrete Materials-Protection of Buildings.
AD-P001 710	Analytical and Experimental Studies on Penetration into Geological Targets.
AD-P001 711	Penetration Behavior of Highly Deformable Projectiles in Concrete Slabs.
AD-P001 712	Rapid Runway Cutting With Shaped Charges.
AD-P001 713	Modeling the Burn-to-Violent Reaction to Simulate Impact Damaged GP Warheads.
AD-P001 714	Predicting Response of Munitions to Massive Secondary Fragment Impact: A Proposed Analytical Method.
AD-P001 715	Microplane Model for Fracture Analysis of Concrete Structures.
AD-P001 716	A Plastic Fracture Model for Concrete Materials.
AD-P001 717	The Effects of Curing and Aging on the Triaxial Properties of Concrete in Underground Structures.
AD-P001 718	Strength Criteria for Anisotropic Materials.
AD-P001 719	Constitutive Properties of Steel Fiber Reinforced Concrete in Multiaxial Loading.
AD-P001 720	A simplified Viscoplastic Theory for Frictional Materials.
AD-P001 721	Constitutive Relations of Concrete Subjected to a Varying Strain Rate.
AD-P001 722	Rock/Elastomer Composites as Impact Resistance Materials.
AD-P001 723	Behavior of Fiber Reinforced Concrete Slabs Under Impact Loading.
AD-P001 724	Experimental Modeling of Strength and Deformation Behavior of Concrete in Direct Shear.
AD-P001 725	Finite Element Analysis of Concrete Failure in Shear.

AD#:	TITLE:
AD-P001 726	Shaking Table Tests to Evaluate the Liquifaction Potential of Near Surface Saturated Sand Deposits.
AD-P001 727	Analysis of Buried Reinforced Concrete Arch Structures Under Dynamic Loads.
AD-P001 728	The Use of Compendia Design Manuals and Reference Texts in Prediction of Nonnuclear Weapons Effects.
AD-P001 729	Analysis of Containment Rings for Flywheel Burst Protection.
AD-P001 730	A Rational Approach to the Analysis of Structures Subjected to Underground Blasts.
AD-P001 731	Extreme Dynamic Loading Effects on Steel and Concrete Shell Structures.
AD-P001 732	Fracture Diagnosis in Structures Using Circuit Analogy.
AD-P001 733	Dynamic Loading More than Just a Dynamic Load Factor.
AD-P001 734	The Effects of Indirect Fire Munitions on Framed Structures.
AD-P001 735	Models for Damage Diagnosis in SDF Structures.
AD-P001 736	Today's Constraints Drive Ammo Magazines Underground.
AD-P001 737	Swedish Design Manual for Protective Structures.
AD-P001 738	Design of Underground Shelters Including Soil-Structure Interaction Effects.
AD-P001 739	Gas Pressure Loads from Explosions within Vented and Unvented Structures.
AD-P001 740	Structural Response of RC-Members in Case of Impulsive Loading: Failure Analysis in Bending and Shear.
AD-P001 741	Comparison of Predictive Methods for Structural Response to HE Blast Loads.
AD-P001 742	Response of a Linear Structure to an Exponential Pressure Pulse.
AD-P001 743	The Use of Steel Fiber Reinforced Concrete in Containment and Explosive-Resistant Structures.
AD-P001 744	Simulation of Pressure Waves and Their Effects on Loaded Objects, Part I: Outlining the Problem, Description of the Simulation Device.
AD-P001 745	Simulation of Pressure Waves and Their Effects on Loaded Objects, Part II: Experiments and Calculations, Destruction Curves.
AD-P001 746	Response of Structures to Detonations in Sand.
AD-P001 747	Effects of Bare and Cased Explosives Charges on Reinforced Concrete Walls.
AD-P001 748	Tests and Evaluations of Close in Detonations.

SYMPOSIUM PROCEEDINGS

THE INTERACTION OF NON-NUCLEAR MUNITIONS WITH STRUCTURES

U.S. AIR FORCE ACADEMY, COLORADO
MAY 10-13, 1983

This document represents the proceedings of a symposium "The Interaction of Non-Nuclear Munitions with Structures", U.S. Air Force Academy, Colorado, May 10-13, 1983. The symposium was sponsored by the following U.S. Air Force agencies:

Armament Laboratory
Eglin AFB, FL

Engineering & Services Laboratory
Tyndall AFB, FL

Office of Scientific Research
Bolling AFB, DC

Weapons Laboratory
Kirtland AFB, NM

The symposium was coordinated through the University of Florida Graduate Engineering Center, Eglin AFB, FL, under USAF Contract No. F08635-81-C-0302. Dr. C. A. Ross served as the symposium coordinator.

All the manuscripts in this document have been approved for public release either by the author or the cognizant federal agency.

This document was produced at a total cost of $2,550.00 or $8.50 per copy.

TABLE OF CONTENTS

SOIL LIQUEFACTION

SOIL MODELS

STRUCTURAL ANALYSIS

STRUCTURAL DESIGN

STRUCTURAL RESPONSE

STRUCTURAL TESTS

**EFFECTS OF BARE AND CASED EXPLOSIVES
CHARGES ON REINFORCED CONCRETE WALLS**   **221**
H Hader *Ernst Basler & Partners, Switzerland*

AUTHOR INDEX

GROUND SHOCK FROM PENETRATING CONVENTIONAL WEAPONS

James L. Drake and Charles D. Little, Jr.

U. S. Army Engineer Waterways Experiment Station
Vicksburg, Mississippi

ABSTRACT

This paper presents results of an analysis of ground shock data from more than one hundred explosion tests conducted in soil over the past 35 years. Burst positions varied from fully buried to contact detonations in soil and for shallow depths into concrete protective overlays. Soil conditions ranged from loose dry sand to saturated clay. Empirical equations are presented that predict the magnitude and time histories of the expected stresses and ground motions as a function of burst position, soil indices and burster layer thickness.

BACKGROUND

More than one hundred explosion tests have been performed over the past 35 years in soil to characterize the ground shock produced by buried conventional munitions. Lampson (1) conducted pioneering tests during World War II with buried charges in several soil types from which cube root scaling was developed and verified. Following Lampson's lead, the MOLE and UET tests (2,3) were conducted in the early 1950's to extend the ground shock data base to other soils and rocks. Since that time many other buried burst tests have been conducted in a wide variety of soils with charges from 1 pound to 500 tons (4-11). Many other small-scale tests have gone unreported.

Tests performed for special projects produced the first measurements of stresses directly beneath near-surface explosions on burster slabs (12,13). Coupling of shallow explosions from penetrating weapons was investigated by Ingram (3) in the CDDE program and by Drake and Little (unreported). Brown, et al (14), investigated the propagation of ground shock through rock rubble overlays. All totaled, more than 50 tests have been conducted just to determine explosive coupling from partially buried weapons in burster slabs.

Ground shock data from these tests were drawn together and analyzed to provide an update to the Army design manual, TM 5-855-1, "Fundamentals of Protective Design for Conventional Weapons." The result of that analysis is the basis for this paper. Due to the limited space provided, only the empirical prediction equations are given.

GROUND SHOCK THREAT

The ground shock produced by bombs exploding on or within the ground near buried structures generally provides the dominant threat to these facilities. Stresses from buried bursts can be greater in magnitude and much longer duration than corresponding bursts in air.

Significant enhancement of the stresses and ground motions will occur as the weapon penetrates more deeply into the surrounding soil or backfill before it detonates. Often, protective layers of concrete or rock rubble are provided over the structure to limit the weapon penetration thus reducing the effective coupling of the explosion and increasing the weapon standoff.

Important variables affecting the intensity of the loading are: a) weapon size and distance to the structure, b) the mechanical properties of the soil or rock, and c) the depth of penetration of the weapon. Of these factors, the effect of soil or rock properties is least predictable by simple handbook methods. Ground shock intensity may vary by more than two orders of magnitude when the soil is varied from low density dry soils to saturated clays.

There are two important cases to consider in assessing the ground shock threat to buried facilities: 1) bombs that explode overhead, generally on or within the protective concrete or rock rubble overlay, causing a direct loading of the roof slab, and 2) weapons that penetrate into the surrounding soil and detonate beside the facility loading the walls and floor. While the same general ground shock prediction equations apply for both cases, the role of the site geology and the protective overlay requires a somewhat different application of these equations. These cases are shown in Figure 1.

SOIL PROPERTY EFFECTS

Ground shock propagation in earth media is a complex function of the dynamic constitutive properties of the soil, the explosive products and the geometry of the explosion. No single soil index or combination of indices can adequately describe this process in a simple way for all cases.

Water can have a profound influence on ground shock propagation in cohesive soils, particularly
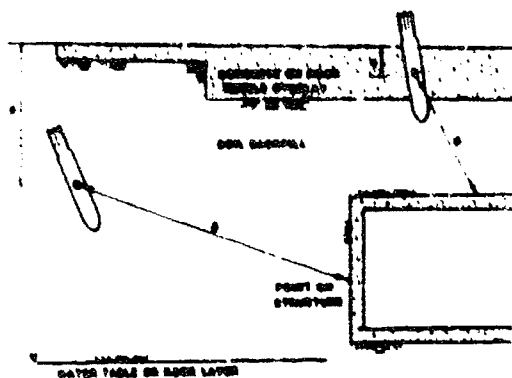
Figure 1. Geometry for explosion against a
buried facility;

as saturation reaches 95 percent or greater.
Typically water is fully bound with the skeletal
structures for these soils, providing signifi-
cant contribution to the overall stiffness and
strength of the soil structure. As saturation
approaches 100 percent, pronounced increases in
peak stresses and accelerations have been ob-
served in wet clays, clay shales and sandy clays.
Stresses similar to shock waves in free water
have been noted in saturated clays. Saturation
as measured by free standing water in boreholes
may not be an accurate measure of the true sat-
uration depth, particularly where seasonal water
table fluctuations introduce small amounts of
air into the soil. Seismic surveys generally
will show a sharp jump in the wave speed to more
than 5000 feet per second at this depth.

Granular soils with high relative density
are generally not strongly influenced by water
saturation as are cohesive soils. The stiffness
of granular soil is provided by the grain to
grain contacts in the skeleton with only a small
contribution by the free water. Consequently,
controlled laboratory and field experiments in
dense nearly saturated sands did not show large
influence of the pore water on the resulting
shock wave propagation. However, the effects of
water in low relative density sands can produce
similar effects as those seen in cohesive
soils (15). In these cases, the soil skeleton
can collapse, and the grain to grain contact
lost resulting in high pore pressures as the
sand liquifies. These sites would not normally
be considered for construction of hardened
facilities.

Seismic velocity, c , is often used as a
crude index of soil or rock properties for ground
shock prediction purposes. It provides a simple
measure of the stiffness and the density of the
soil thru the relationship

$$c = \sqrt{\frac{M}{\rho}}$$

where M is the stiffness or modulus of the soil
and ρ is its mass density. The seismic veloc-
ity also provides a relationship between distance
and time.

A great deal of caution must be used in gen-
eralizing the use of seismic velocity as a ground
shock index. Cementation in granular soils such
as dry desert alluvium may result in abnormally
high propagation velocities (approaching 4000 feet
per second). Yet these materials may exhibit very
high air filled voids and low relative densities--
qualities that would classify them as very poor
transmitters of ground shock. Low seismic veloc-
ities, on the other hand, would generally indicate
poor ground shock transmission qualities.

The attenuation rate with range of the ground
shock magnitude is controlled by the irreversible
crushing of the void volume within the soil matrix
by the passage of the stress wave. In cohesive
soils, the volume of the air filled voids is an
index for attenuation of ground motions, while the
best index for attenuation rates in granular media
is the relative density. Because relative density
is not always available, dry unit weight can be an
effective index for ground shock attenuation.
Soils with high relative density (high dry density)
or low air voids will attenuate the ground shock
more slowly than low relative density or high air
void materials. Figure 2 shows the peak stress
from explosions in typical soils.
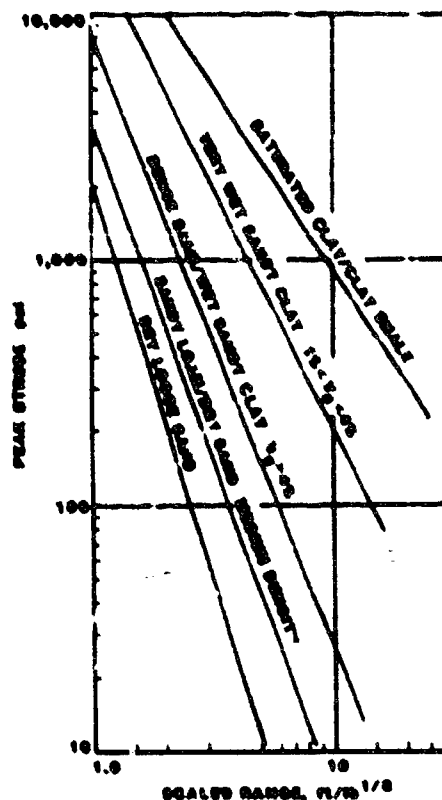
Figure 2. Peak stress from explosions
in varying soil types

GROUND SHOCK PREDICTIONS

Stress and particle velocity pulses can be characterized by exponential like time histories that decay rapidly in amplitude and broaden as they propagate outward from the explosion. The characteristic time for these time histories can be measured in arrival time from the source, t_a, where

$$t_a = \frac{R}{c} \qquad (1)$$

R is the distance from the explosion and c is the seismic or propagation velocity. Initially these wave forms rise sharply to the peak with the rise time, t_r

$$t_r = 0.1\, t_a \qquad (2)$$

this is about 1/10 of the travel time to the target point. From the peak, the pulse decays monotonically with time to nearly zero in 1 to 4 travel times given by the following equations

$$P(t) = P_0\, e^{-\alpha t/t_a} \qquad t > 0 \quad (3a)$$

$$V(t) = V_0(1 - \beta t/t_a)e^{-\beta t/t_a} \qquad t > 0 \quad (3b)$$

where $P(t)$ is the stress, V is the particle velocity, and α and β are time constants. While the time constants generally vary with specific site conditions, they can be taken as

$$\alpha = 1.0 \qquad \beta = \frac{1}{2.5}$$

for most applications. P_0 and V_0 are values of the peak stress and particle velocity to be determined by the following equations. Other waveform parameters such as impulse, displacement and accelerations may be derived from these functions.

Since the characteristic time is inversely proportional to seismic velocity, explosions in high velocity media such as saturated clay will produce very short, high frequency pulses with high accelerations and low displacements. On the other hand, detonations in dry loose materials will cause much longer duration, low frequency ground motions.

Peak particle velocity and peak stress are related by

$$P_0 = \rho c\, V_0 \qquad (4)$$

where ρ is the mass density. Free-field stresses and ground motions from bombs detonating on and within burster layers or in the soil alongside the structure are given in the following expressions:

$$P_0 = f \cdot \rho c \cdot 160 \cdot \left(\frac{R}{W^{1/3}}\right)^{-n} \qquad (5a)$$

$$V_0 = f \cdot 160 \cdot \left(\frac{R}{W^{1/3}}\right)^{-n} \qquad (5b)$$

$$A_0 \cdot W^{1/3} = f \cdot 50 \cdot c \cdot \left(\frac{R}{W^{1/3}}\right)^{-n-1} \qquad (5c)$$

$$\frac{d_0}{W^{1/3}} = f \cdot 5.0 \cdot \left(\frac{R}{W^{1/3}}\right)^{-n+1} \qquad (5d)$$

$$\frac{I_0}{W^{1/3}} = f \cdot 1.1 \cdot \left(\frac{R}{W^{1/3}}\right)^{-n+1} \qquad (5e)$$

where P_0 is the peak pressure (psi), V_0 is the peak particle velocity (ft/sec), A_0 is the peak acceleration (g's), d_0 is the peak displacement (ft), I_0 is the peak impulse (psi-sec), ρ is the mass density (lb-sec²/ft⁴), c is the seismic velocity (ft/sec), ρc is the acoustic impedance (psi/ft/sec), R is the distance to the explosion (ft), W is the charge weight (lb), and f is the coupling factor for near surface detonations. For preliminary design considerations the following table is suggested for selecting the seismic velocity, acoustic impedance and attenuation coefficients:

SUGGESTED COEFFICIENTS FOR DESIGN

Material Description	Seismic Velocity (ft/sec)	Acoustic Impedance (psi/ft/sec)	Attenuation Coefficient n
Loose, dry sands and gravels with low relative density	600	12	3.0-3.25
Sandy loam, loess, dry sands and backfill	1000	22	2.75
Dense sand with high relative density	1600	44	2.5
Wet sandy clay with air voids (greater than 4 percent)	1800	44	2.5
Saturated sandy clays and sands with small amount of air voids (less than 1 percent)	5000	48	2.25-2.5
Heavy saturated clays and clay shales	>5000	150-180	1.5

A more detailed description is provided in Table 1 for soils encountered in explosion test programs. Simple soil parameters such as wet and dry unit weights, air filled voids and seismic velocity are shown to assist in relating the explosion

3

effects parameters to the design soil conditions. Note that the attenuation coefficient and seismic velocity are closely related to dry unit weight for granular soils while air void content is important for cohesive soils.

GROUND SHOCK COUPLING FACTOR

The magnitude of the stress and ground motions will be greatly enhanced as the weapon penetrates more deeply into the soil or the protective burster layer before it detonates. A concept of an equivalent effect coupling factor is introduced to account for this effect on the ground shock parameters and is defined as follows:

The coupling factor, f , is defined as the ratio of the ground shock magnitude from partially to shallow buried weapon to the ground shock magnitude from a fully buried burst in the same medium.

$$f = \frac{(P, V, d, I, a) \text{ near surface}}{(P, V, d, I, a) \text{ contained}}$$

A single coupling factor is applicable for all ground shock parameters that depends upon the depth of burial of the center of the weapon and the medium being penetrated, i.e., soil, concrete or air. It is important to note that the coupling

factor concept used here does not produce an equivalent charge but rather, it is a scale factor to reduce the ground shock computed from a buried burst with the full charge weight to account for the shallow burial.

Coupling factors are different for bursts in air, soil and concrete and depend upon the scaled depth of burst of the weapon. These factors are shown in Figure 3. The coupling factor for air is a constant

$$f = 0.14$$

and is recommended for contact bursts.

In the case where a weapon penetrates into more than one material, i.e., a long bomb that penetrates the concrete slab and is partly buried in soil, the coupling factor is computed as the sum of the coupling factors in each of the materials weighted in proportion to the charge weight contained within each medium.

$$f = \sum f_i\left(\frac{W_i}{W}\right) \tag{6}$$

where f is the total coupling factor, f_i is the coupling factor for each component material, i.e.,
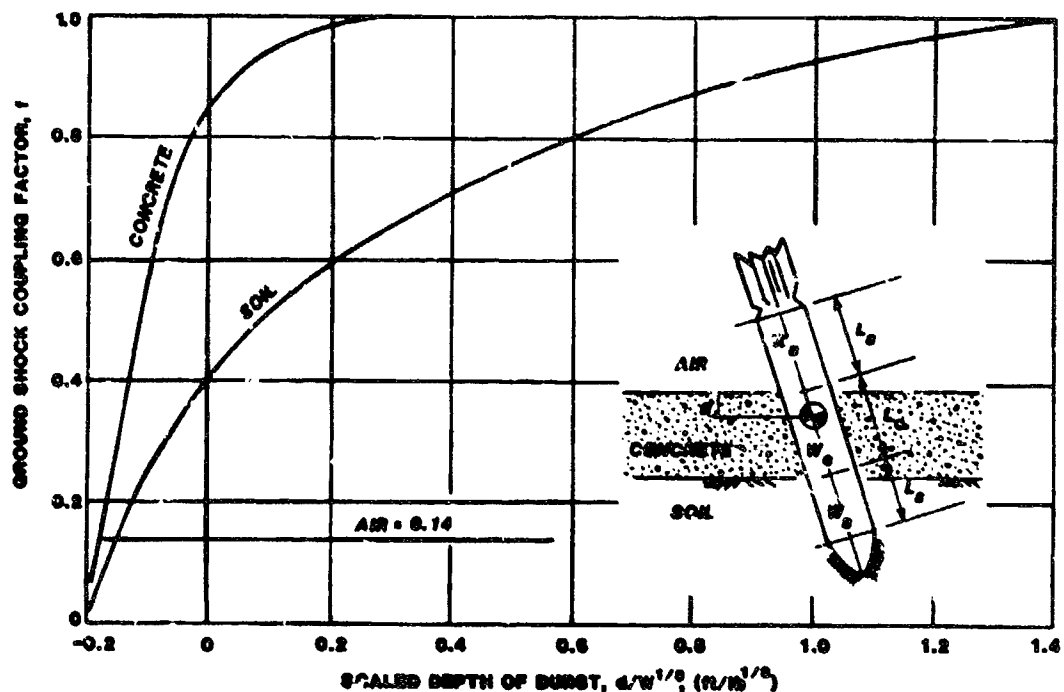
Figure 3. Ground shock coupling factor as a function of scaled depth of burst for air, soil and concrete

4

air, soil, concrete, W_i is the weight of the charge in contact with each component material, and W is the total charge weight. Since most bombs are cylindrical, the coupling can also be defined as

$$f = \sum f_i\left(\frac{L_i}{L}\right) \qquad (7)$$

where L_i is the length of the weapon in contact with each material and L is the total weapon length.

DISCUSSION AND CONCLUSIONS

Empirical expressions were derived from a fit to a large body of ground shock data from buried and near-surface bursts in soil. Several important observations were made concerning the role of soil properties on scaling of ground shock:

1. Near the explosive source, peak particle velocities in soils tend to a single curve that is nearly independent of the soil properties. This observation can be explained in part by the interaction of the detonation wave in the explosive with the soil.

2. Peak stresses scale in proportion to the seismic velocity.

3. Attenuation of the peak ground shock magnitudes is strongly dependent on the relative density in granular soils or to the air void volume in cohesive soils. Because the seismic velocity is also influenced by these parameters, the attenuation coefficient, n, can be estimated from the seismic velocity as

c(fps)	n
500–600	3–3.5
750–1000	3
1000–1400	2.75
1400–1600	2.5
>5000	1.5–2.25

4. Time scales in proportion to the time of arrival. Thus, the pulse tends to spread in proportion to the distance traveled, with a rise time of about 1/10 of the travel time and a duration on the order of 2-3 travel times.

5. Because of the time scaling, peak accelerations are proportional to the seismic velocity, peak displacements are inversely proportional to the seismic velocity while the peak impulse is only sensitive to density variation.

REFERENCES

1. C. W. Lampson, "Final Report on Effects of Underground Explosions," NDRC A-479, National Defense Research Committee, Washington, DC, March 1946.

2. D. C. Sachs and L. M. Swift, "Small Explosion Tests—Project MOLE," AFSWP-291, Stanford Research Institute, Stanford, CA, December 1955.

3. R. B. Vaile, Jr., "Underground Explosion Tests at Dugway," Stanford Research Institute, Stanford, CA, March 1952.

4. W. R. Perret, et al, "Project Scooter," TID-4500, Sandia Laboratory, Albuquerque, NM, October 1963.

5. P. R. Kintzinger, "Air Vent Phase I - Earth Particle Motion," SC-RR-64-549, Sandia Laboratory, Albuquerque, NM, October 1964.

6. W. T. Harvey, "Preliminary Results Report, ESSEX-1, Phase 2: Nuclear Cratering Device Simulation," WES PR-E-74-1, U. S. Army Engineer Waterways Experiment Station, Vicksburg, MS, April 1974.

7. A. E. Miller, "Preliminary Results Report, ESSEX-1, Phase 2: Nuclear Cratering Device Simulation," WES PR-E-75-1, U. S. Army Engineer Waterways Experiment Station, Vicksburg, MS, March 1975.

8. J. K. Ingram, "CENSE Explosion Tests Program - CENSE 2, Explosions in Soil," TR N-77-6, U. S. Army Engineer Waterways Experiment Station, Vicksburg, MS, December 1977.

9. J. D. Day and C. E. Joachim," Cable Vulnerability Study," MP SL-81-19, U. S. Army Engineer Waterways Experiment Station, Vicksburg, MS, August 1981.

10. C. E. Joachim and L. K. Davis, "Project MBCE - Munitions/Bare Charge Equivalence in Soils," TR SL-81- (Draft), U. S. Army Engineer Waterways Experiment Station, Vicksburg, MS.

11. W. R. Perret and R. C. Bass, "Free-Field Ground Motion Induced by Underground Explosions," SAND 74-0252, Sandia Laboratories, Albuquerque, NM, February 1975.

12. J. L. Drake, "Ground Shock Threat to Buried Structures from Conventional Weapons," presented at the Protective Design Symposium, 22-23 September 1975, Brussels, Belgium.

13. W. J. Flathau and J. L. Drake, "Loading of Buried Structures for Conventional Bombs," 100th Symposium on Weapons Effects on Protective Structures, Mannheim, Germany, 14-16 November 1978.

14. J. W. Brown, et al, "Propagation of Explosive Shock Through Rubble Screens," MP SL-80-7, U. S. Army Engineer Waterways Experiment Station, Vicksburg, MS, July 1980.

15. Josef Henrych, "The Dynamics of Explosion and Its Use," Elsevier Publishing Company, New York, NY, 1979.

5

TABLE 1 SOIL PROPERTIES FROM EXPLOSION TESTS

Soil Description	Dry Unit Weight γ_{dry} lb/ft^3	Total Unit Weight γ lb/ft^3	Air-Filled Voids %	Seismic Velocity c ft/sec	Acoustic Impedance ρc psi/ft/sec	Attenuation Coefficient n
Dry desert alluvium and playa, partially cemented	87	93–100	>25	2100–4200[1]	40	3–3.25
Loose, dry, poorly graded sand	80	90	>30	600	11.6	3–3.5
Loose wet poorly graded sand-free standing water	97	116	10	500–600	12.5–15	3
Dense dry sand, poorly graded	99	104	32	900–1300	25	2.5–2.75
Dense wet sand, poorly graded-free standing water	108	124	9	1000	22	2.75
Very dense dry sand, relative density ≈100%	105	109	30	1600	44	2.5
Silty-clay, wet	95–100	120–125	9	700–900	18–25	2.75–3
Moist loess, clayey sand	100	122	5–10	1000	28	2.75–3
Wet sandy clay, above water table	95	120–125	4	1800	48	2.5
'Saturated' sand-below water table in marsh	--	--	1–4[2]	4900	125	2.25–2.5
'Saturated' sandy clay, below water table	78–100	110–124	1–2	5000–6000	130	2–2.5*
'Saturated' sandy clay, below water table	100	125	<1	5000–6600	130–180	1.5
Saturated stiff clay saturated clay-shale	--	120–130	0	>5000	135	1.5

(1) High because of cementation.
(2) Estimated.
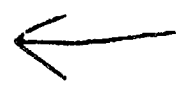
6

CALCULATIONAL EVALUATION OF THE INCLUSION EFFECTS
ON STRESS GAGE MEASUREMENTS IN ROCK AND SOIL

A. L. Florence, D. D. Keough, and P. Mak

SRI International, Menlo Park, California 94025

ABSTRACT

Explosion-induced stress waves in rocks
and soils are frequently measured by flatpack
stress gages grouted in boreholes. The stress
gage measurements differ from the free-field
stresses if the grout forms on inclusion be-
cause of a mismatch of material properties or
inadequate bonding with the medium. Calcula-
tional results are presented for a tuff medium
to illustrate inclusion effects in elastic and
elastic-plastic regimes. The main effect occurs
if the inclusion-medium bonding is inadequate.
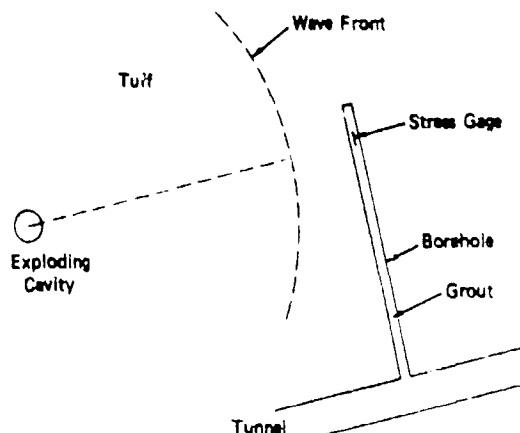
FIGURE 1   IN-SITU STRESS GAGE EMPLACEMENT

INTRODUCTION

Experiments for investigating the vulnerability
of military civil engineering structures to attack
loads applied through the ground involve measuring
stresses in rock and soil. Stress gage signals are
often difficult to interpret because the gages and
the immediate surroundings disturbed by gage in-
stallation perturb the free-field stresses to be
measured.

This paper treats the influence of the gage
installation procedure on the free-field stresses.
For installation in rock, the procedure is to drill
from a tunnel, cavity, or ground surface, insert
the gage, and pack the borehole with rock-matching
grout, as illustrated in Figure 1. Because it is
impossible to match all the properties of the rock
in the neighborhood of the gage and to ensure per-
fect bonding with the rock, the grout-filled bore-
hole forms a cylindrical inclusion, so the gage is
in general not subjected to the same stresses as
the far field. To interpret these stress gage
signals, one must determine the relationship bet-
ween the inclusion and medium stress fields. The
influence on the stresses of the gage, which is
itself an inclusion, is not treated here; that in-
vestigation will be the subject of a future publi-
cation.

The calculational investigation is simplified
by assuming plane strain conditions, by confining
attention to the two extreme cases of perfect bond-
ing (no slip) and no bonding (no shear transfer),
between the grout and the rock, and by considering
proportional static compressional loading, which
prevents bond separation. Illustrative results
based on a rock-matching grout (designated 2C4) in-
clusion in Nevada Test Site (NTS) tuff are presented.

MATERIAL MODEL

To show how a gage installation procedure can
make stress measurement difficult, calculations are
performed for a borehole in NTS tuff filled with
2C4 grout, as shown in Figure 1. Figures 2 and 3
show the tuff and grout strength properties. A
strong tuff is intentionally chosen to magnify the
effects of poorly matched properties. Both the
grout and the tuff are modeled as Mohr-Coulomb ma-
terial with the properties listed in Table 1.

7
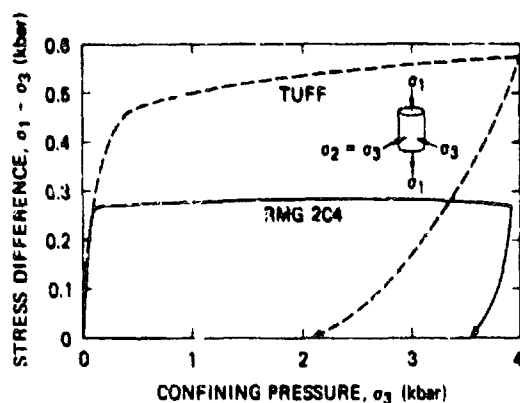
FIGURE 2 UNIAXIAL STRAIN RESPONSE OF ROCK-MATCHING GROUT RMG 2C4 AND NEVADA TEST SITE TUFF: STRESS DIFFERENCE VERSUS CONFINING PRESSURE
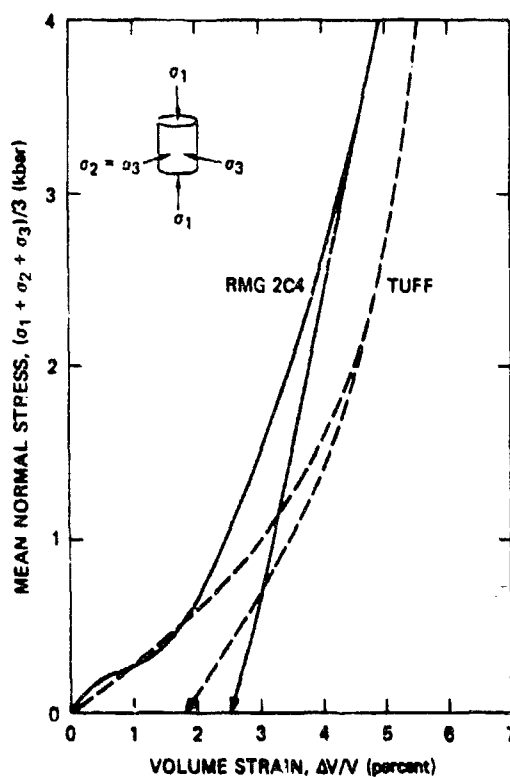
FIGURE 3 UNIAXIAL STRAIN RESPONSE OF ROCK-MATCHING GROUT RMG 2C4 AND NEVADA TEST SITE TUFF: MEAN NORMAL STRESS VERSUS VOLUME STRAIN

Table I

MATERIAL PROPERTIES

Material	Young's Modulus (psi)	Poisson's Ratio ν	Friction Angle ϕ (deg.)	Cohesion c (psi)
Tuff	1.66×10^6	0.32	6.36	2.85×10^3
Grout (2C4)	2.64×10^6	0.28	1.46	1.91×10^3

FINITE ELEMENT MODEL

The spherical wave engulfing the borehole and gage is approximated by a quasi-static biaxial stress-plane strain state, as shown in Figure 4.
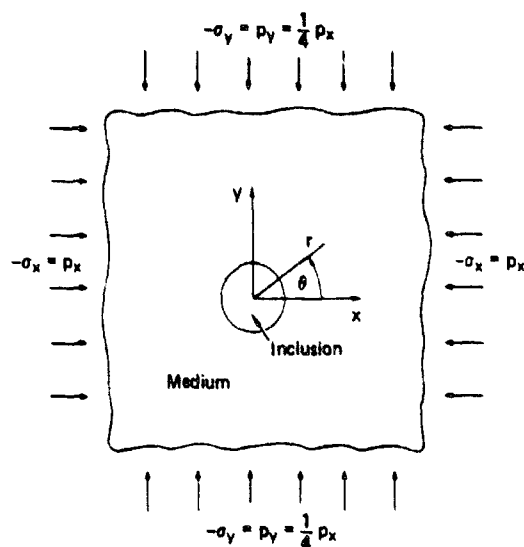
FIGURE 4 CIRCULAR INCLUSION UNDER BIAXIAL STRESS AND PLANE STRAIN

For pulses with rise times longer than several inclusion diameter transit times and where densities of different materials match each other, a quasi-static analyses gives reasonable estimates of the dynamic response. As a further simplification, proportional loading is assumed. The ratio between free-field stresses is chosen as $\sigma_x/\sigma_y = 4$ to avoid creating tensile stresses across the inclusion-medium interface. Figure 5 shows the two gage locations for measuring the free-field stress components $\sigma_x = -p$ and $\sigma_y = -p/4$ (p > 0). Because of symmetry, only the first quadrant needs to be modelled. Stresses σ_x and σ_y are calculated in the inclusion along the radii on the y and x axes, respectively. The inclusion effect of the gage itself is not considered and these calculated stresses are taken to be the stresses acting on the gage for comparison with the uniform free-field stress.

8
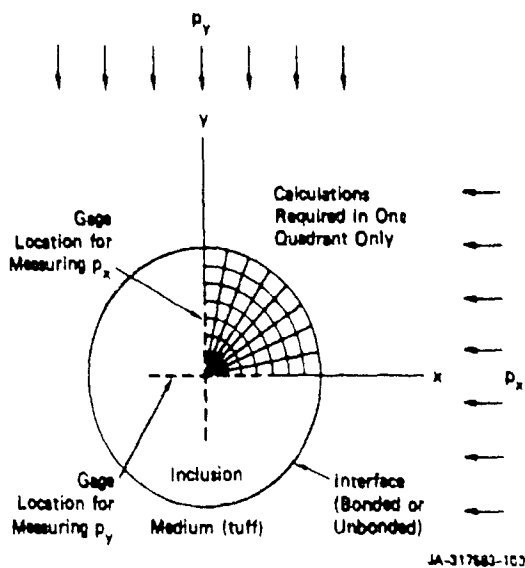
FIGURE 5   GAGE LOCATIONS IN BOREHOLE

The analysis was performed with the finite element code NONSAP. The finite element grid extended to 10 times the radius of the inclusion, as shown in Figure 6. Four node plane-strain quadrilateral elements were used.
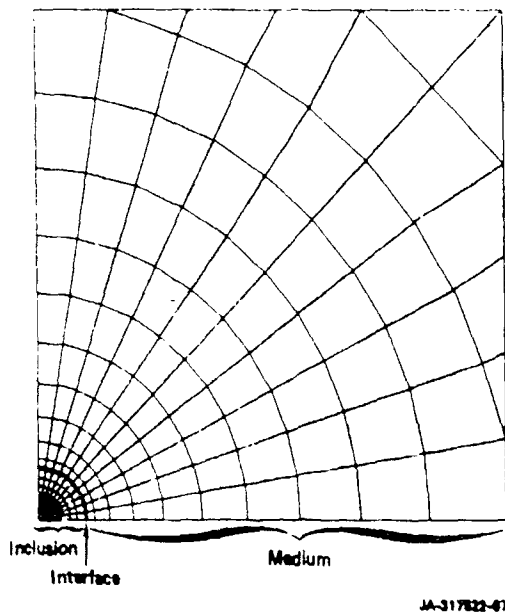
FIGURE 6   FINITE ELEMENT GRID

INTERFACE MODEL

Two inclusion-medium interface conditions are investigated. These conditions are perfectly bonded and free-sliding, and they provide bounds on the real solution behavior. The bonded interface transfers both compressive and shearing loads. The free-sliding interface transfers compressive loads only.

The perfectly bonded interface requires no special modeling technique because the usual finite element node-element connectivity describes this condition.

The free-sliding interface is modeled by a thin ring of two-dimensional Mohr-Coulomb quadrilateral elements to transfer compressive load. The elements are weak in shear to eliminate transfer of shearing stress. The thickness of the ring is 5% of the inclusion radius. Young's modulus and Poisson's ratio of the ring material are the same as the averages of the surrounding material. Numerical tests indicate that cohesion and friction angle values of 10 psi and 0.1° are satisfactory for the tuff-2C4 grout combinations.

NUMERICAL RESULTS

Stress distributions along the gage locations for three cases of an inclusion in tuff are calculated. They are

1) a perfectly bonded grout inclusion,
2) a perfectly unbonded tuff inclusion, and
3) a perfectly unbonded grout inclusion.

The first case illustrates the effect of mismatched material properties; the second case illustrates the effect of an unbonded interface and the third case combines both effects.

In each case, calculations were made for three or four free-field stress levels, the lowest value in each case providing an entirely elastic response.

Case 1. Bonded Grout Inclusion. Figure 7 shows uniform stress distributions along the x and y axes of the grout inclusion for free-field compressive stress of p_x = 4, 5, and 6 ksi, with p_y = $p_x/4$. The calculated stresses at the gage locations are σ_x and σ_y. A gage located on the y axis would measure the x component of free-field stress exactly if σ_x/p_x = -1. When p_x = 4 ksi, this ratio is σ_x/p_x = -1.11, so the gage would read 11% high. As p_x is increased, the readings become more accurate. A gage located on the x axis would measure the y component of free-field stress exactly if σ_y/p_y = -1. When p_x = 4 ksi, this ratio is σ_y/p_y = -0.94, so the gage would read 6% low. When p_x = 5 ksi, the gage would read 9% high and when p_x = 6 ksi, the gage would read 36% high. The stress ratio trend is to increase further because the stress components are confined to the yield surface. The mismatch of properties in this example allows a reasonably accurate measurement of p_x, the larger component of free-field stress. The same is true for measurement of

9

the smaller component under elastic or small plastic deformations. As the loading increases to produce larger plastic deformations, measurement of p_y becomes increasingly inaccurate.
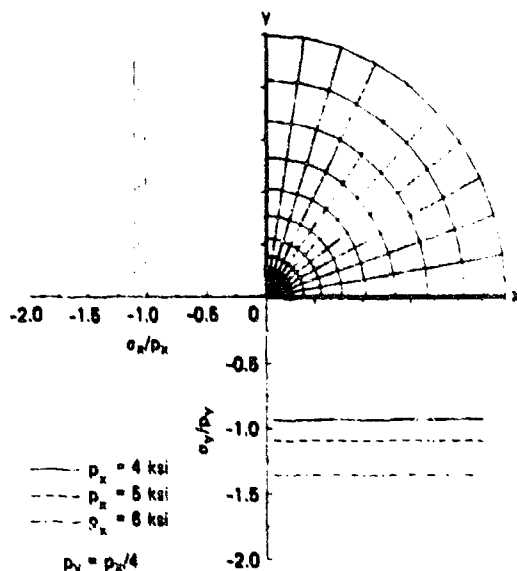
FIGURE 7   GAGE STRESS FOR GROUT INCLUSION WITH BONDED INTERFACE, EXAMPLE 1

FIGURE 8   GAGE STRESS FOR TUFF INCLUSION WITH SLIP INTERFACE, EXAMPLE 2

Case 2. Unbonded Tuff Inclusion. Figure 8 shows the stress distributions along the x and y axes of an unbonded tuff inclusion for free-field compressive stresses of p_x = 5, 7, and 8 ksi, with p_y = p_x/4. A gage located on the x or y axis would measure the free-field stresses exactly if σ_y/p_x and σ_x/p_x are unity. The effect of an inclusion/medium interface that does not transfer shear stress is to produce nonuniform stress distributions. When p_x = 5 ksi the tuff response is elastic and the stress distributions shown (full lines) are parabolic. At the center of the inclusion, the x and y stress components are 15% higher and 61% lower, respectively, than their free-field counterparts. Increasing the free-field loading enough to cause yielding in the inclusion flattens the stress distribution at the center. Approximate measurement of the larger free-field stress, p_x, is possible if the gage does not occupy too much of the inclusion diameter. Measurement of the smaller free-field stress, p_y, can only be regarded as a rough estimate, the value of which depends on the stress level.

Case 3. Unbonded Grout Inclusion. Figure 9 shows the stress distribution along the x and y axes of an unbonded grout inclusion for far-field compressive stresses of p_x = 1-1/2, 4, 5, and 6 ksi, with p_y = p_x/4. This combines the effects of the mismatching of properties of the first case and the lack of bonding of the second case. The main conclusion is that the bonding effect dominates so, as

case 2, approximate measurement of the larger free-field stress p_x is possible but measurement of the smaller free-field stress is not.
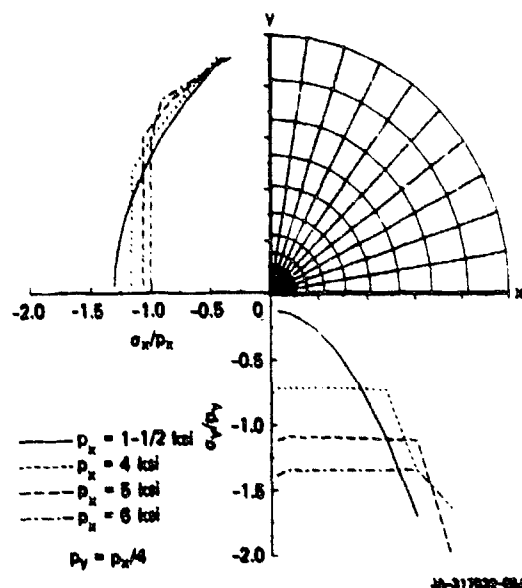
FIGURE 9   GAGE STRESS FOR GROUT INCLUSION WITH SLIP INTERFACE, EXAMPLE 3

CONCLUSION

Based on the numerical examples treating a
grout inclusion in NTS tuff, we conclude that:

- A mismatch of the inclusion and medium
  properties retains a uniform stress
  distribution along the gage locations.
  As loading increases the measurement of
  the larger free-field stress becomes
  more accurate while the measurement of
  the smaller free-field stress becomes
  less accurate. This occurs because the
  smaller stress component in the grout
  becomes related to the larger stress
  component through the yield condition.

- Lack of interface bonding produces non-
  uniform stress distributions along the
  stress gage location. As increased
  loading causes increased plastic flow
  in the inclusion the stress distribu-
  tions become more uniform in such a
  way that the larger free-field stress
  is measurable but the smaller free-
  field stress is not measurable. This
  occurs because the smaller stress com-
  ponent in the grout becomes related to
  the larger stress component through the
  yield condition.

H

FREE-FIELD GROUND SHOCK PRESSURES FROM BURIED DETONATIONS IN SATURATED AND UNSATURATED SOILS

Peter S. Westine
and
Gerard J. Friesenhahn

Southwest Research Institute
San Antonio, Texas

ABSTRACT

Free-field ground shock pressures at various distances from the buried detonation of high-explosive charges, mortar and artillery rounds, and large bombs have been measured by Southwest Research Institute and independently by Waterways Experiment Station personnel. This paper presents an empirical solution capable of predicting these pressures in unsaturated soils. In saturated soils, a very different energy dissipation process occurs which is predicted by modifying a hydrodynamic solution, and comparing it to tests on bombs in saturated soils.

INTRODUCTION

We have been developing a general solution for predicting ground shock pressures and impulses imparted to shelters from the detonation of buried ordnance. Unfortunately, all the results cannot be shown in this short paper; however, one aspect, free-field ground shock pressures, will be presented in detail. Those wishing additional details can refer to reference [1].

Our solution was developed using modeling techniques and test results from a large compilation of ground shock pressure data. Under most conditions, a log-linear curve fit can be used to predict pressures over four orders of magnitude in value. The exception to the general solution arises when soils are saturated. Then, a modified hydrodynamic solution works. In this paper, we will present the general solution, compare results to measured pressures, show that problems can arise and derive the modified hydrodynamic solution.

GENERAL SOLUTION

An empirical equation for predicting free-field ground shock pressure from the detonation of buried explosive is given by:

$$\frac{\left(\dfrac{P}{\rho c^2}\right)}{(4.35+\frac{Y}{d})\left[0.25+0.75\tanh\left(0.48\dfrac{\rho^{1/3}c^{2/3}d}{W^{1/3}}\right)\right]} = 0.0175\left(\frac{W^{1/3}}{\rho^{1/3}c^{2/3}R_{eff}}\right)^{3.42} \quad (1)$$

where
- P = maximum pressure (F/L^2)
- ρ = mass density of soil (FT^2/L^4)
- c = speed of sound in soil (L/T)
- d = depth of ordnance buried to its C.G. (L)
- Y = depth of point below C.G. of ordnance (L)
- W = energy release of explosive (FL)
- R_{eff} = effective slant range which accounts for ordnance geometry and orientation (L).

All ratios in Equation (1) are nondimensional which means that predictions can be made using any self-consistent set of metric or English units. The quantity R_{eff} accounts for bomb length ℓ and orientation θ. This quantity R_{eff} is a first approximation to where an equivalent point source of the same energy release should be located so that the same scaled energy $W/\rho c^2 R^3$ occurs for the distributed energy in a line source of finite length as in the equivalent point source. R_{eff} is given by:

$$\frac{R_{eff}}{\ell} = \left[\frac{N - N^2 - \frac{1}{4}}{\dfrac{N+0.5}{(N+M)^{1/2}} - \dfrac{N-0.5}{(N-M)^{1/2}}}\right]^{1/3} \quad (2)$$

where $N = (Z/\ell)^2+(X/\ell)^2+(Y/\ell)^2+1/4$

$M = (Y/\ell)\cos\theta+(Z/\ell)\sin\theta$

and
- Z = horizontal distance of location in vertical plane through the bomb (L)
- X = transverse distance of location (L)
- ℓ = length of explosive source (L)
- θ = bomb's orientation ($\theta=0$ degrees is a vertical bomb).

COMPARISON WITH DATA

Equation (1) has a format permitting scaled pressure on the left-hand side of the equation to be plotted versus a scaled effective standoff distance on the right-hand side. Many different symbols are seen in Figure 1 because there were many variations in size of explosive energy release (1.8, 0.327, and 0.216 lb sources), orientation of the charge (0, 90, and 45 degrees), depth of burial
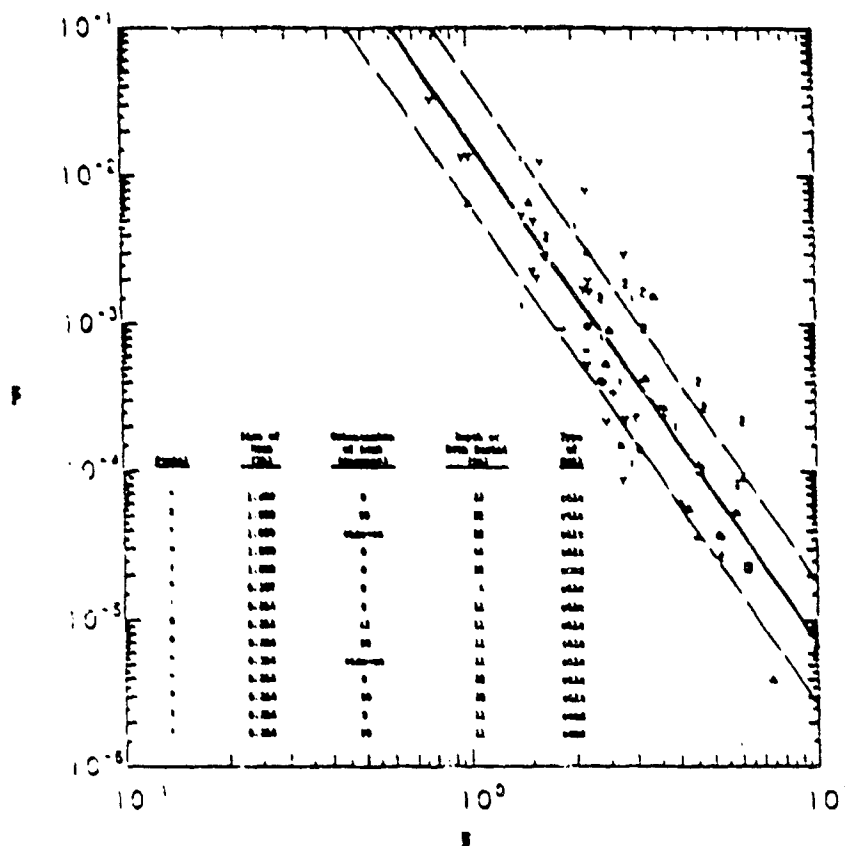
Figure 1. Scaled Pressure Versus Distance in SwRI Tests

of the charge (6, 51, and 22 inches) depth of burial of transducer, and type of soil (silt and sand). All tests were performed outdoors with a natural variation in soil conditions recorded by measuring soil density ρ and velocity c during each test.

The solid line through the pressure data is Equation (1). The dashed lines on each side of the prediction line is a statistical one sigma standard deviation for a normal distribution in log of pressure about the prediction line. Although this scatter may appear to be large, it is of the same magnitude for results from other experiments.

Personnel at Waterways Experiment Station [2] have been conducting tests in which free-field ground shock pressures were monitored at various sites around buried C-4 charges, mortar shells, howitzer rounds, and bombs. In Figure 2 our solution and its scatter is shown so it can be compared to ground shock pressures for 155-mm howitzer shells containing 15.6 lb of TNT, 105-mm howitzer shells containing 4.8 lb of Comp-B, and 4.2-inch mortar shells with 7.8 lb of TNT fired at White Sands Missile Range.

A final comparison conducted at White Sands by WES personnel involved 16, 5, and 8-lb explosive C-4 charges. These scaled pressures are compared to Equation (1) in Figure 3. Because the results seen in Figures 2 and 3 are similar to those seen in Figure 1, the same comments about accuracy and scatter apply.

HYDRODYNAMIC SOLUTION

At another test site, Fort Knox, Kentucky, WES personnel conducted ground shock pressure measurements using live MK-82 (500-lb) and MK-84 (2000-lb) bombs. These bombs contain, respectively, 191 lb and 945 lb of tritonal. Measured pressures were all higher than expected as can be seen by looking at the results in Figure 4. A reason does exist for these pressures being higher than expected, but to understand, we must discuss Fort Knox field conditions.

The soil at Fort Knox is a 10 foot upper layer of soft brown clay overlying a soft clay mixed with gravel. The density of both layers is the same average wet density of 125 lb/ft^3 and water content of 22.5 percent. The major difference between the layers is that the upper layer has a P-wave velocity of 1200 ft/sec; whereas, the lower layer has a
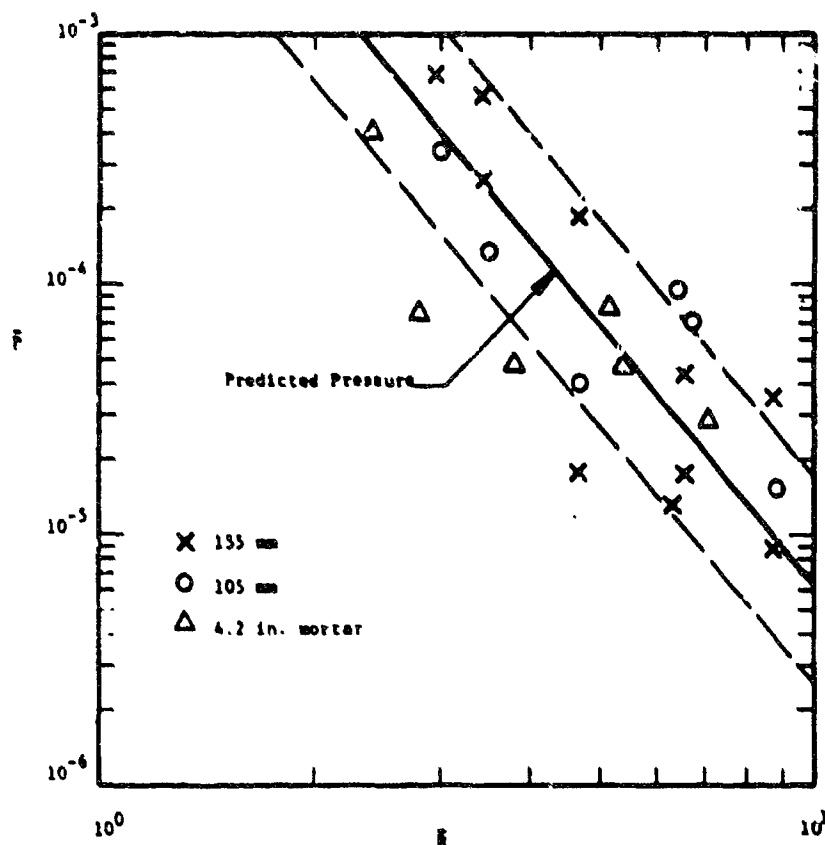
Figure 2. Comparison of Free-Field Pressure Solution to Test Results with 155-mm Artillery Shells

velocity of 4800 ft/sec. Both soils are essentially saturated with the ground water table at the 10-foot depth separating these layers. The upper layer is saturated by capillary action. The change in seismic velocity from 1200 to 4800 ft/sec demonstrates the existence of the ground water table at the 10-foot depth, because 4800 ft/sec is the speed of sound in water.

All other test sites were much drier than Fort Knox. Moisture contents did reach 12 percent, but these are low relative to 22.5 percent. When the pores of a soil are filled with water rather than air, an almost incompressible pore fluid exists. Energy dissipation associated with collapse of the pores and shearing of soil grains over each other is not as great, and pressures are, therefore, higher at various standoff distances.

Instead of using a soil solution, the propagation of shock through saturated soils can be approximated by modifying a solution for shocks in water. In his book on underwater explosions, Cole [3] presents test data which can be curve-fitted using a log-linear approximation to give an equation for shock pressures in water.

$$P(\text{psi}) = 24,650 \left[\frac{W^{1/3}(\text{lb TNT})^{1/3}}{R \ (\text{ft})} \right]^{1.16} \quad (3)$$

By inserting the invariant ρ and c into Cole's dimensional equation, converting Equation (3) to a self-consistent set of dimensionless units, assuming that $\frac{\rho^{1/3}c^{2/3}R_d}{W^{1/3}}$ is large, and that the pressure gauge and bomb are at the same depth, Equation (3) can be rewritten as:

$$\left[\frac{P}{4.15c^2} \right] = 0.04224 \left[\frac{\rho^{1/3}c^{2/3}R}{W^{1/3}} \right]^{-1.16} \quad (4)$$

Equation (4) is the hydrodynamic equation which is shown in Figure 4 and compared to the unsaturated soil solution and test data on MK-82 and MK-84 bombs. As can be seen, the hydrodynamic solution works much better and predicts much higher scaled pressures. The Fort Knox test site with its high ground water table behaves like a liquid. That is to say, provided one assumes that the bombs are in a special "heavy water" with a weight density of 125 lb/ft³ and water that propagates shocks at the measured P-wave velocity, either 1200 ft/sec for shallow burials above 10 feet or 4800 ft/sec

44
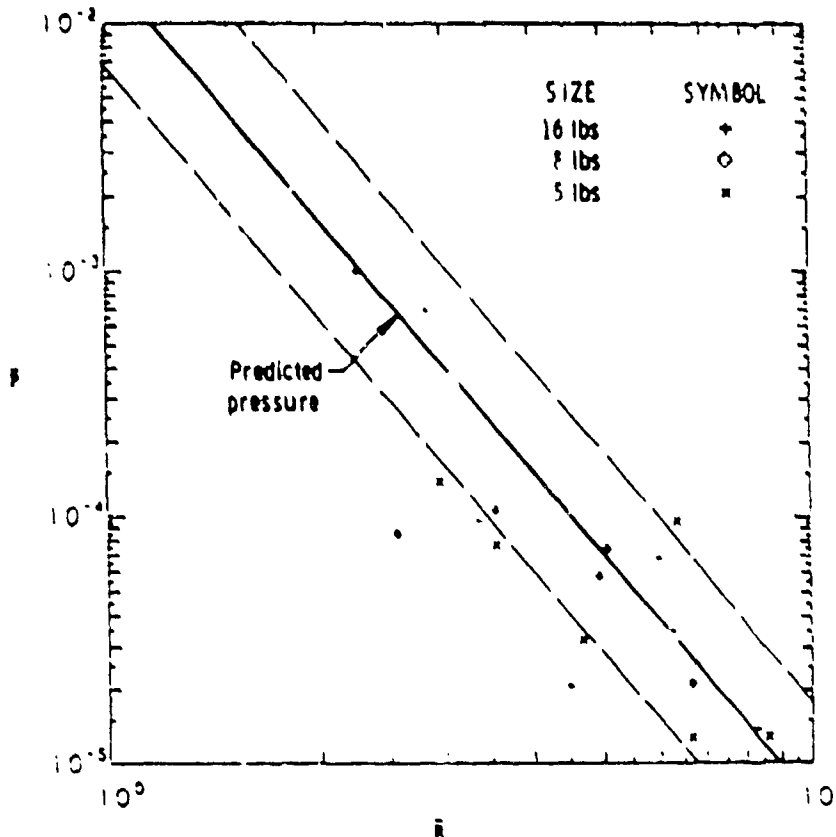
Figure 3. Pressure Versus Distance for WES C-4 Charges

below the ground water table, energy is not dissipated as rapidly in saturated soils, and test results appear to be predicted by this modified hydrodynamic solution.

Obviously some transition regime must exist between the soil and water solutions. Although the data to demonstrate when and how a transition occurs are unavailable for degrees of saturation equal to or less than 50 or 60 percent, the soil solution is recommended. Further study is required to understand and separate these two solutions.

CONCLUSIONS

This paper only presents the results from one small segment of a large report containing information on free-field, oblique, and normally reflected ground shock pressures. In this report, impulse as well as pressures are studied and details are presented on how predictive equations and the R_{eff} concept are derived and test results measured.

In this particular discussion, we showed that free-field ground shock pressures dissipate in very different manners dependent upon whether soils are saturated or unsaturated. Empirical equations are presented which allow free-field pressures to be predicted at various standoff distances in

saturated and unsaturated soils. Test data from a variety of buried ordnance detonations are presented in dimensionless format to demonstrate the validity of these solutions.

References

[1] Peter S. Westine and Gerard J. Friesenhahn, *Ground Shock Loads From Buried Bomb and Ordnance Detonations*, U.S. Air Force Armament Laboratory, Eglin Air Force Base, Florida, Report No. AFATL-TR-82-19, 1982.

[2] As yet unreported data, obtained through personal correspondence with Waterways Experiment Station.

[3] Robert H. Cole, *Underwater Explosions*, Dover Publications, Inc., New York, 1948, p 240.
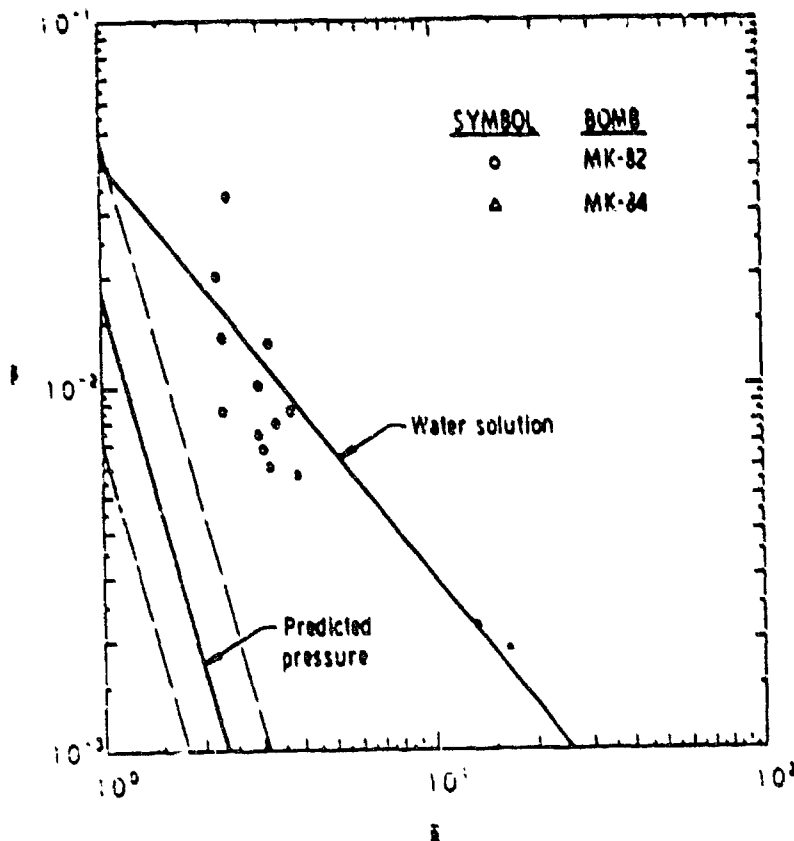
Figure 4. Pressure Versus Distance in Saturated Fort Knox Soils

HIGH VELOCITY PENETRATION INTO FIBRE-REINFORCED CONCRETE MATERIALS - PROTECTION OF BUILDINGS

William F. Anderson, Alan J. Watson, Paul J. Armstrong

Department of Civil and Structural Engineering
University of Sheffield, U.K.

ABSTRACT

Fibre reinforced concrete suitable for spray-
ing onto existing structures is being examined to
assess its resistance to penetration by 7.62mm
diameter armour piercing projectiles. A major test
programme is being carried out to examine the
influence of aggregate type and fibre type. For
each aggregate/fibre combination a statistical
method is being used to plan test series which will
lead to optimisation of the concrete in terms of
water/cement ratio, fibre content and aggregate/
cement ratio. The minimum thickness of optimised
concretes to resist penetration by the projectile
and minimise spall and scabbing, will be determined.
The mechanics of the impact and penetration event
are being studied and a possible method of deflect-
ing the projectile within the concrete is suggested.

INTRODUCTION

During the course of its useful life, a
structure, particularly a military one, may be
subjected to attack from small arms fire, or
perhaps indirect impact from close-proximity
explosions. Hence, high-risk structures should be
constructed from impact resistant materials, and
the capability to rapidly upgrade the protection
afforded by an existing structure would be advant-
ageous. Any such impact resistant material must be
able to contain several different facets of the
impact event. It must be able to resist perfor-
ation from the projectile, it must be of
sufficient thickness to resist tensile scabbing
from the back face and it must also be cohesive
enough to prevent spalling material flying from the
front face, both because this material may be
dangerous in itself and also because it leads to a
local weakening which may then be breached by
repeated impact.

Concrete has a reasonable resistance to
projectile penetration, due to its relatively
homogeneous and massive properties. So far as the
front and rear face damage is concerned, however,
the low tensile strength of an ordinary concrete
matrix ensures that a large amount of material is
ejected from the slab faces with a velocity high
enough to be potentially dangerous. Incorporation
of fibres into the concrete matrix has been shown
to considerably reduce the scabbing and spalling

associated with dynamic loading of concrete (1, 2).
In general, fibres act to increase the toughness
of the composite material by improving the tensile
properties of normal concrete, absorbing the stress
wave energy by either pulling out of the matrix or
perhaps by necking and breaking, depending upon the
characteristics of the particular fibre.

Many different types of fibre are available
commercially, the properties of the fibre rein-
forced concrete being dependent not only on the
standard concrete variables such as aggregate size
and type, aggregate/cement ratio and water/cement
ratio, but also on the type, aspect ratio and
proportion of the included fibres. A comprehensive
testing programme is being carried out to study
the effects of these variables and to optimise the
fibre reinforced concrete to minimise penetration
by 7.62mm NATO armour piercing bullets impacting at
approximately 800 m/s. Attempts are being made to
examine the mechanics of impact and penetration, so
as to understand the failure modes of the fibre
reinforced concrete under dynamic loading.

VARIABLES CONSIDERED

In order to fully utilise the adaptability
of the optimum material, it was felt that a
concrete suitable for sprayed application should
be developed, since this would be equally useful
for new construction and also for quickly rein-
forcing existing structures.

Aggregates

To ensure easy application by either the
'wet' or 'dry' spraying process, and to allow a
reasonable fibre distribution through the matrix a
Concrete Society (3) recommendation of a maximum
aggregate size of 10mm has been adopted.

Tests on rock aggregate/elastomer composites
subjected to impact by projectiles similar to
those used in this study, showed that resistance
to penetration was a function of the rock aggregate
hardness (4). In order to examine the effect of
aggregate hardness on the penetration resistance
of fibre reinforced concrete, crushed basalt
(relatively hard) and crushed limestone (relatively
soft) were chosen as aggregates. The shape of the
aggregate particles has an effect on the concrete
bond also, and thus on the homogeneity of the

composite. Since the crushed rock aggregates are both angular in shape, a rounded river gravel is included in the study to give a comparison. Aggregate/cement ratios vary from 1:3.0 to 1:5.0 in the statistically based test plans.

Fibres

Since it is impractical to include all the commercially available fibre types in an experimental series, various constraints had to be used to select the materials to be tested. On grounds of health and/or durability, vegetable, asbestos and glass fibre materials were rejected, whilst carbon fibre was rejected because it was considered that the likely high fibre content required for the intended purpose would render the unit cost of the fibrous composite too high to be viable. Finally three types of steel fibre, one type of polypropylene fibre and two lengths of the organic polyamide fibre, KEVLAR 29, were chosen for detailed examination. Where appropriate, a length: diameter ratio of 100 was selected to give a composite which could reasonably be mixed in both a field and laboratory situation.

Cement Matrix

In order to ensure that the optimum fibre reinforced concrete can have universal application, Ordinary Portland Cement is being used and it was initially assumed that the type of fine aggregate used would be unimportant. A range of water/cement ratios between 0.35 to 0.50 by weight is recommended by the Concrete Society (3), for ordinary sprayed concrete. However, due to the apparent decrease in workability caused by the inclusion of large volumes of reinforcing fibre, a range between 0.35 to 0.70 was selected for the main statistical series.

OPTIMIZATION OF THE VARIABLES

For each combination of fibre type (six varieties) and aggregate type (three varieties) it is necessary to optimize the water/cement ratio, aggregate/cement ratio and fibre content. To give a reasonable range of these last three variables it was decided that specimens should be prepared with five levels of each variable. This gives 5^3 (=125) possible combinations for each particular fibre and aggregate. Since it would be unacceptable to test all of these combinations (a total of 2,250 tests) a statistical method known as surface response theory has been used to plan a programme. Details of this method have been given by Cochran and Cox (5). For each of the eighteen fibre/aggregate combinations a rotatable design utilising 14 extreme combinations and 6 main combinations of the mix design parameters is used to indicate the combination of mix design parameters which will be most effective in reducing projectile penetration. The response surface derived from the actual test results may not indicate an optimum mix within its (star-shaped) boundaries. Thus the optimum mix design may be indicated as not part of the actually tested range. In this case a "corner filling" technique

as described by Anderson et al (4) may be used to identify and check the optimum mix.

SPECIMEN PREPARATION

In a full scale structure, the fibre-reinforced concrete would be applied over a large area, hence it was considered vital that local and global effects were separated in the laboratory tests, only local effects being considered important. For this reason slabs of various plan dimensions were tested, using a typical steel fibre reinforced concrete mix to determine the minimum target area required to ensure that gross cracking did not occur in most cases. In conjunction with these tests, slabs of various thicknesses were tested in order to obtain a value at which perforation was unlikely to occur in most cases. As a result of these tests, a standard specimen size of 450 x 450 x 125mm was defined.

Since one end use of this material is to be a capability to rapidly upgrade the potential resistance of a existing structure, a major consideration is that age to gain sufficient strength to resist attack must be minimised. Without using fine-ground cements and/or concrete admixtures, the extent to which the commissioning time may be reduced is limited; however it was felt that an age-to-test of three days represented a reasonable compromise.

All mix designs were developed assuming completely dry aggregates. Since it is not possible to justify this assumption with available material, a moisture content calculation, using a standard siphon-can test (British Standard 812 (7)) is carried out on each aggregate immediately prior to casting. The percentage moisture content by dry aggregate mass is calculated, this contribution being allowed for by an increase in aggregate weight and a decrease in weight of water in the final mix designs.

All mixing is carried out in a horizontal rotating pan mixer; the concrete constituents are charged in a standard order, that is, fine and coarse aggregates mixed together before the cement and water are simultaneously added to the mix. For all the various fibre types it was found that the optimum fibre distribution was established by adding the fibre to the already mixed concrete matrix. This ensures a minimum of 'balling' of the discrete fibre lengths. In the case of both the steel and polypropylene fibres, sufficient separation can be achieved by shaking the fibres slowly into the surface of the rotating matrix, through a large mesh. A more rigorous and time-consuming process is necessary to persuade the very fine (12μm) KEVLAR-29 single filaments to separate to an acceptable degree. The procedure adopted is to initially separate the matted fibre by hand to reduce it to reasonably small conglomerations. It is then pneumatically injected directly onto the surface of the rotating concrete so as to further encourage it to separate. The more open mat can thus be worked into the concrete by the action of the mixer paddles. Whilst this

method does not ensure a complete separation of all the fibre conglomerations it does give a composite mix of reasonably uniform appearance, becoming less acceptable towards the maximum fibre volumes which can be incorporated. In a field situation it would perhaps be more viable to use a technique in which the sprayed concrete passes through a pneumatically held curtain of fibre, though the practical problems of this kind of approach have not yet been fully considered.

All specimens are de-moulded after one day and stored in a standard high humidity room (20 ± 1°C:90% + R.H.) until immediately prior to testing.

TEST TECHNIQUE

After curing specimens are rigidly fixed in a target frame offering firm edge support to the back face of the specimen, with the 450mm square cast face pointing towards the projectile firing equipment.

The projectiles are fired remotely in an enclosed 20m long firing range. A 7.62mm diameter rifle barrel is attached to a pressure housing incorporating a breech, firing pin, bolt and trigger mechanism with safety catch. The pressure housing is itself rigidly attached to a steel frame which in turn is bolted to the range floor. The trigger mechanism is connected by a detachable linkage rod to an 11.4kg pullout, 18mm stroke length mains solenoid. For safety reasons the solenoid is activated remotely using a firing box fitted with an arming key and off-biased switch. Connection wires are coaxial and a capacitor is used across the switch to reduce electrical interference with ancillary equipment.

Bullet velocities are monitored using photodiode-based trigger circuits to start and stop an electronic timer. Usually, two stations are used, placed close to the target and one metre apart, although the option of using three stations, both to give a velocity check and also to calculate deceleration, is available. The timer is triggered by a change in voltage output experienced by the photodoide circuit when the bullet passes between a focussed light source and the light-sensitive photodiode. A 70-80% success rate is normally achieved with this equipment, failure being due usually to external interference causing premature triggering.

High speed photography is being used in an attempt to capture the detail of the impact event. Using a Barr and Stroud rotating mirror camera, capable of a framing rate up to two million frames per second over 30 frames, a series of photographs of the bullet in flight taken at 1.5µs interframe has been produced. The variable nature of both the bullet detonation and the velocity in flight make it difficult to accurately predict the time to impact of the projectile with any degree of precision (relatively to the camera's capabilities). Hence, any attempt at photographing the bullet in this way must carry only a limited probability

of success. In order to offset this, a rotating prism camera, capable of up to 20,000 frames per second is also being used, though this is not capable of the same amount of detail.

Various types of detector to measure crack velocity, spall characteristics, stress wave propagation and projectile retardation through the target are also under development.

POST TEST ANALYSIS

Damage to an impacted target consists of front face spall damage, a burrow and possibly back face scab damage. Spalling and scabbing result in craters being formed, the extent of damage may then be quantified in terms of the dimensions of these depressions. With fibre inclusions a lot of damaged material remains loosely attached to the target. This is removed to expose the true crater whose depth at various grid points can be found using a specially constructed rig with depth gauge connected to a displacement transducer which in turn is connected via an analogue/digital converter to a microcomputer. This automatically produces crater profiles and calculates crater volumes. Details have been given by Anderson et al (6).

Preliminary tests in which target perforation occurred showed that the projectile exit hole was rarely in line with the initial impact hole. Deviation of the projectile from its original flight path must have taken place within the target. Since to assess the resistance of the particular specimen it is necessary to measure the penetration path length, a 150mm diameter core is taken perpendicular to the target front face and containing the damaged section of the sample. If the slab has not been perforated, thin slices are sawn from the rear face of the core, and parallel to it, until the hardened steel tip of the projectile is encountered. Using both this point and the entrance position of the projectile, a most probable path may now be estimated to allow the core to be sectioned, thus exposing the burrow formed in the composite.

RESULTS AND COMMENT

This experimental programme is still in progress and very few statistical series have been completed, those serving only to establish the arithmetical correctness of the microcomputer based analysis. Various practical difficulties have yet to be overcome, including control of the aggregate moisture content and a valid method of assessing its contribution to the concrete matrix. Since using the dry mix spraying process water/cement ratio is controlled by the spray gun operator, it is important that a fundamental understanding of the effect of varying water content is attained. It is considered that, providing a rigorous control of the fibre concrete constituents can be ensured, the surface response theory approach should give an acceptable solution, within the limits dictated by the nature of dynamic testing.

Experimental work is proceeding to establish the mechanisms of failure and also to record the characteristics of the overall impact event. Examination of a sectioned sample, after penetration, typically shows a crater of approximately 100-130mm diameter and 30-40mm depth developing into a burrow, which may be straight for the first 20-30mm. However, probably at the point where the copper jacket strips from the hardened steel core, the penetration path deviates from the original flight path (i.e. normal to the impact face) by an angle of up to approximately 80°, the position of this deviation is marked both by the presence of the jacket and also by a local widening of the burrow, as shown in Plate 1.

The hardened steel core may then continue along the new straight path for a distance of up to 70-80mm before coming to rest, Plate 2. Alternatively the same sort of distance may be travelled on a curving path, Plate 3, which may, in extreme cases, lead to the projectile coming to rest in a direction totally opposite to its orientation on entry, Plate 4. It should be noted that these targets have been sectioned and the full thickness is not shown in Plates 3 or 4. If the change of projectile direction is extreme, and perhaps dependent upon whether the core is in collision with aggregate or mortar immediately after the copper jacket is stripped, the hardened steel core may undergo a stress which exceeds the material strength, hence the core fractures and rapidly comes to rest, Plate 5.

Preliminary penetration tests carried out on specimens prepared to determine the maximum volume of KEVLAR-29 which could be incorporated in the concrete mix indicated an interesting trend. In several cases it was observed that normal penetration depth, as opposed to penetration path length, was much lower than expected because of gross deviation of the projectile during penetration. This change in path seems to have occurred as the projectile travelled through conglomerations of fibre within the composite. These conglomerations of fibre were a result of trying to incorporate too much fibre in the mix. This behaviour suggests that the projectile may be induced to deviate during penetration by incorporating a series of "relative voids" (compared to the density of the concrete) into the composite. First indications are that the voids need to be slightly smaller than the projectile length to induce instability.

Some problems exist with this type of approach however, the first being that it is necessary to fully understand the mechanisms involved in the projectile/composite interaction in order to ensure that deviation does occur. Another problem is the reduction in structural integrity which will result from deliberately including voids in the concrete. It may perhaps be necessary to restrict the use of such a material, employing it solely for up-grading pruposes on existing structures. The difficulty of ensuring a reasonable distribution of "relative voids" using

Projectile impact trajectory

Spall region

Copper sheath

Aggregate particle

Lead plug

Hardened steel core

Saw cut
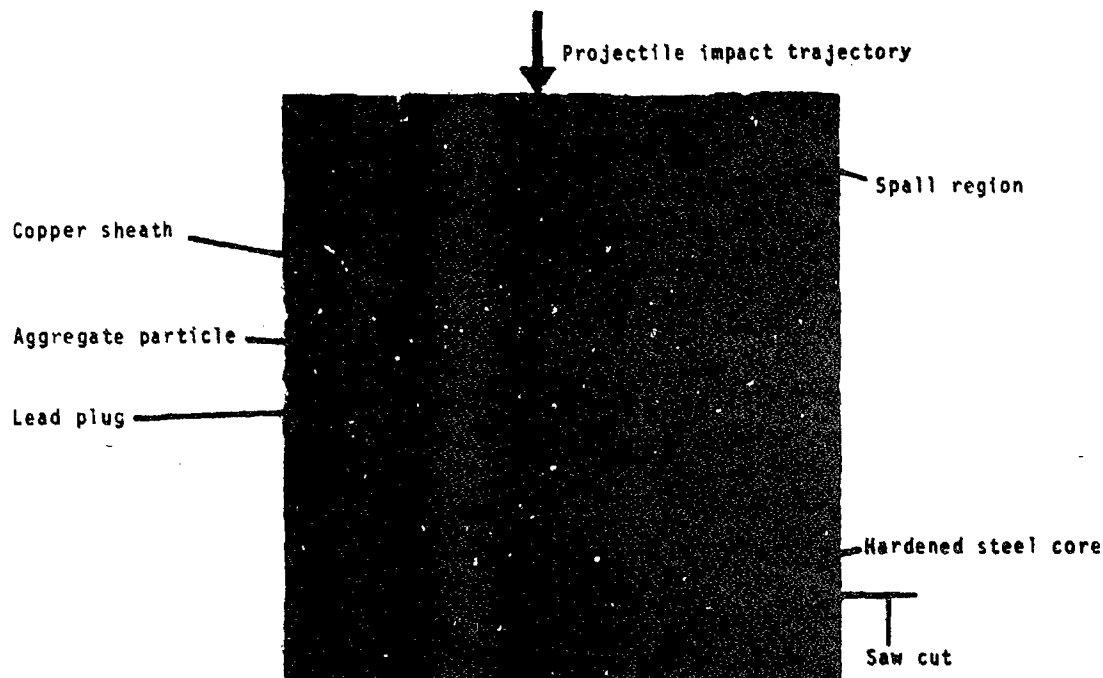
Plate 1   Penetration of hardened steel core projectile through a fibre reinforced concrete target showing deviation of projectile path where sheath is stripped from projectile core

Plate 2   Deviation of projectile along a
           straight path

Plate 4   Deviation of projectile to complete
           a U-turn
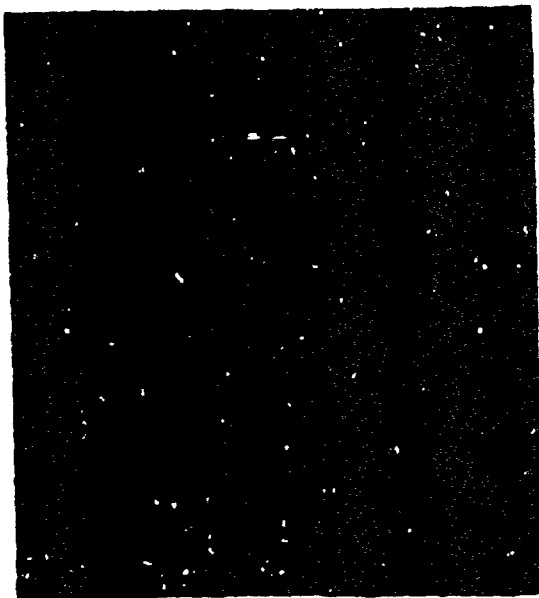
Plate 3   Deviation of projectile along a
           curved path

Plate 5   Deviation of projectile causing
           fracture of the hardened steel core

a sprayed concrete process would also need to be overcome.

REFERENCES

1. MAYRHOFER, C. and THOR, H.J. Dynamic response of fibre and steel reinforced concrete plates under simulated blast load. Proc. Symposium on Concrete Structures under Impact and Impulsive Loading, West Berlin, 1982, pp. 279-288.

2. BULSEWIG, M., STILP, A. and PAHL, H. Behaviour of fibre reinforced concrete slabs under impact loading. Proc. Symposium on Concrete Structures under Impact and Impulsive Loading, West Berlin, 1982, pp. 322-328.

3. CONCRETE SOCIETY. The concrete soceity code of practice for sprayed concrete. Cement and Concrete Association, Wexham Springs, Slough, 1980.

4. ANDERSON, W.F., WATSON, A.J., JOHNSON, M.R. and McNEIL, G.M. Optimization of rock/polymer composites to resist projectile penetration. RILEM Materials and Structures, in press, 1983.

5. COCHRAN, W.G. and COX, G.M. Experimental Designs. Wiley Publications, New York, 1953.

6. ANDERSON, W.F., WATSON, A.J. and ARMSTRONG, P.J. High velocity projectile impact on fibre reinforced concrete. Proc. Symposium on Concrete Structures under Impact and Impulsive Loading, West Berlin, 1982, pp. 367-378.

7. BRITISH STANDARDS INSTITUTION. B.S. 812 : Methods for sampling and testing of mineral aggregates, sands and fillers, Part 2 : Physical Properties, 1975.

ANALYTICAL AND EXPERIMENTAL STUDIES ON PENETRATION INTO GEOLOGICAL TARGETS

M. J. Forrestal

D. B. Longcope   L. M. Lee

Sandia National Laboratories   Ktech Corp.
Albuquerque, NM 87185   Albuquerque, NM 87110

ABSTRACT

This paper summarizes some recent analytical and experimental work on penetration into geological targets. Results from several elastic-plastic type theoretical models which predict forces on penetrators for normal impact into dry porous rock, concrete, and sea ice targets are presented and compared with measurements from field tests. Rigid-body acceleration data from newly developed laboratory scale experiments for impact velocities between 0.2 and 1.2 km/s are also presented.

ANALYTICAL MODELS

In recent papers, Forrestal and Longcope [1,2,3] develop several elastic-plastic type theories to predict forces on conical-nosed penetrators. Constitutive target description consists of a linear hydrostat and a Mohr-Coulomb failure criterion with a tension cutoff [4]. Mathematically,

$$p = K\eta \tag{1a}$$

$$\sigma_r - \sigma_\theta = \mu p + \tau_0 \quad , \quad \tau_0 = (1 - \mu/3)Q \tag{1b}$$

$$\sigma_\theta \geq - Y \tag{1c}$$

where p is hydrostatic pressure, η is volumetric strain, σ_r, σ_θ are radial and circumferential stress components, measured positive in compression, Q is unconfined compressive strength, and Y is tensile strength. As shown in [1,2], these equations provide reasonably accurate data fits to triaxial material test data for dry porous rock, concrete, and sea ice. These analyses use the cylindrical cavity approximation [5] which idealizes the target as thin independent layers normal to the penetration direction and simplifies the problem to one-dimensional wave propagation in the radial direction. Governing equations are subsequently reduced to

nonlinear ordinary differential equations with a similarity transformation and solved numerically or in closed form.

Layers of target material are expanded by the penetrator nose which opens a cavity large enough to permit penetration. This expansion produces annular regions of plastic and elastic response. Forrestal and Longcope [1,2,3] develop four target response models; rigid-plastic, elastic-plastic, rigid-cracked-plastic, and elastic-cracked-plastic. The elastic-plastic model is derived first and results show that circumferential target stresses in excess of reported tensile failure values [4] can be developed. To correct for this inadequacy, the rigid-cracked-plastic model is developed. This model has three regions of response; a plastic region next to the penetrator nose, a radially cracked region with circumferential stress set to zero, and a rigid region. As typical with rigid regions in plasticity solutions, particle velocity is taken as zero and the stresses are taken as those from the static solution [6]. For the elastic-cracked-plastic model, the rigid region is replaced by an elastic region.

To calculate penetration resistance, radial stress on the penetrator nose is required as a function of the target material properties, penetrator nose shape, and penetrator axial velocity. As derived in [7], the axial resultant force on a conical nose is given by

$$F = \pi a^2 \sigma_r \tag{2}$$

where a is the radius of the cylindrical afterbody and σ_r is the radial stress on the penetrator nose calculated from the target motion analyses described above. Radial stresses on the penetrator nose from the four response models for a sea ice target with $\rho_0 = 0.92$ Mg/m^3, K = 4.0 GPa, $\tau_0 = 10.5$ MPa, $\mu = 0$, Poisson's ratio $\nu = 0.27$, and Y = 0.86 MPa are shown in

23

in Fig. 1. These data and equation (2) can easily be applied to obtain penetrator rigid-body motion. Radial stress curves of the type shown in Fig. 1 are given in [1] for a concrete target and in [2] for a dry porous rock target.

COMPARISON OF PREDICTIONS WITH FIELD TEST DATA

Test results for penetration into pack ice targets located in the Lincoln Sea, near Alert, Northwest Territory, Canada, are reported by Young [9]. The penetrators had total length 1.07 m, outer diameter 70 mm, a conical nose with length 140 mm, and mass 23 kg. Four penetrators were air-dropped and impacted the pack ice layer at $V_g = 159$ m/s. Onboard accelerometers, signal conditioning equipment, and a transmitter were contained within the penetrators. The transmitter package occupied the aft 18 mm of the penetrator and was stripped from the main penetrator by fins which eventually interacted with the ice target near the surface. Thus, the transmitter remained near the ice surface, remained electrically connected to the main penetrator with a trailing line, and transmitted acceleration-time data to an airborne receiving station. Four deceleration-time records with 1 kHz resolution are presented by Young [8] and one of these records is shown in Fig. 2.

Predictions of rigid-body penetrator decelerations using bounds on the shear strength data are also shown in Fig. 2. From Fig. 1 and equation (2), deceleration is calculated from

$$m \frac{dV_g}{dt} = -F \qquad (3)$$

where m is the penetrator mass. The penetrator strikes the target at $V_g = 159$ m/s and the calculation starts when the nose is fully embedded. After nose penetration, $t > 1$ ms, the theory predicts a slight decay. At $t = 8$ ms, the penetrator has traveled one body length and it is assumed that the transmitter package with mass 3.2 kg has been suddenly removed by the ice crater. This mass change produces the acceleration jumps shown in Fig. 2. After $t = 8$ ms, the penetrator progresses with mass 19.5 kg and eventually comes to a sudden stop. The sudden deceleration change occurs because a minimum threshold value of radial stress is required to open a cavity and permit penetration. This threshold stress is the quasi-static solution shown in Fig. 1 for V approaching zero.

Comparison of predictions and measurement from a field test into Antelope tuff, a dry porous rock target, at the Sandia Tonopah Test Range, Nevada, is shown in Fig. 3. This penetrator has total length 1.56 m, afterbody diameter 0.156 m, mass 162 kg, and an ogival nose with 6.0 CRH. The previously discussed theories are developed for conical-nosed penetrators, whereas this penetrator has an ogival nose. Data from several hundred soil penetration tests [10] indicate that a 6.0 CRH ogival nose and a conical nose with half apical angle $\phi = \tan^{-1} 0.30$ are nearly equivalent and this is used for the trajectory calculation. For this test the penetrator was propelled with a Davis gun and impacted the Antelope tuff layer at 520 m/s; other test details are reported in [2].

As discussed in [2,9], sliding frictional forces produce an additional source of resistance to penetration and the predictions shown in Fig. 3 include and neglect sliding friction. Frictional resistance is velocity dependent [11] and this mechanism is required in order to qualitatively predict deceleration-time profiles into dry porous rock targets.

LABORATORY SCALE EXPERIMENTS

Recent laboratory experiments were devised [12] in order to complement field test programs and to obtain data at impact velocities beyond the current field test capability. Gas guns are used to accelerate foundry core targets (a simulated soft sandstone) to steady velocities after which the targets impact 20.6 mm diameter penetrators instrumented with piezoelectric accelerometers. Rigid-body acceleration data are recorded for one ogival and two conical nose shapes over impact velocities between 0.2 and 1.2 km/s. Data from these penetration experiments show a departure in the scaling law which relates force to penetrator velocity for all three nose shapes at impact velocities in the neighborhood of 0.5 to 0.6 km/s, which is currently the limiting impact velocity for full scale tests.

Data and a power law fit for a 6.0 CRH nose shape are shown in Fig. 4. Penetration data in Fig. 4 were obtained from experiments conducted on the Air Force Weapons Laboratory 102 mm bore gas gun and the University of Dayton Research Institute 178 mm bore gas gun. Majority of the data were obtained with the 102 mm gun and the experiments with the 178 mm gun were conducted in order to demonstrate that sample size did not significantly affect penetration resistance.

24

The analytical models discussed previously are elastic-plastic models. However, triaxial test data for the foundry core material [12] indicate no yielding of the material and the existing models are not directly applicable. Work on modeling of the foundry onre material and developing a penetration theory for this target material will be conducted in the future. Since empirical models are widely used as predictive tools, the data in Fig. 4 can be described conveniently in the form

$$P = KV^n \quad , \quad 0.5 < V < 1.2 \text{ km/s} \qquad (4)$$

where $K = 109$, $n = 1.29$, and P, V have units of kN, km/s. The root mean relative error for the data fit is 0.6 percent.

REFERENCES

1. M. J. Forrestal and D. B. Longcope, "Closed-Form Solutions for Forces on Conical-Nosed Penetrators Into Geological Targets With Constant Shear Strength," Mechanics of Materials, Vol. 1, No. 4, Dec. 1982, pp. 285-295.

2. D. B. Longcope and M. J. Forrestal, "Penetration of Targets Described by a Mohr-Coulomb Failure Criterion With a Tension Cutoff," to be published Journal of Applied Mechanics.

3. M. J. Forrestal, "Forces on Conical-Nosed Penetrators Into Targets With Constant Shear Strength," submitted for publication.

4. R. E. Goodman, Introduction to Rock Mechanics, John Wiley and Sons, New York, 1980.

5. R. F. Bishop, R. Hill, and N. F. Mott, "The Theory of Indentation and Hardness Tests," The Proceedings of the Physical Society, Vol. 57, Part 3, pp. 147-159, May 1945.

6. R. Hill, The Mathematical Theory of Plasticity, Clarendon Press, Oxford, 1950.

7. M. J. Forrestal, F. R. Norwood, and D. B. Longcope, "Penetration Into Targets Described by Locked Hydrostats and Shear Strength," International Journal of Solids and Structures, Vol. 17, pp. 915-924, 1981.

8. C. W. Young and L. J. Keck, "An Air-Dropped Sea Ice Penetrometer," SC-DR-71-0729, Sandia Laboratories, Albuquerque, NM, Dec. 1971.

9. M. J. Forrestal and D. E. Grady, "Penetration Experiments for Normal Impact Into Geological Targets," International Journal of Solids and Structures, Vol. 18, No. 3, 1982, pp. 229-234.

10. C. W. Young, "Depth Prediction for Earth Penetrating Projectiles," Journal of Soil Mechanics and Foundation, Division of ASCE, May 1969, pp. 803-817.

11. F. P. Bowden and D. Tabor, "The Friction and Lubrication of Solids," Part II, Chapter 22, Oxford, 1968.

12. M. J. Forrestal, L. M. Lee, B. D. Jenrette, and R. E. Setchell, "Penetration Into Simulated Geological Targets at Impact Velocities Between 0.2 and 1.2 km/s," submitted for publication.
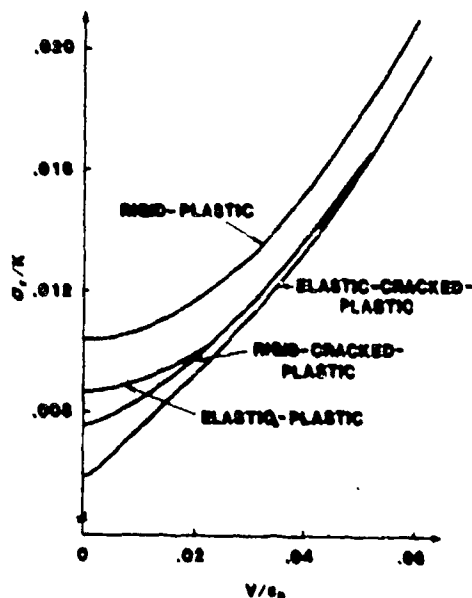
Fig. 1. Radial stress on the penetrator conical nose. $V = V_z \tan \phi$, $C_p^2 = K/\rho_0$ where V_z is axial penetrator velocity and ϕ is the half apical nose angle.
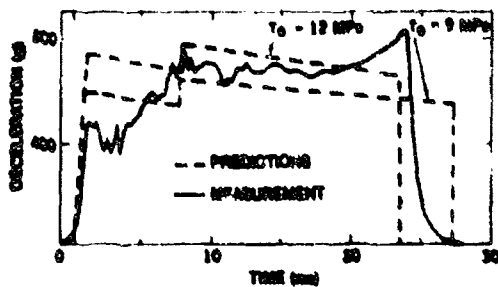
Fig. 2. Deceleration-time measurement and prediction bounds for a sea ice target.
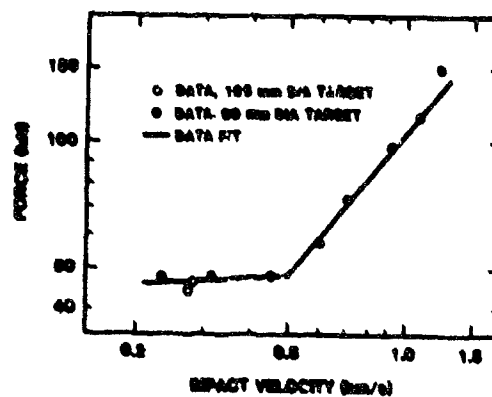
Fig. 4. Laboratory scale data and power law fit for a 6.0 CRH ogival nose.
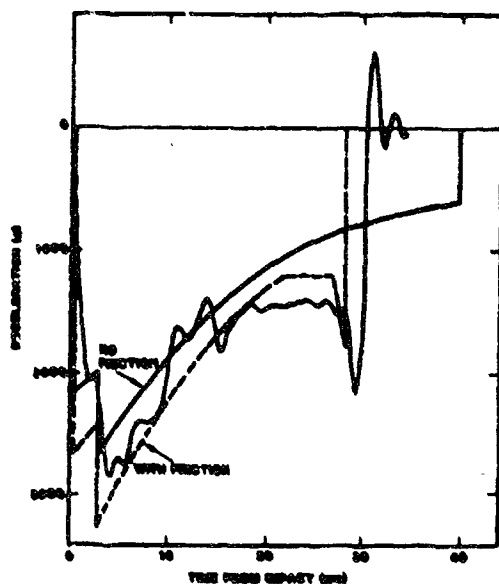
Fig. 3. Deceleration-time measurement and predictions for a dry, porous rock target.

26

PENETRATION BEHAVIOUR OF HIGHLY DEFORMABLE
PROJECTILES IN CONCRETE SLABS

M. Hülsewig, E. Schneider and J. Stilp

Ernst-Mach-Institut, Freiburg, FRG
Terminal Ballistics and Impact Physics Division

ABSTRACT

Investigations of the penetration be-
haviour of deformable projectiles in re-
inforced concrete slabs show that
classical penetration formulas develop-
ed for rigid projectiles are not appli-
cable to describe the penetration at im-
pact velocities between 100 and 400 m/s.
The measured crater depths are smaller,
the divergence increases with higher ve-
locities, because the projectile de-
formation itself consumes a considerable
amount of the kinetic energy of the pro-
jectile.

INTRODUCTION

Before and during World War II many
experimental investigations concerning
penetration and perforation of projec-
tiles into concrete slabs have been per-
formed. The results of these tests formed
a data base for many empirical and semi-
empirical formulas. However, these for-
mulas are strictly applicable only for
these input data.

In recent years special emphasis
has been given to the problems of impact
of highly deformable projectiles, e.g.
airplane crash on a nuclear power plant.
The purpose of investigations performed
at the Ernst-Mach-Institut, Freiburg, is
to study the penetration as well as de-
formation of highly deformable projec-
tiles within the velocity range between
100 and 400 m/s. The influence of target
dimensions on the crater depth will be
discussed.

FACILITY DESCRIPTION, PROJECTILE
AND SABOT DESIGN

The launcher (Fig. 1) is a com-
pressed air gun for the low velocity re-
gime (50 - 250 m/s) and a normal powder
gun for the higher impact velocities.
For both configurations the same launch
tube is used. The launcher consists of a
pressure reservoir and a smooth-bore

100 mm diameter launch tube. A diaphragm
separates the two parts, mylar or aluminium
are used as diaphragm materials. Pressure
reservoir and launch tube are coupled with
a hydraulic clamp. The velocity of the test
item is controlled by varying the pressure
in the case of air gun. The gun is fixed
on a stable platform.

The gun fires into a closed range.
This range consists of three parts (Fig.2):
a blast tank (3), the velocity measurement
station (4) and the impact tank (5). Sabot
separation from the projectile takes place
in the blast tank. Measurements of projec-
tile velocity are typically performed on
each test using two direct shadowgraph
stations with point light sources and an
electronic counter. The point spark light
sources are triggered by laser light
screens or by rupture of a thin copper
wire.

Two typical shadowgraph pictures with
the nose of the projectile are shown in
Fig. 3. The projectile velocity is deter-
mined to an accuracy of about $\pm$ 0.5 %.
The concrete slabs are suspended in the
impact tank. The angle of incidence can be
varied from $0°$ up to the ricochet angle by
rotating the target suspension. The pro-
jectiles are scaled 500 lbs and 1000 lbs
general purpose bomb-models (scale factor
1 : 4,5). Bomb-models and targets have
been scaled according to the scaling laws
[1]:

1. All linear dimensions of the targets
   and projectiles should be reduced in
   proportion to the scale.
2. Original and model should have the
   same geometrical shape.
3. The models and the originals should
   have the same densities and strength
   properties.
4. The impact velocities of full scale
   and model tests should be equal.

The scaled bomb-models are shown in
Fig. 4. Only the mean dimensions of the
bomb-models are scaled exactly. Details
like fins, fuse etc. have been ignored.

Fig. 1 Photo of impact facility
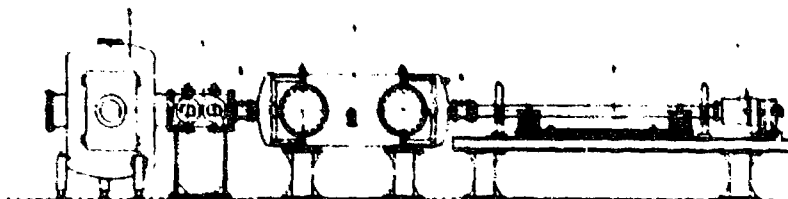
Fig. 2 Schematic of impact facility

The sabot for the 1 : 4.5 scaled GP-bomb-models is a four pieces sabot with a polyethylene pusher. Its function is to protect the bomb-model from high pressure and to guide and accelerate the projectile in the launch tube. It must serve as a good pressure sealing during the acceleration. The sabot should be as light as possible and as strong as possible. Hard styrofoam is used for the four pieces, because this material is light and relatively strong. For higher velocities the foam-material can be reinforced with stronger materials, fibers etc. The sabot configuration is shown in Fig. 5.

The targets are concrete slabs of quality BW35 with cubic reinforcement. The size of the targets was 80 x 80 x 40cm, thick enough to prevent spallation at the
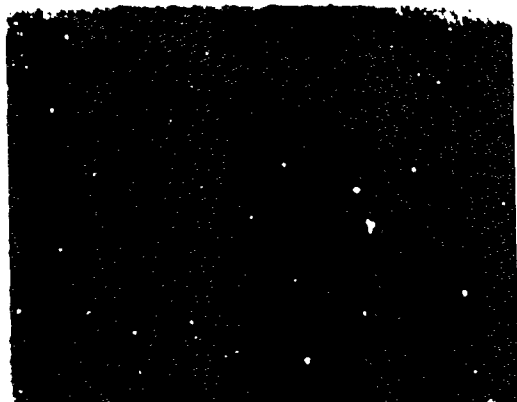
Fig. 3 Shadowgraphs of the projectile
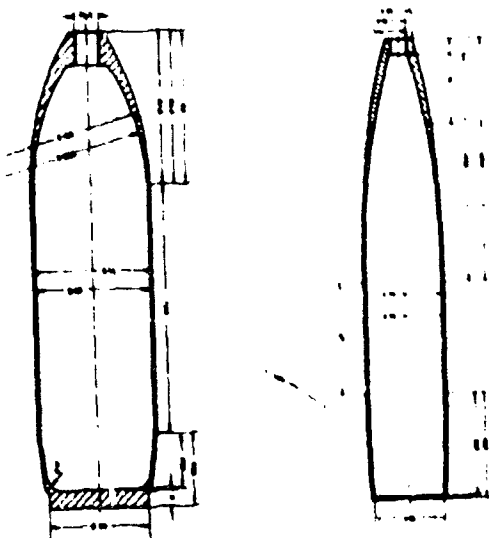
Fig. 4 Bomb models

Fig. 5 Sabot configuration

rear side of the target. Thus, the target can be considered semi-infinite, because the target thickness was substantially thicker than the crater depth for all tests.

RESULTS

The measured crater depths produced by the 500 lbs-GP bomb-model are shown in Fig. 6 in comparison with well known penetration formulas: Petry Formula, Corps of Engineers formula (COE) and National Defence Research Committee (HN-NDRC) formula.

Within the velocity range investigated a considerable discrepancy between measured and predicted crater depths is obvious. All experimental data range below the calculated ones, only the Petry formula gives some accordance with the experimental data at low velocities (100 - 150 m/s). The reason for this discrepancy can be derived from Fig. 7. It shows that the projectiles behave as rigid bodies only up to a velocity of about 100 m/s, for higher velocities plastic deformation is of increasing influence. An increasing amount of kinetic energy is needed for the deformation, reducing the energy portion available for cratering. In addition, an
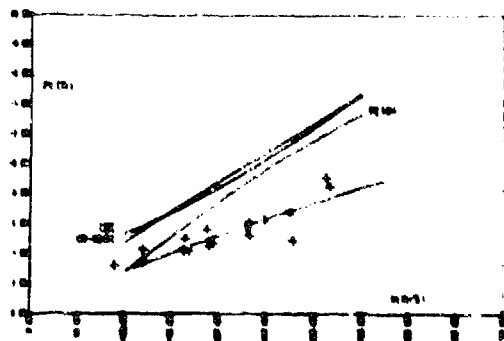
Fig. 6 Penetration depth versus impact
velocity (comparison with formulas)

Fig. 8 Penetration depth versus impact
velocity (comparison with Kar-
formula)

Fig. 7 Deformed bomb models
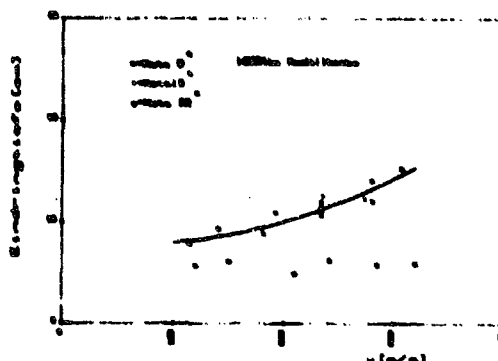
Fig. 9 Penetration depth for different
impact angles

increase of the projectile cross section
is observed, which leads to lower pene-
tration depths. Since 1975 several impact
formulas have been developed for deform-
able projectile penetration. One of them
is the Kar-formula [2,3].

In Fig. 8 the Kar formula is plotted
together with the penetration depths ob-
tained from the 500 lbs and 1000 lbs mo-
del-bombs. It is in good accordance with
the experimental data obtained with the
1000 lbs model-bombs having a smaller
caliber/wall thickness ratio than the
500 lbs model-bombs. For the more de-
formable 500 lbs bomb models, however,
accordance is only observed at lower ve-
locities (< 150 m/s). The penetration
formula of Kar, therefore seems to be
valid only for weakly deformable pro-
jectiles. Furthermore the influence of
the angle of incidence on cratering has
been investigated. In Fig. 9 correspond-
ing penetration depths for 0°, 15° and
30° are plotted versus the impact ve-
locity. The 30° values are only in

accordance up to velocities of about
150 m/s. For higher velocities the pene-
tration depths are no longer increasing.

The considerable scatter of data for
oblique impact is due to an increasing
influence of the reinforcement. It is well
known that no influence of plate thickness
on crater depth is measurable if the plate
thickness is more than three times the
crater depth. For lower values we observe
a more or less strong influence of the
plate thickness on the crater depth. Only
little is known about the influence of the
lateral plate dimensions on crater depths.
In order to study this influence, plates
with different lateral dimensions have
been impacted and also plates with iden-
tical dimensions were impacted are differen
distances from the edge of the plates. The
results show that in both cases only a
small increase of crater depth was ob-
served as long as the crater depths are

30

much smaller than the thickness of the plates.

CONCLUSION

The results demonstrate that the penetration behaviour of highly deformable projectiles in concrete is substantially different from the penetration of rigid bodies and therefore "classical" penetration formulas cannot be applied.

REFERENCES

[1] Development of a Scaling Law and
Technique to Investigate Penetration
in Concrete
J.A. Canfield and I.G. Clator
NWL Report No. 2057 (August 1966)

[2] Assessment of Empirical Concrete
Impact Formulas
G.E. Sliter
Journal of the Structural Division
(May 1980)

[3] Projectile Penetration into Buried
Structures
A.K. Kar
Journal of the Structural Division,
(Jan. 1978)

RAPID RUNWAY CUTTING WITH SHAPED CHARGES

Charles E. Joachim

U. S. Army Engineer Waterways Experiment Station

ABSTRACT

Research has shown that removal of large, partially damaged, concrete runway slabs is a major element in the time required to perform a runway repair operation. A rapid method for cleanly cutting away damaged sections would significantly reduce overall repair time. Shaped charges are potentially just such a rapid runway cutting technique. This paper presents the results of field tests designed to evaluate the runway cutting abilities of standard and linear shaped charges. A series of 25 runway cutting tests was conducted on the 1-ft-thick (4 in of asphalt + 8 in of concrete) undamaged taxiway segments constructed for a recent Air Force test program at the White Sands Missile Range. Although TOW warhead charges successfully penetrated well into the subgrade, no cracks were observed between holes, even at the closest charge spacing. Arrays of linear shaped charges were successfully fired to produce a relatively smooth, uniform cut through the concrete. It was found that inexpensive, "homemade" linear charges gave results comparable to commercially manufactured charges.

BACKGROUND

The U. S. Army Corps of Engineers is charged with responsibility for runway repairs at U. S. Air Force (USAF) airfields damaged by conventional attack when such repairs exceed USAF on-site capabilities. The importance of this wartime mission is obvious in light of our commitments in both Europe and the Middle East, where rapid aerial reinforcement and resupply will be essential. Research on Repair and Restoration of Paved Surfaces (REREPS) has been performed at the Waterways Experiment Station (WES) to develop an improved Army capability for rapid runway repair under combat conditions.

REREPS research has shown that removal of large, partially damaged, concrete runway slabs is a major element in the time required to perform a runway repair operation. A rapid method for cleanly cutting away the damaged portions of these slabs is needed to significantly reduce overall repair time. Some cutting techniques currently under investigation include concrete saws, water jets and shaped charges. This paper presents the results of shaped charge runway cutting tests

conducted by the WES Structures Laboratory (with the assistance of personnel from Company D, 52nd Engineer Battalion (Ft. Bliss, TX)) at the White Sands Missile Range, NM.

OBJECTIVE

The study objective was to evaluate shaped charges as a means for rapidly cutting damaged runways. Specific test objectives were to evaluate the runway cutting abilities of conical shaped charges, and commercially manufactured and "homemade" linear shaped charges.

APPROACH

Shaped charge runway cutting tests were conducted on undamaged taxiway segments constructed for recent Air Force quantity-distance experiments at the Queen 15 site on the White Sands Missile Range, NM. The taxiways were built to design standards currently in use at USAF Europe bases in Germany. Pavements consisted of 8 in thick unreinforced concrete slabs overlain by 4 in of asphalt, and underlain by a 6 in stabilized aggregate base course over a compacted subgrade (Figure 1).

WES obtained a number of surplus TOW (Tube-launched, optically-tracked, wire-guided, antitank weapon) warheads. The TOW warhead consists of a conical shaped charge approximately 5 in diameter containing 5.4 lb Composition B explosive (Figure 2). The warheads were fired individually to determine optimum standoff and in linear arrays to determine if the slab would fracture between penetrations. The charges were statically fired with the windbreak left inplace giving a minimum shaped charge standoff of 4.2 in. Standoffs for individual firings ranged from this minimum to a maximum of 2.85 ft. The linear arrays were fired with spacings of 9, 12, and 18 in, all using the minimum standoff.

Commercial linear shaped charges were purchased "off the shelf" from Jet Research, Inc (JR), Arlington, Texas, in 2.5 and 4.5 lb/ft designs. The charges contained Composition B as the primary explosive. The manufacturer's quoted price was $125 and $145 per ft length, respectively. The 2.5 lb/ft charge came with an underwater housing

(Figure 3), giving a minimum standoff of 1.75 in. The 4.5 lb/ft charge (Figure 4) could be placed directly on the target surface (0 in minimum standoff, i.e., with no standoff).

In an earlier study at WES, the effectiveness of nitromethane (NM) as an explosive source in "homemade," conical shaped charges was investigated. Although it was found that twice as much NM was needed to obtain the same shaped charge penetration depth as standard shaped charges using solid explosive, it was felt that NM has several overriding advantages. The advantages of using for example; 1) it is classified as a flammable liquid and is shipped and stored as such, and 2) as a liquid it has uniform properties and assumes the shape of the container used. Conventional shaped charges, on the other hand, use high explosives and are subject to the shipping and storage restrictions of those materials, with controls much more stringent than those for flammable materials. Because of these reduced restrictions, the use of NM for runway cutting charges could be a distinct advantage at USAF Europe bases, with their congestion and limited munition storage capacities.

The NM linear shaped charge container used in these tests was designed and fabricated at WES. This container is shown in Figure 5 (plan and cross-sectional view). A 3/16 in thick brass liner with 60° included angle and 4 in throat width was selected for this charge. Thus, the liner thickness is 4.7 percent of the throat width, which is larger than the normal range of 0.5 to 3 percent for conical shaped charges. Limited comparative testing with 1/8 and 3/16 in thick liners at WES indicates that the thicker liner performed better for soil penetration. A 4 ft charge length was selected to insure that the detonation would propagate in a linear fashion.

RESULTS

Shot geometry and penetration data are presented in Table 1. The holes produced by all TOW warhead firings are sketched in Figure 6. The TOW penetrated the pavement without difficulty, reaching a maximum hole depth of 7.2 ft at the minimum standoff of 0.35 ft. Typically, the warhead cratered the 4 in thick bituminous surface layer of the pavement, and punched a hole on the order of 2 in in diameter through the underlying concrete and well into the subgrade. However, no interhole concrete cracking was noted in any of the linear arrays (even with a charge spacing as close as 9 in), although the asphalt layer was usually excavated between shot holes by the blast.

The NM linear shaped charge craters are sketched in Figure 7. These charges showed a capacity to satisfactorily penetrate the taxiway. The maximum penetration of 1.0 ft was obtained from charges at 4 in standoff, or one throat

width above the surface. Typically, the crater width in the asphalt was 2 ft, or 3 to 4 times the crater width in the underlying concrete. When individually-boosted NM linear shaped charges were placed end-to-end and detonated through a primacord ring main, they successfully sustained a relatively uniform cutting action over the length of the array.

Craters produced by the JR commercial linear shaped charges are sketched in Figures 8 and 9 (2.5 and 4.5 lb/ft charges, respectively). The charges performed best at the manufacturer's built-in standoffs of 1.75 and 2.25 in for the 2.5 and 4.5 lb/ft charges, respectively. The smaller charge did not completely penetrate the concrete. The larger JR charge, like the NM charge, was just adequate for this purpose. It also demonstrated the capability to excavate a relatively smooth cut over whatever distance might be desired, including a cut around a 90° corner (Shot 25).

DISCUSSION AND CONCLUSIONS

An early Picatinny Arsenal report (Reference 1) indicates that the conical shaped charge penetration roughly scales in proportion to the cube root of the explosive charge weight in permafrost. Using the analogy of spherical cratering charges to linear cratering (ditching) charges, square root scaling of linear shaped charge penetration is suggested as a logical extension. The maximum penetration of the 2.5 and 4.5 ft/lb JR charges and the WES 12 lb/ft NM charge are plotted in Figure 10 in an attempt to provide information for prediction of the linear shaped charge necessary to cut various runway thicknesses.

Square root scaling curves are presented in Figure 10 for the 4.5 lb/ft JR charge and the WES 12 lb/ft NM charge. The 2.5 lb/ft JR charge penetration data point falls 38% below the prediction curve. This is probably due to the fact that the smaller JR charge was not an exact physical model of the larger charge, and partly due to normal data scatter. A larger sample of penetration versus optimum standoff data is necessary before a statistical scaling relation can be determined.

The TOW warheads are not by themselves usefull in cutting runway slabs. Linear shaped charges are a feasible method for rapidly cutting runways so as to permit removal of damaged slabs. Final proof of this awaits a full scale demonstration to include removal of a slab.

REFERENCES

1. Klamer, Oscar A., "Shaped Charge Scaling," Technical Memorandum 1383, March 1964, Ammunition Engineering Directorate, Picatinny Arsenal, Dover, NJ.
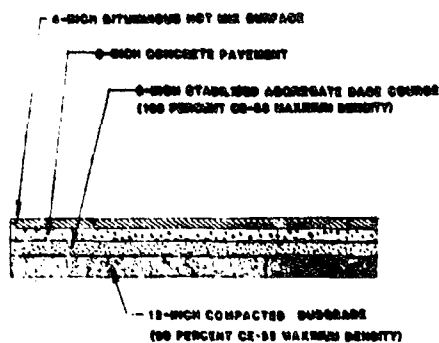
Figure 1. Typical DISTANT RUNNER taxiway cross-section. "CE-55" refers to a standardized compactive effort developed by the American Association of Highway Officials.

Figure 2. TOW warhead being placed nose down on pavement for firing.

Figure 3. Two 2.5-lb/ft JR charges with underwater housing.

Figure 4. Two 4.5-lb/ft JR charges mounted end-to-end on manufacturer-furnished standoff.

Figure 5. Design of 12.0-lb/ft mm linear shaped charge.
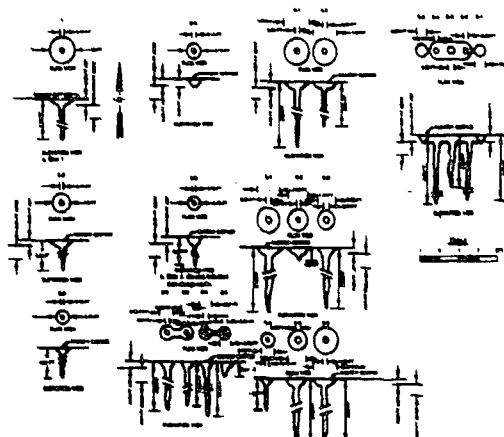
Figure 6. Results of TOW warhead shots. "CONC" and "ASP" identify concrete and asphalt.

34
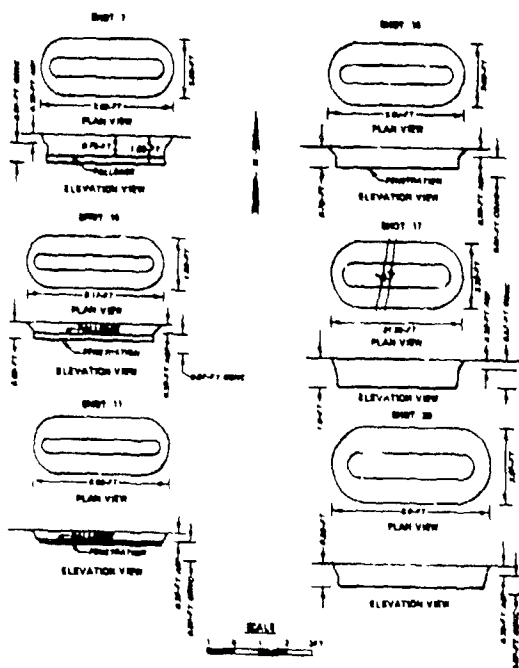
Figure 7. Results of NM charges.
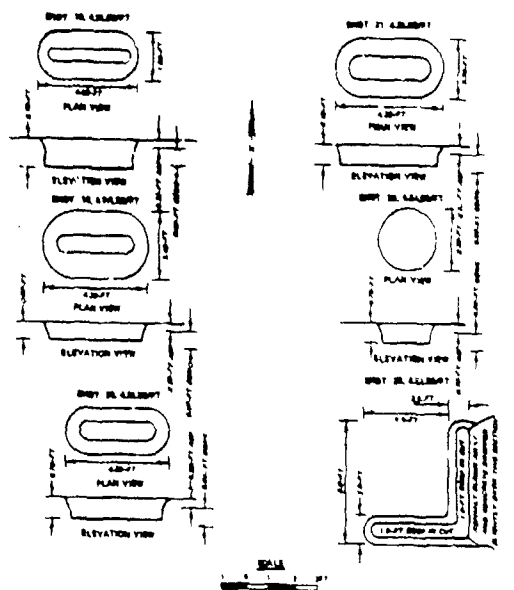
Figure 9. Results of JR 4.5-lb/ft charges.
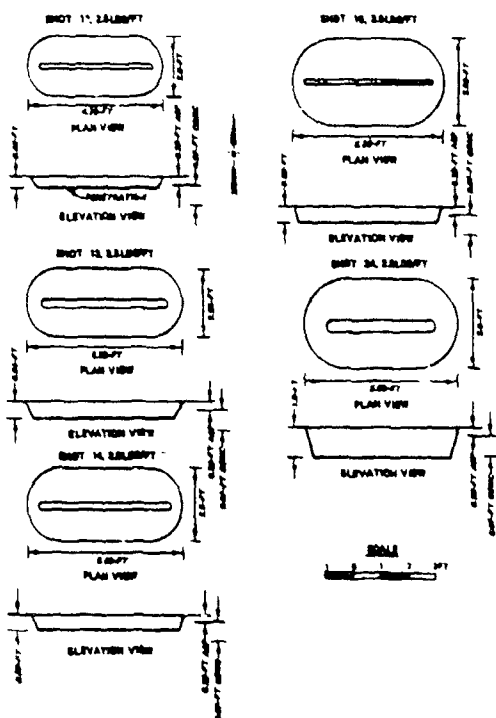
Figure 8. Results of JR 2.5-lb/ft charges.
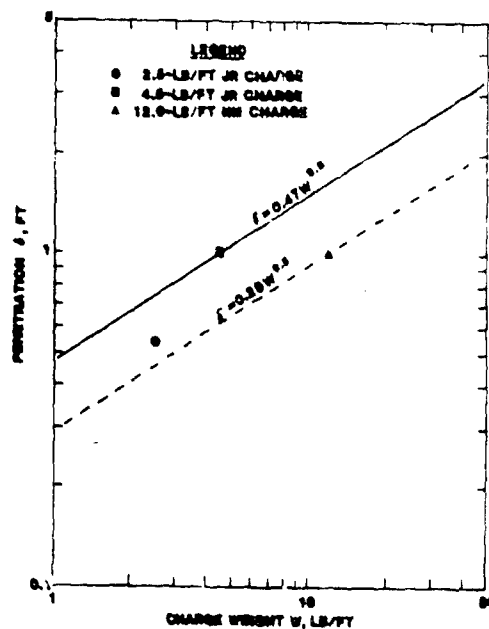
FIGURE 10. LINEAR SHAPED CHARGE TAXIWAY PENETRATION VERSUS CHARGE WEIGHT.

35

Table 1. Shot Schedule and Results

Shot Day/Time August 1982	No.	Charge No.	Type	Location	Standoff ft	Spacing ft	Shot Geometry Description	Penetration ft	Results Description	Figure No.
16/0958	1	--	TOW	E-12	0.35**	--	Nose cone on pavement	7.17	0.17 ft diameter	8
16/1104	2	-1	TOW	E-12	0.83	--	--	--	Fell over during detonation; shallow crater	8
		-2	TOW	E-13	1.35	--	--	5.25	0.17 ft diameter	8
		-3	TOW	E-13	1.85	--	--	5.67	0.12 ft diameter	8
		-4	TOW	E-14	2.35	--	--	0.42	Hole plugged	8
		-5	TOW	E-14	2.85	--	--	5.33	0.12 ft diameter	8
16/1208	3	-1	TOW	C-13	0.35	1.00	Nose cone on pavement	--	Malfunctioned?	
		-2	TOW	C-13	0.35	1.00	Nose cone on pavement	4.83	0.21 ft diameter; shallow connection to 3-3	8
		-3	TOW	C-13	0.35	1.00	Nose cone on pavement	4.42	0.17 ft diameter; shallow connection to 3-2	8
		-4	TOW	C-13	0.35	1.00	Nose cone on pavement	5.42	0.21 ft diameter; shallow connection to 3-5	8
		-5	TOW	C-13	0.35	1.00	Nose cone on pavement	0.71	0.21 ft diameter; shallow connection to 3-4	8
16/1330	4	-1	TOW	C-12	0.35	1.5	Nose cone on pavement	5.83	0.25 ft diameter	8
		-2	TOW	C-12	0.35	1.5	Nose cone on pavement	3.25	0.21 ft diameter	8
		-3	TOW	C-12	0.35	1.5	Nose cone on pavement	--	Malfunctioned?	
		-4	TOW	C-12	0.35	1.5	Nose cone on pavement	--	Malfunctioned?	
		-5	TOW	C-12	0.35	1.5	Nose cone on pavement	--	Malfunctioned?	
16/1447	5	-1	TOW	C-12	0.35	1.5	Nose cone on pavement	5.75	0.33-ft diameter	8
		-2	TOW	C-12	0.35	1.5	Nose cone on pavement	0.67	0.21-ft diameter	8
		-3	TOW	C-12	0.35	1.5	Nose cone on pavement	5.50	0.33-ft diameter	8
		-4	TOW	C-12	0.35	1.5	Nose cone on pavement	1.58	0.12-ft diameter	8
		-5	TOW	C-12	0.35	1.5	Nose cone on pavement	5.42	0.33-ft diameter	8
		-6	TOW	C-12	0.35	1.5	Nose cone on pavement	5.42	0.25-ft diameter	8
17/0934	6	-1	TOW	W-13	0.35	0.75	Nose cone on pavement	--	Shallow crater through asphalt only	8
		-2	TOW	W-13	0.35	0.75	Nose cone on pavement	4.83	0.29-ft diameter; connected to 6-3 by trench through asphalt	8
		-3	TOW	W-13	0.35	0.75	Nose cone on pavement	2.25	0.38-ft diameter; connected to 6-2 and 6-4	8
		-4	TOW	W-13	0.35	0.75	Nose cone on pavement	4.50	0.25-ft diameter; connected to 6-3 by trench through asphalt	8
		-5	TOW	W-13	0.35	0.75	Nose cone on pavement	--	Shallow crater through asphalt only	8
17/1103	7	--	NM	E-11	0.33	--	--	1.0	0.25 ft fallback	9
17/1239	8	--	NM	E-11	0.67	--	--	--	Misfire	
17/1321	9	--	NM	E-11	0.67	--	--	--	Misfire	
17/1405	10	--	NM	E-11	0.67	--	--	0.58	Some fallback	9
17/1453	11	--	NM	C-11	1.50	--	--	0.46	Some fallback	9

Table 1. Concluded

Shot Day/Time August 1982	No.	Charge No.	Type	Location*	Standoff ft	Spacing ft	Shot Geometry Description	Penetration ft	Results Description	Figure No.
18/1036	12	--	JR 2.5 lb/ft	W-11	0.15	End to end	4 charges	0.42	Some cracking below penetration	10
18/1127	13	--	JR 2.5 lb/ft	W-12	0.48	End to end	2 charges	0.54	--	10
18/1250	14	--	JR 2.5 lb/ft	CW-11	0.31	--	--	0.50	--	10
18/1337	15	--	JR 2.5 lb/ft	E-11	0.15	--	--	0.50	Concrete cracked below penetration	10
18/1430	16	--	NM	CW-12	1.00	--	--	0.75	--	9
18/1522	17	--	NM	C-10	0.33	End to end	5 charges	1.00	--	9
19/1015	18	--	JR 4.5 lb/ft	C-11	0.19	End to end	2 charges	0.79	--	11
19/1050	19	--	JR 4.5 lb/ft	C-10	0.00	End to end	2 charges	0.67	--	11
19/1127	20	--	JR 4.5 lb/ft	C-11	0.38	End to end	2 charges	0.79	--	11
19/1248	21	--	JR 4.5 lb/ft	C-10	0.56	End to end	2 charges	0.79	--	11
19/1327	22	--	JR 4.5 lb/ft	E-10	0.28	End to end	2 charges	0.75	--	11
19/1413	23	--	NM	C-10	0.00	--	Single charge	0.83	--	9
19/1455	24	--	JR 2.5 lb/ft	E-11	-0.19	End to end	2 charges placed over crack in concrete from shot 15 (below original surface).	1.00	Total penetration shots 15 and 24	10
20/0944	25	--	JR 4.5 lb/ft	E-9	0.19	End to end	Charges in "L" formation. 5 charges in each leg.	1.00	--	11

* Expansion-joint "coordinates": east, center, west (E, C, W)--joint no.
** Includes built-in standoff in nose (0.35 ft).
† Apparently detonated, but produced no penetration or crater.

36

BEST AVAILABLE COPY

MODELING THE BURN-TO-VIOLENT REACTION
TO SIMULATE IMPACT-DAMAGED GP WARHEADS [+]

Herman Krier [*], Martin Dahm [**], and P. Barry Butler [**]

University of Illinois at Urbana-Champaign, 61801

ABSTRACT

Impact forces from hardened, concrete targets to a General Purpose Warhead (bomb) can in some cases cause outer-case failure and breakup of the high explosive (HE) filler prior to fuse initiation. The detonation that is expected to occur under reliable penetration and for totally confined conditions can be reduced to that of a rapid deflagration with reduced damage to the target/structure. This paper presents the solution to the dynamic equations of motion for gas-particle systems that simulate in one-dimension, the high pressure, subdetonation speed reactions in such beds of fragmented high explosive. It is clear from the results presented that initiation of a damaged, fragmented explosive will not necessarily result in a strong detonation if the mass and momentum losses from side vents (caused by the impact) are sufficiently large.

INTRODUCTION

The application of GP warheads on expensive, high priority sorties against hardened targets requires maximum reliability of penetration and detonation. Conditions can exist (off-axis impact; superior hardening) in which the conventional munitions fail to penetrate and detonate. The warhead failures are most often case failures (where the loads during impact cause rupture of the case and fragmentation of the high explosive) prior to fuse functioning. The result can be low-order detonation or unsteady deflagrations within the damaged explosive itself. However, such "explosive" reactions can still exhibit measurable lethal effects against substantial concrete structures, especially if the explosive is partially contained (by the surrounding soil, for example.)

Figure 1 is a sketch of a GP bomb that has cratered a concrete surface by impact only, causing partial case failure, and more importantly, causing sections of the high explosive to be fragmented into a configuration which is similar to a packed bed of explosive grains.

What is envisioned to follow the impact and fragmentation is initiation of the fragmented explosive either by the fuse at one end or by friction/rapid shear at the case-filler interface. By separating the impact and material breakup/fracture from the initiation process, it is possible to perform the unsteady two-phase reactive flow analysis in order to predict whether DDT (deflagration to detonation transition) can be expected.
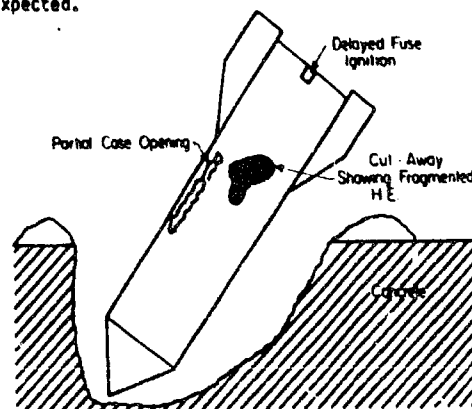
Fig. 1. Cratering of concrete surface by GP bomb impact

ASSUMPTIONS

(1) The analysis considered in this paper explicitly assumes that at time $t = 0$, initiation by the fuse or rapid shear mechanism will allow a deflagration with the supporting pressure buildup to penetrate into the damaged (rubblized) explosive.
(2) The deflagration and possible detonation occurs in only one dimension, x.
(3) The surface-to-volume ratio of the

37

packed particles (explosive) is
sufficiently high to be equivalent to
spheres of the millimeter and
submillimeter diameter size (i.e. S_p/V_p
= $6/d_p$).

(4) The possibility of mass, momentum and
energy loss is treated by psuedo-side
venting from cracks of prescribed sizes,
located at prescribed distances along
the bed. (Details are presented below.)

(5) The separated two-phase flow analyses
previously developed in Refs. 1 and 2
represent the basis on which we build
the modeling effort presented in this
paper.

(6) The decision on whether the fragmented
bed of explosive will transit into a
detonation is based on the transient
reacting flow events occuring in the
first 10 to 20 cm of length. A run-up
of length greater than 20 cm requires
times well beyond established
experimental DDT events.

(7) The explosive particles, ignited if a
critical prescribed energy is
transferred to the solid, will burn at a
rate, $r = ap^n$, where a and n are known
values for typical warhead explosives
(tritonal or H-6).

(8) The porosity of the fragmented bed (gas
volume/total volume)is uniform and
typically of the order of 0.2 to 0.3 .

THE FLUID MECHANICS MODEL (WITH VENTING)

Our analysis of the ruptured shell casing
problem represents an extension of previous work
done at the University of Illinois for the
analysis of two-phase, one-dimensional reactive
flows [1, 2]. Modifications were made to account
for the mass, momentum and energy losses occurring
through the shell opening. A detailed derivation
of the governing equations for totally confined
(no loss) conditions can be found in Ref. 1.

In the analysis one must describe the
conservation of mass, momentum and energy
throughout the domain for both the solid particle
phase as well as the gaseous products phase. Each
phase separately is assumed to be a continuum and
the system of governing differential equations can
be expressed as:

Gas Continuity

$$\frac{\partial \rho_1}{\partial t} = \frac{-\partial (\rho_1 u_g)}{\partial x} + r - \beta_g \quad (1)$$

Solid Continuity

$$\frac{\partial \rho_2}{\partial t} = \frac{-\partial (\rho_2 u_p)}{\partial x} - r - \beta_p \quad (2)$$

where $\qquad r = (S/V)_p \rho_2^r$

Gas Momentum

$$\frac{\partial (\rho_1 u_g)}{\partial t} = -\frac{\partial (\rho_1 u_g^2)}{\partial x} - \phi \frac{\partial P_g}{\partial x} - D + r u_p - \beta_g u_g \quad (3)$$

Particle Momentum

$$\frac{\partial (\rho_2 u_p)}{\partial t} = -\frac{\partial (\rho_2 u_p^2)}{\partial x} - (1-\phi)\frac{\partial P_g}{\partial x} + D - r u_p - \beta_p u_p \quad (4)$$

Gas Energy

$$\frac{\partial (\rho_2 E_{gT})}{\partial t} = -\frac{\partial (\rho_1 u_g E_{gT} + \phi u_g P_g)}{\partial x} - D u_p - \dot{Q} + r[E^g_{CHEM} + \frac{u_p^2}{2}] - \beta_g (E_{gT} + \frac{P_g}{\rho_2}) \quad (5)$$

Particle Energy

$$\frac{\partial (\rho_2 E_{pT})}{\partial t} = -\frac{\partial (\rho_2 u_p E_{pT} + (1-\phi)u_p P_p)}{\partial x} + r[E^p_{CHEM} - \frac{u_p^2}{2}] + D u_p + \dot{Q} - \beta_p E_{pT} \quad (6)$$

Here, the relations for the total internal energy
in each phase are

$$E_{gT} = C_{vg}T_g + \frac{1}{2} u_g^2$$

and

$$E_{pT} = C_{vp}T_p + \frac{1}{2} u_p^2 \quad (7)$$

The subscripts g and p denote gas and particle,
respectively. In Eqs. (1)-(6), the phase
densities ρ_1 and ρ_2 are defined as

$$\rho_1 = \rho_g \phi \quad \text{and} \quad \rho_2 = (1-\phi)\rho_p \quad (8)$$

The porosity ϕ is defined as the ratio of the
instantaneous gas volume to the mixture volume.
Hence, the solids fraction is $1 - \phi$.

In addition to the six conservation
equations, three constitutive relations are needed
in order to solve for the nine unknown variables.

Because of the restricted length of this
manuscript, it is not possible to include a

38

discussion and description of the constitutive relations in any detail. However, in functional terms these represent:

(i) An equation of state (E. O. S.) for the product gases of the explosive, $P = P_g(\rho_g, E_g)$. The particular equation of state used was discussed in Ref. 3.

(ii) An equation of state for the solid phase, $P = P_p(\rho_p, E_p)$, specifically the Tait equation of state (see Ref. 2)

(iii) A heat transfer coefficient which fixes Q in Eqs. 5 and 6 (see Ref. 2, 3)

(iv) A gas-particle drag coefficient which determines D in Eqs. 3 and 4 (see Ref. 3)

(v) An ignition criterion, $T_{ignit} \geq T_{crit}$ (Ref. ?)

(vi) A burning rate relation (as discussed above)

In equations (1-6) β_g represents the loss of mass (gas phase) as a result of the hole present in the shell casing. The appropriate variation of this term also appears in the momentum and energy equations.

Mass Loss Due to Exterior Opening

Figure 2 shows the fragmented bed being modeled. Superimposed on the front face of the illustration are the expected pressure-distance profiles showing the pressure drop associated with the opening in the case wall (x = 0.3 cm). A simplified derivation for the mass loss throughout the bed length is as follows:

Consider the control volume shown below with gas being ejected out the hole:
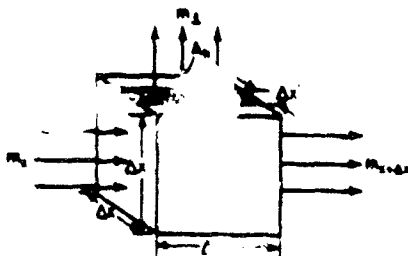
The mass rate of gas lost per unit volume

$$\beta_g = \frac{\dot{m}}{V_{cv}}$$

$$\dot{m} = \rho_g u A_h \qquad (9)$$

where: ρ_g = gas density
u_g = velocity of gas leaving the control volume
A_h = area of hole
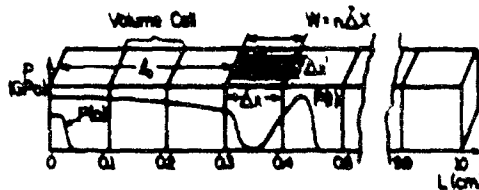
Fig. 2. Schematic of fragmented bed being modeled

Due to the extremely high gas pressures in the bed, the gas escaping the control volume will always be choked. Hence u will equal the local speed of sound:

$$u = [(\frac{\partial P}{\partial \rho})_s]^{1/2} = u_s \qquad (10)$$

The area of the hole is defined as: $A_h = \Delta x' \Delta x \phi$ where ϕ = gas phase volume fraction. The volume of the control cell is given as:

$$V_{c.v.} = \Delta x^3$$

Substituting into the definition of β_g, one obtains

$$\beta_g = \frac{\dot{m}}{V_{c.v.}} = \frac{\rho_g u_s \Delta x \Delta x \phi}{\Delta x^3} = \frac{\rho_g u_s \phi}{\Delta x}(\frac{\Delta x'}{\Delta x}) \qquad (11)$$

or,

$$\beta_g = \frac{\rho_g u_s \phi}{\Delta x} C_0 \qquad (12)$$

where C_0 is an assumed "opening ratio", $0 \leq C_0 \leq 1$.

If one is to consider entrainment of the unburned solid particles in the gas escaping through the hole, the mass loss per unit volume for the solid phase becomes

$$\beta_p = \frac{\rho_p u A_h}{\Delta x^3} = \frac{\rho_g u_s D_0}{\Delta x} C_0 \qquad (13)$$

where D_0 is a drag factor between entrained

39

particles and escaping gas. The parameter D_0 has a range from zero to unity.

Numerical Solution

The system of differential conservation equations described in the previous section, because of their nonlinearity, do not admit an analytic solution. In order to obtain a solution to the time-dependent differential equations, we chose to discretize the governing equations over the domain and write the x-derivatives as center differenced first order approximations with the appropriate artificial smoothing to assure stability for the hyperbolic problem. The partial differential equations are then reduced to ordinary differential equations for a given time step and solved by a standard ODE numerical solver. The preceeding steps are repeated for each time step.

The results of two-phase reactive flow calculations are presented in the following section. A CDC Cyber 175 computer was used to numerically integrate the equations. A "typical" computer run consisted of a bed domain with 100 nodes and a total elapsed time of over 200 CP seconds.

Computed Results

The solutions to the conservation equations (Eqs. 1-8) with their required constitutive relations will (a) show that even with a fragmented explosive bed, a detonation could occur if the container walls remained intact; (b) show that the over pressures could still be significantly high, and (c) most importantly, that a vented bomb condition could prevent a strong detonation and severely limit the over-pressurization.

In all cases the container (see Figure 2) walls remained fixed. The pressures that are predicted (in the calculations to be presented) would obviously result in eventual explosion of the case wall with additional cratering and damage of nearby structures.

Figure 3 presents the predicted pressure development history for a completely confined accelerating deflagration process (C_0 = 0, thus β_p and β_n = 0). The effective surface-to-volume ratio of the explosive (fragmented) particles was $6/dp = 120$ cm^{-1} loaded at $(1 - \phi_0)$ = 70% solids volume fraction.
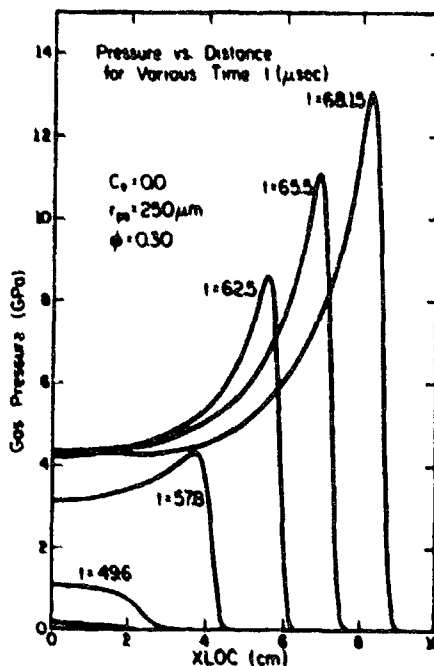
Fig. 3. Pressure history for completely confined accelerating deflagration.

At time t = 0, only 4 mm of the bed is assumed ignited at an initial low pressure of 1 MPa. The results show that within 70 μsec a detonation is about to form and the peak pressure (at the 9 cm location) is almost 14 GPa (140 kbar = 2 x 10^6 psi). The detonation (CJ) pressure for this overall density (ρ_o) explosive is only somewhat greater than this value.

Of course this result is greatly dependent on the assumed particle size, d_{po}. If the particles averaged out to be even smaller, the gas pressure
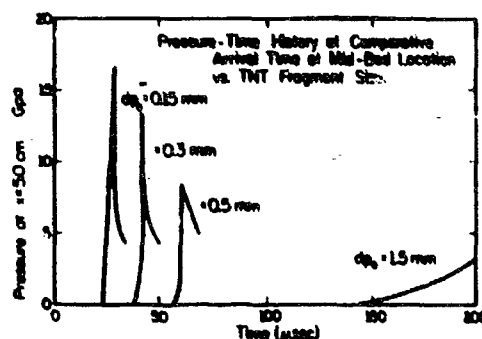
Fig. 4. Pressure-time profiles for varying size propellant particles.

40

shock would form even sooner. Figure 4 shows the pressure-time profile at the bed midpoint, (x = 5 cm) for four different average particle diameters. (The results shown in the previous figure, Fig. 3, assumed d_p = 1/2 mm.) When the average fragment diameter exceeds approximately 1 mm the resultant pressures will be approximately too low to allow a detonation.

The effect of even a small crack which can relieve the pressure and weaken the developing deflagration front is significant, as shown in the results presented in Figure 5. There, only one "hole", 4 mm in length, located at ℓ_0/ℓ = 1/4, with an "opening ratio", C_0 = 1/2 is considered. The mass loss is evident in the indented pressure profiles at the hole site.

The reduction in peak pressure, at the bed midpoint is also severe, depending on the crack opening ratio, C_0, as is shown in Figure 6, where the pressure-time history predictions are compared.

The effect on the rate of deflagration as C_0 is increased is evident in the results shown in Figure 7. Again, only one hole is assumed, located at ℓ_0 = 2.5 cm. Note that the slope of the flame-front location versus time locus, which is the reaction front speed, has reduced the detonation front velocities, (those evaluated at x = 8 cm) from 5.3 mm/μsec (C_0 = 0) to 4.3 mm/μsec (C_0 = 1/2), a 19% reduction.

Figure 8 shows the comparisons. Note the crack opening ratio, C_0 is only 0.10, 1/5 the value considered in earlier calculations shown in Figure 5.

More importantly there is a marked reduction in the speed of the detonation front, as can be seen in the comparison shown in Figure 9. For the condition of W = 0.16 (a 16 mm long crack) one obtains the speed of only 2.7 mm/μsec, a velocity that could be interpreted to be a "low-order" detonation.
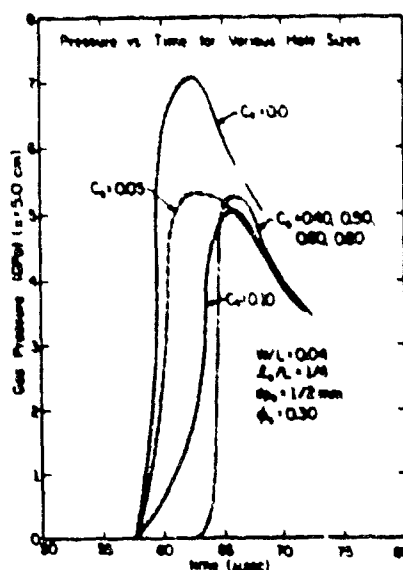
Fig. 6. Effect of hole size on pressure-time history at x = 5.0 cm.

Fig. 5. Pressure history for packed bed with hole at x = 2.5 cm (C_0 = 0.50)
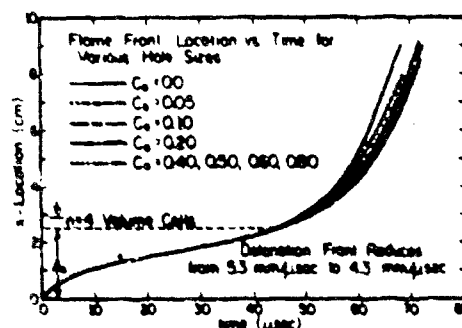
Fig. 7. Reduction in flame front velocity due to increased hole size.

Extending the size (length) of the crack [from the value of 4 mm (W = 0.04) considered in the results shown in the previous two figures] to 8 mm and 16 mm has an even more pronounced effect on reducing the pressure front development.
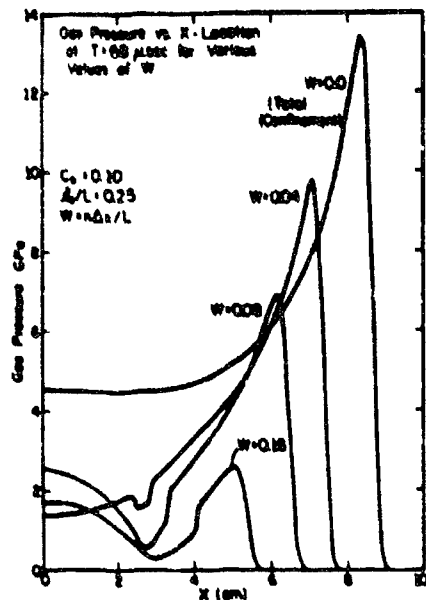
Fig. 8. Effect of hole size on pressure development (t=68 μsec)
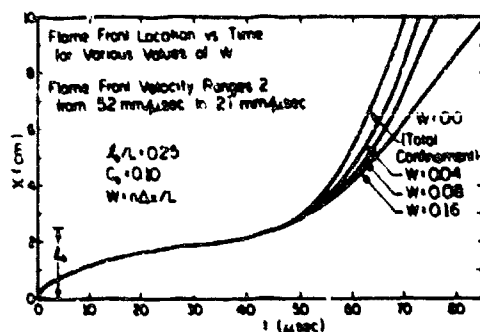
Fig. 9. Flame front velocity for varying hole sizes.

Erupting Vent Holes

A final set of calculations considered an alternate constraint. Instead of prescribing in advance the location, length and the opening ratio of the vent holes, the opening is not assumed to take place until some critical pressure, P_{erupt}, is attained. Figure 10 shows the pressure development history when P_{erupt} = 0.5 GPa (5 Kbar). That is, when the internal pressure reaches 0.5 GPa, a "vent hole" occurs instantly to relieve the pressure. We have specified for this hole that C_0 = 0.10 and W = $\Delta x/L$ = 0.01. The

pressure reductions caused by the mass, momentum and energy losses are significant for this particular case.

While the oscillations in the waveforms of the P vs X plot for this case may appear to be caused by numerical instabilities, they are actually being caused by the intermittent rupturing of the propellant casing caused by bed pressurization. Each trough on a particular waveform represents a point along the propellant bed where the casing was ruptured due to high pressure at some time during the burn, while each peak represents a location where the casing did not rupture. One can note that as a perpendicular is dropped to the abscissa from a peak (or trough) on any waveform, all waveforms passing by that particular point in the bed will also exhibit a peak (or trough). This is of course due to the fact that once the rupturing pressure is exceeded at any point along the bed, a hole forms in the casing at that time and remains for all subsequent time thereafter. To further insure that these oscillations were not caused by numerical instability, these calculations were repeated utilizing a time step, Δt, equal to one-half the previous time step. The results were identical.
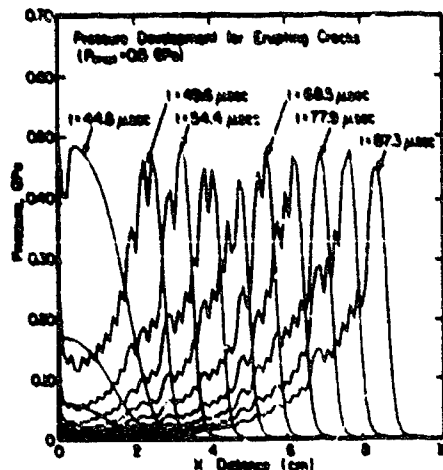
Fig. 10. Pressure history for shell rupture at P = 0.5 GPa.

Figure 11 again shows the locus of deflagration fronts as a result of the pressure history shown in the previous figure. Note that if the internal pressure can rupture the case at pressures less than 1 GPa the result (at t = 70 μsec) is a "low-order detonation", moving at D < 2 mm/μsec. Also shown in Figure 11 is the locus of the erupting vent holes which occur about 5 to 10 μsec after the reaction front has passed. Obviously, internal pressures can more easily rupture an already damaged warhead case, so that the results shown in Figures 10 and 11 may not necessarily be unreasonable. Additional

42

calculations in which the "size" of the erupting holes are increased show the expected result of "quenching" the detonation wave that would have resulted had there been total confinement.
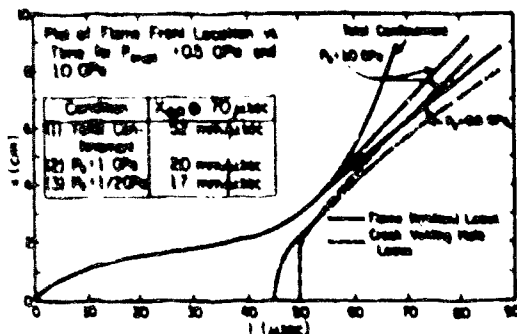
Fig. 11.   Flame-front velocity and venting-hole locus for shell rupture at P = 0.5 GPa and P = 1.0 GPa.

Concluding Remarks

The results presented in the last section verify the fact that a fracture of the exterior casing of a GP warhead with breakup of the explosive can reduce the effectiveness of the explosive filling. Cases were presented where the accelerating flame propagates through (a) a shell casing intact, (b) a shell casing which has fractured due to ground impact, and (c) a shell casing which has fractured due to localized internal pressurization.

Given the proper surface-to-volume ratio of the totally confined explosive, pressures exceeding 10-15 GPa can be predicted as the ignition front propagates through the porous explosive bed. However, when the shell casing is opened and product gases are allowed to escape, the overall pressure profiles are greatly reduced.

The final cases presented in this paper modeled a casing fracture occurring at a prescribed stress on the exterior walls. Future work on this problem should couple the stress mechanics of the encasing structure with the applied stresses caused by the burning explosive grains.

A final point which should be discussed deals with the one-dimensional analysis made to simplify the numerical model. Given the proper computer resources, a detailed two-dimensional analysis would probably lead to conclusions which are lost in the one-dimensional version.

Our ongoing work will also include analysis

which will consider:

(a) Strong shock initiation (at x = 0), instead of weak shock flame initiation now assumed.

(b) Variation in the axial (propagation) direction of particle size and/or bed porosity.

(c) Coupling of internal pressures to case wall stresses in order to predict actual time delays prior to fracture of the case.

(d) A two-dimensional deflagration to detonation transition model, as previously mentioned, which will allow for more accurate side vent loss calculations.

(e) Variations in explosive chemical and physical properties.

References

1. H. Krier and J. A. Kezerle, Seventeenth Combustion Symposium, The Combustion Institute; pp. 23-24 (1979).

2. S. J. Hoffman and H. Krier, AIAA Journal, Vol. 19, No. 12, pp. 1571-1578 (1981).

3. P. B. Butler, M. F. Lambeck, and H. Krier, Combustion and Flame, Vol 46, pp. 75-93 (1982).

PREDICTING RESPONSE OF MUNITIONS TO MASSIVE SECONDARY FRAGMENT IMPACT
A Proposed Analytical Method

Anatol Longinow
Illinois Institute of Technology, Chicago, IL

Edward E. Hahn
Multitech Engineering Associates, Chicago, IL

Myle Napadensky and Edmund Snider
IIT Research Institute, Chicago, IL

ABSTRACT

This paper presents an analytic method for studying the mechanisms that lead to the detonation of cased munitions filled with molten explosives when impacted by large concrete fragments, representing failed wall sections. This is a single degree of freedom dynamic structural analysis method which makes use of predetermined, nonlinear load-deflection characteristics of the shell casing. In the analysis described, the method was applied to predict the pressure-time history in the molten explosive when subjected to impact. A reasonable comparison between analytic and experimental results was obtained.

INTRODUCTION

At one state of the munition production process, molten explosives are poured into empty shell casings. At this, and most stages of the production process there is a finite probability that an accidental explosion may occur. To limit the propagation of an accidental explosion, the pouring area is subdivided into smaller areas separated by reinforced concrete walls. This does not completely eliminate the danger of propagation because an explosion in a cubicle can cause some breakup of dividing walls, producing energized fragments which may impact shell casings in neighboring cubicles thus possibly producing additional detonations. Whether or not an explosion is produced by such impact depends on the dynamic pressures produced within the molten explosive, which in turn depends on the mass of the impacting fragment, its impact velocity, point and angle of the impact, etc. The size of fragments produced by a separation wall depends on the physical characteristics of the wall, i.e. reinforcement details, concrete strength, aggregate size, thickness, span, support conditions, etc. It also depends on the intensity and distribution of the blast load produced by the donor charge on the dividing wall.

This paper describes a project (Ref. 1) whose objective was to study the mechanisms controlling the impact sensitivity of shell casings filled with molten explosives when impacted by secondary fragments. (It was determined in earlier experimental investigations that a shell in the molten or just-poured state was more sensitive to initiation than when the explosive was cool and hardened). The project was divided into two parts.

The first part was an analytic effort whose purpose was to predict the pressure buildup within the molten explosive when the casing and the contained explosive interact with a secondary fragment. It is hypothesized that pressure buildup (or the rate of pressure buildup) and the resulting rise in temperature is a good measure of explosive detonation sensitivity.

The second part was an experimental effort whose aim was to ascertain the credibility and accuracy of the analysis. Instrumented, full scale experiments were performed to obtain quantitative data for comparison with analytic results. The experiments also provided an insight into what was occurring during the impact process and thus helped guide the analysis.

ANALYSIS OF SHELL EXPLOSIONS DUE TO IMPACT BY LARGE CONCRETE FRAGMENTS

Figure 1 is a schematic showing the shell-fragment configuration analyzed. The shell casing, open at its apex and completely filled with molten explosive, is stationary on the ground plane. At the time of impact the explosive is at a sufficiently high temperature to be in a liquid state. The fragment, a concrete cylinder, is moving in a horizontal direction with velocity, V. The conditions are assumed to be such that during impact the shell casing will be plastically deformed and will experience an acceleration. The plastic deformation of the casing will cause the molten explosive to be pressurized and to be forced to flow up and through the filling orifice at the apex of the casing. This pressure buildup during the time of impact and the associated temperature rise, is hypothesized to be a measure for determining if the explosive will detonate. The analytic procedure used to obtain the pressure-time relationship in the explosive during impact is described next.

44
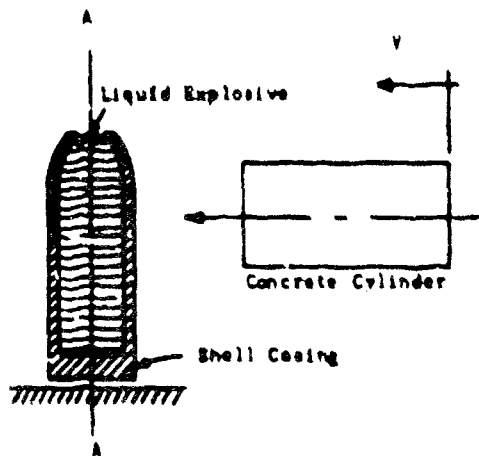
FIG. 1.- Shell-Fragment Configuration

Analytic Solution Requirements

The analytic solution is a single-degree of freedom dynamic analysis which requires certain postulated explosive, shell casing, and fragment interaction characteristics which are the following:

1. Force-deflection characteristics (resistance function) of the shell casing
2. Volume versus deflection characteristic of the shell casing
3. Orifice area versus deflection characteristics

For the purpose of determining the force-deflection characteristics, the shell casing was assumed to be restrained in the horizontal direction only all along the line formed by the intersection of the midplane of the shell surface and the vertical plane whose edge view is indicated by line A-A in Fig. 1. Making use of the shell symmetry, one quarter of the shell surface is modeled for finite element analysis as shown in Fig. 2. Thickness is varied along the height in discrete intervals. ANSYS (Ref. 2) finite element computer program which meets the requirements of large deflection and plastic deformation of the casing material, was used in the analysis. Force-deflection characteristics were obtained by imposing deflections and then computing the corresponding forces required to produce them. Deflections were imposed on the shell casing at nodes representing an area approximately equal to the contact area between the casing and the impacting concrete cylinder. Load deflection characteristics were determined for three pressures applied to the interior of the shell. Results are shown in Fig. 3. Along with force-deflection characteristics of the shell casing, volume-deflection and orifice area-deflection characteristics were obtained from this analysis. These results are shown in Fig. 4 and Fig. 5 respectively. It will be noted that both of these characteristics are independent

of internal pressure. Also, at least for this shell casing, there was essentially no change in the orifice area with change in deflection, see Fig. 5.
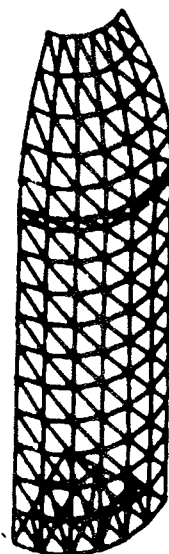
FIG. 2.-Finite Element Mesh of One Quarter of the Shell
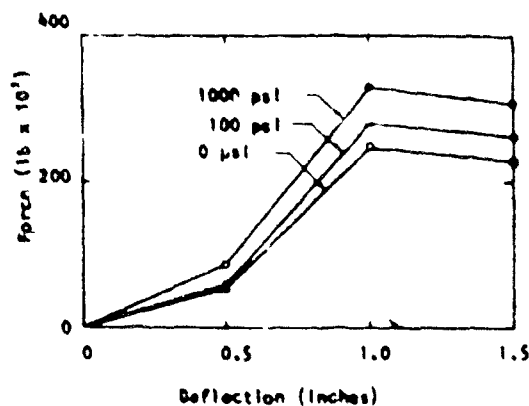
FIG. 3.-Force Versus Deflection Characteristics of the Shell Casing for Indicated Internal Pressures
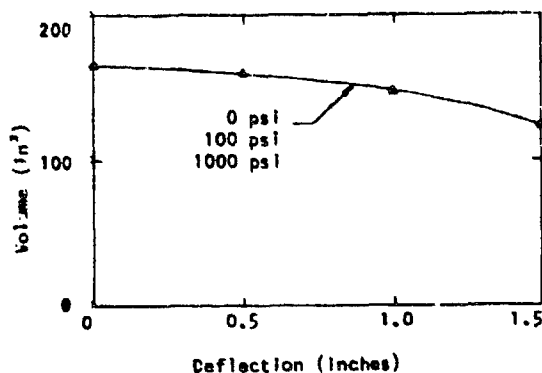
FIG. 4.-Volume Versus Deflection Characteristic
of the Shell Casing
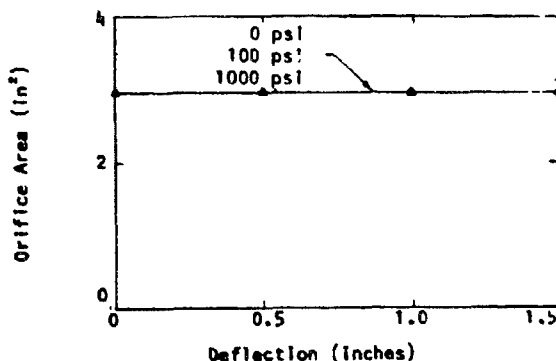
FIG. 5.-Orifice Area Versus Deflection
Characteristic of the Shell Casing

Next, we were concerned with the flow
characteristics of the molten explosive through
the filling orifice of the casing. The flow is
dependent on the orifice area, the fluid pressure,
viscosity and the orifice coefficient. The
following formula (Ref. 3) was used to relate the
flow rate, Q to the internal pressure, p of the
liquid explosive and other parameters.

$$Q = C_c A \sqrt{2gp/\gamma} \qquad (1)$$

where C_c = the orifice coefficient, taken as 0.64

A = the orifice area

g = acceleration due to gravity

γ = weight density of the molten explosive,
taken as approximately 85 lb/cu ft

Flow characteristics are shown in Fig. 6 for three
orifice areas.
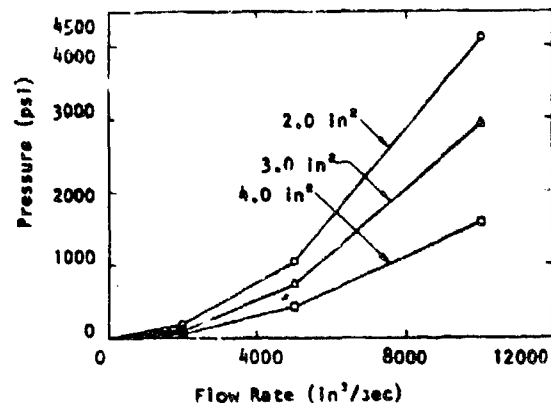
FIG. 6.-Pressure Versus Flow Rate for Three
Orifice Areas

In the initial analysis it was assumed that the
molten explosive was incompressible. Analytic
results using this assumption showed large rapid
changes in the liquid explosive pressure, suggest-
ing compressibility. The analysis was modified to
take into account fluid compressibility. In the
modified analysis the characteristics shown in
Fig. 6 are still used, however the corresponding
internal pressure is modified on the basis of the
bulk modulus of the explosive, i.e.

$$B = \rho \frac{\Delta p}{\Delta \rho} \qquad (2)$$

where B = the bulk modulus taken as 580,000 psi

ρ = the weight density of the molten
explosive

Δp = change in internal pressure

Analytic Solution Procedure

As indicated earlier, the analytic solution is
a single-degree of freedom analysis. Referring
to Fig. 1, assuming that the concrete cylinder and
the shell move in a straight line, the equations
of motion and initial conditions are given as
follows:

$$M_c \ddot{x}_c = -F \qquad (3)$$
$$M_s \ddot{x}_s = F \qquad (4)$$

where M_c and M_s represent the mass of the cylinder
and the shell casing respectively. F is the inter-
action force between the shell and the concrete
cylinder, and $\ddot{x}_c$ and $\ddot{x}_s$ are the center of gravity
accelerations of the concrete cylinder and the
shell respectively.

The initial conditions for the concrete
cylinder and the shell are (at t=0, impact is
initiated) $\dot{x}_c$; the initial velocity of the cylin-
der is equal to V; $\dot{x}_s$, the initial velocity of the
shell is equal to zero. The initial displacements
x_c and x_s, of the cylinder and the shell are equal
to zero. Euler equations were used in the inte-
gration process, i.e.

46

$$\dot{x}(t + \Delta t) = \dot{x}(t) + \ddot{x}(t)\Delta t \qquad (5)$$

$$x(t + \Delta t) = x(t) + \dot{x}(t)\Delta t \qquad (6)$$

The solution procedure is detailed below.

Solution Procedure

1. Read data describing the system
2. Set time to zero (t=0) and displacements and velocities to their initial values. Set initial internal pressure to zero, and the orifice area and the casing volume to the initial values.
3. Print out time and pressure
4. If time exceeds maximum value, stop.
5. From force-deflection-pressure curves (Fig. 3) determine the interaction force, F. Note that the casing deflection δ, is the difference in the cylinder and shell motions (displacements), i.e. $\delta = x_c - x_s$.
6. Compute cylinder and shell accelerations, see equations (3) and (4).
7. Use the Euler integration formulas, expressions (5) and (6), to determine velocities and displacements of the cylinder and the casing at time $t + \Delta t$. Update time to $t + \Delta t$.
8. Determine shell casing volume using volume-deflection-pressure curve (Fig. 4). Compute volume rate of flow from difference in volume from previous time step divided by time step, Δt.
9. Determine orifice area from orifice area-deflection-pressure curves (Fig. 5).
10. Determine new internal pressure from pressure-volume flow rate-area curves (Fig. 6).

> Steps 11 through 13 represent an iterative procedure used to take into account the compressibility of the liquid explosive.

11. Determine the change in pressure over the time step Δt and compute the change in the weight density of the liquid explosive, see Eq. (2).
12. Determine the new weight density.
13. Determine the change in volume due to the change in the weight density. Compute the volume rate of flow.

> Continue the iteration until the change in volume is smaller than a preassigned value.

14. Return to step 3 and continue.

EXPERIMENTAL EFFORT

The purpose of the experimental effort was to measure the pressure-time history within the molten explosive when the shell containing it is impacted by a concrete fragment. The experimental setup is depicted in Fig. 7. A shell casing, containing a liquid, Glycerol, of the same density as molten composition B explosive is mounted (propped) on a pedestal, see "target" in Fig. 7. An air gun is then used to launch the concrete fragment at the shell casing to impact at a specified aiming point. The concrete fragment is in the shape of a cylinder. Two sizes and weights were used in this study (Ref. 1), 2-ft and 4-ft long and weighing 200-lbs and 400-lbs respectively. The instrumentation consisted of a pressure sensor located within the liquid for measuring the pressure-time history during impact. Photographic coverage was provided to measure the impact velocity of the concrete cylinder.
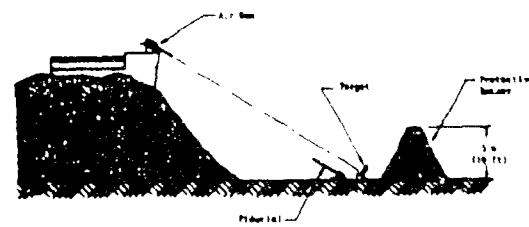
FIG. 7.-Secondary Fragments Impact Test Site

Selected Results

Figure 8 shows an experimentally determined and the corresponding analytic pressure-time history. This particular experiment dealt with a 4.2-in. mortar shell filled with Glycerol and water at ambient temperature. A concrete cylinder, simulating a wall fragment and weighing 200 lbs., impacted the shell at 272 ft/sec at a point 4.25 in below the filling orifice. In terms of the shape of the pressure-time history, duration and peak pressure, the comparison between experimental and analytic results appears to be favorable. Similar comparisons were obtained for other experiments conducted in the course of the study.

CONCLUSIONS AND RECOMMENDATIONS

A simple analytic method was formulated for predicting pressure-time histories in shell casings filled with molten explosives when impacted by secondary fragments. Analytic results compared favorably with experiments.

Additional analyses are required to study the sensitivity of results for a larger set of experiments with the objective of improving the accuracy of the predictive method. To date four other experimental programs have been conducted on the sensitivity to impact, by large concrete fragments, of a variety of molten and ambient temperature

explosive-filled shells. For these previous
experimental programs analytical predictions of
time curves should be performed. With a larger
number of curves, and hence larger number of test
conditions, one would be able to distinguish
between pressure-time conditions for explosion and
no reaction. The scope of this method needs to be
further expanded to study whether the peak pressure
in the liquid explosive, rate of pressure rise,
etc. are parameters which individually or in com-
bination will predict the onset of detonation.

TIME IN SECONDS
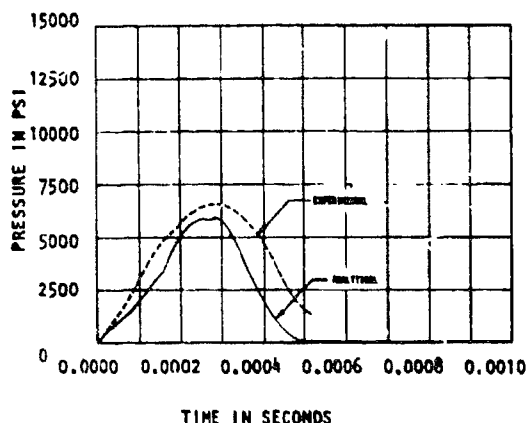
FIG. 8.-Pressure Versus Time Graph for
Experiment 4 (Concrete Projectile 200 lb.
at 272 ft/sec Velocity)

ACKNOWLEDGMENT

REFERENCES

1. Swider, E., Napadensky, H., Hahn, E.,
   "Determination of Fragment Impact Sensitivity
   Prediction Methods," for U.S. Army Armament
   R & D Command (ARRADCOM), Dover, New Jersey,
   Contract No. DAAK10-80C-0160, IIT Research
   Institute, Chicago, Illinois, July, 1982.
2. "ANSYS, Engineering Analysis System
   Theoretical Manual," Swanson Analysis Systems,
   Inc. P. O. Box 65, Houston, Pennsylvania.
3. Michelson, I., "The Science of Fluids", Van
   Nostrand Reinhold Company, 1970.

MICROPLANE MODEL FOR FRACTURE ANALYSIS
OF CONCRETE STRUCTURES

Zdeněk P. Bažant and Byung H. Oh

Center for Concrete and Geomaterials

The Technological Institute

Northwestern University, Evanston, IL. 60201

ABSTRACT

Dynamic fracture analysis of concrete structures necessitates a triaxial stress-strain relation that describes gradual strain-softening with reduction of tensile stress to zero. A new model which does that and is applicable under general loading, including rotating principal stress directions, is proposed. It is based on accumulating stress relaxations due to micro-cracking from the planes of all orientation within the microstructure. Comparisons with tensile test data are given.

Introduction

Fracture analysis of certain brittle heterogeneous materials, such as concretes and many rocks, requires consideration of progressive micro-cracking in the fracture process zone as the fracture is being formed. This type of fracture may be efficiently modeled with the crack band approach, in which the material behavior in the fracture process zone is described by a strain-softening triaxial stress-strain relation, provided that the strain-softening behavior is associated with a zone of a certain characteristic width that is treated as a material property or is determined in advance by stability analysis. A suitable tri-axial stress-strain relation of the total strain type (deformation theory type) has been recently formulated and has been shown to lead to satisfactory agreement with essentially all existing fracture test data available in the literature [1, 2]. This stress-strain relation is, however, limited to situations in which the direction of the maximum principal stress does not significantly rotate during the fracture formation. This is not so in certain important situations, especially various dynamic problems. Here, a longitudinal wave may produce only a partial tensile fracture (i.e., distributed microcracking) and the fracture may be completed subsequently when a shear wave arrives, causing a principal tensile stress in a different direction. For such situations of progressive fracturing, it is necessary to develop a triaxial strain-softening stress-strain relation which is path-dependent and is formulated incrementally. A model called microplane model is developed to fill this need. We propose here a model in which the constitutive properties are characterized by a relation between the stresses

and strains acting within the microstructure on planes of various orientation, called the micro-planes. This formulation involves no tensorial invariance restrictions. The restrictions can then be satisfied by a suitable combination of planes of various orientation. E.g., in the case of isotropy, each orientation must be equally frequent. Thus, one circumvents the difficulty of setting up a general nonlinear constitutive equation in terms of proper invariants.

The idea of defining the inelastic behavior independently on planes of different orientation within the material, and then in some way super-imposing the inelastic effects from all planes, appeared in Taylor's work [3] on plasticity of polycrystalline metals. Batdorf and Budianski [4] formulated the slip theory of plasticity, in which the stresses acting on various planes of slip are obtained by resolving the macroscopic applied stress, and the plastic strains (slips) from all planes are then superimposed. The same super-position of inelastic strains was used in the so-called multilaminate models of Zienkiewics et al. [5] and Pande et al [6, 7] and in many works on plasticity of polycrystals. While the previous works dealing with plasticity of polycrystals [3, 4, 8, 9, 10-14] or soils [15,16] the stresses on various microplanes were assumed to be equal to the resolved macroscopic stress, this new model uses a similar assumption for part of the total strains.

Fundamental Hypotheses

The resultants of the stresses acting on the microplanes over unit areas of the macroscopic continuum will be called the microstresses s_{ij}, and the strains of the macroscopic continuum accumulated from the deformations on the microplanes will be called the microstrains, e_{ij}. With regard to the interaction between the micro-and macro-levels, one may introduce the following basic hypotheses.

Hypothesis I. - The tensor of macroscopic strain, ϵ_{ij}, is a sum of a purely elastic macro-strain ϵ_{ij}^a that is unaffected by cracking, and an inelastic macrostrain e_{ij} which reflects the stress relaxation due to cracking, i.e.,

$$\epsilon_{ij} = \epsilon^a_{ij} + e_{ij} \tag{1}$$

Here, latin lower case subscripts refer to cartesian coordinates x_i ($i = 1,2,3$).

Hypothesis II. – The normal microstrain e_n which governs the progressive development of cracking on a microplane of any orientation is equal to the resolved macroscopic strain tensor e_{ij} for the same plane, i.e.,

$$e_n = n_i n_j e_{ij} \tag{2}$$

in which n_i = direction cosines of the unit normal $\vec{n}$ of the microplane and the repeated latin lower case subscripts indicate a summation over 1, 2, 3.

Hypothesis III. – The stress relaxation due to all microcracks normal to $\vec{n}$ is characterized by assuming that the microstress s_n on the microplane of any orientation is a function of the normal microstrain e_n on the same plane, i.e.,

$$s_n = (2\pi/3) \, F(e_n) \tag{3}$$

The factor $(2\pi/3)$ is introduced just for convenience, as it will later cancel out.

The last hypothesis is similar to that made for shear microstresses and microstrains in the slip theory of plasticity. Hypothesis II is however opposite. There are three reasons for hypothesis II.

1. Using resolved stresses rather than resolved strains on the microplanes would hardly allow describing strain-softening, since in this case there are two strains corresponding to a given stress but only one stress corresponding to a given strain.

2. The microstrains must be stable when the macrostrains are fixed. It has been experienced numerically that, in the case of strain-softening, the model becomes unstable if resolved stresses rather than strains are used.

3. The use of resolved strains rather than resolved stresses seems to reflect the microstructure of a brittle aggregate material more realistically. The use of resolved stresses is reasonable for polycrystalline metals in which local slips scatter widely while the stress is roughly uniformly distributed throughout the microstructure. By contrast, in a brittle aggregate material consisting of hard inclusions embedded in a weak matrix, the stresses are far from uniform, having sharp extremes at the locations where the surfaces of aggregate pieces are nearest. The deformation of the thin layer of matrix between two aggregate pieces, which yields the major contribution to inelastic strain, is determined chiefly by the relative displacements of the centroids of the two aggregate pieces, which roughly correspond to the macroscopic strain. The microplanes may be imagined to represent the thin layers of matrix and the bond planes between two adjacent aggregate pieces, since microcracking is chiefly concentrated there.

In Hypothesis III, the relaxation of shear microstresses s_{nt} caused by the shear and normal microstrains e_{nt} and e_n is neglected. This assumption is probably quite good for very small crack openings, since it has been deduced from test data on shearing of cracks in concretes that no relative shear displacements on the rough interlocked cracks is possible before a certain finite crack opening is produced, and that the shear stiffness of the cracks decreases rather slowly as the crack gradually opens. One must admit, however, that Eq. 3 (Hypothesis III) is also justified by its simplicity. It would be much more complicated to assume a general relation between the normal and shear microstresses and microstrains on each plane.

Tangential Stiffness Matrix

The virtual work of stresses per unit volume may be written, according to Eq. 1, as $\delta W = \sigma_{ij} \, \delta\epsilon_{ij} = \sigma_{ij} \, \delta\epsilon^a_{ij} + \sigma_{ij} \, \delta e_{ij}$. Summing the virtual work due to $\delta\epsilon^a_{ij}$ and δe_{ij}, we further have $\delta W = \sigma^a_{ij} \, \delta\epsilon^a_{ij} + s_{ij} \, \delta e_{ij}$, in which s_{ij} is the macrostress tensor resulting from s_n on all planes, and σ^a_{ij} is the stress tensor corresponding to ϵ^a_{ij}. Since both expressions for δW must hold for any $\delta\epsilon^a_{ij}$ and any $\delta\epsilon_{ij}$, we must have $s_{ij} = \sigma^a_{ij} = \sigma_{ij}$.

Equilibrium conditions may be expressed by means of the principle of virtual work:

$$\delta W^c = \frac{4}{3}\pi \, \sigma_{ij} \, \delta e_{ij} = 2 \int_S s_n \, \delta e_n \, f(\vec{n}) dS \tag{4}$$

in which S represents the surface of a unit hemisphere, the factor $(4\pi/3)$ is due to integrating over the surface of a sphere of radius 1, and $dS = \sin\phi \, d\theta \, d\phi$ (Fig. 1b). Note that we do not need to integrate over the entire surface of the sphere, since the values of σ_n or e_n are equal at any two diametrically opposite points on the sphere. Function $f(\vec{n})$ defines the relative frequency of the planes of various orientations $\vec{n}$, contributing to inelastic stress relaxation.

Substituting Eqs. 2-3 into Eq. 4, we get $\sigma_{ij} \, \delta e_{ij} = \int_S F(e_n) \, n_i n_j \, \delta e_{ij} \, f(\vec{n}) \, dS$, and because this must hold for any δe_{ij}, we must have

$$\sigma_{ij} = \int_0^{2\pi} \int_0^{\pi/2} F(e_n) \, n_i n_j \, f(\vec{n}) \, \sin\phi \, d\phi \, d\theta \tag{5}$$

Furthermore, according to Eq. 2, $dF(e_n) = F'(e_n)de_n = F'(e_n)n_k n_m \, da_{km}$, and thus differentiation of Eq. 5 finally yields

$$d\sigma_{ij} = D^c_{ijkm} \, de_{km} \tag{6}$$

Fig. 1

Model of Strain Inter-
action, Spherical Co-
ordinates, and Tensile
Stress-Strain Diagram.

(a)

(b)

(c)

σ_{11}

σ_{11}

tension

compression

σ_n

ϵ_n
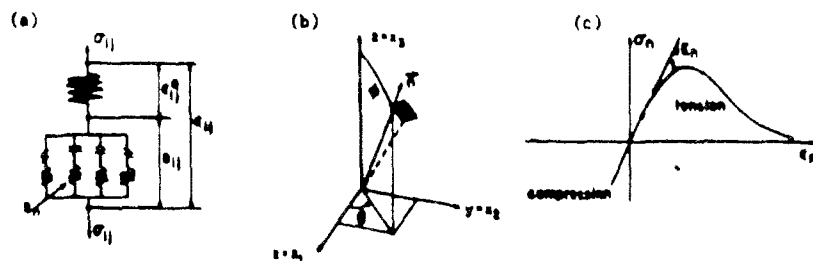
Fig. 2

Response Curves
for Uniaxial
Stress at
Various
Orientations

2 x 16 points

Stress (psi)

300

200

100

$C_b/C_a = 0.99999999$
$C_c/C_a = 1.00000000$
$C_d/C_a = 1.00000008$
$C_e/C_a = 1.00000000$
$C_f/C_a = 1.00000000$

0   0.0002   0.0004   0.0006

2 x 21 points

Stress (psi)

300

200

100

$C_b/C_a = 0.99999992$
$C_c/C_a = 0.99999990$
$C_d/C_a = 0.99999994$
$C_e/C_a = 0.99999998$
$C_f/C_a = 0.99999997$

0   0.0002   0.0004   0.0006

2 x 25 points

Stress (psi)

300

200

100

$C_b/C_a = 1.00000008$
$C_c/C_a = 1.00000000$
$C_d/C_a = 1.00000008$
$C_e/C_a = 1.00000000$
$C_f/C_a = 1.00000008$
$C_g/C_a = 1.00000008$

0   0.0002   0.0004   0.0006

Strain

51

in which

$$D^c_{ijkm} = \int_0^{2\pi}\int_0^{\pi/2} a_{ijkm} F'(e_n) f(\vec{n}) \sin\phi \, d\phi \, d\theta, \text{ with} \tag{7}$$

$$a_{ijkm} = n_i n_j n_k n_m$$

D^c_{ijkm} may be called the tangent stiffnesses of the microplane system. Note that the sequence of subscripts of D^c_{ijkm} is immaterial; therefore, there are only six independent values of incremental stiffnesses. Eq. 7 applies to initially anisotropic solids. For isotropic solids, we may substitute $f(\vec{n}) = 1$.

The mathematical structure of the present model may be geometrically visualized with the rheologic model in Fig. 1a.

The compliance corresponding to the additional elastic strain σ^a_{ij} must satisfy isotropy conditions, and so

$$C^a_{ijkm} = \frac{1}{9K^a} \delta_{ij} \delta_{km} + \frac{1}{2G^a}(\delta_{ik} \delta_{jm} - \frac{1}{3} \delta_{ij} \delta_{km}) \tag{8}$$

in which K^a and G^a are certain bulk and shear moduli which cannot be less than the actual initial bulk and shear moduli K and G. For fitting of test data, it was assumed, with success, that $1/G^a = 0$.

Recalling Eq. 1 (and Fig. 1a), we may now write the incremental stress-strain relation as

$$d\sigma_{ij} = D_{ijkm} dc_{ij}, \text{ with } [D_{ijkm}] =$$
$$[(D^c{}^{-1})_{ijkm} + (C^a_{ijkm})]^{-1} \tag{9}$$

Applying Eq. 7 to elastic deformations (with $f(\vec{n}) = 1$), one finds that the matrix in Eq. 7 always yields Poisson's ratio $\nu = 1/4$. This is because the slips on all microplanes are neglected. Since $\nu = 1/4$ is not quite true for concrete, the additional elastic strain must be used to make a correction. Let us now determine the value of K^a needed to achieve the desired Poisson's ratio ν. Let superscripts c and a distinguish between the values corresponding to D^c_{ijkm} and C^a_{ijkm}. For uniaxial stress we have $c_{11} = \sigma_{11}/9K^a + \sigma_{11}/E^c$ and $c_{22} = \sigma_{11}/9K^a - \nu^c \sigma_{11}/E^c$ in which $\nu^c = 1/4$ and $E^c = 2\pi E_n/5$, $E_n = F'(0) = $ initial normal stiffness for the microplane. Since $c_{22} = -\nu c_{11}$, we must have

$$K^a = \frac{1 + \nu}{9(\nu^c - \nu)} E^c \quad \text{(for } \nu \leq \nu^c) \tag{10}$$

This is, of course, under the assumption that $1/G^a = 0$.

The stress-strain relation for the microplanes, relating σ_n to ϵ_n, must describe cracking all the way to complete fracture, at which σ_n reduces to zero. In view of the kinematics visualized in Fig. 1b, it is clear that σ_n as a function of ϵ_n must first rise, then reach a maximum, and then gradually decline to zero. We choose the final zero value to be attained asymptotically, since no precise information exists on the final strain at which $\sigma_n = 0$, and since a smooth curve is convenient computationally. The following expressions were used in computations [19] (Fig. 1c):

$$\text{for } \epsilon_n > 0: \quad \sigma_n = E_n \epsilon_n e^{-(k\epsilon_n^p)},$$
$$\text{for } \epsilon_n \leq 0: \quad \sigma_n = E_n \epsilon_n \tag{11}$$

in which E_n, k, and p are positive constants; $k = 1.8 \times 10^7$, $p = 2$.

The integral in Eq. 7 has to be evaluated numerically, approximating it by a finite sum:

$$D^c_{ijkm} = \sum_{\alpha=1}^N w_\alpha [a_{ijkm} F'(\epsilon)]_\alpha \tag{12}$$

in which α refers to the values at certain numerical integration points on a unit hemisphere (i.e., certain directions), and w_α are the weights associated with the integration points.

Since in finite element programs for incremental loading the numerical integration needs to be carried out a great number of times, a very efficient numerical integration formula is needed. For the slip theory of plasticity, the integration was performed using a rectangular grid in the $\theta-\phi$ plane. This formula is, however, computationally inefficient because the integration points are crowded near the poles, and also because in the $\theta-\phi$ plane the singularity arising from the pole takes away the benefit from a use of higher-order integration formula.

Optimally, the integration points should be distributed over the spherical surface as uniformly as possible. A perfectly uniform subdivision is obtained when the microplanes normal to the α-directions are the sides of a regular polyhedron. A regular polyhedron with the most sides is the icosahedron, for which $N = 10$ (half the number of sides). Such a numerical integration formula was proposed by Albrecht and Collatz [18].

Numerical experience revealed, however, that 10 points are not enough when strain-softening takes place; it was found that the strain-softening curves calculated for uniaxial tensile stresses oriented at various angles with regard to the α-directions significantly differ from each other, even though within the strain-hardening range the differences are negligible. Therefore, more than 10 points are needed, and then a perfectly uniform

Table 1 - Direction Cosines and Weights for 2 x 21 Points (Orthogonal)
$O(h^8)$

α	x_1^α	x_2^α	x_3^α	w^α
1	1	0	0	0.07652141274
2	0	1	0	"
3	0	0	1	"
4	0.7071067812	0.7071067812	0	0.01993014153
5	0.7071067812	-0.7071067812	0	"
6	0.7071067812	0	0.7071067812	"
7	0.7071067812	0	-0.7071067812	"
8	0	0.7071067812	0.7071067812	"
9	0	0.7071067812	-0.7071067812	"
10	0.3879072746	0.3879072746	0.8360956240	0.02507124272
11	0.3879072746	0.3879072746	-0.8360956240	"
12	0.3879072746	-0.3879072746	0.8360956240	"
13	0.3879072746	-0.3879072746	-0.8360956240	"
14	0.3879072746	0.8360956240	0.3879072746	"
15	0.3879072746	0.8360956240	-0.3879072746	"
16	0.3879072746	-0.8360956240	0.3879072746	"
17	0.3879072746	-0.8360956240	-0.3879072746	"
18	0.8360956240	0.3879072746	0.3879072746	"
19	0.8360956240	0.3879072746	-0.3879072746	"
20	0.8360956240	-0.3879072746	0.3879072746	"
21	0.8360956240	-0.3879072746	-0.3879072746	"

$\beta = 33.269905°$

Table 2 - Direction Cosines and Weights for 2 x 25 Points.
$O(h^{10})$.

α	x_1^α	x_2^α	x_3^α	w^α
1	1	0	0	0.01269841058
2	0	1	0	"
3	0	0	1	"
4	0.7071067812	0.7071067812	0	0.02257495612
5	0.7071067812	-0.7071067812	0	"
6	0.7071067812	0	0.7071067812	"
7	0.7071067812	0	-0.7071067812	"
8	0	0.7071067812	0.7071067812	"
9	0	0.7071067812	-0.7071067812	"
10	0.3015113354	0.3015113354	0.9045340398	0.02017333557
11	0.3015113354	0.3015113354	-0.9045340398	"
12	0.3015113353	-0.3015113354	0.9045340398	"
13	0.3015113354	-0.3015113354	-0.9045340398	"
14	0.3015113354	0.9045340398	0.3015113354	"
15	0.3015113354	0.9045340398	-0.3015113354	"
16	0.3015113354	-0.9045340398	0.3015113354	"
17	0.3015113354	-0.9045340398	-0.3015113354	"
18	0.9045340398	0.3015113354	0.3015113354	"
19	0.9045340398	0.3015113354	-0.3015113354	"
20	0.9045340398	-0.3015113354	0.3015113354	"
21	0.9045340398	-0.3015113354	-0.3015113354	"
22	0.5773502692	0.5773502692	0.5773502692	0.02109375117
23	0.5773502692	0.5773502692	-0.5773502692	"
24	0.5773502692	-0.5773502692	0.5773502692	"
25	0.5773502692	-0.5773502692	-0.5773502692	"

$\beta = 25.239401°$
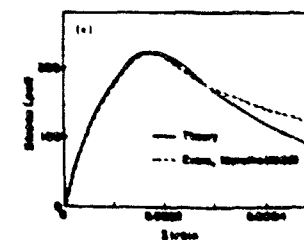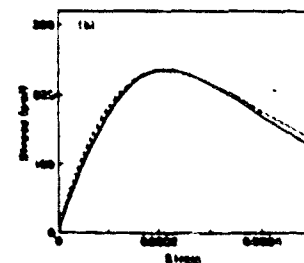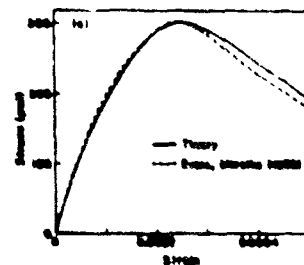
Fig. 3

Comparison with some of the Test Data of Evans and Marathe (1968)

spacing of a- directions is impossible.

Bažant and Oh [17] developed numerical integration formulas with more than 10 points, which give consistent results even in the strain-softening range. The most efficient formulas, with a nearly uniform spacing of a-directions, are obtained by certain subdivisions of the sides of an icosahedron and/or a dodecahedron [17]. Such formulas do not exhibit orthogonal symmetries. Other formulas which do were also developed [17]. Taylor series expansions on a sphere were applied and the weights v_a associated with the integration

points were solved from the condition that the greatest possible number of terms of the Taylor series expansion would cancel out. The angular directions of certain integration points were further determined so as to minimize the error term of the expansion. Formulas involving 16, 21, 25, 33, 37 and 61 points were derived, with errors of 8th, 10th and 12th order [17]. Table 1 defines two of these numerical integration formulas, with 21 and 25 points, one without, and one with orthogonal symmetry. These formulas give accuracy that suffices for most pratical purposes. For crude calculations, a formula with 16 points [17] may sometimes also suffice. The directions of integration points are illustrated in Fig. 2. Also shown are stress-strain diagrams calculated with the formula for uniaxial tension in various directions with regard to the intergration points (directions a, b, c, d,...); the spread of the curves characterizes the range of error.

Numerical Algorithm

The following numerical algorithm may be used for the microplane model in each loading step.

1. Determine $e_n^{(a)}$ from Eqs. 1 and 2 for all

directions $a = 1,...K$. In the first iteration of the loading step, use c_{ij} for the end of the previous step, and in subsequent interations use the value of c_{ij} determined for the mid-step in the previous iteration. In structural analysis, repeat this for all finite elements and for all integration points within each finite element.

2. For all directions $F^{(a)}$, evaluate $F'(e_n)$

for use in Eq. 7. Also check for each direction whether unloading occurs, as indicated by violation of the condition $s_n \Delta e_n \geq 0$. If violated, replace $F'(e_n)$ with the unloading stiffness (which may be approximately taken as E_n; however, a better expression exists.)

3. Evaluate D^c_{ijkm} from Eq. 7 and D_{ijkm} from

Eq. 9. In structural analysis, repeat this for all elements and all integration points in each element. When solving stress-strain curves, calculate then the increments of unknown stresses and unknown strains from Eq. 9. In structural analysis, solve (by the finite element method) the increments of nodal displacements from the given

load increments, and subsequently calculate the increments of c_{ij} and o_{ij} for all elements and all integration points in each element. Then advance to the next iteration of the same loading step, or advance to the next loading step.

In simulating uniaxial tensile loading of fixed direction, the unloading cirterion is not important since the only unloading occurs at moderate compressive stresses, for which a perfectly elastic unloading may be assumed.

The microplane model can be calibrated by comparison with direct tensile tests which cover the strain-softening response. Such tests, which can be carried out in a very stiff testing machine and on sufficiently small test specimens, have been performed by Evans and Marathe [20] as well as others [21-23].   Optimal values of the three parameters of the model, E_n, k, and p, have been found [19] so as to achieve the best fits of the data of Evans and Marathe. Some of these fits are shown as the solid lines in Fig. 3, and the data are shown as the dashed lines. A better test of the model would, of course, be a tensile test under rotating principal stress directions, but such tests have not yet been performed.

Note that with this theory, one has only two material parameters, E_n and k, to determine by fitting test data. Trial and error approach is sufficient for that.

Conclusion

The microplane model is capable of simulating realistic tensile stress-strain curve with strain-softening and reduction of stresses all the way to zero. Combined with the blunt crack band concept, in which the strain-softening is restricted to a region of a certain characteristic width that is a material property [1,2], this model should give a realistic representation of fracture. The model is general and does not preclude application to stress histories in which the principal stress directions rotate. These features are particularly attractive for the analysis of the response of concrete structures subjected to dynamic loads.

References

1. Bažant, Z. P., and Oh, B. H., "Crack Band Theory for Fracture of Concrete," Materials and Structures (RILEM, Paris), Vol. 16, 1983, in press (based on "Concrete Fracture via Stress-Strain Relations, Center for Concrete and Geomaterials, Report No. 81-10/665c, Oct. 1981, Northwestern University)

2. Bažant, Z. P., "Crack Band Model for Fracture of Geomaterials," 4th Intern. Conf. on Numerical Methods in Geomechanics, ed. by Z. Eisenstein, Univ. of Alberta, Edmonton, Vol. 3, 1982.

3. Taylor, G. I., "Plastic Strain in Metals," J. Inst. Metals, Vol. 62, 1938, pp. 307-324.

4. Batdorf, S. B., and Budiansky, B., "A Mathematical Theory of Plasticity Based on the Concept of Slip," NACA TN1871, April 1949.

5. Zienkiewicz, O. C., and Pande, G. N., "Time-Dependent Multi-laminate Model of Rocks — A Numerical Study of Deformation and Failure of Rock Masses," Int. Journal of Numerical an. Analytical Method in Geomechanics, Vol. 1, pp. 219-247, 1977.

6. Pande, G. N., and Sharma, K. G., "Multi-Laminate Model of Clays — A Numerical Evaluation of the Influence of Rotation of the Principal Stress Axes," Report, Dept. of Civil Engng., University College of Swansea, U.K., 1982; see also Proceedings, Symposium on "Implementation of Computer Procedures and Stress-Strain Laws in Geotechnical Engineering" Ed. By C. S. Desai and S. K. Saxena, held in Chicago, Aug. 1981, Acorn Press, Durham, N.C. 1981, pp. 575-590.

7. Pande, G. N., and Xiong, W., "An Improved Multi-laminate Model of Jointed Rock Masses," Proceedings, Intern. Symposium on Numerical Model on Geomechanics, ed. by R. Dungar, G.N. Pande, and G. A. Studer, held in Zurich, Sept. 1982, Balkema, Rotterdam, 1982, pp. 218-226.

8. Kröner, E., Zur Plastischen Verformung des Vielkristalls, Acta Metullurgica, Vol. 9, Feb. 1961, pp. 155-161.

9. Budiansky, B., Wu, T. T., "Theoretical Prediction of Plastic Strains of Polycrystals," Proc., 4th U. S. Nat. Congress of Appl. Mechanics, ASME, New York 1962, pp. 175-1185.

10. Lin, T. H., Ito, M., "Theoretical Plastic Stress-Strain Relationship of a Polycrystal," Intl. J. of Engng. Science, Vol. 4, 1966, pp. 543-561.

11. Hill, R., "Continuum Micromechanics of Elastoplastic Polycrystals," J. of Mechanics and Physics of Solids, Vol. 13, 1965, pp. 89-101.

12. Lin, T. H., Ito, M., "Theoretical Plastic Distortion of a Polycrystalline Aggregate under Combined and Reversed Stresses," J. of Mechanics and Physics of Solids, Vol. 13, 1965, pp. 103-115.

13. Hill, R., "Generalized Constitutive Relations for Incremental Deformations of Metal Crystals by Multislip," J. of Mechanics and Physics of Solids, Vol. 14, 1966, pp. 95-102.

14. Rice, J. R., "On the Structure of Stress-Strain Relations for Time-Dependent Plastic Deformation of Metals," J. of Appl. Mechanics ASME, Vol. 37, Sept. 1970, pp. 728-737.

15. Bažant, Z. P., Ozaydin, K., and Krizek, R.J. "Micromechanics Model for Creep of Anisotropic Clay," J. of the Engng. Mechanics Div., ASCE, Vol. 101, 1975, pp. 57-78.

16. Calladine, C. R., "A Microstructural View of the Mechanical Properties of Saturated Clay," Geotechnique, Vol. 21, 1971, pp. 391-415.

17. Bažant, Z. P., Oh, B. H., "Efficient Numerical Integration on the Surface of a Sphere," Report No. 83-2/428n, Center for Concrete and Geomaterials, Northwestern University, Evanston, IL. 60201.

18. Albrecht, J., and Collatz, L., "Zur numerischen Auswertung mehrdimensionaler Integrale," Zeitschrift für Angewandte Mathematik und Mechanik, Band 38, Heft 1/2, Jan/Feb., pp. 1-15.

19. Bažant, Z. P., and Oh, B. H., "Model of Weak Planes for Progressive Fracture of Concrete and Rock," Report No. 83-2/428m, Center for Concrete and Geomaterials, Northwestern University, Evanston, IL., Feb. 1983.

20. Evans, R. H., and Marathe, M. S., "Microcracking and Stress-Strain Curves for Concrete in Tension," Materials and Structures (Paris), No. 1, Jan.-Feb., 1968, pp. 61-64.

21. Heilmann, H. G., Hilsdorf, H. H., and Finsterwalder, K., "Festigkeit und Verformung von Beton unter Zugspannungen," Deutscher Ausschuss für Stahlbeton, Heft 203, W. Ernst & Sohn, West Berlin, 1969.

22. Hughes, B. P., and Chapman, G. P., "The Complete Stress-Strain Curve for Concrete in Direct Tension," Bulletin RILEM, No. 30, pp. 95-97, 1966.

23. Rusch, H., and Hilsdorf, K., "Deformation Characteristics of Concrete under Axial Tension." Vorunterschunge, Bericht Nr. 44, Munich, May 1963.

56

A PLASTIC-FRACTURE MODEL FOR CONCRETE MATERIALS

W. F. Chen

Professor of Structural Engineering

Purdue University

West Lafayette, Indiana

T. Y. P. Chang

Professor of Civil Engineering

The University of Akron

Akron, Ohio

ABSTRACT

Recent research in structural concrete under static and dynamic loading has been moving toward the development of three-dimensional stress-strain relations based on the principles of plasticity as well as elasticity. Although significant progress in this area has been made in recent years, no unified treatment of the various existing mathematical models of concrete has been attempted from which a comprehensive elastic-plastic-fracture stress-strain relationship for concrete can be formulated. This unified approach is attempted in the present work.

In this theoretical development, the five-parameter failure surface of Willam-Warnke model, the technique of mixed hardening for cyclic loading, the concept of crushing coefficient and the dual criterion for crushing, cracking, and mixed types of failure of concrete will be considered as the basis for this comprehensive development.

1. INTRODUCTION

For the most part, analytical studies of the nonlinear response of reinforced concrete structures have been focused, by necessity, on the behavior of isolated simple structural elements such as beams and columns. As quantitative information on the load-deformation behavior of concrete developed and computing capability expanded, the scope of nonlinear analysis has broadened to include such triaxially loaded concrete structures as floating vessels, offshore platforms, submerged structures, the usual land-based or underground containment vessels, prestressed concrete reactor vessels and dams. Although large-scale finite-element software packages now have a wide range of applications in many areas of stress analysis, inadequate material models are often one of the major factors in limiting a structural analysis. This is especially true for reinforced concrete, where basic characteristics of reinforced concrete materials do not exist. The problem of modeling the mechanical behavior of

concrete for use in analytical studies of reinforced concrete structures remains one of the most difficult challenges in the field of structural concrete engineering.

Current analysis procedures for reinforced concrete problems under short-term loading are essentially one- or two-dimensional. A common approach uses two concrete parameters: concrete modulus and concrete fracture strength. Various empirical equations for these have been established by curve fitting many biaxial-loading-test data. The best known of these expressions is probably either the one proposed by Liu, Nilson, and Slate, of Cornell University, or the one proposed by Gerstle et al of the University of Colorado (see Chen, 1981). Their equivalent one- or two-dimensional approach is appealing because of its simplicity, its broad data base, and the correlations that have been established between the concrete modulus and a variety of concrete strength and strain characteristics. It is well known that these models are mainly applicable to planar problems such as beams, panels, and thin shells, where the stress is predominantly biaxial.

At present, multi-dimensional analyses are usually made by taking the concrete to be incrementally elastic. When this is done, Poisson's ratio must be defined. However, it is not possible to describe the three-dimensional stress-strain behavior of concrete materials accurately in the framework of an incremental Hooke's law with variable moduli which are functions of the maximum stress and/or strain levels. Recent research in structural concrete under static and dynamic loading has been moving toward the development of three-dimensional stress-strain relations based on the principles of plasticity as well as elasticity. Although some work in this area has been done in recent years, no unified treatment of the various existing mathematical models of concrete has been made from which a comprehensive elastic-plastic-fracture stress-strain relationship for concrete can be formulated. This unified

approach is attempted in the present
paper.

In this paper, empirical equations
for modulus an fracture strength under
biaxial loading, empirical expressions
for bulk and shear modulus under mul-
tiaxial stress states, orthotropic elas-
ticity, perfect and work-hardening plas-
ticity, which have been treated as an
individual technique in the mathematical
modeling of concrete behavior, are con-
sidered in relation to a common struc-
ture. Some of the interrelationships
between the empirical equations, elasti-
city, and plasticity are examined criti-
cally and synthesized in order to formu-
late a comprehensive elastic-plastic-
fracture stress-strain relationship for
concrete. In particular, the five-
parameter failure surface of Willam-
Warnke model, the technique of mixed
hardening for cyclic loadings, the sim-
ple concept of crushing coefficient and
the dual criterion for crushing type,
the cracking type and the mixed type of
failure of concrete are considered as
the basis for this comprehensive
development.

It is also expected that the
three-dimensional finite element
analysis program currently under
development at Purdue University will be
the foundation for a general purpose
nonlinear reinforced concrete analysis,
steel-concrete interaction program. In
this development, the comprehensive con-
stitutive equations developed in the
present work for concrete material will
be implemented into the computer code in
the form of subroutines, which can be
readily adapted by any nonlinear finite
element computer program in which the
solution method is based on the incre-
mental approach with a tangent modulus
formulation for solving elastic-
plastic-fracture problems.

2. **THE LITERATURE ON THE STATE-OF-THE-
ART**

No attempt will be made here to
review the vast literature on the
mathematical modeling and nonlinear
analysis of reinforced concrete
structures. A comprehensive state-of-
the-art summary on the constitutive
modeling of reinforced concrete materi-
als based on the theories of linear and
nonlinear elasticity as well as the
theories of perfect and work-hardening
plasticity together with their finite
element applications is given in a
recent comprehensive book entitled
"Plasticity in Reinforced Concrete" by
Chen (McGraw-Hill, 1981). Further, a
comprehensive state-of-the-art review on

constitutive modeling of materials and
finite-element analysis of reinforced
concrete structures with typical exam-
ples of recent applications, together
with an extensive list of references,
and compilation of available computer
programs is contained in the special
report of the ASCE Committee (1982) on
finite element analysis of reinforced
concrete structures (A. H. Nilson of
Cornell University, Chairman). In par-
ticular, the materials presented in
Chapter 2 of the ASCE Report entitled
"Constitutive Relations and Failure
Theories" by W.F. Chen (Chairman), Z.P.
Bazant, O. Buyukosturk, T.Y. Chang, D.
Darwin, T.C.Y. Liu and K.J. Willam pro-
vide a valuable source of information on
the current state-of-the-art in
mathematical modeling of reinforced con-
crete materials. Detailed and extensive
discussions of the three-dimensional
elastic-plastic-fracture constitutive
equations for concrete are given in the
two references mentioned above and
therefore will not be repeated here.
Instead, a discussion of the particular
features to be included in the present
formulation of a comprehensive elastic-
plastic-fracture stress-strain relation-
ship for concrete is given in the forth-
coming.

It is worth mentioning here that a
strong impetus to research in this gen-
eral area has been the studies required
for the design of prestressed concrete
reactor vessels. More recent work in
this area can be followed through the
Proceedings of the International Confer-
ence on Structural Mechanics in Reactor
Technology, published regularly since
1971. Special proceedings dealing with
the nonlinear finite-element analysis of
reinforced concrete structures have been
published by IASS (1978), Politecnico di
Milano (1978), and IABSE (1979). Most
recent proceedings that have just been
published are the two-volume IABSE pub-
lication on "Advanced Mechanics of Rein-
forced Concrete" (Colloquium, Delft,
1981) and the Workshop on Constitutive
Relations for Concrete held in Albu-
querque, New Mexico, on April 28-29,
1981 sponsored and published by the Air
Force Weapons Laboratory and the New
Mexico Engineering Research Institute.

3. **CONSTITUTIVE EQUATIONS FOR CONCRETE**

Concrete, like many other engineer-
ing materials, exhibits brittle behavior
for tensile and small compressive
stresses and becomes ductile in the
presence of large hydrostatic pressures.
It is therefore meaningful and con-
venient to seek yield criteria and plas-
tic stress-strain relationships for con-

crete in the ductile state and to seek fracture criteria and stress-strain relationships for fractured concrete in the brittle state. These brittle and ductile models can then be combined to provide a proper description of the pre- and post-failure behavior of concrete in the ductile-brittle state.

In the following, we summarize the special features in formulating an elastic-plastic-fracture model for the finite-element analysis of concrete structures. Based on the recent developments, we adopt the five-parameter fracture (or yielding) criterion of Willam-Warnke (1975) as the failure model for concrete. Isotropic elastic and anisotropic elastic theories are applied for the description of the initial loading and the post-failure behaviors of concrete. A plastic model displaying mixed hardening is used to describe the concrete behavior between the initial yielding and the fracture failure. Incremental stress-strain relationships are then derived based on the associated flow rule and mixed hardening rule of isotropic and kinematic models. In the present development, three different types of failure modes are considered. A simple crushing coefficient is defined based on a dual criterion to identify the crushing type, the cracking type and the mixed type of failure. Details of this development are given in the forthcoming.

3.1 Elastic-Plastic-Fracture Model

Different stages of the 3-D model mentioned above can be illustrated schematically in a typical uniaxial stress-strain curve for a plain concrete shown in Fig. 1.
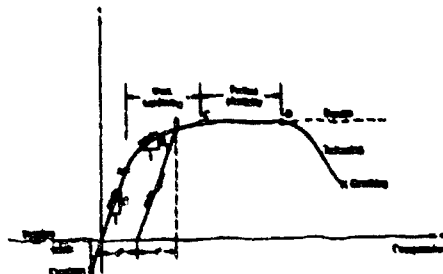
Figure 1. Uniaxial stress-strain curve, pre- and post-failure regions

For tensile failure, the behavior is essentially linearly elastic up to failure load, the maximum stresses coincide with the maximum strains, and no plastic strains occur at the failure moment. For compressive failure, the material initially exhibits almost linear behavior up to the proportional limit at point A, after which the material is progressively weakened by internal microcracking up to the end of the perfectly plastic flow region CD at point D. The nonlinear deformations are basically plastic, since upon unloading only the portion ϵ^e can be recovered from the total deformation ϵ. It is clear that the phenomenon in the region below point A, in the region AC, and in the region CD corresponds exactly to the behavior of a linearly elastic, a work-hardening elastoplastic, and an elastic perfectly plastic solid, respectively. The use of an elastic-work-hardening-plastic model to describe the stress-strain behavior of concrete materials is therefore very attractive in view of these apparent similarities.

We shall therefore assume a linear or nonlinear elastic stress-strain relationship until the combined state of stress reaches an initial yield surface. The initial yield criterion is assumed to have the same geometrical shape in the stress space as the failure criterion. The five-parameter failure criterion of Willam-Warnke is used to define the ultimate state of stress. A further discussion on the choice of the Willam-Warnke's five-parameter model is given in Sec. 4.2.

Between the initial yielding state and the failure state, an incremental stress and strain relationship is assumed to define the plastic behaviors. The plastic relations are developed on the basis of a mixed-hardening rule and the classical associated flow rule. This development is discussed in Sec. 4.3.

For the post-failure models, the concrete behaviors are defined by three types of failure modes, namely, cracking, crushing, and a mixed mode. A crushing coefficient based on a dual criterion has recently been proposed by Hsieh et al (1982) to identify each of the failure modes. This feature of the development is described in Sec. 4.4.

For a fractured concrete, procedures have been developed to handle the stress-strain redistribution of a fractured element (Suzuki and Chen, 1981). These procedures are tailored for the finite-element analysis of con-

crete structures. For the fractured
concrete stress-strain relation, an
anisotropic elastic model is used.
Details of this are given in Sec. 4.3.

3.2 Failure Criteria

In early finite-element analyses
the von Mises or Tresca type of yield
surface for ductile metals is generally
used for concrete under compressive
stresses. This type of pressure-
independent yield surface corresponds to
a pure shear or octahedral shear τ_{oct}

dependence. To account for the limited
tensile capacity of concrete, the von
Mises or Tresca surface usually is aug-
mented by a separate tension-failure
surface, e.g. the maximum-principal-
stress surface or tension-cutoff sur-
face.

The Drucker-Prager surface is prob-
ably the simplest type of pressure-
dependent yield or failure criterion
where the pure shear or octahedral shear
τ_{oct} depends linearly on the hydro-
static pressure I_1 or octahedral normal
stress σ_{oct}. It can be looked upon as a
smooth Mohr-Coulomb surface. The latter
has frequently been used as failure sur-
face for concrete, while the Drucker-
Prager surface has most frequently been
used for soils. The Drucker-Prager sur-
face has two basic shortcomings in con-
nection with concrete modeling: the
linear relationship between τ_{oct} and
σ_{oct} and the independence of the angle
of similarity θ (see Fig. 2). The
$\tau_{oct} - \sigma_{oct}$ relation has been experimen-
tally shown to be curved, and the trace
of the failure surface on deviatoric
sections is not circular. Two-parameter
models with straight lines as meridians
are therefore inadequate for describing
the failure of concrete in the high-
compression range.

The generalized Drucker-Prager sur-
face proposed by Bresler and Pister
(1958) assumes a parabolic dependence of
τ_{oct} on σ_{oct}, while the deviatoric sec-
tions are independent of θ. On the
other hand, the early version of the
three-parameter surface developed by
Willam-Warnke (1975) retains the linear
$\tau_{oct} - \sigma_{oct}$ relation, but deviatoric
sections exhibit θ-dependence. The
four-parameter models of Ottosen (1977)
and Hsieh et al (1982) and the refined
five-parameter model of Willam-Warnke

constitute both a parabolic $\tau_{oct} - \sigma_{oct}$
relation and a θ-dependence. Most of
these refined models give a close esti-
mate of the relevant experimental data
(1981), contain all the three stress
invariants, reflect all the required
characteristics concerning smoothness,
convexity, symmetry, curved meridians,
etc. But the Willam-Warnke's five-
parameter model includes most of the
earlier one-, two- and three-parameter
models as special cases and becomes
increasingly popular in recent years.
We therefore adopt the five-parameter
failure model of Willam-Warnke as the
basic surface for the development of the
present elastic-plastic-fracture model
for concrete.
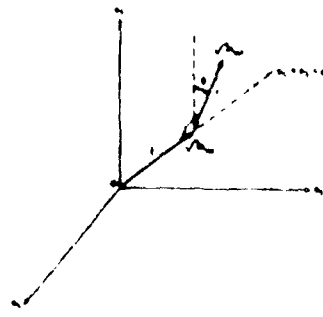
Figure 3. Planned and present representation of Willam-Warnke model.

The five-parameter model is illus-
trated in Fig. 3, where it is compared
with triaxial test data. Close agree-
ment can be observed for both hydros-
tatic and deviatoric sections. In the
low-compression regime the surface
strongly resembles a tetrahedron, the
plane of which bulges with increasing
hydrostatic compression approximating a
circular cone asymptotically.

In summary, the Willam-Warnke's
five-parameter model reproduces the
principal features of the triaxial
failure surface of concrete (Chen,
1982). It consists of a conical shape
with curved meridians and noncircular
base sections as well as nonaffine sec-
tions in the deviatoric plane. In view
of the fluctuations of experimental
results, there is little need for
further refinements of this model. Thus,
we choose this surface as the basic
forms for yielding, loading and failure
surfaces. Further discussions will
therefore be focused on the development
of stress-strain relationships of con-
crete under general stress states.

3.3 Mixed Hardening Rule

It is convenient to assume a criterion for initial yielding to have the same functional form as the failure criterion. In the present model based on the five-parameter failure criterion of Willam and Warnke (1975), the material constants are also assumed to remain the same, except that the nondimensional constant, the compressive strength f_c' is replaced by a different value $f_c' = 0.3 \sim 0.6 f_c'$. The exact value of f_c' can be taken from the uniaxial compressive stress-strain curve of the specific concrete used.

The initial yielding criterion and the failure criterion define the limits of the elastic region, the plastic region, and the post-failure region. Within the elastic region and the post-failure region, theories of <u>linear elasticity</u> and <u>nonlinear anisotropic elasticity</u> can be applied to concrete from the

Hydrostatic Section   Deviatoric Sections
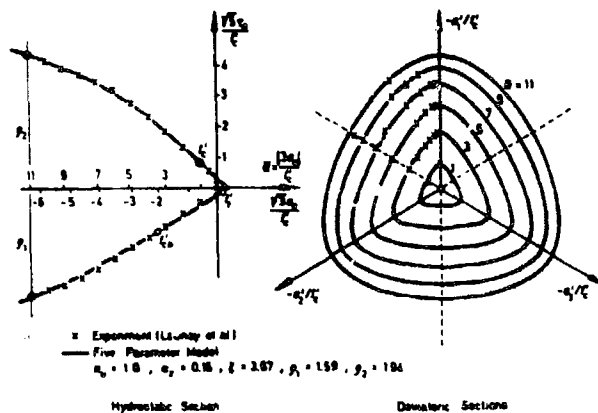
Figure 3 Comparison of test results for Willam-Warnke Failure Mode. (Willam and Warnke, 1974)

macroscopic point of view (Chen and Saleeb, 1982). For a state of stress beyond the initial yielding <u>irreversible</u> deformations become significant. It is convenient to follow the <u>work-hardening plasticity theory</u> to develop the required incremental form of stress-strain relationships. This requires the consideration of a hardening rule.

The hardening rule defines the motion of the subsequent yield surfaces during plastic loading. A number of hardening rules have been proposed to describe the growth of subsequent yield surfaces for work-hardening materials. The choice of a specific rule depends on the ease with which it can be applied and its ability to represent the hardening behavior of the material being considered. Three types of hardening rules are most frequently considered:

1. Isotropic hardening (Hill, 1950)

2. Kinematic hardening (Prager, 1955; Ziegler, 1959)

3. Mixed hardening (Hodge, 1957)

The isotropic-hardening rule assumes a uniform expansion of the initial yield surface. It applies mainly to monotonic proportional loadings; for cyclic and reversed types of loadings for materials with a pronounced Bauschinger effect, the kinematic hardening rule is more appropriate. It considers the Bauschinger effect in an idealized manner and also the development of anisotropy due to plastic deformation. Combinations of isotropic and kinematic hardening are called <u>mixed hardening</u>, which is found to be more suitable for concrete materials.

In the present model, we consider the plastic strain increment in the form

$$d\varepsilon_{ij}^{p} = d\varepsilon_{ij}^{pi} + d\varepsilon_{ij}^{pk} \qquad (1)$$

$$= M \, d\varepsilon_{ij}^{p} + (1-M) \, d\varepsilon_{ij}^{p}$$

and introduce a constant parameter M to define the isotropic hardening effect $d\varepsilon_{ij}^{pi} = M \, d\varepsilon_{ij}^{p}$. The remaining plastic strain increment $d\varepsilon_{ij}^{pk}$ is then due to the kinematic hardening. The strain increment $d\varepsilon_{ij}^{pi}$ is related to the isotropic hardening function through the concept of <u>effective stress</u> - <u>effective plastic strain</u> which makes it possible to extrapolate from a simple uniaxial compression test into the multidimensional situation. The strain increment $d\varepsilon_{ij}^{pk}$ is related to the kinematic hardening rule of Prager's or Ziegler's.

In this mixed hardening model for concrete, the weighting coefficient M (0 < M < 1) is introduced to allow the freedom of selecting different proportions of isotropic and kinematic effects

in the mixed model. M can also be a negative value, so that isotropic softening can also be considered. The advantage of using the concept of mixed hardening have been demonstrated by Axelsson and Samuelsson (1979) in describing the loading cycles of metals and by Hsieh et al (1982) in describing the reversed loading behavior of concrete materials.

In developing an elastoplastic model for work-hardening material, three basic assumptions are general employed:

1. The existence of initial yield surface and subsequent loading surfaces.

2. The formulation of an appropriate hardening rule that describes the evolution of subsequent loading surfaces.

3. A flow rule that specifies the general form of the stress-strain relationship.

In the present work, the first assumption is satisfied by the choice of the five-parameter model of Willam and Warnke (Sec. 4.2). As for the second assumption, we have chosen the mixed hardening rule as described here.

The third assumption states that for an idealized plastic material, it is possible to define a plastic potential function $g(\sigma_{ij}, \epsilon^p_{ij}, k)$,

$$d\epsilon^p_{ij} = d\lambda \frac{\partial g}{\partial \sigma_{ij}} \qquad (2)$$

The gradient of the potential surface defines the direction of the plastic-strain increment, while the length is determined by the loading parameter $d\lambda$.

The flow rule is associated if the plastic potential has the same shape as the yield condition

$$g(\sigma_{ij}, \epsilon^p_{ij}, k) = f(\sigma_{ij}, \epsilon^p_{ij}, k)$$

$$d\epsilon^p_{ij} = d\lambda \frac{\partial f}{\partial \sigma_{ij}} \qquad (3)$$

The associated flow rule is applied here for practical reasons, since there is very little experimental evidence on subsequent loading surfaces. In a few cases observations are available, e.g. on the volume change during plastic flow, we may use this information, in the subsequent development to construct

a plastic potential independently of the yield surface for controlling dilatancy or compaction (Chen, 19??).

With the help of these three assumptions, we can now determine uniquely the stresses which arise during any iteration in a numerical analysis in which known, finite changes in strain $\Delta\epsilon_{ij}$ are imposed. This is the subject of a later discussion.

2.4 Post-Fracture Modeling

Concrete fails or fractures in extremely complex modes. Aggregate types, mixed design, and loading conditions among many other factors all play roles in the cause of failure. It is difficult to classify and define precisely the failure modes. However, in a general sense, the mode of failure may be categorized into three types, namely, the cracking, crushing and a mixture of cracking and crushing. Documented test results for tension-tension or tension-compression biaxial conditions show the cause of fracture is primarily a brittle splitting in the plane normal to the maximum tensile strain direction (see for example, Chen and Ting, 1980). For the triaxial compression tests, depending on the magnitude of confinement pressure, it seems that all the three types of mode are possible. When the confinement pressure is much lower than the axial compression, rough crack surfaces can be formed in the direction normal to the maximum tensile strain, possibly due to the connection of numerous microcracks. For nearly uniform hydrostatic condition, crushing failure is more common, possibly due to the rupture of mortar in the concrete.

In view of the failure modes due to various types of loading conditions, a crushing coefficient α has been proposed to identify the mode being either a pure cracking, a pure crushing, or a mixture of the above (Hsieh et al, 1982). The coefficient can also be used to estimate the proportions of the cracking effect of the crushing effect in a mixed type of failure. This concept is found to be particularly appealing when the post-failure behaviors of the fractured concrete are considered. This concept is further refined in the present work.

The concept of crushing coefficient is based on the consideration of a dual criterion in defining the pure cracking zone and the pure crushing zone in the overall spectrum of failure mode. In the early development, the pure cracking zone is assumed to satisfy the maximum

tensile stress condition

$$\sigma_1 > 0 \qquad (4)$$

which can be written in terms of the stress invariants as

$$J_2 \cos\theta + \frac{1}{2\sqrt{3}} I_1 > 0 \qquad \theta < 60° \quad (5)$$

where

$I_1 = \sigma_{ii}$ = the first stress invariant

$$J_2 = \frac{1}{2} s_{ij} s_{ij}$$

= the second deviatoric stress invariant

$$J_3 = \frac{1}{3} s_{ij} s_{jk} s_{ki}$$

= the third deviatoric stress invariant, and

$$\cos 3\theta = \frac{3\sqrt{3}}{2} \frac{J_3}{J_2^{3/2}}$$

= angle of similarity, Fig. 2.(6)

It may be shown that the upper limit of the pure cracking condition satisfies the uniaxial and the biaxial compression failure test data, see Fig. 4. For the pure crushing type, it was assumed, as a first approximation, that all three principal strain components are all compressive strains, so that the crack mechanism can not be developed in the light that no tensile strain could appear in any direction. This implies that the maximum principal strain is non-positive

$$\varepsilon_1 < 0 \qquad (7)$$

Using the Hooke's law, this condition may be expressed in terms of the stress invariants as

$$\sqrt{J_2} \cos\theta + \frac{(1-2\nu)}{2\sqrt{3}(1+\nu)} I_1 < 0 \qquad (8)$$

combining these two conditions for cracking and crushing, a crushing coefficient α may be defined

$$\alpha = \frac{I_1}{2\sqrt{3}\sqrt{J_2}\cos\theta} \qquad \theta < 60° \quad (9)$$

such that

i. pure cracking mode, when $\alpha < 1$

ii. pure crushing mode, when $\alpha > \frac{1+\nu}{1-2\nu}$

iii. mixed mode, when

$$1 < \alpha < \frac{1+\nu}{1-2\nu} \qquad (10)$$

If Poisson's ν is taken to be 0.2, we have the simple values of $\alpha = 1.0$ and 2.0 as the boundary values separating the three different failure zones. This is illustrated schematically in the octahedral normal and shear stress space as shown in Fig. 4.
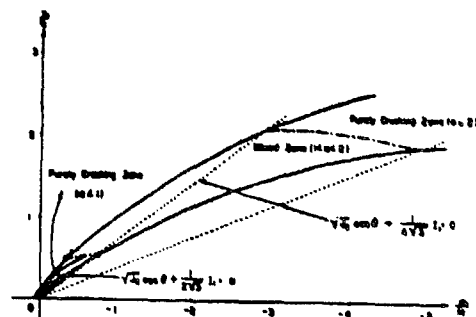
Fig.4. Failure zones in octahedral shear and normal stress planes.

Note that in obtaining the simple crushing coefficient α, Hooke's law of elasticity was employed to obtain the stress criterion. Strictly speaking, this is inconsistent in an elastic-plastic-fracture model; Hooke's law may not apply immediately before crushing. However, judging by the complex nature of concrete failure and the simplicity in the application of the concept of the crushing coefficient, the elasticity assumption may represent an acceptable first approximation. For more accurate descriptions, the original dual criterion, i.e. $\sigma_1 > 0$ and $\varepsilon_1 < 0$, may also

be used. A further refinement on the concept of crushing coefficient will be made in the subsequent work.

To complete the constitutive model for the post-fracture behaviors of concrete corresponding to each of the failure modes, we use the following possible approaches for the mathematical modeling.

For the pure crushing zone, the crushed concrete may be viewed to behavior like a granular material under the confinement of neighboring materials. Material stiffness in compression or shear, although reduced, should still exist. For simplicity, we may neglect the residual stiffness and the residual

strength of a crushed concrete element completely in an analysis. A more refined model may consider the orientation of failure planes and use a partially collapse failure surface in the form of no-tension, no-cohesion or no-friction models (Argyris st al, 1976). This aspect of modeling is not considered in the present work.'

For the pure cracking zone, the customary procedures is to assume that the cracked concrete remains a continuum, i.e. the cracks are smeared out in a continuous fashion. It is assumed that the concrete becomes orthotropic (or more accurately, transversely isotropic) after the first cracking has occurred, one of the material axes being oriented along the direction of cracking. Such formulations easily allow for gradual build-down of strength in the direction of tension (tension stiffening). Also shear-strength reserves due to aggregate interlocking and dowel action of reinforcement can be accounted for by retaining a positive shear modulus. The continuous model for cracking has been used in most of the computational models for concrete and is therefore adopted here for further development. An extensive discussion of the kinematics of a cracked concrete element has been reported by Chen and Suzuki, (1980).

For the mixed failure zone, the value of the crushing coefficient is between 1.0 and 2.0 for $v = 0.2$, for example. If the crushing coefficient is adopted as a measure of the degree of crushing in this partially cracking and partially crushing concrete element, then we may view that the post-failure behavior is also a linear interpolation of the perfectly deformable behavior and the anisotropic elastic behavior. Hence '¦ is proposed that the concrete element will lose its rigidity in the cracked plane according to the maximum tensile strain direction and the anisotropic stiffness of the fractured element will also be proportionally reduced according to the magnitude of α. Note that for $v = 0.2$, mixed failure lies between $\alpha = 1.0$ and 2.0. Thus, the value of α behind the decimal point represents the percentages of crushing and also the percentages of stiffness reduction.

References

[1] Chen, W.F., "Plasticity in Reinforced Concrete," McGraw-Hill, 1982. 474 total pages.

[2] IABSE Colloquium on Advanced Mechanics of Reinforced Concrete, June 2-4, Delft, The Netherlands, 1981.

Introductory Report, Vol. 33, Final Report, Vol. 34, Zurich, Switzerland, December, 1981.

[3] Chen, W.F., "Plasticity in Reinforced Concrete," Proceedings of the Workshop on Constitutive Relations for Concrete held in Albuquerque, New Mexico, on April 23-29, 1981. The Workshop was sponsored by the Air Force Weapons Laboratory and the New Mexico Engineering Research Institute.

[4] Chen, W.F. (Chairman), Z.P. Bazant, O. Buyukozturk, T.Y. Chang, D. Darwin, T.C.Y. Liu and K.J. Willam, "Constitutive Relations and Failure Theories (Chapter 2)," In the state-of-the-art Committee Report on Finite Element Analysis of Reinforced Concrete Structures, ASCE Special Publication, 1982, pp. 34-148.

[5] Willam, K.J. and E.P. Warnke, "Constitutive Models for the Triaxial Behavior of Concrete," IABSE Seminar for Concrete Structures subjected to Triaxial Stresses, Bergamo, Italy, 1974, IABSE Proceedings, Vol. 19, 1975, pp. 1-30.

[6] Hsieh, S.S., E.C. Ting and W.F. Chen, "A Plastic-Fracture Model for Concrete" International Journal of Solids and Structures, Vol. 18, No. 3, 1982, pp. 181-197.

[7] Suzuki, H. and W.F. Chen, "Elastic-Plastic-Fracture Analysis of Concrete Structures," Computers & Structures, Vol. 14, 1982.

[8] Bresler, B. and K.S. Pister, "Strength of Concrete Under Combined Stresses," Journal of American Concrete Institute, Vol. 55, September, 1958, pp. 321-345.

[9] Ottosen, N.S., "A Failure Criterion for Concrete," Journal of the Engineering Mechanics Division, ASCE, Vol. 103, No. EM4, August, 1977, pp. 527-535.

[10] Axelsson, K., and A. Samuelsson, "Finite Element Analysis of Elastic-Plastic Materials Displaying Mixed Hardening," International Journal for Numerical Methods in Engineering, Vol. 14, 1979, pp. 211-225.

[11] Hill, R., "The Mathematical Theory of Plasticity," Oxford University Press, London, 1950.

[12] Prager, W., "The Theory of Plasticity: A Survey of Recent Achievements," Proceedings of the Institute of Mechanical Engineering, Vol. 169, No. 41, 1955, pp. 3-19.

[13] Ziegler, H., "A Modification of Prager's Hardening Rule," Quarterly of Applied Mathematics, Vol. 17, No. 55, 1959, pp. 55-65.

[14] Hodge, P.G., Jr., "Discussion [of Prager (1956)]", Journal of Applied Mechanics, Vol. 23, 1957, pp. 482-484.

[15] Chen, W.F. and Saleeb, A.F., "Constitutive Equations for Engineering Materials," Vol. 1 "Elasticity and Modeling," 1982, Vol. 2 "Plasticity and Modeling," 1983, John Wiley Inter-Science, New York.

[16] Chen, W.F. and E.C. Ting, "Constitutive Models for Concrete Structures," Journal of the Engineering Mechanics Division, ASCE, Vol. 106, No. EM1, 1980, pp. 1-19.

[17] Argyris, J.H., G. Faust and K.J. Willam, "Limit Load Analysis of Thick-Walled Concrete Structures - A Finite Element Approach to Fracture," Computer

Methods in Applied Mechanics and Engineering, Vol. 8, North-Holland Publishing Company, 1976, pp. 215-243.

[18] Chen, W.F. and Suzuki, H., "Constitutive Models for Concrete," Computers and Structures, Vol. 12, 1980, pp. 23-32.

THE EFFECTS OF CURING AND AGING ON THE TRIAXIAL PROPERTIES
OF CONCRETE IN UNDERGROUND STRUCTURES

M. M. Hightower

Sandia National Laboratories
Albuquerque, NM 87185

ABSTRACT

To accurately predict the response of a concrete structure for a given loading condition some knowledge of shear strength and compressibility is required. Several studies have shown that these properties vary as concrete cures and ages; therefore, the response of a concrete structure changes with time. In order to address this problem, Sandia initiated a material test program to study the curing and aging of underground concrete structures. Material properties were obtained from cores taken periodically from two underground concrete structures constructed at the Sandia Tonopah Test Range, Nevada. Results of this continuing study are presented.

INTRODUCTION

The effect of curing and aging on the material properties of concrete is always a design consideration. However, most research in this area is driven by construction considerations and, normally, only the effects of these factors on the uniaxial compressive strength are studied. The effects of curing and aging on the response of concrete structures to munition type loadings require additional considerations. For munition type loadings, the multi-dimensional response of concrete is important. Also, concrete structures are cured under in situ rather than laboratory conditions. Since it is difficult to test large structures, it is common to test laboratory cured scale model structures which are only several months old. To accurately apply structural response and munition effectiveness results from these models to the prototypes requires that the difference between the multi-axial properties of the model and the prototype be defined. Therefore, in the interaction of munitions with concrete structures, the effects of the variation in curing and aging on the multiaxial properties of concrete are very important.

One of the most common types of defense structures is the buried concrete structure which has been used in many applications. Depending on the geologic material in which a buried structure is constructed, the in situ curing conditions can vary from dry to saturated and at other than optimal curing temperatures. Since it is difficult to obtain samples or cores from buried structures, little data is available to date on the effect of these types of in situ curing conditions on concrete properties.

In support of concrete penetration programs, Sandia constructed several buried concrete structures at the Tonopah Test Range, Nevada. In order to determine the effect of in situ curing and aging on concrete properties for these structures, Sandia has periodically cored two of these structures. With this test program, we hoped to determine the rate at which these structures cure and the maximum strengths attained.

TEST PROGRAM

Two buried structures constructed for concrete penetration studies were tested in this program.

The first structure (Structure A) consists of several layers of heavily reinforced concrete slabs which were two to three feet thick and buried from six to 27 feet deep. The concrete was nominally 34 MPa (5000 psi) unconfined compressive strength at 28 days with one inch maximum size aggregate. The second structure (Structure B) is eight feet thick, ten feet in diameter, non-reinforced, and buried eight feet deep. The concrete was nominally 14 MPa (2000 psi) unconfined compressive strength at 28 days with no coarse aggregate. Structure A was constructed at Antelope Dry Lake and Structure B was constructed in Pedro Dry Lake. The material properties of the soil in both of these dry lake beds down through

the levels at which these structures were built are listed in Table I.

All material property tests were conducted by Terra Tek, Salt Lake City, Utah. The data obtained included physical properties (density, porosity, and saturation) and hydrostatic and triaxial compression data to confining pressures of 400 MPa (58000 psi). Concrete samples were taken as each structure was constructed. These samples were tested at the time of the first penetration test into each structure which, in both cases, was a few months after construction. After construction, each of these structures was cored at approximately two year intervals so that material properties of the aging concrete could be obtained. Structure A was constructed in 1980 and was cored in 1982, while Structure B was constructed in 1979 and was cored in 1981 and 1983.

Physical Property Data

A summary of the physical property data for the concrete in these two structures is presented in Table II. Included in this table are the average density, porosity, and saturation of each concrete sample at each time interval. An examination of these properties indicates that density and porosity vary slightly from sample to sample in each structure. These data also indicate that the saturation of the concrete has decreased with time for both structures.

Hydrostatic and Triaxial Compression Data

Figures 1 and 2 show the results of the triaxial and hydrostatic compression data for the concrete in Structure A. The triaxial compression data indicate that the triaxial strength of the concrete increased dramatically over a 24 month period. The hydrostatic compression data indicate that the compressibility of the concrete had increased slightly over the same 24 month period. These results are indicative of a material that obeys the effective stress theory and has a decrease in saturation.

Figures 3 and 4 show the results of the triaxial and hydrostatic compression data for the concrete in Structure B. The triaxial compression data indicate that the triaxial strength of the grout increased dramatically over a 24 month period; however, triaxial strength decreased slightly over the 24 to 46 month period. The hydrostatic compression data indicate that compressibility of the grout increased continuously over the same 46 month period. The results up to the 24 month age of this grout also are indicative of a material that obeys the effective stress theory and has a decrease in saturation over this period. The physical properties of the grout in Structure B show that the saturation of the grout did not change from the 24 to 46 month period. This could explain why there is little difference in the triaxial compression data over this period. The grout probably did not continue to decrease in saturation since it had already reached the saturation level of the surrounding soil.

In order to compare the hydrostatic and triaxial compression data of the concretes in Structures A and B, the data is normalized and presented in Figures 5 and 6. In Figure 5, the triaxial compression data from Figures 1 and 3 are normalized by the design unconfined compressive strength at 28 days, f'_c, of the concrete in each structure. The normalized data show that the strengths of each concrete at each age are similar, which indicates that the rates of curing of these buried structures are similar. This might be expected since these two structures were constructed near the same location at similar depths in soil with similar saturation. In Figure 6, the hydrostatic compression data from Figures 2 and 4 have been normalized by the design unconfined compressive strength at 28 days and the average porosity of the concrete in each respective structure. The data plotted in this form shows volumetric strain increases nearly bilinearly with confining pressure with the slopes of the two linear portions nearly constant in all cases. The transition occurs near the point at which the air voids are eliminated and the samples become saturated. These data show that the rates of change of the hydrostatic compression of these concretes are similar.

Conclusions

Results indicate that these concretes obey the effective stress theory and that the saturation of the concrete strongly influences triaxial strength and compressibility. The data also show the saturation of the concrete slowly decreases to the saturation level of the surrounding medium for buried structures.

TABLE I. Near surface soil properties of
Antelope and Pedro Dry Lakes,
Tonopah Test Range, Nevada.

Antelope Dry Lake

Depth (ft)	Density (g/cc)	Porosity (%)	Saturation (%)	Soil Classification
	1.92	40	78	
10	1.94	39	78	silty clay
	1.96	35	82	

Pedro Dry Lake

Depth (ft)	Density (g/cc)	Porosity (%)	Saturation (%)	Soil Classification
10	1.92	38	83	sandy silt
12.5	1.91	40	73	sandy silt
20	2.00	34	75	sandy silt

TABLE II. Physical properties of the
concrete in Structures A and
B.

Structure	Age (Months)	Density (g/cc)	Porosity (%)	Saturation (%)
A	4	2.24	17	98
	24	2.18	20	84
B	3	2.10	29	83
	24	2.00	31	74
	46	2.00	30	74

FIGURE 2. Hydrostatic compression data
for Structure A at two differ-
ent ages
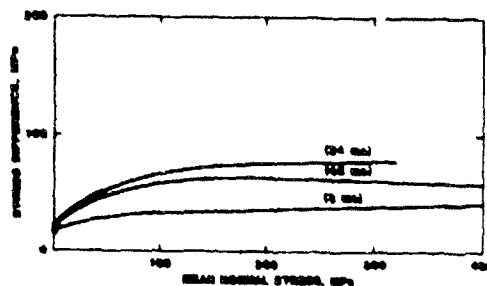
FIGURE 3. Triaxial compression data for
Structure B at three different
ages
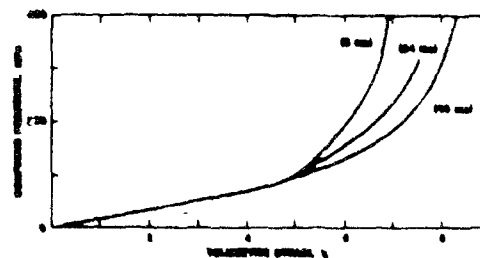
FIGURE 4. Hydrostatic compression data
for Structure B at three
different ages

FIGURE 1. Triaxial compression data for
Structure A at two different
ages

67
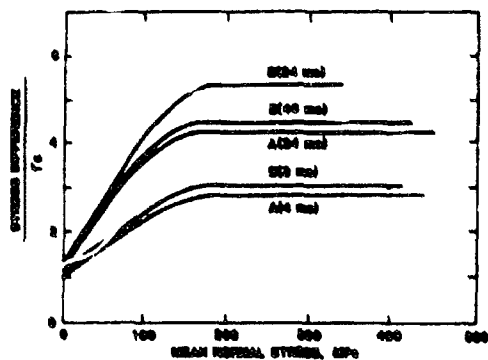
FIGURE 5. Normalized triaxial com-
pression data for Structures
A and B

References:

1. Gerhard, P. C., "Additional Geo-
    technical Services, Tonopah Test
    Range, Tonopah, Nevada," Woodward-
    Cyde Consultants, Denver, CO, March
    1980.

2. Sakellariou, C., "Testing of Grout
    Specimens, EP3E, EP5," Terra Tek,
    Salt Lake City, UT, letter report
    to M. M. Hightower, July 1980.

3. Cooley, C. H., "Testing Program on
    Sandia Cement," Terra Tek, Salt
    Lake City, UT, letter report to
    M. M. Hightower, April 1981.

4. Smith, R. H., "Triaxial Compression
    Tests on EP5 Grout," Terra Tek,
    Salt Lake City, UT, letter report
    to M. M. Hightower, March 1982.

5. Smith, R. H., "Triaxial Testing Pro-
    gram on Concrete," Terra Tek, Salt
    Lake City, UT, letter report to M. M.
    Hightower, September 1982.

6. Nye, C. V., Jr., "Triaxial Compres-
    sion Tests on EP5 Grout," Terra
    Tek, Salt Lake City, UT, letter
    report to M. M. Hightower, January
    1983.

FIGURE 6. Normalized hydrostatic com-
pression data for Structures
A and B

68

STRENGTH CRITERIA FOR ANISOTROPIC MATERIALS

C.L.D. Huang and H.S. Walker

Department of Mechanical Engineering

Kansas State University

Manhattan, KS 66506

ABSTRACT

In this paper, the criteria of strength for some anisotropic materials are investigated. The existence of a strength function, which is a function of invariants of a stress tensor, is assumed. The invariants for each class of anisotropic materials are obtained.

INTRODUCTION

For the purpose of material characterization and design, a rational simple strength criterion for composites is essential and important. As pointed out by Tsai and Wu [1], the majority of proposed criteria are limited in their ability to include the correlating stress effects. In order to remove such a limitation, Gol'denblat and Kopnov [2] proposed a new criterion of strength for anisotropic materials. They investigated explicitly the form of strength criterion for orthotropic materials. In particular, they verified their results for glass-reinforced plastics experimentally and showed the suitability of the proposed criterion of strength for practical usage. In this paper, the criteria of strength for some anisotropic materials are investigated. We assume the existence of a strength function [3] which is a function of invariants of a stress tensor. The invariants for each class of anisotropic materials are obtained. Consequently, the strength functions proposed by Tsai and Wu [1] for triclinic and rhombic (orthotropic) materials, by Gol'denblat and Kopnov [2] for rhombic, and by Hill [4] for orthotropic materials can be obtained readily from the appropriate invariants given in this paper.

Strength Criteria for Anisotropic Materials

Consider a strength function [3]

$$F(\sigma_{ij}) = 0 \qquad (1)$$

which is required to be invariant under a group of transformations (t_{ij}), characterizing the material anisotropy, i.e.,

$$F(\bar{\sigma}_{ij}) = F(\sigma_{ij})$$

and $\bar{\sigma}_{ij} = t_{im}t_{jn}\sigma_{mn}$ $\qquad (2)$

Invariants for each system of anisotropic materials are obtained in the followings by using Eq. (2), [4,5]. The contracted notation is used;

$$(\sigma_{11}, \sigma_{22}, \sigma_{33}, \sigma_{23} = \sigma_{32}, \sigma_{13} = \sigma_{31}, \sigma_{12} = \sigma_{21}) = (\sigma_1, \sigma_2, \sigma_3, \sigma_4, \sigma_5, \sigma_6).$$

1. Triclinic System

Pedial $\quad$ I
Pinacoidal $\quad$ I, C $\qquad$ (t_{ij})

For crystals having triclinic symmetry, there is no restriction on the orientation of the preferred direction; any rectangular coordinate system can be used as a reference frame. Thus, the invariant (I_i) for both classes are

$$I_i^{(1)}: \ \sigma_1, \sigma_2, \sigma_3, \sigma_4, \sigma_5, \sigma_6 . \qquad (3)$$

2. Rhombic System

Rhombic-pyramidal $\qquad$ I, R_2, R_3, D_1
Rhombic-disphenoidal $\qquad$ I, D_1, D_2, D_3 $\qquad$ (t_{ij})
Rhombic-dipyramidal $\qquad$ $I, C, R_1, R_2, R_3, D_1, D_2, D_3$

$$I_i^{(1)}: \ \sigma_1, \sigma_2, \sigma_3 ;$$

$$I_i^{(2)}: \ \sigma_4^2, \sigma_5^2, \sigma_6^2 ;$$

$$I_i^{(3)}: \ \sigma_4\sigma_5\sigma_6 . \qquad (4)$$

$\qquad$ (I_i)

3. Traverse Isotropy

It is supposed that the material is transversely isotropic with respect to an axis x_3. Thus, the transformations characterizing transverse isotropy are I and

$$R_\alpha(x_1' + ix_2' = e^{-i\alpha}(x_1 + ix_2), x_3' = x_3 | \text{for all values}$$

of α).

Therefore, the invariants are

$$I_i^{(1)}: \quad \sigma_3, \; \sigma_1 + \sigma_2 ;$$

$$I_i^{(2)}: \quad \sigma_1\sigma_2 - \sigma_6^2, \; \sigma_4^2 + \sigma_5^2 ;$$

$$I_i^{(3)}: \quad \det|\sigma_i|$$

$$(I_i) \tag{5}$$

When the terms of degree three ($I_i^{(3)}$) for F are omitted, the results (Eq. (3), (4), (5)) yield the forms of the quadratic strength function. In particular, the strength function for an orthotropic material can be written readily from Eq. (4) with the $I_i(3)$ omitted. This is

$$(F_1\sigma_1 + F_2\sigma_2 + F_3\sigma_3)^\alpha + (F_{11}\sigma_1^2 + F_{22}\sigma_2^2 + F_{33}\sigma_3^2$$

$$+ 2F_{12}\sigma_1\sigma_2 + 2F_{23}\sigma_2\sigma_3$$

$$+ 2F_{13}\sigma_1\sigma_3 + F_{44}\sigma_4^2 +$$

$$+ F_{55}\sigma_5^2 + F_{66}\sigma_6^2)^\beta = 1 \tag{6}$$

This result can be reduced to the result in the Ref. [1] by taking $\alpha = \beta = 1$, and in the Ref. [2] by taking $\alpha = 1$ and $\beta = 1/2$. Furthermore, if the absence of a Bauschinger effect is assumed and the material constants α and β are taken to be unity, Eq. (6) yields the Hill criterion [6];

$$F(\sigma_2 - \sigma_3)^2 + G(\sigma_3 - \sigma_1)^2 + H(\sigma_1 - \sigma_2)^2 + 2L\sigma_4^2$$

$$+ 2M\sigma_5^2 + 2N\sigma_6^2 = 1. \tag{7}$$

where the coefficients of the strength function are defined as;

$$F = -F_{13}, \; G = -F_{23}, \; H = -F_{12}, \; 2L = F_{44},$$

$$2M = F_{55}, \; 2N = F_{66},$$

$$F_{11} = G + H, \; F_{22} = H + F, \text{ and } F_{33} = F + G.$$

REFERENCES

1. S. W. Tsai and E. M. Wu, A General Theory of Strength for Anisotropic Materials, J. Composite Materials, Vol. 5 (1971), p. 58.

2. I. I. Gol'denblat and V. A. Kopnov, Strength of Glass-Reinforced Plates in the Complex Stress State, Mekhanika Polimerov, Vol. I (1965) p. 70; (English translation) Polymer Mechanics, Vol. 1 (1966), P. 84, Faraday Press.

3. A. Nadai, Theory of Flow and Fracture of Solids, McGraw-Hill, New York, pp. 175-228, 1950.

4. C. L. Huang, The Energy Function of Anisotropic Materials with Couple Stresses - Cubic and Hexagonal System, Int. J. Engg. Sci., Vol. 6, (1968), p. 609.

5. C. L. Huang, The Energy Function for Crystal Materials with Couple Stresses, Int. J. Engg. Sci., Vol. 7, (1969), p. 1221.

6. R. Hill, A Theory of the Yielding and Plastic Flow of Anisotropic Metals, Proc. Royal Soc. (London), A, Vol. 1973, (1948), pp. 281-297.

CONSTITUTIVE PROPERTIES OF STEEL FIBER REINFORCED CONCRETE IN MULTIAXIAL LOADING

Hon-Yim Ko, Roger W. Meier, Daniel E. Egging, Stein Sture and Chuan C. Feng

Department of Civil, Environmental and Architectural Engineering
University of Colorado, Boulder, Co. 80309

ABSTRACT

The constitutive perperties of steel fiber reinforced concrete (FRC) are being studied experimentally in a unique fluid cushion multi-axial cubical test cell at the University of Colorado. In the first phase of the program, the behavior of FRC was tested under three-dimensional compressive loading. The strength and stress-strain properties are analyzed by using constitutive models available in the literature. In the second phase, a modification to the existing test apparatus was made for testing cubical specimens under direct tension loading. The modification consists of brushes with individual bristles glued to the specimen. In this paper, results are shown from the biaxial tension-compression test program to demonstrate the strength interaction.

INTRODUCTION

The addition of fibers to cementitious materials improves many of the engineering properties by providing for a different deformation and failure mechanism from that of the plain matrix material. Although a significant amount of research has been carried out on steel fiber reinforced concrete (FRC) in the past two decades, there is still a considerable void in the knowledge of the strength and stress-strain behavior of FRC under complex states of stress. This stems mainly from a lack of suitable equipment for applying multidimensional stress and, in particular, for simultaneously applying combinations of tension and compression. Thus, most FRC applications to-date have been limited to situations where the predominant stress condition can be simulated in the laboratory, e.g., flexural loading in bridge deck overlays, highway and airfield pavements. It appears that the improved properties of FRC over plain Portland cement concrete were also desirable in many other applications, but wider applications of FRC could only be brought about if a better understanding of its engineering properties under complex stress states is available.

A research program, sponsored by the Air Force Office of Scientific Research has been underway at the University of Colorado at Boulder for the past few years to examine the strength and behavior of steel fiber reinforced concrete subjected to both three-dimensional compressive loading and biaxial tension-compression loading. In this paper, the results of the test program are presented.

MATERIAL

From a preliminary test series in which several types of steel fibers were used in conjunction with one common plain concrete mix, Egging [1] selected for the test program the Dramix 30/0.4 fibers manufactured by Bekaert Steel Wire Corp. These fibers are straight, round wires with patented hooked ends to increase their resistance to pullout. The wires, 30 mm in length and 0.4 mm in diameter, are available in collated clips, held together by a water soluble glue. The glue dissolves within one minute after the clips are added to the plain concrete, allowing dispersion of the individual fibers. A volume fraction of 0.6 percent was used in the mixing of the FRC. This value may appear low in comparison with those used for straight fibers without bent ends. However, it was selected on the basis of manufacturer's claim of the higher pullout resistance afforded by the deformed fibers. With this volume fraction, no balling or segregation of the fibers was observed during mixing and good workability was obtained.

The plain concrete mix design consisted of the following parameters:

water/cement ratio = 0.5
cement content = 770 lb/cu yd
maximum size of coarse aggregate = 3/8 in
fineness modulus = 2.5
percent of fine aggregate = 53% of total aggregate

This plain concrete mix has a uniaxial compressive strength of 7,900 psi, while the FRC obtained by adding fibers at 0.6 percent by volume has a strength of 9,150 psi.

TEST EQUIPMENT AND PROCEDURE

The multiaxial cubical test cell developed for compressive testing of concrete, rocks and composite materials (Ko and Sture [2]) was used for the test program on FRC. For the combined tension-compression testing, a new addition to the test cell was made. The equipment is briefly described in the following.

The test cell consists of a rigid frame onto which are mounted six walls. The frame has three orthogonal square holes machined through it as shown in Figure 2. The intersection of these holes forms a cubical cavity in the center of the frame, within which the 4 in. cubical test specimen resides. The six square openings in the frame, together with the adjoining walls, act as pressure chambers. Each face of the test specimen becomes the interior wall of one chamber. A fluid cushion system is established in each chamber through the use of a flexible polyurethane membrane attached to the inside face of each wall. This membrane, which fits into the square opening in the frame, retains the hydraulic fluid pumped into the chamber. The fluid pressure generated within the membrane is resisted by the specimen and exterior wall. A typical wall assembly with the fluid cushion is also shown in Figure 1.

On the interior face of each wall and within the fluid cushion system is mounted a set of three proximity transducers, manufactured by Bentley Nevada Corp., for detecting the movement of brass targets glued to the surface of the test specimen. The pressurizing medium in the fluid cushions is silicon fluid, chosen for its inert properties and noninterference with the performance of the proximity probes. The pressures to the three pairs of opposite fluid cushions are generated by three hand pumps, and the plumbing is arranged in such a way that each pump can be used to deliver the pressure to one, two or all axes in the test cell. The design capacity of the system is 25,000 psi.

The fluid cushion loading system employed in the test device has been shown to provide the least boundary constraint on the test specimen, and to have distinct advantages over other methods of load application (e.g. rigid platens with or without lubrication) in the testing of concrete materials [3,4]. In essence, the application of a known, uniform normal compressive stress through the flexible membrane in the fluid cushion system ensures complete control of the applied three-dimensional stress state. In addition, since the specimen is unrestrained by the fluid cushions, the mode of deformation and failure in the test specimen is uninhibited by the test equipment. Thus, the response measured in testing with this equipment reflects the true material property.

The system described above has been used in the constitutive characterization of many concrete and rock materials under arbitrary, compressive loading. To accommodate the needs of the current project on FRC, an additional feature was installed to provide the capability of tension testing in one axis, Meier [5]. The tension loading device adopted utilizes a pair of brush platens glued to the opposite surfaces of the test cube for applying the tension load. One half of the tension loading device is shown schematically in relation to its mounting on the frame in the cubical test cell in Figure 2.

Each brush platen is made of 225 aluminum bristles, arranged in a square pattern and keyed into an aluminum anchoring block. This block is connected to a double acting hydraulic cylinder through a spherical seat assembly designed to accommodate rotation and translation of the test cube, and to maintain concentricity of the applied tension force.

The tension generated by the hydraulic cylinder to pull on the brush platen is resisted by a pair of stand-offs mounted on the cubical cell frame. The specimen deformation in the direction of the applied tensile stress is measured by proximity transducers that monitor the movement of targets mounted on the brush block.

The brushes are glued to the FRC test specimen by means of a commercial structural concrete epoxy (Sikadur 31 Hi-Mod Gel). The gaps between bristles in a brush platen are filled with a silicone rubber material to prevent penetration of the epoxy. The rubber is soft enough so as not to restrain the lateral movement of the bristles. After each test, the brushes are cleaned by sandblasting the tips of the bristles in order to prepare a clean surface for the epoxy bonding for the following test. The epoxy develops its full strength in 24 hours.

Data acquisition in the test system is handled by a multiplex scanner controlled by a HP 9830 calculator. The output signals from the 18 proximitor transducers are scanned and sent in digital form to the calculator which then computes the changes from the initial conditions. The specimen deformations are then computed by reference to a calibration curve. It is necessary to allow for the flexibility of the test system which is not negligible in comparison to the deformations of the FRC test specimen. The system is calibrated by testing a dummy aluminum cube of known properties.

TEST PROGRAM

Two phases of the test program have been completed, as described in the following.

In Phase 1, three-dimensional compressive loadings were applied along the stress paths as shown in Figure 3. These stress paths consisted of hydrostatic (isotropic compression) loading to the selected mean stress level of 4, 6 or 8 ksi, followed by deviatoric (pure shear) loading in that deviatoric plane in the direction of triaxial compression (TC: $\sigma_1 > \sigma_2 = \sigma_3$), triaxial extension (TE: $\sigma_1 = \sigma_2 > \sigma_3$), or simple shear (SS: $\sigma_1 > \sigma_2 > \sigma_3$, σ_2 = constant). During the deviatoric loading, the mean stress, $1/3 (\sigma_1 + \sigma_2 + \sigma_3)$, remained constant. For each test path, several replicate experiments were performed.

In Phase 2, biaxial tests were performed along the stress paths as shown in Figure 4. There were two groups of biaxial tests in this

Phase. The first group consisted of biaxial com-
pression tests with proportional loading with the
stress ratio σ_3/σ_1 equal to 0/1, 1/10, 1/3, 2/3,
and 3/3, while σ_2 remained at zero. The first
stress ratio represents uniaxial compression,
while the last represents equi-biaxial compres-
sion. The second group of biaxial tests consisted
of combined tension-compression loading, with the
compressive stress first applied, to be followed
by tensile loading in a transverse direction. The
compressive preloading was taken to 0.1, 0.3, 0.4,
0.5, 0.65, 0.8 and 0.85 of the unconfined compres-
sive strength. Of course, direct tension loading
without any compressive preloading was also
employed.

The objectives of the Phase 1 test program
were to obtain both the strength and the behavior
of the FRC under multiaxial compressive loading
for constitutive modeling. Similar test programs
have previously been conducted on plain concrete
[3,4], so that the new results on FRC could be
examined and compared with existing data, despite
the difference in materials. In the Phase 2 prog-
ram, attention was focused on obtaining the bi-
axial failure envelope and on the effects of
combined loading on the tensile strength of FRC.

RESULTS

Phase 1

Typical stress-strain curves obtained from
Phase 1 are shown in Figure 5 where the major
principal stress normalized with respect to the
mean stress is plotted versus the principal
strains in the x, y and z directions, and the
volumetric strain ε_V. The first portion in each
stress-strain curve represents the hydrostatic
loading to the ratio of $\sigma_1/\sigma_{om} = 1$, where in the
case shown $\sigma_{om} = 8$ ksi. The three principal
strains showed almost equal magnitudes under hyd-
rostatic loading, indicating an isotropic mater-
ial. However, any assumption regarding isotropy
must be based on more extensive investigation in
which different directional loadings are used.

The behavior shown for the TC test path in
Figure 5 is typical of all deviatoric loadings
used in Phase 1. At point A identified on the
volumetric strain curve, volume dilation began to
occur. This point, sometimes referred to as the
point of discontinuity, has been taken to repre-
sent the condition under which uncontrolled crack
growth would develop, eventually leading to physi-
cal failure of the specimen if sufficient time is
allowed. Under normal testing conditions, where
the rate of loading is fast in comparison to the
crack growth rate, continued increase in the
applied load leads to physical failure at a level
15-20 percent above the point of discontinuity.

In Phase 1 of this investigation, the points
of discontinuity obtained under different stress
paths were plotted in principal stress space to
define a failure envelope. Two different cross-
sections of this envelope are shown in the devia-
toric plane in Figure 6 and in the Rendulic (tri-

axial) plane in Figure 7. Three sets of data are
plotted in Figure 6, from the tests on the 4, 6
and 8 ksi deviatoric planes, respectively. In
addition to the laboratory test data, Figures 6
and 7 also show the failure envelope predicted by
the William-Warnke theory, which was obtained in
the following manner.

A theory commonly used in representing the
failure conditions of concrete under multiaxial
stress states has been proposed by William and
Warnke [6], which prescribes a conical surface in
principal stress space with curved, parabolic
meridians and a deviatoric cross-section that has
an elliptical variation between the extremes of TC
and TE conditions within a typical 60° sector.
The theory containing five parameters is usually
calibrated with input information from (1) uni-
axial compressive strength, (2) equi-biaxial com-
pressive strength, (3) uniaxial tensile strength,
(4) shear strength in TC at high compressive
stress level and (5) shear strength in TE at high
stress level. In Phase 1 of the present test
program, only shear strength data along TC, TE and
SS paths were available. Using TC and TE data in
the three deviatoric planes, the William-Warnke
model was calibrated (Egging, [1]). The parameter
values obtained from the calibration are shown in
Figures 6 and 7. It can be seen that reasonable
representation of the test data is obtained. The
comparison along the SS test path provides a
measure of the accuracy of this model.

The strength data from Phase 1 were also used
to fit the model proposed by Lade [7], while the
stress-strain data were fitted to the formulation
proposed by Gerstle [8]. While reasonable success
was obtained in both efforts, the reader is
referred to Egging [1] for further details.

Phase 2

The strength results from the Phase 2 test
program are shown in Figures 8 and 9. The data
points in these figures represent the stress
states at which physical failure occurred. In the
tension-compression tests, volume dilation occurr-
ed throughout the tensile portion of each stress
path, which precludes the use of the point of dis-
continuity as a definition of failure.

In Figure 9, the tension-compression results
are shown normalized with respect to both the uni-
axial compressive and tensile strengths in order
to show the trend in the strength behavior more
clearly. The most significant feature in Figure 9
is the well-defined inflection point in the
strength envelope. Although an inflection point
has been seen in past investigations on plain con-
crete [9,10], the rate of change in slope in Fig-
ure 9 is significantly greater than has been seen
previously. An explanation for this is given
next.

In direct tension, failure of the FRC was the
result of the fibers pulling out of the concrete
matrix shortly after the matrix failed. As a

result, the tensile strength of the FRC was only ten percent greater than that of an identical mix of plain concrete. The application of a small transverse compressive stress, while doing little damage to the concrete matrix, increases the resistance of the fibers to pullout by providing a clamping force. Therefore, at stress levels less than approximately 40 percent of the uniaxial compressive strength, the decrease in strength normally seen in plain concrete is offset by the increased resistance to pullout. In comparison, at 0.. .ie uniaxial compressive strength, the plain concrete strength was 25 percent less than in uniaxial tension. At compressive stress levels above 0.4, however, crack propagation is initiated under the influence of the compressive stress. Pre-existing flaws at the fiber-matrix interface will begin to extend and the pullout resistance is quickly lost, resulting in a sharp drop in strength which tends toward the strength of the plain concrete as the compressive stress level is increased.

In summary, the strength benefits afforded by the addition of the fiber reinforcing are greatest in biaxial tension-compression situations where the compressive stress is small in comparison to the uniaxial compressive strength.

ACKNOWLEDGEMENTS

REFERENCES

[1] Egging, D.E., "Constitutive Relations of Randomly Oriented Steel Fiber Reinforced Concrete Under Multiaxial Compressive Loadings", M.S. Thesis, Univ. of Colorado, Boulder, 1982.

[2] Ko, H-Y., and Sture, S., "Three-Dimensional Mechanical Characterization of Anisotropic Composites," J. Comp. Mat., 8, 1974, pp. 178-190.

[3] Gerstle, K.H., et al, "Behavior of Concrete Under Multiaxial Stress States," J. Eng. Mech. Div., ASCE, 106, 1980, pp. 1383-1403.

[4] Gerstle, K.H., et al, "Strength of Concrete Under Multiaxial Stress States," Proc. McHenry Symp. Conc. and Conc. Struct., ACI Publ. SP-55, 1978, pp. 103-131.

[5] Meier, R.W., "The Strength and Behavior of Steel-Fiber Reinforced Concrete Under Combined Tension-Compression Loading," M.S. Thesis, Univ. of Colorado, Boulder, 1983.

[6] Willam, K.J., and Warnke, E.P., "Constitutive Model for the Triaxial Behavior of Concrete," IABSE Reports 19-21, 1974-75.

[7] Lade, P.V., "Three-Parameter Failure Criterion for Concrete," Paper presented at Joint ASME/ASCE Mechanics Conf., Boulder, Co., June 22-24, 1981.

[8] Gerstle, K.H., "Simple Formulation of Triaxial Concrete Behavior," J.ACI, 18, 5, 1981, pp. 382-387.

[9] McHenry, D. and Karni, J. Strength of Concrete under Combined Tensile and Compressive Stress," J.ACI, 54, 1958, pp. 829-839.

[10] Vile, G.W.D., "The Strength or Concrete under Short-Term Static Biaxial Stress," The Struct. of Concrete and Its Behavior under Load, London, 1965, pp. 275-288.
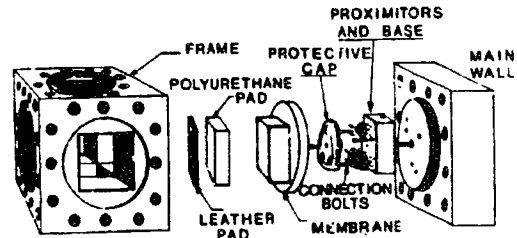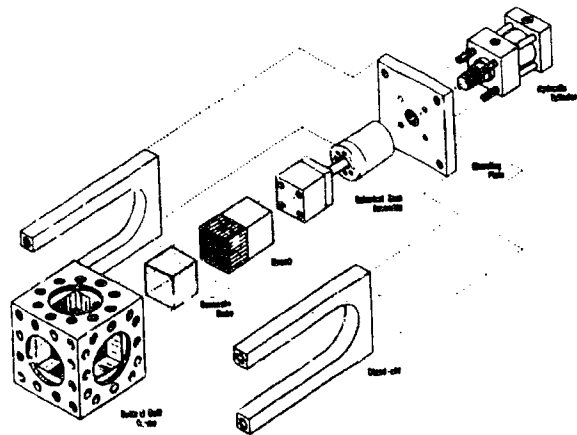
Fig. 1. Exploded View of Test Cell
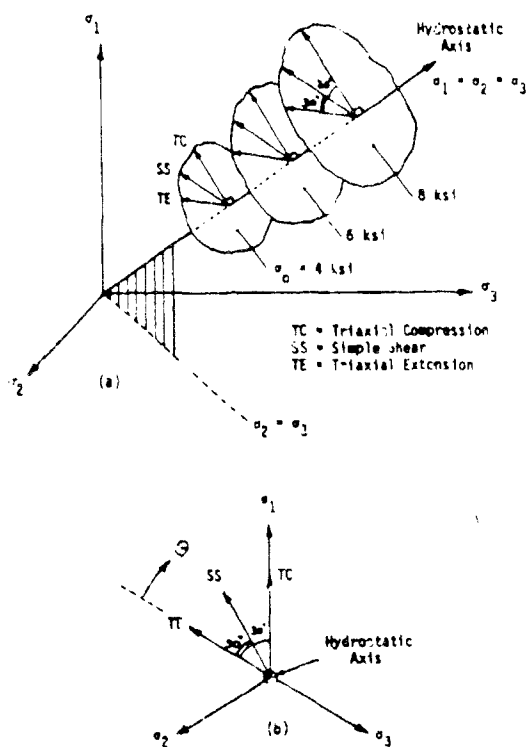

Fig. 2. Tensile Loading Apparatus

Fig. 3. Stress paths in (a) 3-D Stress Space;
(b) Devitoric Plane

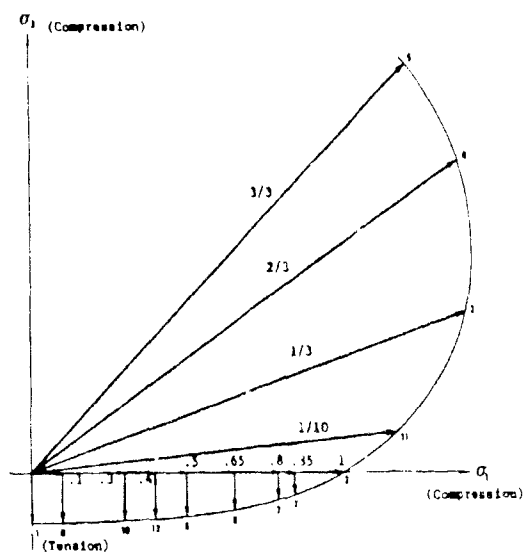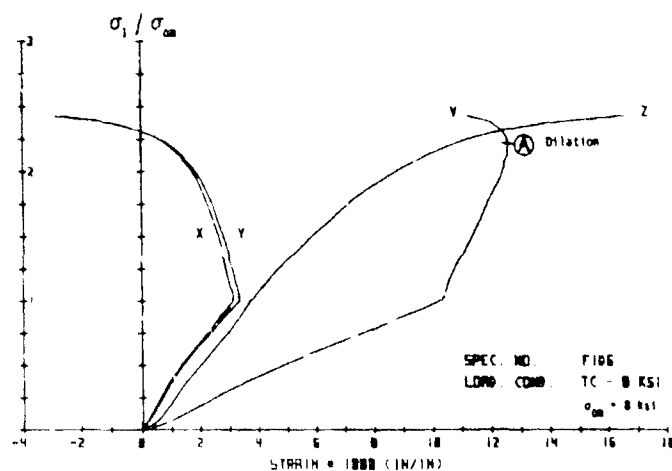Fig. 4. Biaxial Stress Paths

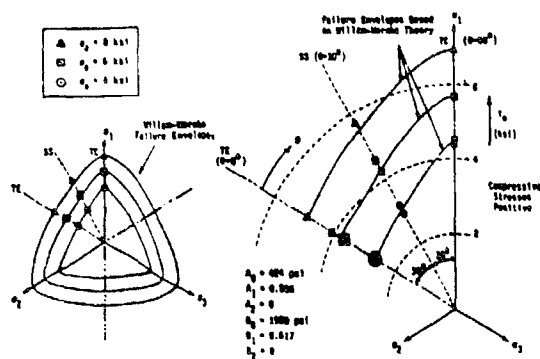

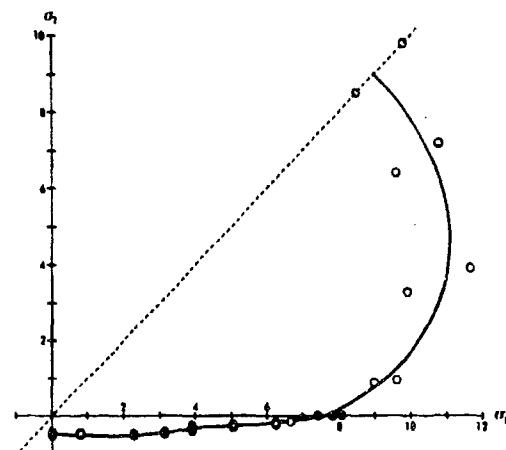Fig. 5. Typical Stress-Strain Data

Fig. 6. Failure Data in Deviatoric Plane

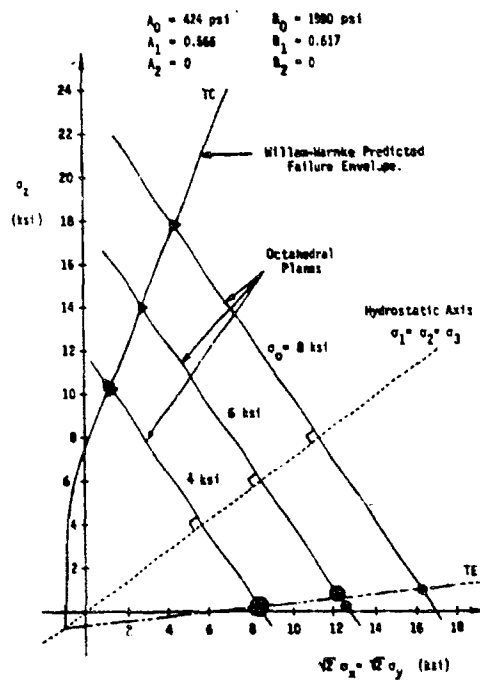Fig. 8. Biaxial Failure Envelope.

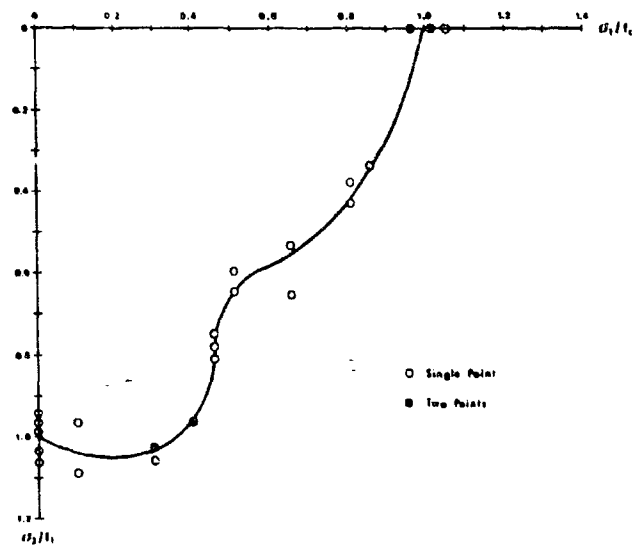Fig. 7. Failure Data in Rendulic Plane

Fig. 9. Failure Data in Combined Tension-Compression

76

A SIMPLIFIED VISCOPLASTIC THEORY FOR FRICTIONAL MATERIALS

Howard L. Schreyer and James E. Bean

New Mexico Engineering Research Institute
University of New Mexico
Albuquerque, NM, USA 87131

ABSTRACT

A viscoplasticity theory is described in terms of the mean pressure and a new third invariant which involves a shifted stress tensor. The flow rule is nonassociated with respect to the pressure. Illustrative results for limit states and stress paths are given for a variety of frictional materials.

INTRODUCTION

The conventional theory of plasticity has a long history of successful use in applications involving metals. The theory is well-founded on a physical and a mathematical basis with numerous applications to engineering problems through the use of computer programs. This wealth of experience and familiarity has led to numerous attempts to apply the theory to frictional materials such as concrete, rock, soils, ice, and snow. Although there is no fundamental reason why the theory of plasticity should be appropriate for these materials, there are now several formulations that provide correct behavioral characteristics. Unfortunately many of these relations are so complicated that their use is limited to the simplest engineering applications. This presentation is the result of an attempt to formulate a model that captures essential response characteristics without recourse to a large number of parameters or special conditions. The introduction of a new third invariant leads to a plasticity theory that appears to be natural for frictional materials in the same sense that the von Mises formulation works so well for a wide class of metals.

LIMIT SURFACES

Limit surfaces for frictional materials depend on the first invariant of stress, or mean pressure, and on a measure of shear which can be expressed through the second and third invariants of stress. The conventional approach has been to express a limit surface in terms of the mean pressure and the second invariant of the stress deviator

$$P = -\frac{1}{3} \, \text{tr} \, \underline{\sigma} \qquad J_2' = \frac{1}{2} \, \text{tr} \, (\underline{\sigma}^d)^2 \qquad (1)$$

with modifications provided by incorporating a third invariant as dictated by experimental observations. Lade and Duncan [1] and Lade [2] have shown if a particular form of the third invariant is used, the second invariant is not required in the expression for a limit surface for at least particular classes of soils and concrete. A modification of their approach is proposed to utilize this feature, which may hold for all frictional materials.

With the use of a shift in stress, $\underline{\sigma}_s$, a convenient definition for a third invariant is

$$L = - [\det (\underline{\sigma} - \underline{\sigma}_s) + \det (\underline{\sigma}_s)]^{1/3} \qquad (2)$$

in which the second term in the brackets is included to make L equal to zero for a state of zero stress. Analogous to the square root that is often used with the second invariant, a cube root is introduced to provide the dimension of stress.

A limit point is the point on a prescribed stress or strain path at which the state of stress is stationary with respect to increments in strain. If such points for a variety of paths are plotted in stress space, the result of interpolating between the points is a limit surface (often called a failure surface). A fit to limit points for concrete, granite, marble, dense and loose sands, and clay is postulated to be the line

$$L = \lambda_L P - \sigma_s \qquad (3)$$

described with two parameters consisting of a limit slope, γ_L, and the intercept on the L-axis represented by the shift stress, σ_s, with the assumption $\underline{\sigma}_s = \sigma_s \underline{1}$. The fits, which are shown in Figure 1, are remarkably good considering the elementary formulation.

For the development of a plasticity relation, the initial flow surface can be developed from the point of deviation from linearity on stress-strain curves. Then this yield surface can be assumed to evolve out to a limit surface to represent the strain hardening phase of deformation. Strain softening can be obtained by letting the flow surface collapse in a controlled manner.

Since the limit surface is conveniently represented by a line in a space involving the third invariant, a flow surface of a similar nature can be postulated as follows:

$$\phi = \gamma P - L - \sigma_s \qquad (4)$$

in which γ is a strain-hardening function with the restriction $\gamma > \gamma_L$. A surface $\phi = 0$ defines the flow state. For stress states above this line, $\phi < 0$, which represents an elastic state, and $\phi > 0$ is not permitted.

A general hardening description is obtained by allowing the flow surface to rotate toward the limit line, i.e., to let γ decrease with some measure of inelastic strain to the value γ_L. Then with further deformation, the flow surface rotates back and this represents strain softening. The representation of such behavior together with typical loading paths in the P-L plane is shown in Figure 2.

Figure 2. Stress paths and flow surfaces in the P-L plane.

To control the amount of dilatation a nonassociated flow rule is adopted with the nonassociativity related only to the mean pressure. This is accomplished by using a potential function similar to the flow function but with the parameter γ replaced by another one, γ^*, where

$$\gamma^* = \gamma + \gamma_a \qquad (5)$$

in which γ_a is a material constant.

Figure 1. Limit curves for frictional materials.

Deformation results have been compared with experimental data [7] for two materials with vastly different properties. One is a high-strength concrete that displays shear enhanced compaction and considerable dilatation. The other is a porous foundry core that simulates cemented sand. Volumetric compaction up to 30 percent is exhibited under uniaxial strain and the shear enhancement is considerable. All of these characteristic features are displayed by the constitutive model and the quantitative comparison with experiments is good for several stress paths.

VISCOPLASTIC FORMULATION

Most frictional materials show a rate dependence although specific experimental data are rare and difficult to obtain [8]. Since these data were obtained for a single path, there are essentially no guide lines to assist in developing a three-dimensional theory. It is assumed that a reasonable representation can be obtained by allowing the parameter γ to vary with inelastic strain rate in addition to inelastic strain. Furthermore, the relation is taken to be separable in strain and strain rate with the following form adopted for illustrative purposes:

$$\gamma_r = \gamma \left(1 - A \tanh \frac{\dot{\bar{\varepsilon}}}{\dot{\bar{\varepsilon}}_0}\right) \qquad (6)$$

in which γ_r denotes the parameter used for rate effects, γ is the rate independent value, A is an amplification factor, $\dot{\bar{\varepsilon}}$ denotes a measure of inealstic strain rate, and $\dot{\bar{\varepsilon}}_0$ is a reference strain rate. The result is a theory that is robust from a numerical point of view and that provides a smooth dependence on two additional material parameters, A and $\dot{\bar{\varepsilon}}_0$.

Representative response curves have been obtained numerically for loose sand and are shown in Figure 3 to illustrate the effects of these parameters. These preliminary results indicate that fits to existing data should be a relatively easy matter which is desirable for analysts who use large general purpose computer codes.

ACKNOWLEDGEMENT

(a) Triaxial compression.

(b) Triaxial extension.
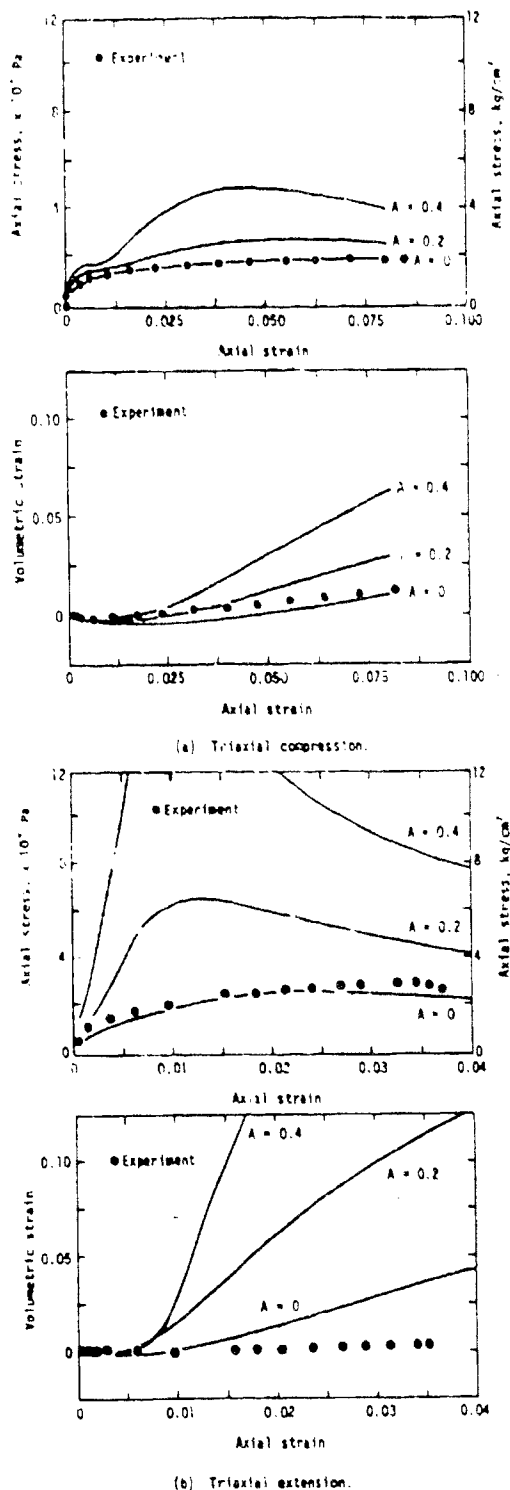
Figure 3. Theoretical predictions for a range of rate effects and static experimental results (Ref. 1) for loose sand.

REFERENCES

1. P. V. Lade and J. M. Duncan, "Cubical Triaxial Tests on Cohesionless Soil," Journal of the Soil Mechanics and Foundations Division, ASCE, 99: 793-812 (1973).

2. P. V. Lade, "Three-Parameter Failure Criterion for Concrete," Journal of the Engineering Mechanics Division, ASCE, 108: 850-863 (1982).

3. L. A. Traina, S. M. Babcock, and H. L. Schreyer, Reduced Experimental Stress-Strain Results of a Low-Strength Concrete Under Multiaxial States of Stress, AFWL-TR-83-3, Air Force Weapons Laboratory, Kirtland Air Force Base, New Mexico (1983).

4. S. J. Green and S. R. Swanson, Static Constitutive Relations for Concrete, AFWL-TR-72-244, Air Force Weapons Laboratory, Kirtland Air Force Base, New Mexico (1973).

5. P. N. Michelis, "Work-Softening and Hardening Behavior of Granular Rocks," Rock Mechanics, 14: 187-300 (1981).

6. P. V. Lade and H. M. Musante, "Three-Dimensional Behavior of Remolded Clay," ASCE Journal of the Geotechnical Engineering Division, 104: 193-209 (1978).

7. H. L. Schreyer, "A Third-Invariant Plasticity Theory for Frictional Materials," Submitted for publication to the Journal of Structural Mechanics.

8. J. G. Jackson, Jr., J. Q. Ehrgott, and B. Rohni, "Loading Rate Effects on Compressibility of Sand," Journal of the Geotechnical Engineering Division, ASCE, 106: 839-852 (1980).

CONSTITUTIVE RELATIONS OF CONCRETE
SUBJECTED TO A VARYING STRAIN RATE

S. P. Shah
Professor of Civil Engineering

Northwestern University
Evanston, Illinois 60201

ABSTRACT

Experiments conducted on concrete subjected to impact loading in uniaxial tension, uniaxial compression and in flexure, indicate that (1) the strain effects in concrete are not isotropic, (2) the stress-strain curves becomes less non-linear with increasing strain rate and (3) the rate of growth of internal microcracking decreases with increasing strain rate. A continuous damage model is proposed to establish the constitutive relationship of concrete. To include the effect of strain rate on internal damage, an inertial term is introduced in the damage evolution equation. The damage is expressed as a tensor quantity. The Helmholtz free energy function is expressed in terms of both the invariants of strain tensors and damage tensors. Equations predicted by the model are compared with the experimental results.

1. INTRODUCTION

It is widely accepted that the failure of concrete is brought about by the nucleation and growth of a number of microcracks. A review of the dynamic test results available for concrete also indicate that the strain-rate effects observed for concrete can be, to a large extent, attributed to the rate dependence of this microcracking process [1, 2]. It appears, therefore, that the continuous damage theory is a rational choice for predicting the mechanical behavior of concrete under both quasistatic and dynamic loading.

2 FORMULATION OF A CONSTITUTIVE MODEL

A vectorial representation is adopted for the damage which is motivated by the planar nature of the microcracks in concrete. The damage vector is chosen to be normal to the plane of the crack field and having a magnitude equal to the area density of the cracks. A vectorial damage variable, in contrast to a scalar damage variable, is also capable of modeling the crack induced anisotropy observed in concrete. Damage is treated as an internal state variable which influences the free energy of the material. For the present formulation the Helmholtz free energy function (ψ) is defined in terms of the coupled invariants of damage and strain as,

$$\rho\psi = \frac{1}{2}(\lambda + 2\mu)\, \varepsilon_{kk}\, \varepsilon_{kk} - \nu(\varepsilon_{kk}\, \varepsilon_{kk} - \varepsilon_{kl}\varepsilon_{kk})$$
$$+ \gamma_1 \left(\omega_i^\alpha \omega_i^\alpha\right)^{-\frac{1}{2}} |\varepsilon_{kk}|\omega_k^\alpha \varepsilon_{kl}\, \omega_l^\alpha$$
$$+ \gamma_2 \left(\omega_i^\alpha \omega_i^\alpha\right)^{-\frac{1}{2}} \left(\omega_k^\alpha \varepsilon_{kl}\, \omega_l^\alpha\right)^n \qquad (1)$$
$$+ \gamma_3 \left(\omega_i^\alpha \omega_i^\alpha\right)^{-\frac{1}{2}} \left(\omega_k^\alpha \varepsilon_{kl}\, \varepsilon_{lm}\, \omega_m^\alpha\right)$$

where λ, μ are the lamé parameters, ω_i is the damage vector, ε_{ij} is the stress tensor and ρ the density of the material. The three parameters γ_i which define the influence of the microcracks on the state of the material, are considered to be constants in the present formulation. The superscript α indicates the possibility of the occurrence of more than one independent damage field.

This particular form of the free energy function differed from the form chosen by Davison, L. and Stevens, A. L. [3] by virtue of the power n associated with the fourth term. This term can thus be of a different order in strain and damage. This provided for the obtainment of an equilibrium damage configuration from the free energy function.

A consistent thermodynamic approach yields the constitutive equation,

$$\sigma_{ij} = \rho\, \frac{\partial\psi}{\partial\varepsilon_{ij}} \qquad (2)$$

and the damage evolution equation,

$$\rho k\, \ddot{\omega}_i = g_i^D\, (\varepsilon_{ij},\, \omega_i,\, \dot{\omega}_i) - \rho\, \frac{\partial\psi}{\partial\omega_i} \qquad (3)$$

where σ_{ij} is the stress tensor and k is the inertia associated with the microcrack growth [4].

g_i^D should satisfy the entropy production inequality resulting from the thermodynamic formalism and is chosen as,

$$g_i^D = -\gamma_4 \left(\dot{\omega}_o\, \dot{\omega}_o\right)^{1/m} \frac{\dot{\omega}_i}{\dot{\omega}_o} \qquad (4)$$

where w_0 is the magnitude of w_1 and γ_4 and m are constants.

Eqs. 1-4 can be combined to yield the stress-strain relations for a particular state of the material. Due to the assumption of the planar nature of the microcracks however, the theory appears to yield reliable results only for planar problems where cleavage strains are small enough to keep the crack openings small. Also, since friction is not yet considered, it is not possible to simulate biaxial compression and strain softening.

3. COMPARISON WITH EXPERIMENTAL RESULTS

Instrumented impact tests on flexural beams have been conducted by the authors [1, 5, 6]. To obtain reliable mechanical properties with instrumented tests with brittle material such as concrete, it is necessary to reduce internal effects [5]. Results of this continuing experimental investigation were compared with the theory.

The analytical and experimental moment vs. strain curves at two strain rates are given in Figure 1. It can be noticed that increasing the strain-rate has no significant effect on the initial tangent modulus but results in decreasing the nonlinearity of the curves.

The analytical predictions for the strength increase in tension, flexure and compression are compared with results obtained by the authors and other available results in Figure 2. The constitutive model can be observed to be successful in predicting higher strain-rate sensitivity in the tensile mode as compared to the compression mode.

Figure 3 gives the variation of the apparent Poisson's ratio (calculated at a strain corresponding to the peak stress (under quasi static loading) with strain-rate. This value exhibits an increasing trend in tension and a decreasing trend in compression, as the strain-rate is increased. Such trends conform with the available experimental results [2].

4. CONCLUSIONS

A constitutive model was developed for the quasistatic and dynamic behavior of concrete, based on the continuous damage approach. The constitutive equations as well as the damage evolution equations were derived consistently from thermodynamic consideration. The model was calibrated by the use of flexural and compression test results over a range of strain-rates. The model was also found to be capable in predicting certain other phenomena of the dynamic response of concrete.

ACKNOWLEDGMENT

REFERENCES

1. Suaris, W., and Shah, S. P., "Properties of Concrete Subjected to Impact,". Accepted for publication in the ASCE J. of the Structural Division.

2. Suaris, W., and Shah, S. P., "Mechanical Properties of Concrete Subjected to Impact,". Introductory report for the Interassociation (RILEM, CEB, IABSE, IASS) Symposium on concrete structures under impulsive loading, West Berlin, June 1982.

3. Davison, L., and Stevens, A. L. "Thermomechanical Constitution of Spalling Elastic Bodies," J. Appl. Phys., Vol. 44, 1973, pp. 668-674.

4. Suaris, W., "Dynamic Behavior of Concrete: A Phenomenological Theory and Instrumented Impact Testing,". Thesis submitted in partial fulfillment of the requirements for the degree of Ph.D. at Northwestern University, Nov. 1982.

5. Suaris, W., and Shah, S. P., "Inertial Effects in the Instrumented Impact Testing of Cementitious Composites," ASTM Journal of Cement, Concrete and Aggregates," Vol. 3, No. 2, 1981.

6. Suaris, W., and Shah, S. P., "Strain Rate Effects in Fiber Reinforced Concrete Subjected to Impact and Impulsive Loading," Composites, Vol. 13, No. 2, April 1982.
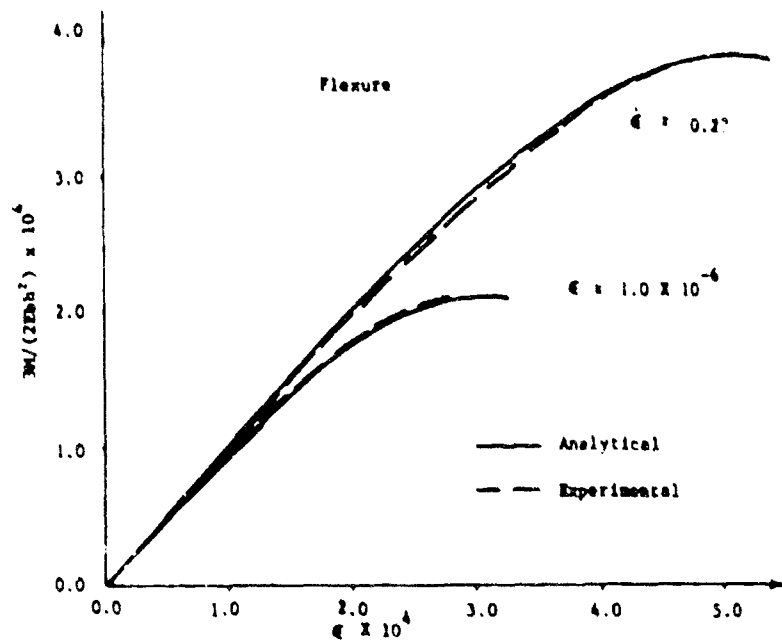
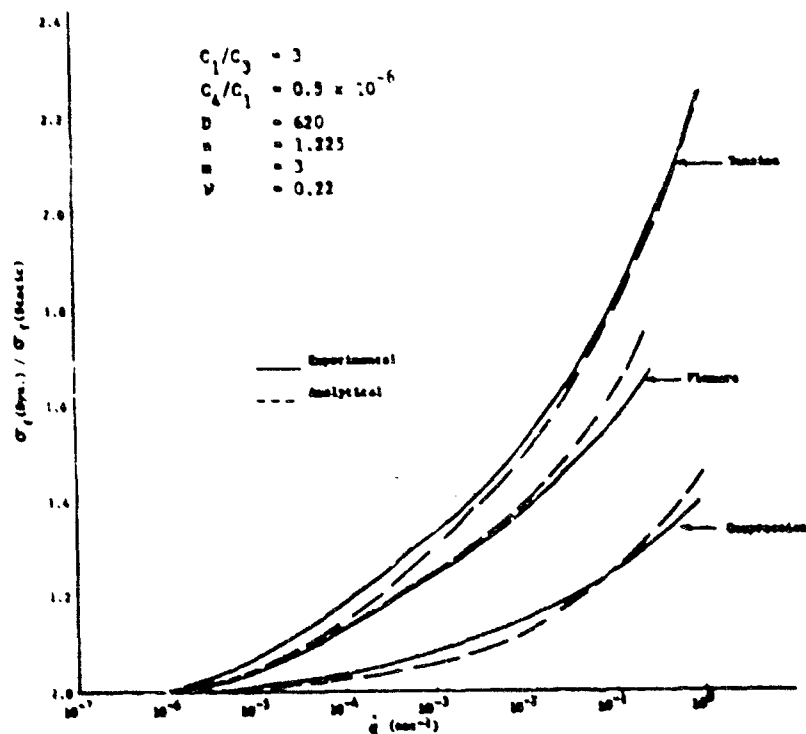Fig. 1 Analytical and Experimental Moment vs. Strain Curves in Flexure

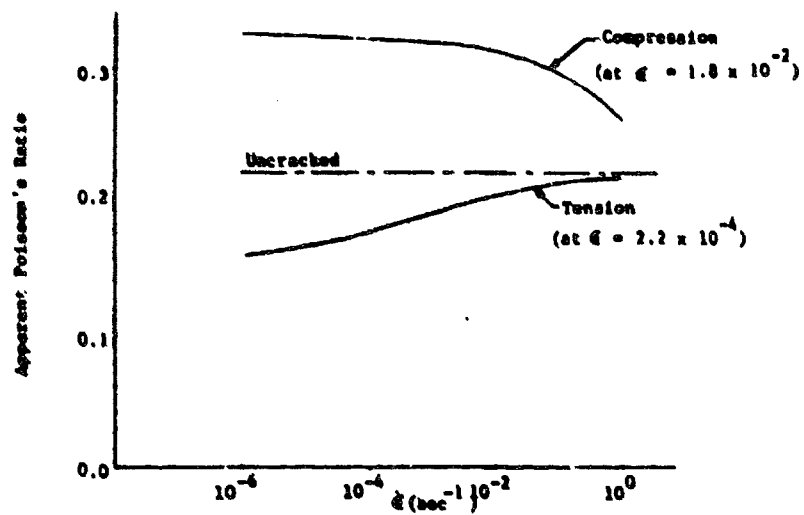Fig. 2 Analytical and Experimental Curves for the Effect of Strain-Rate on the Ultimate Strength

Fig. 3 The Effect of Strain-Rate on the Apparent Poisson's
        Ratio

ROCK/ELASTOMER COMPOSITES AS IMPACT RESISTANT MATERIALS

William F. Anderson[*], Alan J. Watson[*], Martyn R. Johnson[*], George M. McNeil[+]

[*]Department of Civil and Structural Engineering, University of Sheffield, U.K.
[+]Military Vehicles and Engineering Establishment, Christchurch, Hamp hire, U.K.

ABSTRACT

Composites cast from polymers, rock aggregates and sand have been examined to determine their resistance to penetration by 7.62mm diameter high velocity projectiles. The effects of using different polymer and rock aggregate types have been investigated, and the resultant composites optimised in terms of cost effectiveness and penetration resistance.

Optimisation was carried out using response surface theory and variables considered were mix proportions, rock aggregate particle size and polymer hardness. Penetration tests were carried out on optimised composites to determine the thickness required for a given confidence level of projectile containment.

INTRODUCTION

An interest in the protection of buildings and other structures against small arms fire led Gibbs and Prescott (1) to undertake a limited experimental study into the behaviour of dry gravel armour which had been used in wire mesh boxes to protect vehicles against infantry fire during World War II. Their tests showed that a theoretical approach to find the optimum gravel particle size, using "billiard ball" theory, was not valid because of the high degree of comminution of the gravel particles. The effectiveness of the armour, however, was proven.

A major problem in using gravel is containment of the material. A flexible binder is desirable because of the extensive fracture which occurs in brittle material on impact. Hence the idea arose of using a cold curing rubbery polymer as the binder, and a study has been carried out to test the effectiveness of this type of rock/ elastomer composite and to optimise the material in terms of its impact resistance.

At an early stage it was realised that a two phase mixture of elastomer and rock particles would be very expensive because of the large percentage voids which had to be filled with high cost elastomer. Hence sand was included in the mix to act as a filler. The resulting composites were unusual because of the relatively low elastic modulus of the matrix materials. No published information on the penetration resistance of this type of composite material could be found, although there was considerable information about penetration into homogeneous and layered materials (2, 3, 4).

Descriptions of penetration mechanics have used the following approaches (i) empirical, (ii) assumed force law, (iii) analytical and (iv) numerical (using computer codes). In the first two categories the parameters must be determined from penetration experiments, and application of the resultant formulae is not valid in any other context. This is because the parameters are not defined explicitly in terms of the constitutive properties of the medium and projectile characteristics. However, such methods usually show good results within these bounds.

In the analytical approach, constitutive and continuum equations are used to describe the event, and, ideally, are solved in a closed form to produce predictions of depth of penetration, projectile deceleration, etc. However, this type of solution has not been achieved without a high degree of simplification.

Numerical approaches are expensive in time and money. However, for situations using materials with well defined properties offering a high degree of reproduceability, their value is apparent

The latter two methods have only been developed to the stage where they can cope with homogeneous materials, possibly in layers. Heterogenous materials such as concrete have been considered, but have been treated as homogeneous. Generally, the projectile sizes used have been orders of magnitude larger than the concrete aggregate size. In the case of the composites in this study, the aggregate size was similar or about one order of magnitude larger in terms of mass than the projectile. This meant that the situation could not realistically be simplified as homogenous or layered. Because of these difficulties an experimental, rather than analytical, approach was adopted.

TEST MATERIALS

The composites were produced by mixing various proportions of sand filler, rock aggregate and elastomer.

Sand Filler

The sand filler reduced the amount of elastomer required to fill the void spaces between the rock aggregate particles. The effect of the sand particle size on penetration resistance was considered insignificant, so Zone II or Zone III sand as defined by British Standard 882 : Part ? (5) was used in all composites.

Rock aggregate

An advantage of the composites being examined is that they are fairly economical because locally available aggregates may be used. To examine the influence of aggregate type on the penetration resistance of the composite, the main series of tests were carried out using three different aggregates: crushed limestone, crushed basalt, and river gravel.

The crushed limestone was a fine grained sedimentary rock, mid grey in colour and angular in shape with a significant amount of dust present. The crushed basalt was a fine grained olivine basalt, dark greyish green in colour and angular in shape with a significant amount of dust present. Most of the dust in these crushed rock aggregates was removed by sieving prior to mixing with the sand filler and elastomer.

The river gravel was predominately quartzite and quartz, with small proportions of other rock types. The particles of the predominant rock types were rounded or irregular, but the minority rock type particles were of all shapes. Very little dust was present, because of the aggregate's mode of deposition from moving water which carried away the fines.

The properties of these rock aggregates as defined in British Standard 812 (6) are listed in Table 1. Also included in this Table are the percentage voids for 27.5 - 37.5mm aggregate found using 300mm dia. x 300mm high cylindrical moulds as recommended in the British Standard, and using 152mm cube moulds similar to those used for composite specimen preparation.

Elastomer

To achieve a relatively inexpensive composite which could be produced without special curing facilities and have a satisfactory penetration resistance within, at most, twenty four hours, it was essential to find an elastomer which satisfied a number of criteria. The elastomer had to be commercially available in large quantities at relatively low cost. For ease of mixing and casting it had to have a low viscosity and a gel time sufficiently long for casting. Thereafter it had to cure quickly at ambient temperature.

	Crushed Limestone	Crushed Basalt	River Gravel
Oven dry specific gravity	2.67	2.75	2.57
Aggregate crushing value, %	23	17	-
Aggregate impact value, %	23	17	16
10% fines load (kN)	160	250	377
% voids - compacted B.S. cylinder test	43%	43.8%	35%
% voids - uncompacted B.S. cylinder test	49.3%	49.4%	39.4%
% voids - uncompacted 152mm cube mould	52.1%	49.4%	43.7%
% voids - compacted 152mm cube mould	44%	45%	39.1%

Table 1   Rock aggregate properties

To act as a flexible binder at impact and during penetration the elastomer had to be elastic at high rates of strain. It also had to give a composite with adequate mechanical properties for large panels to be produced as cladding material or to form free standing units to a reasonable height.

Initially a wide range of cold cure thermo-setting polymers including epoxy resins, natural and synthetic rubbers and polyurethanes were examined. None of the sixteen polymers tested initially satisfied all of the criteria listed for the ideal elastomer. Polyurethanes were found to satisfy most of the criteria and two polyurethanes, a polyester polyurethane (Polymer A) and a blend of two polyether polyurethanes (Polymer B) were chosen for the main investigation. By varying the proportions of the polymer constituents different hardnesses of cured elastomer could be achieved.

SPECIMEN PREPARATION

Single size rock aggregate was used in all specimens and after sieving, the aggregate and sand filler were oven dried. Mixing was carried out using a mechanical bowl mixer. The elastomer constituents were mixed for about 30 seconds to ensure complete blending and then the rock aggregate and sand filler were added to the resin and the mixing continued for a further minute. The composite was cast in layers in 152mm concrete cube moulds, each layer being tamped in a consistent manner. Polymer A composites could be demoulded 1½ hours after casting and Polymer B composites 1 hour after casting.

TEST METHOD

Test specimens with 152mm square face and varying thicknesses were fixed in a target holder which provided support round the rear perimeter of the specimen but with minimal lateral restraint.

Projectiles were either 7.62mm NATO ball ammunition (mass 9.3g with lead alloy core) or 7.62mm NATO Armour Piercing ammunition (mass 9.6-9.9g with hardened steel core). Initially both types of ammunition were used, but indications were that armour piercing projectiles penetrated further than ball projectiles. Armour piercing projectiles were therefore used in the main test series and after the composites had been optimised a subsidiary series of tests using ball ammunition was carried out on an optimised composite to confirm the lower penetrations.

The projectiles were remotely fired from a fixed pressure housing, bolt and barrel arrangement 20m from the target. A photodiode type velocity measuring rig was mounted 1.5m in front of the target and this allowed the projectile velocity to be checked. Mean measured velocity for ball ammunition was 794 m/s and for armour piercing ammunition 907 m/s.

After testing target specimens were sectioned as shown in Figure 1(a). This enabled the penetration depth of the projectile to be determined and the penetration path length could be calculated by taking coordinates as shown in Figure 1(b).

OPTIMIZATION OF THE COMPOSITES

The fundamental aim of the project was to minimise the target thickness necessary to resist perforation, whilst keeping the cure time and the impact damage to the composite to an acceptable level. Thus the normal penetration depth, D, or penetration path length, D', were considered as alternatives for the design criterion. Initially the former was used but preliminary impact tests on composites showed that the penetration path rarely remained straight and normal to the impact face. The penetration path length was thus of more significance in assessing resistance than the penetration depth, and was therefore used as the design criterion in the main series of tests.

In attempting to optimize the composites in terms of their penetration resistance there was a large number of independent variables which had to be considered for each rock aggregate/elastomer combination. These variables are listed in Table 2. It was decided to concentrate the main test programme on the four primary quantitative (x) variables at the top of Table 2, and to keep the other secondary variables constant.

Normally the optimization procedure for four variables would be carried out by keeping three variables constant and varying the fourth. This would be repeated for each of the primary variables in turn. Thus sets of fitted equations
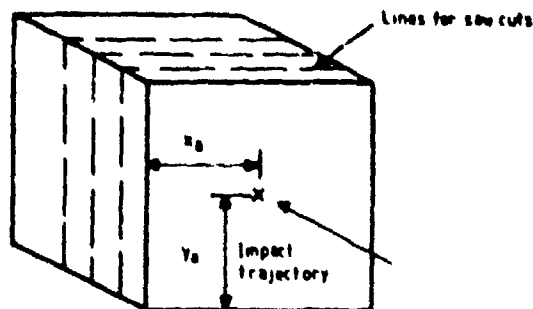
(a) ISOMETRIC ELEVATION ON IMPACT FACE
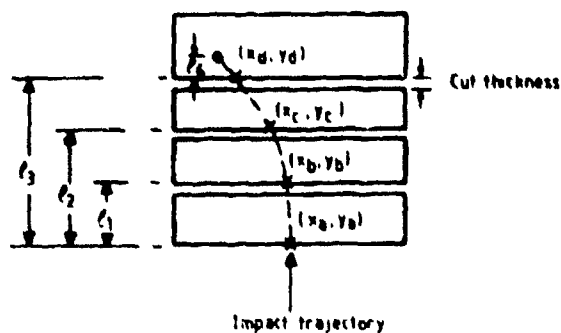
(b) PLAN ON SECTIONED SPECIMEN

Fig. 1   Target sectioning

Variable	Values in optimisation programme
% polymer by weight in mix, x_1	variable (7%-17%)
% rock aggregate by weight, x_2	variable (44%-64%)
% sand filler by weight in mix	variable (19%-49%)
rock aggregate, x_3 mm	variable (9.5-37.5)
polymer hardness, x_4 Shore A°	variable (60-85)
specimen cure temperature, °C	ambient
specimen test temperature, °C	ambient
age of specimen, days	1 day
specimen thickness, mm	152mm
bullet velocity, m/s	approx. 800 m/s

Table 2   Quantitative independent variables

would be obtained, each in only one x variable. From this stage, optimization can only be achieved by examining general trends and carrying out experiments on a trial and error basis. This method may require a very large number of tests and the inter-dependence of the variables may not be appreciated.

These difficulties were overcome by using a statistical method known as response surface theory, the general principles of which have been described by Cochran and Cox (7). Details of the application of this theory to the optimization of rock/elastomer composites are given by Anderson et al (8), and the mixes obtained from the optimization procedures are given in Table 3.

THICKNESS TESTS

During the optimization test series targets which were expected to be sufficiently thick (152mm) to prevent perforation were used. Very occasionally perforation occurred when the worst combination of primary variables was used, but no perforations were recorded with optimum mixes. When each of the optimum mixes had been identified it was necessary to determine the specimen thickness, t_m, which would contain the projectile with a given degree of confidence.

Two confidence levels were examined for the protective capability of the composite. The first, 80-90% containment, was thought to be applicable where the composite was to be used for protecting an existing reasonably strong structure, e.g. brickwork. Most of the projectiles would be contained, but those that were not would have their kinetic energy greatly decreased. The second confidence level, 97.5-99%, was considered sufficient where the composite was to be used alone, or over a weak structure.

Using specimens of varying thickness of optimized composites it was possible to estimate a thickness for each composite at which 80-90% containment would be achieved. Series of 20 tests on identical optimized specimens of this thickness were then carried out to check the 80-90% confidence level and to predict thickness for 97.5%-99% confidence. These tests showed that some adjustment of the mixes obtained from the main optimization test series was required for the Polymer B/basalt and Polymer B/limestone composites. Details of these tests and the various mix adjustmenets have been described by Anderson et al (8), and the results of thickness tests on all the final mixes are summarised in Table 4.

Polymer type	Rock type	% polymer by weight x_1	% rock aggregate by weight x_2	Rock size (mm) (nominal) x_3	Polymer hardness (Shore A°) x_4
A	River gravel	9	60	26.5 - 37.5	75
B	River gravel	9.8	59	26.5 - 37.5	80
B	Basalt	7	56	26.5 - 37.5	80
B	Limestone	7	64	26.5 - 37.5	80

Table 3   Mixes obtained from optimization procedure

Polymer type	Rock type	% Polymer by weight x_1	% rock aggregate by weight x_2	Rock size (mm) x_3	Polymer hardness (Shore A°) x_4	t_m for 80-90% confidence limits (mm)	t_m for 97.5-99% confidence limits (mm)
A	River gravel	9	60	26.5 to 37.5	75	90	115
B	River gravel	9.8	59	26.5 to 37.5	80	75	100
B	Basalt	9	58	26.5 to 37.5	80	110	140
B	Limestone	11	59	26.5 to 37.5	80	100	130

Table 4   Summary of results from thickness tests

SUPPLEMENTARY TESTS

Target Temperature Effects

In practical use the composite may be subjected to extremes of temperature and because the elastomer is very temperature sensitive, it was felt prudent to examine the protective capabilities of one of the optimized combinations (river gravel/Polymer B) at temperatures other than ambient. Three series of twenty tests each were carried out three days after casting on identical specimens 80mm thick (80-90% confidence level). In the first series specimens, after curing, had been cooled in a freezer and the average specimen temperature at testing was -7°C. In the second series specimens were heated in an oven after curing and tested at a mean temperature of +34°C. The third series of tests was carried out on specimens cast, cured and tested at ambient temperature (+15°C). The results of the tests showed that higher than ambient temperatures had little effect on penetration resistance, but a low temperature increased the resistance. This increase in resistance was accompanied by increased brittleness of the target with much greater damage around the impact zone.

Contact Explosive Tests

A limited series of tests was carried out to examine the resistance of rock/elastomer composites to small explosive charges. Slabs 610mm x 610mm x 80mm of optimum mix of the best composite (river gravel/Polymer B) were cast and cured. Similar slabs of concrete were cast with the same proportions and size of river gravel and sand as in the composite slabs.

The slabs were placed on a steel sheet on the ground and a hemispherical charge of plastic explosive was detonated centrally in contact with the slabs. By trial and error the minimum charge required to defeat the slabs, i.e. cause disintegration, was determined.

The results showed clearly the superior performance of the composite over concrete. A 50g charge caused only cratering of the composite slab with no cracking, indicating a high tensile resistance in the composite. A similar charge detonated on a concrete slab caused complete disintegration of the slab. Concrete was defeated by a 12.5g charge whereas the minimum charge necessary to defeat the composite was 150g.

COMMENTS

The tests showed that composites formed by binding rock aggregate together with an elastomeric matrix were effective in stopping small arms fire. The effectiveness of the composite depends on the constituents and the best performances were found with composites containing Polymer B. With all composites the optimized material contained the largest size gravel (26.5-37.5mm) which could easily be mixed with the resin and sand filler.

The aggregate type affects the penetration resistance. In particular, the harder the rock (as described by aggregate impact value) and the denser the rock particle packing (described by percentage voids), the greater will be the composite resistance. A guide to the necessary thickness of composite for any rock aggregate and for any particular confidence level is given in Table 5. It is suggested that the mix should contain 10% by weight of Polymer B (hardness 80 Shore A^C), 60% rock aggregate of the largest available (up to 40mm maximum) and 30% sand. Rocks with aggregate impact values greater than 25 should not be used.

Confidence level	Aggregate impact value between 25 and 15	Aggregate impact value less than 15
80%	110mm	95mm
90%	120mm	105mm
95%	130mm	115mm
97.5%	140mm	120mm
99%	150mm	130mm

Table 5   Suggested thickness of composite containing untested rock aggregate

A major advantage of these composites is their early resistance to penetration. The material has sufficient cohesion for moulds to be removed after 1 - 1½ hours. Static compression, bending and creep tests indicated full strength was achieved about eight hours after casting. These static tests also showed that the composite was strong enough for 80mm thick panels up to 3m square to be handled, or for the material to be free standing to a height of 10 metres.

The limited series of explosive tests showed promising results and this aspect of material behaviour should be further investigated.

REFERENCES

1. GIBBS, P.W. and PRESCOTT, P.P. A preliminary investigation into gravel armour. Tech. Memo, 74d50, M.O.D., M.V.E.E., (Christchurch), 1974.

2. BACKMAN, M.E. and GOLDSMITH, W. The mechanics of penetration of projectiles into targets. Int. J. of Engng. Science, Vol. 16, No. 1, 1978, pp. 1-99.

3. BERNARD, R.S. and HANAGUD, S.V. Development of a projectile penetration theory: Report 1 - Penetration to s allow and moderate depths. Army Engineer Waterways Experiment Station, Vickburg, Missouri, AEWES-TR-S-75-9-1, 1975.

4. BERNARD, R.S. Development of a projectile penetration theory: Part 2 - Deep penetration theory for homogeneous and layered targets. Army Engineer Waterways Experiment Station, Vickburg, Missouri, AEWES-TR-S-75-9-2, 1975.

5. BRITISH STANDARDS INSTITUTION B.S. 822 : Specifications for aggregate from natural sources for concrete. Part 2, 1973.

6. BRITISH STANDARDS INSTITUTION B.S. 812 : Methods of sampling and testing mineral aggregates, 1975.

7. COCHRAN, W.G. and COX, G.M. Experimental designs. Wiley Publications, New York, 1957.

8. ANDERSON, W.F., WATSON, A.J., JOHNSON, M.R. and McNEIL, G.M. Optimization of rock/polymer composites to resist projectile penetration. RILEM Materials and Structures (in press), 1983.
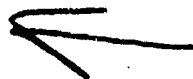
BEHAVIOUR OF FIBER REINFORCED CONCRETE SLABS
UNDER IMPACT LOADING

M. Hülsewig, E. Schneider, A. Stilp

Ernst-Mach-Institut, Freiburg, FRG
Terminal Ballistics and Impact Physics Division

ABSTRACT

The behaviour of steel fiber rein-
forced concrete slabs under impact loads
has been investigated. The results ob-
tained show that fracturing and spallation
effects are reduced to a large extent due
to high energy absorption and the increas-
ed yield strength of this material. Crater
depths are comparable to those obtained
using normal concrete targets. Systematic
tests using different fiber types and
dimensions show that the terminal ballistic
behaviour is strongly dependent on these
parameters.

INTRODUCTION

Concrete, as a wide spread and cheap
building material is also preferably used
for military shelter constructions. For
this application its low yield strength and
its brittle behaviour are of great dis-
advantage. These material properties lead
to harmful spallation processes especially
at the interior of building constructions.
Considerable damage might be caused, even
if the ballistic limit thickness is not yet
overcome. An essential improvement of the
protection properties of concrete can be
expected, if a more plastic behaviour and
an increased yield strength could be
achieved. An appropriate means can be the
mixing in of steel fibers. Many investi-
gations concerning the behaviour of such
fiber reinforced concrete under static
loads have been performed. They show, that
the application of steel fibers leads to a
moderate increase of the yield strength,
and to a considerable improvement of the
plasticity. Though this material seems to
be very promising also under dynamic
loads, only few studies of its dynamic be-
haviour have been performed up to now.
Therefore an extensive experimental pro-
gram has been initiated at Ernst-Mach-In-
stitut with the objective to study the
behaviour of fiber reinforced concrete
under dynamic loads and to optimize its
composition.

EXPERIMENTS AND RESULTS

For preliminary tests plain, normally
reinforced and fiber reinforced concrete
slabs have been produced. They have been
impacted with steel cylinders (mass 50 g)
in the velocity range between about 400 -
700 m/s. A comparison of the damage phe-
nomena (Fig. 1) shows, that plates com-
pletely brake and show rear side spallat-
ion effects already at impact velocities
of about 400 m/s (Fig. 1,left). The nor-
mally reinforced plates not even brake at
impact velocities of more than 700 m/s
due to the high yield strength in the
direction of the plate plane, however,
rear side spallation is not suppressed
by means of the reinforcement (Fig. 1,
center). Up to more than 600 m/s the
fiber reinforcement prevents fracture and
spallation processes (Fig. 1, right). In
addition it has been found that the
fibers are of only minor influence on the
crater depths. These tests show, that
fiber reinforcement well suppresses da-
mage due to shock wave propagation. By
using several different types of fibers
it became evident, that the fiber geo-
metry is of great influence on the ballis-
tic behaviour of this material.

Based on these results, an experimen-
tal program for the optimization of steel
fiber reinforcement has been performed.
In these experiments the dependence of
the damage phenomena on fiber parameters
was investigated. For this, planar im-
pacts resulting in planar shock-wave
loads have been performed. The projectiles
were cylinders, made of fiber reinforced
concrete, with diameters of 9 cm and
thicknesses of 25 to 30 mm. Fiber para-
meters have been varied in the following
manner:

1) Variation of the fiber content

The increase of energy absorption
of concrete due to the fibers should be
proportional to the fiber content. The
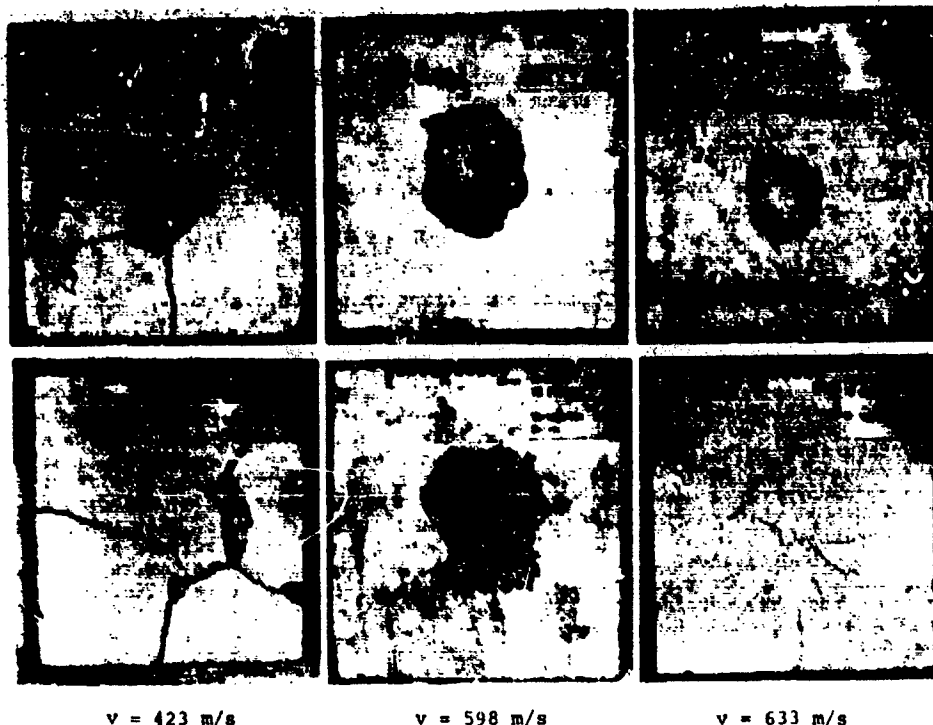influence of the fiber content on the

v = 423 m/s   v = 598 m/s   v = 633 m/s

Fig. 1 Comparison of different concrete types

reduction of braking and spallation pro-
cesses can only be clarified experimentally.
Therefore a fiber type (0.4 x 25 mm) was
used, which was easy to mix in. The degree
of reinforcement was varied between 0 and
10 % by weight in steps of 2 %.

2) Variation of the fiber length at a
   constant fiber diameter

The energy, which is needed to pull
out a fiber from the cement matrix is in-
creasing with increasing fiber length. The
force needed to pull out a fiber as well
as the extension length are both increasing
linearly with increasing fiber length. That
means, the work needed for a complete dis-
connection is proportional to the square
of the fiber length

3) Variation of fiber length and diameter
   at a constant L/D-ratio

It is not easy to predict the influ-
ence of the variation of these parameters,
since opposite effects have to be taken in-
to account.

a) An increase of the fiber length and dia-
meter leads to a decrease of the total sur-
face for a constant fiber content and there-
by the energy absorption is reduced.

b) See consideration to No. 2.

Concerning the variation of the fiber
contents, it was found, that already a
weak degree of reinforcement of only 2 %
by weight leads to an effective suppress-
ion of braking and spallation. Only a
gradual improvement is achieved, if the
fiber content is increased up to 10 %. A
quantitative charaterization of the damage
phenomena at the rear side of the plates
cannot be given due to extensive scatter-
ing of fracture data. Therefore, the
plates have been sectioned. A distinct
conical fragmentation zone can be ob-
served within the slabs, the volume of
which can be measured easily. This vo-
lume of highly fragmented target material
can serve as an integral quantification
of the target damage.

In Fig. 2 the volume of this frag-
mentation zone is plotted versus the
projectile energy for different degrees
of reinforcement. The relation is roughly
linear, e.g. an approximately constant
portion of the kinetic projectile energy
is converted into fracture energy. The
fragmentation zone is getting smaller
with increasing fiber contents.

92

Fig. 2 Volume of fragmentation zone versus impact energy for different degrees of reinforcement

Fig. 3 Volume of fragmentation zone versus impact energy for different fiber lengths and constant D

The variation of the fiber length at constant diameter shows, that a length increase leads to a reduction of the fragmentation zone, too (see Fig. 3). The results obtained by varying fiber length and diameter at a constant L/D ratio are shown in Fig. 4. The fiber of medium dimensions yields best results. The effectiveness of the small fiber is reduced due to a small stiffness and a bad adhesive strength. For tne long fiber the mixing within the concrete is not sufficiently homogeneous and a predominant orientation parallel to the slab surface occurs. Considering all tests, the fiber with L = 25 mm and D = 0.4 mm was found to yield best results under ballistic loads. It can easily be mixed in up to relatively high degrees of reinforcement.

Fig. 4 Volume of fragmentation zone versus impact energy for different L and D and constant L/D

SHOCK WAVE MEASUREMENT

Additional ballistic experiments have been performed in order to measure the shock pressure profile within the target. The experimental set up is shown in Fig. 5.
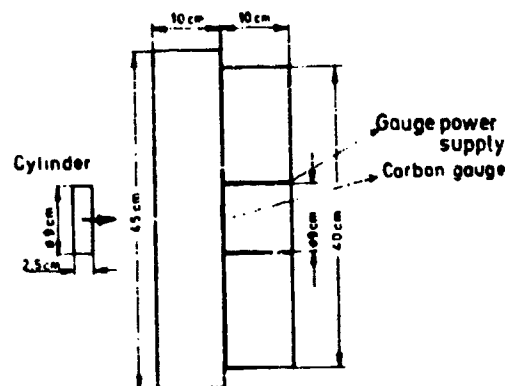
Fig. 5 Set-up for pressure measurement

A piezoresistive carbon gauge is mounted between two concrete slabs of 10 cm thickness each, which have been glued together. The gap between the plates where the carbon gauge is located, is only some tenth of a mm wide, that means the full pressure peak occurs at the gauge position. Fig. 6 shows a typical pressure signal for an impact velocity of 150 m/s. Since the electronic detection system was triggered at the time of projectile-target contact, the oscillogram also reveals the propagation time of the shock wave until it reaches the gauge. It was 25 µs and is

in good accordance with a wave propagation
velocity close to the velocity of sound.
Within 2 or 3 µs the pressure rises to
an amplitude of 9.5 10⁷ Pascal. The width
of the pressure maximum (12 µs) corres-
ponds to the duration of the pressure
phase at the projectile-target inter-
face.

Fig. 6   Pressure signal

CONCLUSION

Fiber reinforced concrete has very
good properties with respect to dynamic
loads due to its high energy absorption
and a suppression of the rear side
spallation.

REFERENCES

HÜLSEWIG, M. and STILP, A.: Vorunter-
suchungen über die Eignung von stahl-
faserarmierten Betonplatten als Splitter-
schutz.
Ernst-Mach-Institut 1978

EXPERIMENTAL MODELING OF STRENGTH AND DEFORMATION BEHAVIOR OF CONCRETE IN DIRECT SHEAR

Stein Sture

Department of Civil, Environmental, and Architectural Engineering,
University of Colorado, Boulder, Colorado.

ABSTRACT

Direct shear experiments on large prismatic specimens of plain concrete were conducted in a large capacity servo-controlled and structurally stiff test apparatus in order to assess the predictive capabilities of nonlinear computational analysis techniques. The objective in these experiments was not to obtain material properties but rather to investigate load-deformation response behavior and strength characteristics of a mini-structure subjected to the complex states of nonproportional loading imposed by the direct shear test. The specimens were loaded to failure under displacement control and constant normal load. The complete spectrum of structure as well as material responses were observed including pre-peak elastic-hardening plastic, post-peak strength strain-softening, and localization of deformation into a shear band and continued shear gliding at a residual strength level.

INTRODUCTION

The direct shear translation test has in the past often been used rather frivolously to evaluate basic strength properties as well as shear stress-shear displacement response behavior of concrete and geomaterials. It has generally been assumed that the normal and shear stresses were uniformly distributed on the imposed shear plane. However, it is well established that both strain and stress distributions within initially homogeneous solid test samples are highly nonuniform during the experiment. The magnitude of the principal stresses varies nonproportionally in the specimen and the principal stress directions rotate with respect to the material fabric to unknown extents during the shearing process, which in turn result in pronounced stress or deformation induced anisotropy. The overall sample response behavior therefore constitutes a combined response of a material that undergoes brittle and ductile fracture in tension and shear gliding. Proper material characterization for the purpose of obtaining basic engineering properties require homogeneous strain and stress states in the test specimen, and these do not exist in the direct shear test. This test is also highly sensitive to boundary conditions and the manner with which a centric or non-centric

tangential shear load is applied with respect to the shear plane. Several authors have discussed the merits of the direct shear test [1-4]. The shear test has been found to be a valuable tool for investigating residual strength characteristics of materials where shear bands or fracture zones already exist. It has also seen successful use for studying interface behavior between soils and structural materials such as steel and concrete. This aspect has been reviewed by Desai [5].

In view of these considerations it was decided to adopt the direct shear test, not as a test for engineering properties, but as a miniature structure test where the boundary conditions can be carefully controlled and where complex states of tensile cracking and shear fracture can be studied. The direct shear structure test constitutes a controlled environment where the entire spectrum of the structure's and its material's responses can be followed through the elastic, hardening plastic, fracture, post-peak, strain-softening, and residual strength states. Investigations of brittle and ductile fracture transitions, progressive damage accumulation and localization of deformation in narrow shear bands in conjunction with degrading stress-starin or load-displacement relationships require a very stable test system.

The general objective in this research effort has been to compare the measured response behavior to the computational analysis predictions and to evaluate the capability of the so-called smeared fracture approach for describing progressive damage and frictional sliding along narrow shear bands. If this is achieved in the complex environment of the direct shear test, it is asserted that the computational analysis algorithm can model almost any three-dimensional boundary value problem involving brittle and ductile materials. The present paper covers apparatus description and the experimental technique used in the project. The computational aspects of this investigation are described in the companion paper by Willam [6].

EXPERIMENTAL APPARATUS

The experiments were conducted in the high precision direct shear device shown in Fig. 1. The apparatus consists of loading actuators, normal and shear load reaction frames, normal and lateral

loading fixtures shown in Fig. 2. The top and bottom shear box compartments shown in Fig. 3 receive 20.3 x 20.3 x 10.2 cm (8 x 8 x 4 in.) samples of prismatic shape. In some instances the specimen width has been as small as 10.2 cm rather than 20.3 cm. The notched and un-notched specimens were fused to the shear box compartments by means of structural epoxy and conventional sulphur capping compound. In order to minimize a reactive moment about the average shear plane the shear box is positioned in the holding fixtures and apparatus support system so that the applied lateral shear load and restraining action lie in the plane of induced shear failure. The top shear box compartment and holding fixture remain stationary in the horizontal direction during shearing, while they are allowed to translate vertically. This feature facilitates observation of dilatancy. The restraining action in the horizontal direction is provided by means of a very stiff horizontal load support frame, which in turn is connected to an extremely stiff structural floor by means of heavy bolts. The top holding fixture together with the top shear box compartment can also undergo small roll and pitch movements in addition to the vertical translation. At present only one average vertical displacement has been monitored by means of a Linear Variable Differential Transformer (LVDT). It is planned to use three LVDTs at a later stage in order to define the rotational movements of the top portion of the specimen during and after fracture. It is also possible to lock the top entirely against rotations as well as vertical translation. The latter can be achieved through displacement control of the vertical actuator. Servo-controlled hydraulic MTS-actuators having 735 kN (165 kip) capacity in the normal direction and 156 kN (35 kip) in the tangential direction were used. The bottom shear box compartment and holding fixture have shapes and stiffness properties that are similar to the top components. The bottom shear holding fixture is supported by two rows of heavy roller bearings which allow translatory motion of several centimeters. The bottom holding fixture is connected to the tangential load actuator by means of a large and stiff load transfer block (Fig. 2). The MTS control system can operate the apparatus under very slow or high displacement rates. Dynamic tests of rock joints subjected to large normal stresses and large relative displacements have been successfully conducted in this device at frequencies ranging from nearly 0 to 10 Hz. Figure 3 shows a schematic illustration of the MTS and apparatus control system. The MTS hydraulic actuators operate independently in separate closed-loop control systems. The Series 204 MTS actuators are equipped with Series 252 servo-valves; Series 661 fatigue-resistant load cells; internal LVDTs; and swivel heads and bases. The control console is equipped with the following components: 430 digital indicator, 436 control unit, 410 digital function generator, and two 406 controllers, which are operated independently. Prior to testing a selection of force or displacement control for each 406 controller must be made. Once the mode of operation has been decided, the proper feed-back signal provided by the internal

LVDT or load cell, is compared with the input signal. If the signals are not equivalent, action is taken by the servo-valve to equilibrate the two signals. This is the basic feature of the closed-loop system.

A Hewlett Packard 3054 A Automatic Data Acquisition/Control System controlled by a HP 9825 T desk top computer was used as the primary control and data acquisition system. The 3054 A system contains a HP 3437 A System high speed voltmeter and a HP 3497 A Data unit scanner. The data collected by the HP 3054 A system were transmitted to the HP 9825 T computer and stored on tape. Real-time observations of load-deformation and strength behavior was recorded by means of an Esterline Angus xyy' 540 plotter. The relative shear displacement was measured by means of two 500HR-DC Schaevitz LVDTs whose feeler rods were inserted into the sample as depicted in Fig. 4. T' LVDTs were connected 'n series.

EXPERIMENTAL TECHNIQUE AND RESULTS

Notched and un-notched plain concrete prismatic specimens having unconfined compressive strengths (f_c') ranging from 26.2 MPa to 28 MPa and unconfined tensile strength (f_t') of 4.1 MPa were initially subjected to nominal normal stress states that varied between 0.69 MPa and 6.9 MPa (100-1000 psi) prior to shearing. The lateral load was increased in displacement control at a constant rate of 0.05 mm/s.

Fig. 1   Large capacity direct shear apparatus
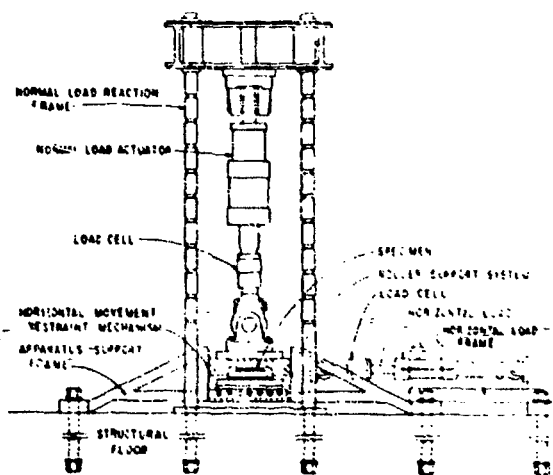
1 - Applied shear load
2 - Reaction frame load
3 - Shear load transmitting block
4 - Top reaction frame
5 - Top support plate
6 - Upper specimen shear box compartment
7 - Lower specimen shear box compartment
8 - Specimen
9 - Bottom support plate
10 - Roller bearing support guides
11 - Channel housing
12 - Support pins
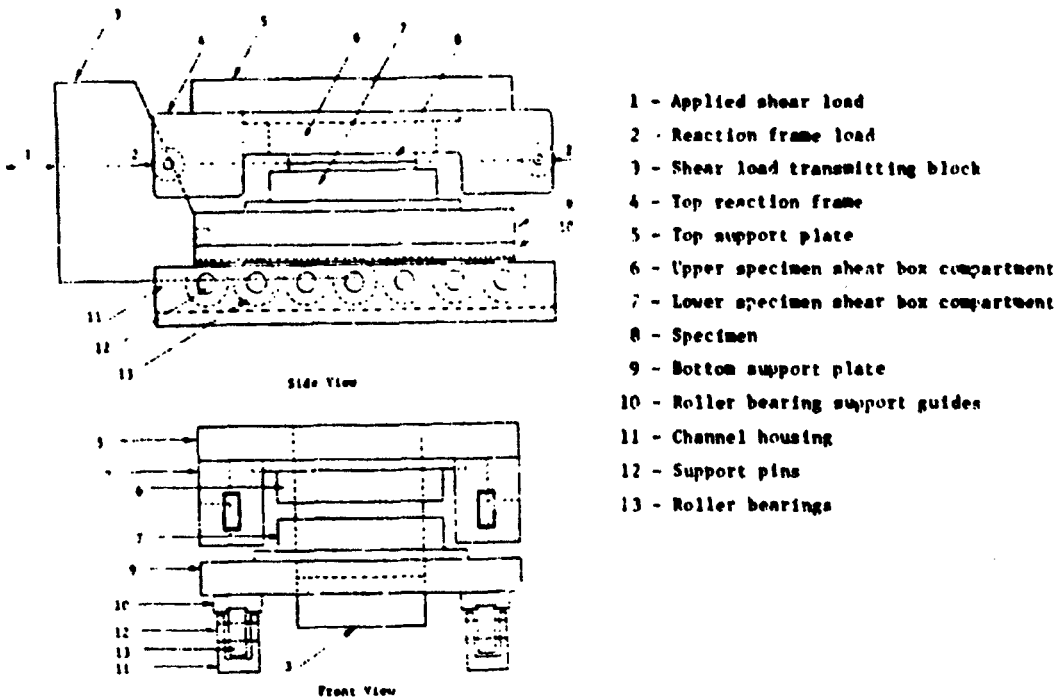13 - Roller bearings

Fig. 2 Specimen holding fixtures and shear box compartments
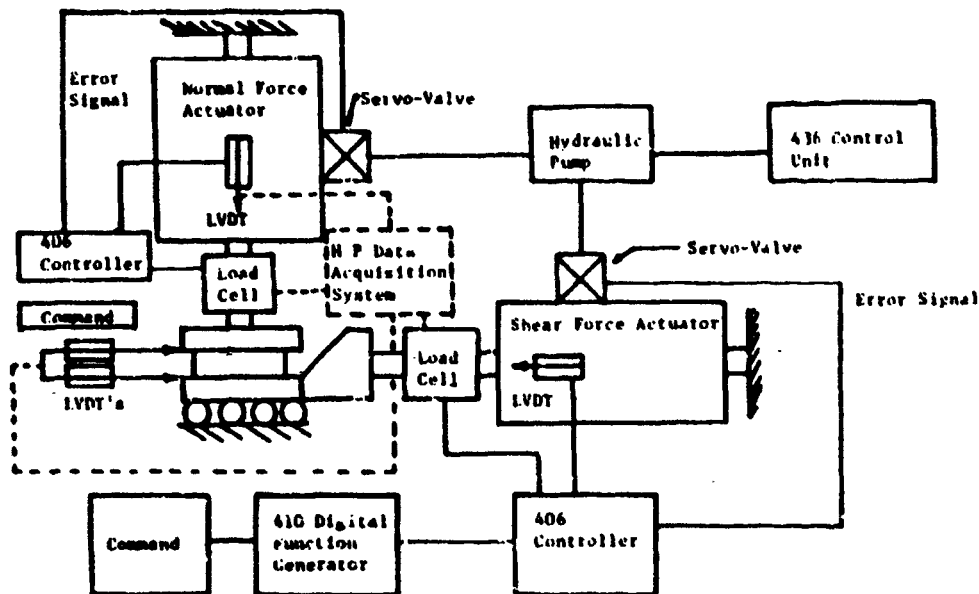

Fig. 3 Schematic diagram of apparatus and load control system

97

The notched and un-notched specimens' widths varied between 10.2 cm and 20.4 cm (4-8 in.), whereas lengths and heights were maintained constant at 20.4 cm and 10.2 cm in all tests. All specimens were sawcut to final size from over-size castings. The exterior side faces of the specimens were exposed for visual and photographic observation. Shear displacement measurements were obtained by LVDTs mounted on control rods embedded in the specimen through ports in the top and bottom shear box compartments. The spacing between the parallel rods varied between 3.8 cm and 10.2 cm in the tests. On one occasion the rods penetrated into the tensile fracture zone. Figures 4 a and b show the notched and un-notched specimens within the shear box compartments. The feeler-rods are shown in Fig. 4a. The specimen was notched at two opposite faces with 90° and 1.27 cm (0.5 in.) deep grooves in order to induce high stress concentrations near the ends. Figure 4a also shows the finite element mesh idealization used in modeling the notched specimen test.

Specimen failure initiated due to tensile cracking rather than shear slip in both the notched and un-notched tests. This happened before any shear band formation. Crack openings were visible before shear failure took place in the center regime. Cracking also took place outside the notches, and fracture propagation from the notch surfaces only took place after significant crack development. Pronounced inclined cleavage cracks later developed across the notched section. In both specimen categories the tensile stress state was responsible for ultimate failure, although the nominal compressive stress on the shear surface was much higher in the un-notched case. Tensile cracking occurred under very small relative displacements, while shear fracture and subsequent gliding took place under relatively large displacements. The shear fracture propagation was rather slow in comparison with the tensile cracking events. Figure 5 shows photographs of the notched specimen prior to and after failure and the exposed bottom of the failed specimen after test disassembly.

(side view)

(top view)

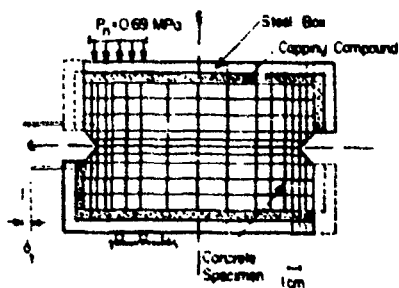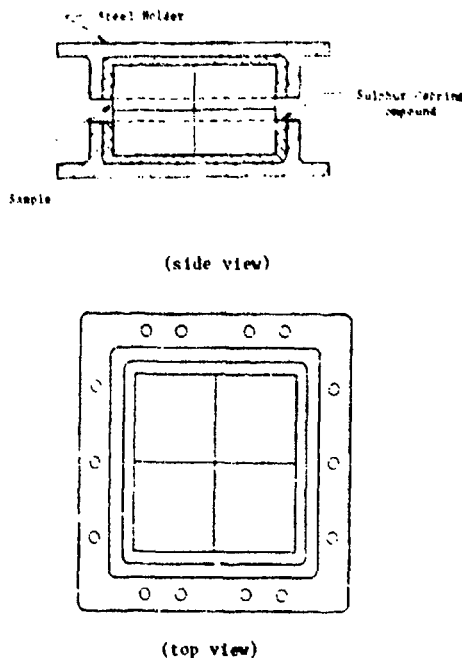Fig. 4b Direct shear box compartment for un-notched specimen
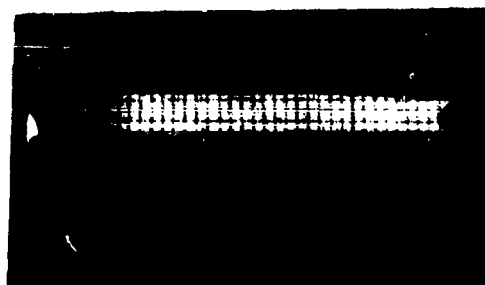
(specimen before failure)

(specimen after failure)

Fig. 4a Direct shear box compartment for notched specimen and LVDT gage rods

Fig. 5 Failure behavior of notched concrete specimen
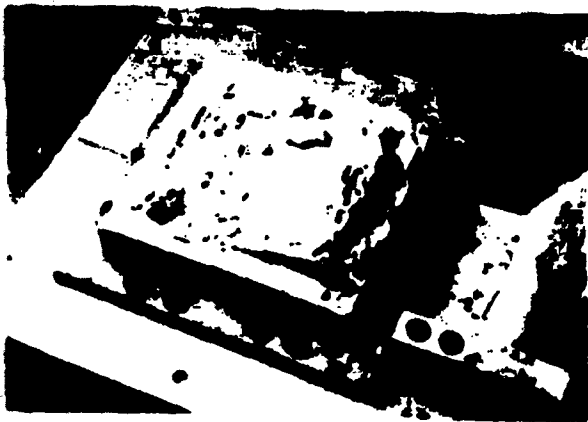
Fig. 5 [continued] Failure behavior of notched
concrete specimen

No debonding was observed between specimens
and shear box compartments after the tests. Both
specimen categories exhibited nearly linear
elastic behavior before reaching peak strength.
The nonlinear shear stress-displacement response
is most pronounced in the un-notched specimen.
Upon continued shearing the lateral force decreas-
ed in both specimens until a residual strength
level was reached. The rate of softening and the
residual strength levels are quite different due
to the applied normal loads which were 143 kN in
the un-notched case, which resulted in a nominal
normal stress of 6.9 MPa (1000 psi), and 24.9 kN
in the notched case, which resulted in a nominal
normal stress of 0.69 MPa (100 psi). The residual
friction angle (ϕ_r) in both cases was found to be
35°. The stick-slip pattern on the shear stress-
shear displacement response curves shown in Figs.
6 and 7 indicates that shearing and crushing of
clasts are far more pronounced for the high
confinement un-notched specimen than for the low
confinement notched specimen. The un-notched speci-
men was subjected to a small unloading-reloading
cycle at approx. 70% of peak strength and signi-
ficant permanent inelastic deformation was observed.
It should also be noted that the relative displace-
ments were recorded by having the LVDT measurement
rods 3.3 cm apart in the notched specimen test and
10.2 cm apart in the un-notched specimen test.

The apparatus and test specimen configuration
was essentially stable throughout the shearing
process, although energy releases in the post-peak
strain-softening branch of the stress-displace-
ment response diagrams indicate rate increases.
Real-time xyy' plots of the events also gave this
impression. Nevertheless, it is maintained that the
strain-softening branches in Figs. 6 and 7 repre-
sent true behavior of the concrete miniature
structure subjected to defined boundary conditions.

CONCLUSIONS
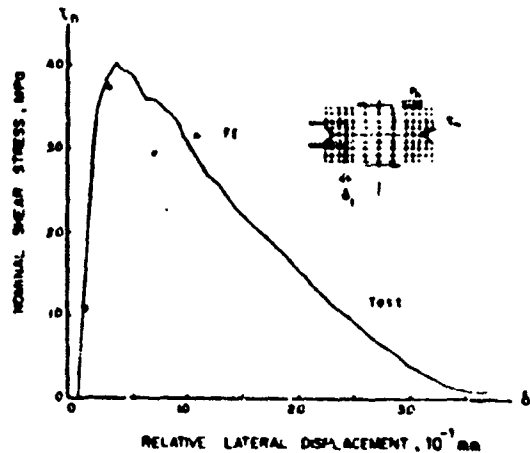
It has been demonstrated that the direct shear test may constitute a favorable environment for evaluating load-displacement as well as nominal shear stress-relative displacement response behavior of small prismatic or other regularly shaped miniature structures of concrete or geomaterials for the purpose of calibrating computational analysis procedures as well as constitutive models. The prismatic direct shear specimen is subjected to complex stress states that vary throughout the experiment. Issues related to tensile cracking and shear gliding as well as their interactions can be investigated in this test. The computational considerations associated with these experiments are described by Willam [6].

ACKNOWLEDGEMENT

REFERENCES

[1] Saada, A.S. and Townsend, F.C., "State of the Art: Laboratory Strength Testing of Soils," Proc ASTM Symp. Laboratory Shear Strength of Soil, ASTM STP 740, pp.7-77, 1981.

[2] Kutter, H.K, "Stress Distribution in Direct Shear Test Samples," Proc. Int. Symp. Rock Mech., Nancy, France, 4-6 Oct., 1971.

[3] Gould, M.C., "Development of a High Capacity Dynamic Direct Shear Apparatus and its Application to Testing Sandstone Rock Joints," M.S. Thesis, Univ. of Colorado, Boulder, 1982.

[4] Christensen, J., Ickert, K., Stankowski, T., Sture, S.. and Willam, K., "Numerical Modeling of Strength and Deformation Behavior in the Direct Shear Test," Proc. Int. Conf. on Constitutive Laws of Engineering Materials, Tucson, Arizona, January, 1983.

[5] Desai, C.S. and Zaman, M.M., "Models for Sliding and Separation at Interfaces under Static and Cyclic Loading," Proc. Int. Conf. on Constitutive Laws of Engineering Materials, Tucson, Arizona, January, 1983.

[6] Christensen, J. and Willam, K., "Finite Element Analysis of Concrete Failure in Shear," Proc. Symp. Interaction of Non-Nuclear Munitions . th Structures, Colorado Springs, Colorado, May, 1983.

FINITE ELEMENT ANALYSIS OF CONCRETE FAILURE IN SHEAR

James Christensen and Kaspar Willam

Department of Civil, Environmental and Architectural Engineering
University of Colorado, Boulder, Co. 80309

ABSTRACT

The main purpose of this study is to assess the current computational methods for predicting the failure behavior of concrete and geomaterials in the form of tensile cracking and frictional slip. The paper concentrates on the peak and post-peak response of plain concrete in shear which is modeled by the "smeared" finite element approach in which localized failure zones are distributed over a finite material region with softening material properties. The computational results are compared with experimental observations of plain concrete specimens which are tested in the large capacity servo-controlled direct shear apparatus described by S. Sture in the companion paper.

INTRODUCTORY REMARKS

In view of the importance of ductility to structural safety a comprehensive research project was recently initiated at UC, Boulder to examine different forms of local material failure and their effect on the response of the overall structure. The main purpose of this work is to scrutinize the value of the current computational strategies to predict progressive material instabilities within the structure up to collapse of the entire configuration. Considerable criticism was voiced in the past whether the so-called "smeared approach" was capable to provide reliable predictions of structural failure. This computational strategy is normally adopted because the complex fracture process can be readily accomodated within traditional procedures for nonlinear material behavior in the form of an equivalent strain softening model. In this way progressive material damage may be accounted for in a conventional finite element program in the form of an averaging technique for highly localized deformations, discrete cracks and shear bands within the structure.

Clearly local material failure implies in reality a change in the topology of the structure. Therefore, the alternative discrete fracture approach incorporates these discontinuities right from the beginning within the structural idealization. However, in three-dimensional components, the discrete fracture analysis involves definition of an initial fracture surface and subsequent propagation with continuous changes of the structural topology which simply overtaxes current computational facilities. Moreover, the specification of the underlying criteria for fracture initation and propagation as well as the definition of prevalent interface conditions introduce additional constitutive difficulties similar to the softening formulation in the smeared approach.

As a result of these controversial issues it is mandatory to scrutinize the shortcomings and limitations of the smeared and discrete failure models in the light of experimental evidence. To this end plain concrete specimens were tested in the large capacity direct shear apparatus which was developed by S. Sture at the University of Colorado, Boulder [1] and which covers the full spectrum of tensile cracking and frictional slip modes of failure. The direct shear specimen forms in reality a structural configuration rather than a material sample because of the non-uniform state of stress resulting from the complex boundary conditions as well as localized material failure. In fact the servo-controlled test set-up reproduces the stress transfer of highly indeterminate structures and covers the entire response regime including the post-peak behavior down to the residual strength response.

RELATED RESEARCH

Due to rapidly increasing demands in computational mechanics and the electronic revolution in testing extensive research efforts are currently devoted to investigate failure in three areas:

(i) Micromechanics of the underlying ductile fracture process

(ii) Constitutive modeling of the material behavior for smeared and discrete failure studies

(iii) Analysis of structural failure within the smeared strength of materials and the discrete fracture mechanics approach

For brevity only those contributions are cited here which are of immediate concern. The direct shear test is probably the oldest and most controversial experiment ever since it was adopted by Coulomb to study shear in soils. The under-

lying morphology and mechanics of discontinuities in the failure zone were examined among others by Morgenstern and Tchalenko [2] in overconsolidated clays. In a recent paper Vallejo [3] recognized that the development of shear bands is the result of different crack discontinuities rather than uniform frictional slip. In fact he claims that the formation of crack discontinuities precludes application of the Coulomb failure theory or alternative continuum models. Based on linear elastic finite element analysis of the direct shear test Kutter [4] noticed previously that tensile stresses remain insignificant for ratios of normal to tangential loading N/T >1. Moreover, he observed for the field of rock mechanics that the direct shear experiment on solid test samples is really not meaningful since the direction of initial slip surfaces does not coincide with the enforced direction of failure. As a result the direct shear test is certainly not the simple material test originally intended and thus requires a full stress analysis of the specimen similar to realistic structural components.

Palmer and Rice [5] adopted a discrete fracture mechanics approach for modeling the behavior of concentrated shear bands in order to interprete strong size effects. On the computational front Cleary and Dong presented recently a discrete interface model for failure in geological materials [6] combining finite elements with a surface integral technique considering the effect of a stationary shear band along a predetermined zone of weakness.

A fundamentally different approach was pursued by Rice et al [7,8] who studied the localization of deformation into a shear band in the form of constitutive instabilities in homogeneous deformations. Following the mathematical theory of bifurcation and uniqueness due to Hill they established conditions for material stability and found a high sensitivity with regard to "normality" and rate effects. Along similar lines Vardoulakis [9], Vermeer [10] and Darve [11] determined very recertly the critical orientation of shear bands in simple test configurations. In analogy to the linearized buckling analysis of structures these material stability studies yield the incipient failure mode for a homogeneous deformation state. However, in this form they provide no insight into the redistribution capacity and reserve strength of realistic structures with slow contained propagation of material instabilities within complex structural configurations.

On the computational front it is intriguing that the first finite element studies of reinforced concrete structures followed the discrete crack approach, see e.g. the state-of-the-art report in ref. [12]. Recently, this methodology has been newly interpreted in terms of the underlying fracture mechanics concepts by Hillerborg et al [13]. Ingraffea et al [14] developed on this basis a discrete fracture analysis program for two-dimensional applications with sophisticated interactive remeshing capabilities. However, the bulk of computational studies relied on the alternative smeared failure approach. The essential shortcoming of this strategy was retrofitted only recently by Bazant et al [15, 16] who adopted the fracture energy concept in order to account for size and gradient effects. The strain softening branch for tensile cracking depends in this case on the mesh size in order to insure mesh-independent release of fracture energy as failure propagates. For frictional slip and the mixed modes of failure a rational concept for simultaneous softening of the cohesive and tensile strength values is still missing and is therefore an immediate objective of the current investigation.

COMPUTATIONAL STUDY

Preliminary results of the current research were presented in ref [17] which contained a detailed substructure analysis of the entire shear box. The purpose was to define appropriate boundary conditions for the actual test specimen which was sheared under displacement control in order to capture the softening regime (relative tangential displacements between the upper and lower halves of the shear box). Fig. 1 shows a typical finite element idealization of the entire shear box which includes the notched concrete specimen, the capping compound, the steel box and the loading frame.

In the main portion of ref [17] experimental data of the direct shear test were compared with the finite element solution using the smeared approach. One principal outcome of this study was that the direct shear test of concrete was in reality a tension test for the ratio of normal to tangential loading N/T = 1/6 at failure. Moreover, the shear test specimen behaved like a structural component with considerable redistribution capacity because of contained material instabilities due to the confinement of the shear box. The Mohr-Coulomb model with tension cut-off in Fig. 2 [18] reproduced fairly well the overall response behavior shown in Fig. 3 with material parameters which were obtained from separate material tests. As a result, the direct shear test could be utilized to verify the computational strategy for predicting structural response behavior in the pre- and post- peak regime. Clearly, the smeared approach did not model the localization of deformation into the discontinuous failure band shown in [17]. however, it was able to capture the stress redistribution and the propagation of material failure in the form of tensile cracking and frictional slip within the structure, see Figs. 4 and 5. Although the fracture energy concept for tensile cracking furnished a rational concept for strain softening as function of mesh size it did not resolve the fundamental short-comings with regard to localization. Moreover, a comprehensive theory for different fracture modes is still lacking, in particular for mode #2 type shear failure which is of primary interest in this context.

To this end a series of direct shear tests are currently on the way which are described in

the companion paper [1]. For different N/T loading ratios the entire failure spectrum is covered from predominantly tensile cracking to frictional slip.

The study below shows computational results for the second test series. The particular case is examined in which the shear box is preloaded with a constant vertical pressure of $p_n = 1$ ksi which corresponds to a load ratio of N/T = 1 at failure. The idealization of the shear box is shown in Fig. 6 with 129 plane strain elements interconnected by 1105 degrees of freedom. As before [17] the shear specimen as well as the shear box are included in the idealization in order to ensure centric application of the tangential force in the prevailing shearing plane. The initial test set-up was slightly modified to accommodate test specimens of different width. The actual size of the hexahedral specimen is in this case L*H*W = 8.0 x 4.5 x 3.0 in. The concrete specimen is fastened to the steel box with an epoxy layer which assures full bond even on the tensile side walls. The material properties were determined with a series of independent uniaxial and triaxial concrete tests yielding the following values

Elastic Stiffness: $E = 3000$ ksi
$\quad\quad\quad\quad\quad\quad\quad v = 0.20$

Strength Values: $f'_c = 4.7$ ksi
$\quad\quad\quad\quad\quad\quad f'_t = 0.55$ ksi
$\quad\quad\quad\quad\quad\quad c = 1.0$ ksi and $\phi = 40°$

In the post-peak regime different softening models are currently examined along the fracture energy concept, whereby brittle collapse and plastic yielding of the tensile, cohesive and frictional strength values are limiting cases. The resulting shear behavior of the brittle strategy is reproduced in Fig. 7 in terms of the nominal shear stress on the prevailing shearing plane and the relative tangential motion of the lower steel box against the upper one. In this case the residual strength values for tension and cohesion are instantaneously reduced to zero when the stress path penetrates the failure surface while the residual friction angle is reduced to $\phi_r = 34°$. The response curve clearly illustrates the effects of local material instabilities in the form of oscillations before the overall degradation of strength takes place down to the residual strength level due to internal friction.

Fig. 8 shows the deformed mesh for the load point in the peak regime where $\delta_t = 20.9 \times 10^{-3}$ in. Together with the plots of displacement vectors and principal stresses in Figs. 9 and 10 this problem illustrates clearly the stress redistribution into axial thrust action between the compressive side walls during progressive shearing and the extent of localized deformations in the specimen. In contrast to the usual notion of a horizontal shear band in geomaterials the failure planes are in this case inclined parallel

to the direction of minor principal stress and a horizontal mode of frictional slip develops only in the final state of shearing. As a result this example demonstrates some of the limitations and capabilities of the smeared approach.

CONCLUDING REMARKS

The computational study clearly illustrates the complex failure mechanisms of plain concrete subjected to shear. As a result the direct shear test is not a simple experiment for determining the stiffness and strength characteristics of a material, it is rather a structural configuration in which considerable stress redistributions take place in the pre- and post-peak regime. Within limits the smeared approach models fairly well the propagation of local material instabilities due to tensile cracking and frictional slip within the structural configuration. However, it does not reproduce the localization of discontinuities failure zones except for a continuous band of failed elements with similar orientation of the individual fracture planes.

REFERENCES

[1] S. Sture, "Experimental Modeling of Strength and Deformation Behavior of Concrete in Direct Shear", paper at Symp. on Interaction of Non-Nuclear Munitions with Structures, USAF Academy, Colorado Springs, CO, May 10-13, 1983.

[2] N.R. Morgenstern, J.S. Tchalenko, "Microscopic Structures in Kaolin Subjected to Direct Shear", Geotechnique, 17, (1967), 309-328

[3] L.E. Vallejo, "Development of a Shear Zone Structure in Stiff Clays," Proc. 4th Intl. Conf. Num. Meth. Geomech. Vol 1, Edmonton, (1982), 255-262.

[4] H.K. Kutter, "Stress Distribution in Direct Shear Test Samples," Proc. Int. Symp. Rock Fracture, Nancy, (1971) II-6.

[5] A.C. Palmer, J.R. Rice, "The Growth of Slip Surfaces in the Progressive Failure of Over Consolidated Clay", Proc. Royal Soc. London A, 332, (1973), 527-548.

[6] M.P. Cleary, J.L. Dong, "Analysis of Deformation and Failure in Geological Materials," Proc. Int. Conf. on Constitutive Laws for Engineering Materials, C.S. Desai and R.H. Gallagher eds., Tucson (1983), 341-348.

[7] J.W. Rudnicki, J.R. Rice, "Conditions for the Localization of Deformation in Pressure-Sensitive Dilatant Materials," J. Mech. Phys. Solids, 23 (1975) 371-394.

[8] J.R. Rice, A.L. Ruina, "Stability of Steady Frictional Slipping", presented at 9th US Natl. Cong. Appl. Mech., Cornell University 1982, submitted for publication in J. Appl. Mech.

[9] I. Vardoulakis, "Bifurcation Analysis of the Triaxial Test on Sand Samples", Acta Mechanica 32 (1979) 35-54.

[10] P.A. Vermeer, "A Simple Shear Band Analysis Usirg Compliances," Proc. IUTAM Symp. on Deformation and Failure of Granular Materials, P.A. Vermeer and H.J. Luger, Eds., Delft (1982) 493-499.

[11] F. Darve, "An Incrementally Non-Linear Constitutive Law of Second Order and its Applications to Localization," paper at Int. Conf. on Constitutive Laws for Engineering Materials, Tucson, Ar., Jan 10-14, 1983.

[12] ASCE State-of-the-Art Report on "Finite Element Analysis of Reinforced Concrete," ASCE Special Publ. 1982.

[13] A. Hillerborg, M. Modeer, P.E. Peterson, "Analysis of Crack Formation and Crack Growth in Concrete by Means of Fracture Mechanics and Finite Elements", Cement and Concrete Research 6 (1976) 773-782.

[14] W. Gerstle, A.R. Ingraffea, P. Gergely, "Tension Stiffening: A Fracture Mechanics Approach", presented at Int. Conf. Bond in Concrete, Paisley, Scotland, 1982.

[15] Z.P. Bazant, L. Cedolin, "Blunt Crack Band Propagation in Finite Element Analysis", J. ASCE 105, EM2 (1979) 297-316.

[16] Z.B. Bazant, B.H. Oh, "Crack Band Theory for Fracture of Concrete," submitted for publication to ASCE-EMD, 1982.

[17] J. Christensen, K. Ickert, T. Stankowski, S. Sture, K. Willam, "Numerical Modeling of Strength and Deformation Behavior in the Direct Shear Test", Proc. Int. Conf. on Constitutive Laws for Engineering Materials, C.S. Desai and R.H. Gallagher eds., Tuscon, Az. (1983) 537-544.

[18] J.A. Argyris, G. Faust, K.J. Willam, "Limit Load Analysis of Thick-Walled Concrete Structures, A Finite Element Approach to Fracture," Comp. Meth. Appl. Mech. Eng. 8 (1976) 215-243.
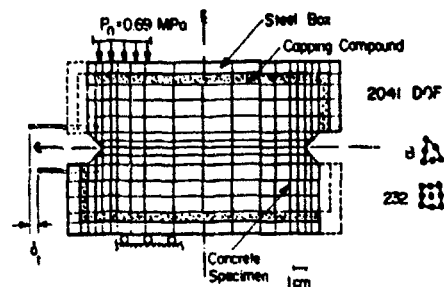
FIG. 1   IDEALIZATION OF DIRECT SHEAR BOX
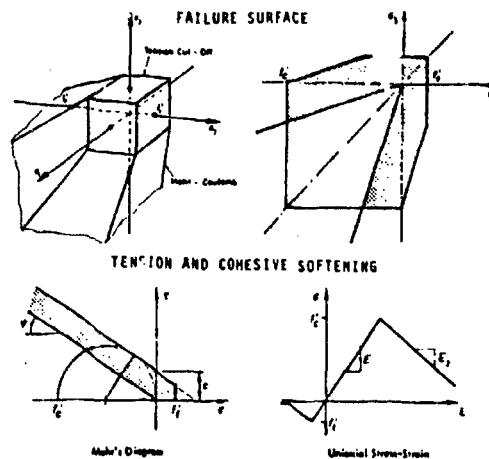
FIG. 2   SOFTENING MOHR-COULOMB MODEL WITH TENSION CUT-OFF
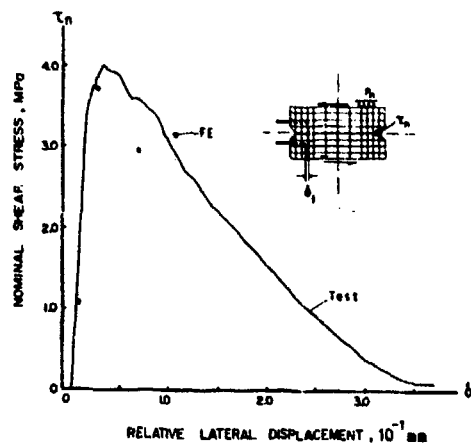
FIG. 3   SHEAR RESPONSE FOR LOAD RATIO N/T = 1/6

Peak: τ_n = 3.75 MPa

-----Tension   —— 5 MPa

Post-Peak: τ_n = 2.91 MPa

-----Tension   —— 5 MPa

FIG. 4 REDISTRIBUTION OF PRINCIPAL STRESSES

Peak: τ_n = 3.75 MPa

Post-Peak: τ_n = 2.91 MPa
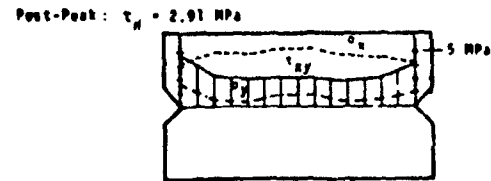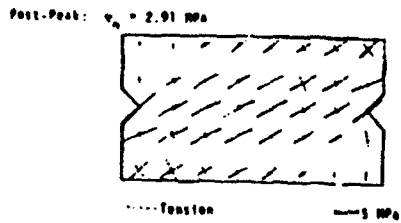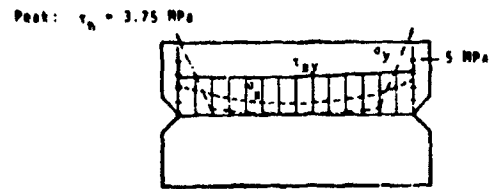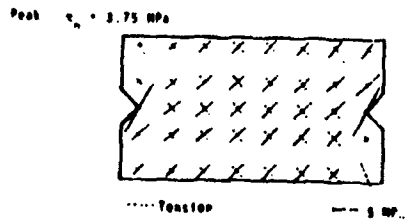
FIG. 5 STRESS DISTRIBUTION ON NOTCHED SECTION

SHEAR SPECIMEN   —— 1 in.

45

p_n = 1 ksi

LOADING FRAME   —— 1 in.

72
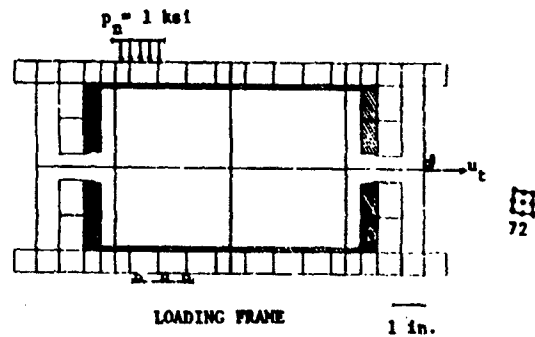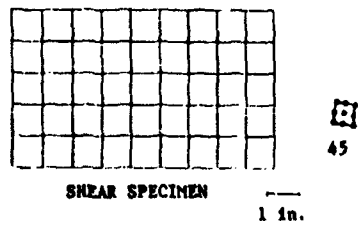
FIG. 6 FINITE ELEMENT IDEALIZATION OF SHEAR BOX
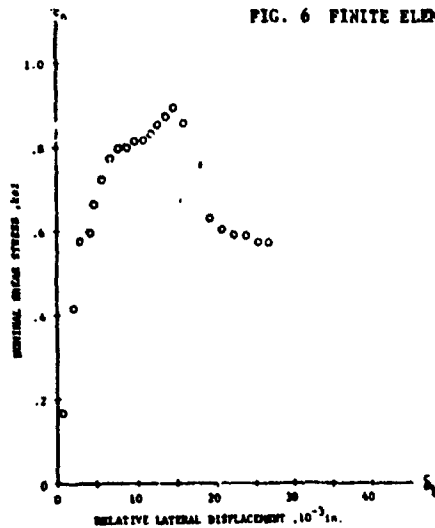
FIG. 7 SHEAR RESPONSE FOR LOAD RATIO N/T = 1/1

ξ_t = 20.9x10^{-3} in.   ⊢—⊣ = .01 in.
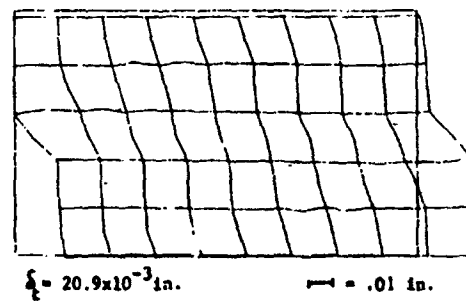
FIG. 8 DEFORMED MESH LAYOUT
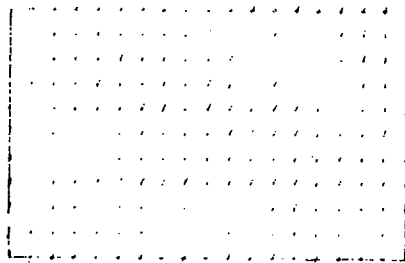
$\delta_t = 3.0 \times 10^{-3}$ in. $\longmapsto$ = 2 ksi
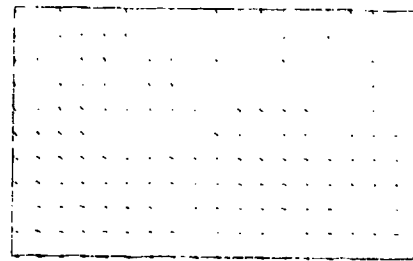
$\delta_t = 3.0 \times 10^{-3}$ in. $\longmapsto$ = .01 in.
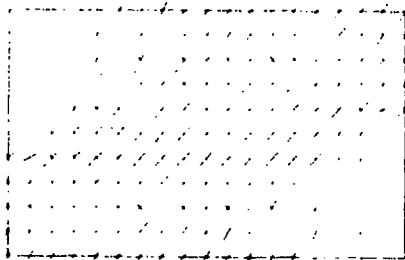
$\delta_t = 7.8 \times 10^{-3}$ in. $\longmapsto$ = 2 ksi
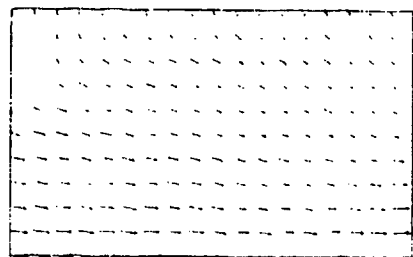
$\delta_t = 7.8 \times 10^{-3}$ in. $\longmapsto$ = .01 in.
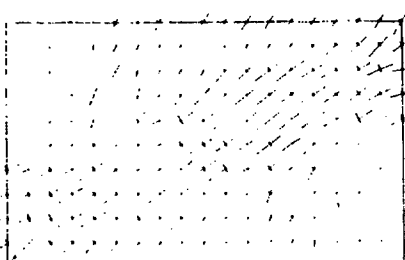
$\delta_t = 14.7 \times 10^{-3}$ in. $\longmapsto$ = 2 ksi
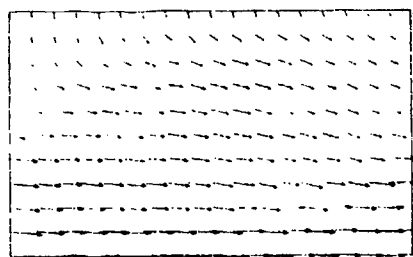
$\delta_t = 14.7 \times 10^{-3}$ in. $\longmapsto$ = .01 in.
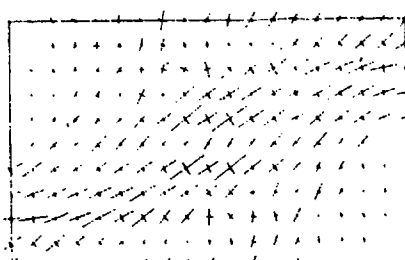
$\delta_t = 20.9 \times 10^{-3}$ in. $\longmapsto$ = 2 ksi
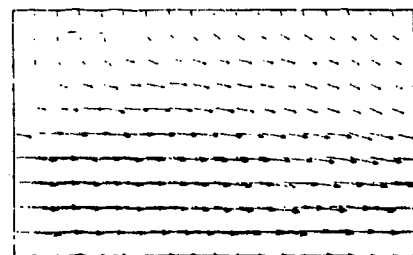
$\delta_t = 20.9 \times 10^{-3}$ in. $\longmapsto$ = .01 in.

FIG. 9 REDISTRIBUTION OF PRINCIPAL STRESSES

FIG. 10 REORIENTATION OF DISPLACEMENT VECTORS

106

SHAKING TABLE TESTS TO EVALUATE THE LIQUEFACTION
POTENTIAL OF NEAR SURFACE SATURATED SAND DEPOSITS

Shaun F. Mason
William E. Wolfe

The Ohio State University
Columbus, Ohio

ABSTRACT

The design and implementation of large-scale testing equipment for liquefaction studies of near surface saturated sands is reported. The test results can be used to determine material properties required for the development of constitutive relationships capable of describing the behavior of saturated sands during dynamic loading.

Specimens of saturated Ottawa sand 16.5 cm by 15 cm by 122 cm were tested and measurements of sample pore water pressure and accelerations taken during shaking. Results of the liquefaction tests have shown that, although qualitative agreement is achieved between the results of this program and those obtained in earlier investigations, the onset of liquefaction as measured in this study takes place at much higher stress levels than previously reported.

INTRODUCTION

The cyclic behavior of soils has attracted considerable attention and extensive research over the last two decades, due mainly to the extensive damage observed in the Alaska and Niigata earthquakes in 1964 (1), and to the more recent findings on the detrimental effects of blast-induced liquefaction (2). Liquefaction, as the term is used in this report, describes the complete loss of shearing strength of sands resulting from an increase in pore water pressure. This increase in pore water pressure is produced by vibratory loading under undrained conditions. Cyclic shear stresses induce saturated sands to compact, but compaction cannot occur under undrained conditions, and this leads to a transfer of part of the stress from the sand grains to the interstitial pore water. Continued cycling can lead to increasing pore water pressure up to the level of the initial confining pressure. The resistance to liquefaction for sands has been related to many factors but has been found to be primarily a function of the relative density of the sand, the initial effective confining pressure and the intensity of vibration.

A complete investigation of the behavior of saturated sands under dynamic loading would ultimately take the form of an analytical model based on fundamental stress-strain relationship for sand. The formulation of such an analytical model requires a basic understanding of the liquefaction phenomenon, with a clear definition of all factors involved, and an accurate representation of the important soil characteristics. However, since there is relatively little field data available on liquefaction, the material constants and coefficients which are needed are determined from laboratory tests. Therefore the accuracy and applicability of any analytical method can only be determined by evaluating how accurately the laboratory tests used to obtain the important soil properties actually simulate field conditions.

In the early stages of laboratory research work on soil liquefaction, the standard triaxial test apparatus was adapted for cyclic testing since it was and still remains the most widely used laboratory device for measuring strength. While such tests are relatively easy to perform, there are several features of the cyclic triaxial test which restrict the applicability of results obtained from tests using the device. These features include: stress concentrations introduced by the sample cap and base, redistribution of water content within samples, necking of samples on the upward stroke, variation of the intermediate principal stress, and rotation through a full 90° of the major principal stress direction during loading. An improvement over the triaxial test is the cyclic simple shear test. In this device samples are horizontally sheared in alternating directions by applying a shear stress to the top and bottom faces of the sample. The simple shear device clearly provides stress conditions in the laboratory closer to stress conditions in the field. However, it also exhibits certain undesirable features including: stress concentrations around the central zone of samples, complimentary shears not being developed along vertical faces of samples, and re-orientation of principal stress directions causing patches of high and low stress along the top and base of samples.

Since the small-scale laboratory tests for determining liquefaction potential share the problem of close-in boundaries adversely affecting sample behavior, the use of larger samples would seem to be the best way of modeling "free field" conditions in a sizeable volume of sand. Thus large-scale testing devices were introduced which could be mounted on a shaking table, and thus provide an excellent means of applying the required cyclic shear stresses to samples. Another advantage with large-scale tests is that small trans-

ducers can be placed inside samples to record the pore pressures, etc. without noticeably affecting the sample behavior. Several investigations have been performed using large samples mounted on shaking tables including programs at the University of California (3) and at the University of British Columbia (4). In the tests performed at the University of California, Seed et al. subjected samples to time varying motions on a shaking table. Samples measured 90 inches long by 42 inches wide 4 inches high, and had sloped sides to avoid contact with rigid boundaries. A steel-shot ballast was placed over the sample to add mass and simulate a further 6 inches of sand, thus achieving shear stress levels sufficient to liquefy the samples. However this ballast was enclosed in a rigid boundary on four sides, was separated from the sample by a membrane, and contained a material of much higher density than the sand. The authors believe that this ballast did not effectively simulate a thicker layer of sand, but rather acted as a "dead weight," inducing faster buildup of pore water pressures.

Thus the main aim of the work reported herein was to design a testing system which could operate without the use of a ballast, and could apply either isotropic or geostatic (k_0) confinement to samples.

TEST APPARATUS

The basic criterion followed in designing the apparatus used in the testing program described below was to make an assessment of the merits of previously used large-scale equipment, attempting to improve upon their ability to simulate free field conditions, and to incorporate newly developed miniaturized transducers. The test chamber or "box" designed by the authors is illustrated in Figure 1 below.

Figure 1: Test Chamber mounted on Shaking Table with lid removed.

Test specimens measured 112 cm (48 inches) long by 15 cm (6 inches) wide by 16.5 cm (6.5 inches) high, giving a length-to-height ratio in the order of 10:1 as proposed by Arango and Seed (5) for minimization of end effects. All parts of the test chamber were made of aluminum to minimize the

total weight. Samples were built while supported by retractable inner side walls, which after applying the confining pressure to the sample could be drawn back, enabling the specimens to deform freely under shaking in plane strain conditions. Several holes were drilled through these inner walls allowing transmittal of confining fluid to the sample (see Figure 1). Two separate fiber reinforced rubber membranes were used to seal the specimen, one flat sheet to seal the top of the sample from the lid and a long open rectangular bag-shaped membrane to seal the base and sides of the sample. Sealing the top of the sample separately from the sides enable anisotropic confinement to be applied if required. The confining fluid (water) was supplied through inlet ports in the outer side walls and lid of the chamber, and bleed lines were provided at the top of the side walls and lid to let out any trapped air. A drainage line was installed in the base of the chamber to allow consolidation of the sample under the static confining pressure. This drainage port was sealed from the confining fluid by screwing down the membrane into the chamber base using a washer. Fixing the washer around the drainage port then sealed the drainage hole in the membrane. A thin mat of highly permeable plastic material was glued to the lower membrane along the chamber base to ensure uniform sample drainage.

In order to record the behavior of the sample before and during liquefaction, instrumentation was designed to measure sample pore water pressure, sample accelerations, table accelerations, and sample displacement relative to the chamber. The table accelerations, pre-programmed using an MTS electro-hydraulic controller-actuator, were recorded by an accelerometer which was permanently mounted to the shaking table. All measurements of sample pore water pressures, displacements and accelerations were made in the middle third of the sample length, as shown in Figure 2 below.
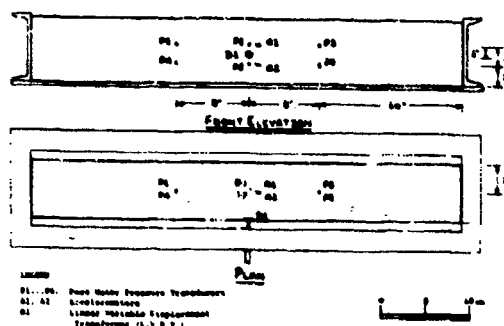

Figure 2: Relative Positioning of Instruments in Specimen

Accelerations of specimens were measured by two miniature accelerometers placed at the one and two third points of the sample height. This positioning would indicate any variation in sample acceler-

ation as a function of depth as pore pressures increased and liquefaction initiated. A linear variable displacement transformer (L.V.D.T.) was mounted on the side of the chamber to measure the displacement of the sample at mid-height relative to the chamber.

Based upon the assumption that the measurement of pore water pressure in samples is the most important record for indicating the onset of liquefaction, a total of six transducers were used to monitor the dynamic pore pressures. The transducers were placed as shown in Figure 2. The pore pressure transducers were modified so that sample pore pressures could be measured without placing the transducers in the sample. This was achieved by sealing a flexible six inch needle in the pressure sensitive port of each transducers, and then feeding the needle through the chamber wall and membrane into the center of the sample. The needles were sealed at the chamber wall and membrane using a silicon rubber sealant. Thus pore water pressures were measured in the sample at the point of a needle and transmitted to the transducers outside the chamber. All the data measured by the instruments during tests was recorded and stored digitally for analysis at a later time.

TEST PROCEDURES

A uniform Ottawa sand (Cu=1.18) was used for all tests carried out on the shaking table. The sand was saturated by boiling under a vacuum using de-aired water. The sand was then placed into the specimen chamber under water in layers at zero drop height. The miniature accelerometers were placed by hand and gently covered over with further layers, making sure not to displace the sensitive axis off the horizontal zero-reading position. Extra care had to be taken in keeping air out of the sand when placing the final layers of sand as there was only about a ½inch of water above the finished surface of the samples. A roller device which could be moved along the chamber walls was used to smooth off the sample surface at the correct height.

Having prepared the sample, the top membrane was placed over the sample surface as shown in Figure 3, and the lid bolted down to seal the sample and confining fluid. Before running a test the sample saturation was measured by increasing the confining pressure applied to the sample in steps, taking measurements of the sample pore water pressure each step. Once the confining pressure was applied, the inner walls could be drawn back to leave the sample free standing. With the desired total confining pressure applied to the sample, the required effective confining pressure was produced by allowing water to drain from the sample, reducing the sample back pressure. Total confinement in tests was limited to 5 p.s.i., with effective confining pressures ranging from 3/4 p.s.i. to about 2 p.s.i. All tests were run at a frequency of 10 Hz. with accelerations in the order of 1 g. Each sample was vibrated for 150 seconds and all the necessary data recorded. After each test the lid and top membrane were

removed to examine the liquefied samples.

Figure 3: Sealing of top membrane over sample surface

PRESENTATION OF RESULTS

The results of tests performed on three samples of saturated sand are presented. The data for each sample are given in Table 1.

Sample	D_r	B	$\bar{\sigma}_0$ psi	$\frac{\ddot{x}}{g}$	$\tau/\bar{\sigma}_0$	N_L
1	56	1.0	2.0	1.20	0.274	1530
2	61	0.99	1.5	1.24	0.378	304
3	54	1.0	0.75	1.27	0.666	85

Table 1. Sample test data

Where: D_r is the relative density in percent; B is Skempton's pore pressure parameter; $\ddot{x}$ is peak horizontal acceleration; g is acceleration due to gravity; τ is shear stress on a horizontal plane; $\bar{\sigma}_0$ is initial effective confining pressure; N_L is the number of applied stress cycles to reach liquefaction

Figure 4 presents results of the pore pressure response for Sample 2 at three different times during base excitation. It can be seen that when the pore pressure time history is superimposed on the on the sample acceleration time history, that both records are harmonic, and that accelerations are leading pore pressure. Peak pore pressures are reached at zero horizontal acceleration, i.e. when shear stresses in the sample are zero. The increase in the mean pore water pressure as a function of number of stress cycles is shown for Sample 2 in Figure 5. In this figure it can be seen that the rate of pore pressure increase is fairly uniform for the majority of the test. However, when the ratio of induced pore pressure to confining pressure reaches approximately 0.7, there is a sharp rise in the rate of pore pressure increase which leads to liquefaction in few additional cycles.
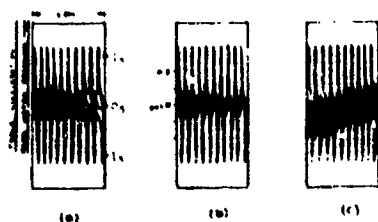
Figure 4: Samples of Pore water Pressure variation and table accelerations, Sample #2.
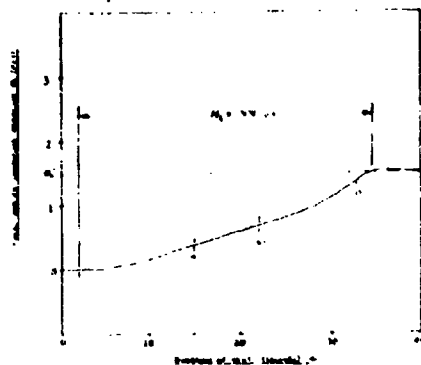
Figure 5: Pore water pressure response, Sample #2, Dr = 56%.

Neither the pore water pressure transducers nor the accelerometers located in the sample indicated any variation in the measured values as a function of location of the instrument during any of the tests conducted. The results of the program reported herein can best be compared with data obtained from other investigations by normalizing the cyclic shear stress with respect to the initial mean confining pressure. In Figure 6 are shown the results of this study compared with those presented by De Alba et. al (3).
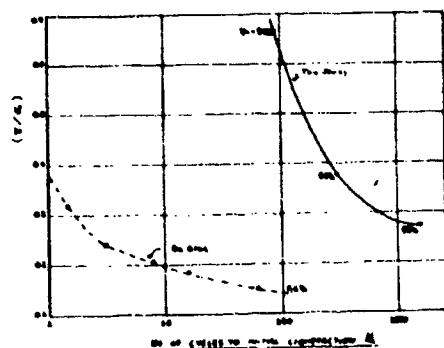
Figure 6: Comparison of Test Results with data from De Alba et. al (3).

CONCLUSIONS

A new liquefaction device has been developed at The Ohio State University for Laboratory shaking table testing of sand samples. This equipment provides control over the main factors which affect the behavior of sand under dynamic loading. The test conditions created are thought to give a closer representation of actual field conditions than has some equipment used in previous investigations. The tests described herein have provided new information on liquefaction potential. While test results agree qualitatively with previous investigations, they do indicate a higher resistance to liquefaction than that indicated by other researchers.

It is felt that the primary reason for the difference in quantitative results presented in this paper and those of De Alba et. al. is the geometry of De Alba's testing device where boundary conditions might have caused a more rapid increase in pore water pressure than would be expected under field conditions. Therefore current practice which consists of modifying the results of standard laboratory tests to make them consistent with the "more realistic" large sample shaking table tests may result in underestimating resistance to failure by liquefaction. A comparison should be made with the liquefaction behavior of sands predicted by analytical methods under similar conditions to assess the applicability of the results obtained in tests. Future tests should include more locations where pore pressures are measured in order to better determine whether or not pore pressure increase actually is uniform throughout the sample as these tests indicate. It is further recommended that additional tests be performed on a variety of sample types under both isotropic and anisotropic stress conditions in order to substantiate the results of the initial tests presented herein.

REFERENCES

1. SEED, H. B. and I. M. IDRISS (1967), "Analysis of Soil Liquefaction: Niigata Earthquake." Journal of the Soil Mechanics and Foundations Division, ASCE, Vol. 93, No. SM3, pp. 83-108.

2. CHARLIE, W. A., MANSOURI, T. A., and RIES, E. R. (1981), "Predicting Liquefaction Induced by Buried Charges." Proc. Xth International Conference on Soil Mechanics and Foundations Engineering, Stockholm, Sweden, June 1981, Vol. 1, pp. 77-80.

3. DeALBA, P., C. K. CHAN and H. B. SEED (1976), "Determination of Soil Liquefaction Characteristics by Large-Scale Laboratory Tests." Report to the U.S. Nuclear Regulatory Commission, NUREG-0027, September.

4. FINN, W. D. L., J. J. EMERY and Y. P. GUPTA (1971), "Liquefaction of Large Samples of Saturated Sand on a Shaking Table." Proceedings of the 1st Canadian Conference on Earthquake Engineering, Vancouver, University of British Columbia, May.

5. ARANGO, I. and H. B. SEED (1974), "Seismic Stability and Deformation of Clay Slopes." Journal of the Geotechnical Engineering Division, ASCE, Vol. 100, No. GT2, February.

6. SEED, H. B., P. P. MARTIN and J. LYSMER (1976), "Pore-Water Pressure Changes during Soil Liquefaction." Journal of the Geotechnical Engineering Division, ASCE, Vol. 102, No. GT4, April.

7. PEACOCK, W. H. and H. B. SEED (1968), "Sand Liquefaction under Cyclic Loading Simple Shear Conditions." Journal of the Soil Mechanics and Foundations Division, ASCE, Vol. 94, No. SM3, May.

111
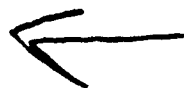
SOIL CHARACTERIZATION FOR NON DESTRUCTIVE IN SITU TESTING

K. Arulanandan
Professor of Civil Engineering, University of California, Davis, CA   95616

A. Anandarajah
Asst. Professor of Civil Engineering, South Dakota School of Mines and Technology, Rapid City, SD   57701

N.J. Meegoda
Graduate Student University of California, Davis, CA   95616

THIS PAPER WITHDRAWN IMMEDIATELY PRIOR TO PUBLICATION, DUE TO CLEARANCE DIFFICULTIES.

ANALYSIS OF BURIED REINFORCED CONCRETE ARCH STRUCTURES UNDER DYNAMIC LOADS

Harry E. Auld and William C. Dass

Applied Research Associates, Inc.
Albuquerque, New Mexico

ABSTRACT

A damped single degree-of-freedom model was developed to represent the gross dynamic behavior of shallow buried reinforced concrete arches subjected to specified nonuniform pressure distributions. Structural parameters were developed for a generic structure based upon available information in the literature and first principal calculations. Values of maximum crown deflection, calculated from numerical integration of the differential equation of motion, were compared with similar results from field experiments. Results utilizing structural parameters selected on this basis of the recommendations in this study provide the best agreement.

INTRODUCTION

The objective of this study was to develop a single degree-of-freedom model capable of representing the gross dynamic behavior of shallow buried reinforced concrete semi-circular arches subjected to specified input loadings resulting from the application of superseismic airblast loadings at the ground surface. Emphasis was placed on large deformation behavior approaching collapse. The soil was assumed to be dry and cohesionless.

BASIC THEORY

In order to analyze a shallow buried structure, it is necessary to know the input load to the structure. The input load is not simply a function of the overpressure applied at the ground surface. It is also related to the flexibility of the structure, the characteristics of the soil type, and perhaps the depth of burial. Determination of the input load for an arbitrary loading function at the ground surface is beyond the scope of this study.

Crawford, et al. (1974) suggest that the general form of the nonuniform pressure distribution shown in Figure 1 is representative of a large majority of the actual loads encountered in the analysis of hardened buried cylinders. Their analysis for cylinders is directly applicable to fixed semi-circular arches.

$P_\theta = q + \bar{p} \cos 2\theta$

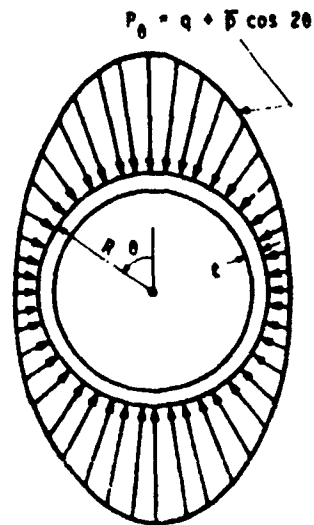Figure 1. Circular Ring Subjected to Nonuniform External Pressure

They give the following results for the internal thrust (N), shear (V), and bending moment (M) resulting from the pressure distribution shown in Figure 1

$$N_\theta = - qR + \frac{\bar{p}R}{3} \cos 2\theta \tag{1}$$

$$V_\theta = - \frac{2}{3} \bar{p} \sin 2\theta \tag{2}$$

$$M_\theta = \frac{\bar{p}R^2}{3} \cos 2\theta \tag{3}$$

where q is the magnitude of the uniform component and $\bar{p}$ is the maximum amplitude of the nonuniform component of applied external pressure. In this formulation the total nonuniform pressure distribution, P_θ, is given by

$$P_\theta = q + \bar{p} \cos 2\theta \qquad (4)$$

Crawford, et al. (1974) also indicate that the elastic deflection of a perfectly round ring subjected to the nonuniform pressure distribution of Figure 1 can be approximated by

$$\delta_\theta = \frac{\bar{p}R^4}{9ET} \cos 2\theta \qquad (5)$$

SINGLE DEGREE-OF-FREEDOM MODEL

The maximum crown deflection relative to the support motion, δ_c, is chosen as the single parameter representative of the general arch response. The dynamic nonuniform, but symmetric, pressure distribution specified by Equation 4 is assumed to obtain and the first symmetric flexural mode shown in Figure 2 is assumed to govern.

Figure 2.   Theoretical First Symmetric Flexural Mode

A viscously damped single degree-of-freedom system can be utilized to represent the specified conditions. The response of this system is defined by the following differential equation of motion:

$$M \ddot{\delta}_c + 2\beta \sqrt{kM} \dot{\delta}_c + R(\delta_c) = \bar{p}(t) \qquad (6)$$

where M is the effective mass, β is the damping ratio or fraction of critical damping, k is the stiffness and $R(\delta_c)$ is a generalized resistance function.

Solutions can be readily obtained for Equation 6 through the use of standard numerical integration techniques if the system parameters and the time varying maximum amplitude of the

nonuniform component of the applied external pressure are known. For the purposes of this study an assumed $\bar{p}(t)$ will be utilized. This function can be obtained experimentally from interface pressure measurements in a dynamic structural test. Equation 4 indicates that $P = q + \bar{p}$ at the crown and $P = q$ at $\theta = \pm 45$ degrees. Thus, interface pressure measurements at these locations completely define the two parameters of the assumed nonuniform pressure distribution function.

STRUCTURAL PARAMETERS

The structural parameters from Equation 6 which require specification are β, M, $R(\delta_c)$, and k. These parameters are developed for a generic semi-circular reinforced concrete arch with the haunches rigidly connected to the floor. The assumed dimensions and material properties are as follows:

Radius, R = 47.2 in
Haunch thickness, t = 6.3 in
Depth of cover at the crown = 23.6 in
Dense dry cohesionless soil
Concrete strength, f'_c = 4500 lb/in²
Reinforcement steel yield strength, f_y = 60,00 lb/in²
Steel percentage, p = 1.45, each face
Depth of steel cover = 1.165 in, each face
Sufficient shear reinforcement is provided to preclude shear failure.

Higgins, et al. (1981) presents results from extensive dynamic soil-structure interaction experiments on test structures resembling scale models of nuclear containment vessels. The reinforced concrete test structures were embedded in dry cohesionless soil from 25 to 200 percent of their height and were subjected to explosively induced ground motions which simulate the strong earthquake excitation of full-scale systems (structural accelerations in the 1 to 10 g range). They observed that damping was uniformly high, typically 10 to 20 percent of critical damping, at the high displacements corresponding to strong motion earthquake response. They further observed that damping typically increased with response level. Based upon this information, the large displacement interaction associated with shallow buried arches loaded close to failure should be highly dissipative with a damping ratio of 20 percent or more.

The effective mass of the shallow buried arch system can be developed utilizing energy considerations. Crawford, et al. (1974) indicate that a single load-mass transformation factor can be utilized to convert a distributed mass system into an undamped single degree-of-freedom model. They indicate that the value of the load-mass transformation factor ranges from 0.66 for a uniformly distributed load to 0.33 for a single concentrated midpoint load on a beam of uniform mass loaded plastically. The system under consideration consists of a uniform circular

beam, with nonuniform depth of soil cover and spatially varying load. The amount of soil which should be included in the analysis is not known, but the full amount is commonly utilized for the analysis of shallow buried structures. A detailed analysis is not considered appropriate because of the large uncertainties associated with the formulation. A load-mass transformation factor of 0.5 is probably adequate for our purposes. Utilizing this value, an equivalent mass equal to 0.0045 lb-s^2/in^3 is obtained for the combined mass of the reinforced concrete section and the average value of the soil cover for an assumed straight beam extending from θ equal $\pm$ 45 degrees.

The resistance function can be derived from one of two possible approaches: evaluation of available experimental data or fundamental analysis of the reinforced concrete cross-section. Axial loads contribute significantly to the maximum resistance and beam-column theory is appropriate for calculating this value.

Meyer and Flathau (1967) present experimental data for the response of unreinforced concrete fixed semi-circular arches buried in dry sand. Their data generally support the assumptions made in this study with regard to load distribution and general arch response. Figure 3 presents measured load versus crown deflection curves for static tests on arches with R/t values of 3, 6, and 12.
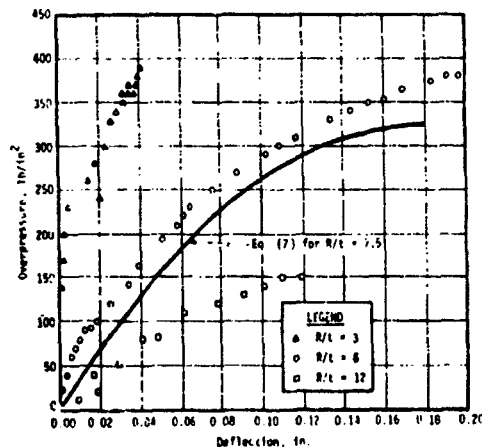
It should be noted that the load in this figure is the uniformly applied surface pressure rather than the maximum amplitude of the nonuniform component of the external pressure applied to the arch. It appears that the surface load versus crown deflection curves are generally parabolic in shape and that they are a linear function of R/t. The surface load versus crown deflection curve developed for R/t equals 7.5 (the value of the generic arch under consideration) is given by

$$F = -10,000 \; (\delta_c - 0.18)^2 + 324, \; \text{lb/in}^2$$

$$\text{for} \quad 0 \leq \delta_c \leq 0.18 \; \text{in} \qquad (7)$$

Assuming that the uncracked moment of inertia is applicable because of the presence of the large axial thrust and that Equation 5 remains applicable at large deflections, $\bar{p}$ is found to be equal to 26 lb/in^2 for the generic section at a crown deflection of 0.18 in. This value corresponds to a surface overpressure of 324 lb/in^2. Because the response is well outside the elastic range the calculated value of $\bar{p}$ may be low by a factor of 2 or more.

Utilizing beam-column theory for reinforced concrete sections, see any standard text, the ultimate bending moment and thrust at the balance point for the generic section are found to be approximately 35,400 in lb/in and 11,800 lb/in, respectively, when the static strengths of both the steel and concrete are increased by approximately 20 percent to account for the influence of dynamic loading. Assuming that the section will try to respond at the balance point and that Equations 1, 2, and 4 are applicable, values of $\bar{p}$ equal to 48 lb/in^2, q equal to 265 lb/in^2, and P equal to 313 lb/in^2 are obtained.

Anderson, et. al. (1966) suggest that the crown deflection at ultimate load for a concrete failure strain of 0.003 can be calculated from

$$(\delta_c)_{ult} = \frac{R(f_y/E_s)}{2 \left\{ 1 - (\frac{87,000}{87,000 + f_y}) \frac{(3\frac{q}{p} - 1)}{(3\frac{q}{p} + 1)} \right\}} \qquad (8)$$

Utilizing the above results for $\bar{p}$ and q, a value of 0.12 in is calculated from Equation 8 for the generic arch. The calculated values of $(\delta_c)_{ult}$ and P are seen to be on the same order as the previously presented experimental data of 0.18 in and 324 lb/in^2, respectively. Utilization of an increased values of the concrete failure strain would further improve the agreement.

Figure 3. Static Surface Load Versus Crown Deflection After Meyer and Flathau (1967).

Park and Pauly (1975) recommend utilizing an idealized elastic-plastic approximation to the moment-curvature curve for a reinforced concrete section. Moment-curvature can be converted to load-deflection through the use of Equations 3 and 8. A proposed idealized elastic-plastic approximation to the load-deflection curve is shown in Figure 4.
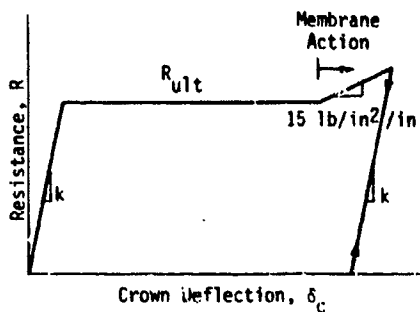
Figure 4. Idealized Elasto-Plastic Approximation to Resistance Function

R_{ult} and k can be arbitrarily defined. The slope of 15 $lb/in^2/in$ is included to represent membrane action which comes into play at very large displacements. The load-unload slope is arbitrarily defined to agree with the initial slope.

The following values of the structural parameters have been selected to best represent the generic structure under consideration:

β = 20 percent

M = 0.0045 $lb-s^2/in^3$

R_{ult} = 46 lb/in^2

k = 511 lb/in^2

SENSITIVITY STUDY

A sensitivity study was run for Equation 6 varying three of the four structural parameters, i.e., β, R_{ult}, and M. Figure 5 presents a typical curve for the time variation of the maximum amplitude of the nonuniform component of external pressure, $\bar{p}(t)$.
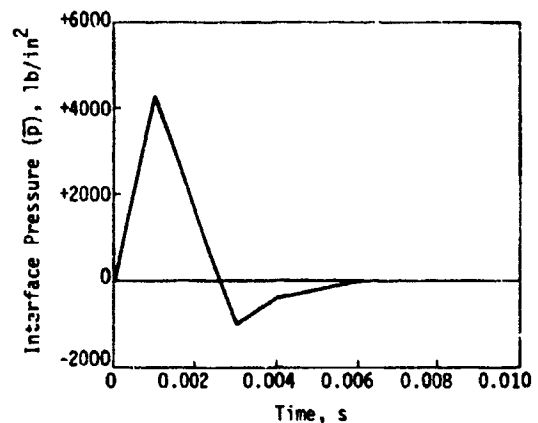
Figure 5. Typical $\bar{p}(t)$ Curve

This loading function was utilized for all of the calculations in the sensitivity analysis. Haltiwanger and Hall (1979) have shown in a similar study of a shallow buried box structure that the solution of Equation 6 is most sensitive to the assumed loading function. Therefore, this study does not vary the most important, and possibly the least known, of the various parameters involved.

Table 1 presents the results of the sensitivity analysis calculations.

TABLE 1
SENSITIVITY STUDY RESULTS

Calculation Number	R_{ult} lb/in^2	M $lb-s^2/in^3$	β %	k lb/in^2	δ_c in
1	46	0.0014	0	511	26.8
2	46	0.0014	10	511	13.3
3	46	0.0014	20	511	8.7
4	46	0.0014	30	511	6.4
5	46	0.0021	20	511	6.9
6	46	0.0045	20	511	4.6
7	92	0.0014	20	511	8.1
8	92	0.0021	20	511	6.4

These calculations indicate that the crown deflection is relatively insensitive to the value selected for R_{ult}. The response becomes less sensitive to the value of β in the 20 to 30 percent range and is most sensitive to the value selected for M.

Betz (1983) has calculated the crown deflections for several generic arches which were

subjected to a loading function similar to that
shown in Figure 5. These results indicate that
the relative crown deflections were on the order
of 5 in or less. It is interesting to note that
calculation number 6 utilizing the recommended
values of the structural parameters gives the
best agreement with this result.

REFERENCES

1. Anderson, R.H., et al., Structural Behavior
    of Ring Sections Under Nonuniform External
    Pressure, AFWL-TR-65-145, Air Force Weapons
    Laboratory, Kirtland AFB, New Mexico,
    March 1966.

2. Betz, J.F., private communication, NTES, Air
    Force Weapons Laboratory, 1983.

3. Crawford, R.E., et al., The Air Force Manual
    For Design and Analysis of Hardened
    Structures, AFWL-TR-74-102, Air Force
    Weapons Laboratory, Kirtland Air Force Base,
    New Mexico, October 1974.

4. Haltiwanger, J.D. and Hall, W.J., ASCE
    Convention, Atlanta, 1979.

5. Higgins, C.J., et al., SIMQUAKE 1 — An
    Explosive Test Series Designed to Simulate
    the Effects of Earthquake-Like Motions on
    Nuclear Power Plant Models, Volume 1,
    Summary Report to Electric Power Research
    Institute, February 1981.

6. Meyer, G.D., and Flathau, W.J., Static and
    Dynamic Laboratory Tests of Unreinforced
    Concrete Fixed-End Arches Buried in Dry
    Sand, TR-1-758, U.S. Army Engineer Waterways
    Experiment Station, Vicksburg, Mississippi,
    February 1967.

7. Park, R., and Paulay, T., Reinforced
    Concrete Structures, John Wiley and Sons,
    1975.

ACKNOWLEDGEMENTS

THE USE OF COMPENDIA, DESIGN MANUALS, AND REFERENCE TEXTS IN PREDICTION OF NONNUCLEAR WEAPONS EFFECTS

W. F. Baker

Southwest Research Institute

ABSTRACT

The literature on nonnuclear weapons effects dates from the 16th century, is extensive, is widely scattered, and includes many classified references. This diffusion presents problems to both neophytes and experts in this field -- the neophyte can be overwhelmed by the volume of the literature, and unable to choose between conflicting references or prediction methods; while the "expert" may be expert in only a narrow specialty in weapons effects, and not truly conversant with other specialties. So, a limited library of broad references on the symposium topic can be very useful.

The broad references include compendia, design manuals and general reference texts. They give rather broad coverage, but the topics covered, depth of coverage, and accuracy and depth of reference to the literature vary considerably between the references. The paper will discuss the coverage of each cited general reference, will note the depth or lack of depth of literature reference, and will also give a brief evaluation of the reference.

INTRODUCTION

Nonnuclear weapons effects include at least the effects on a wide variety of targets of: explosions and shock waves in air, water and the ground; impacts of penetrating projectiles and fragments; penetration by high-speed jets; incendiaries; smokes; and a variety of chemical agents. The spectrum of past, present and future weapons is very broad. The spectrum of "targets" is also very broad. Weaponry is an ancient discipline, and is also highly nationalistic. All of these factors combine to render the literature on the symposium topic voluminous, secretive and very diffuse.

If you are a neophyte to weapons effects, you can easily be overwhelmed by the extensive literature, and inconvenienced by the security classification of some of it. Even if you have been working in this field for many years, you may be rather unaware of some types of weapons effects, and are also inconvenienced by security restrictions.

We have found over the years that your work can be somewhat eased by using a limited basic library of unclassified references which contain useful technical discussions, data bases and/or analysis and prediction methods for a variety of weapons effects. Some of these broad references are obvious and well-known; others are not. We have found

some to be much more useful than others. Some have been quickly outdated, while others retain remarkable usefulness after many years.

This paper presents the author's suggestions for a limited library of broad references which can be useful in describing and evaluating nonnuclear weapons effects. Only unclassified references are included in the list. All were at one time easy for anyone to acquire, but some may now be quite difficult to get. We review in this paper only references in English.

The broad references are divided into three categories, i.e., compendia, design manuals and reference texts. They are discussed in that order. For each reference, we identify it, and then briefly discuss those contents relating to weapons effects. Depth of literature coverage is noted, as are strengths or shortcomings. Usually, the discussion is the author's, but in some instances, reviews by others are substituted. When this is done, the review is in quotes, and the name of the reviewer is included.

The paper includes a brief closure, which includes some discussion on availability of these references.

DISCUSSION OF COMPENDIA

Because compendia usually consist of groups of papers or chapters by different authors, the adequacy of coverage of specific topics tends to vary considerably from chapter to chapter. But, there are some exceptions to this rule in our list, as noted.

White, M. T. (Editor) (1946), *Effects of Impacts and Explosions, Summary Technical Report of Division 2, National Defense Research Council*, Volume 1, Washington, D.C., AD 221-586. (Ref. 1)

Although this reference is rather old, it is a thorough review of U.S. research studies during World War II on explosions in air, water, and earth; ballistic impact effects on steel, concrete, and soil; gun muzzle blast; dynamic materials properties; protection against various weapons effects; and target analysis and weapon selection. Some of the Weapon Data Sheets included in the compendium, particularly those on penetration of projectiles into various media, are useful. The reference list is extensive.

The discussions and descriptions in this work are very clear and readable, and some of the compiled and scaled test data are still the most definitive available. Unlike many other compendia, treatment of all topics, by the various authors, is excellent and thorough. This is a must for your reference shelf.

Annals of the New York Academy of Sciences (1968), Volume 152, Article 1, "Prevention of and Protection Against Accidental Explosion of Munitions, Fuels and Other Hazardous Mixtures," October 28, 1968. (Ref. 2)

This is a very unusual source giving information on accidental explosions and their effects, but this one volume of the Annals contains a wealth of useful information in papers contributed by many researchers and safety engineers from the U.S. and Europe. The quality of the individual papers ranges from excellent to fair. Most of them reference the literature well, but a few omit a number of key references to prior work on the paper topic. The sections most applicable for predicting weapons effects are Part II. Personnel Sensitivity; Part III. Sensitivity of Explosive Materials, and Part IV. Explosive Effects.

Swisdak, M. M., Jr., "Explosion Effects and Properties: Part I - Explosion Effects in Air," NSWC/WOL/TR 75-116, Naval Surface Weapons Center, White Oak, Silver Spring, Maryland, Oct 1975, AD A018 544. (Ref. 3)

This is an excellent compendium giving properties of air blast waves from nonnuclear weapons. The emphasis is on presentation of graphs and equations, and on example problems for their use. Included also are data on air blast from shallow underwater and underground explosions, and cratering for buried explosions. The compendium is based primarily on work in U.S. Navy laboratories, and this is well referenced. A weakness is that the extensive related work by U. S. Army, U. S. Air Force and foreign sources is largely ignored.

Swisdak, M. M., Jr., "Explosion Effects and Properties: Part II - Explosion Effects in Water," NSWC/WOL/TR 76-116, Naval Surface Weapons Center, White Oak, Silver Spring, Maryland, Feb 1978, AD A056694. (Ref. 4)

This is the counterpart to the preceding compendium, but for underwater explosion effects. The type of coverage is similar, with coverage of similitude relations, underwater shock wave parameters for shallow and deep explosions, bubble pulse characteristics, underwater shock from line charges, and related topics. This compendium should be considered as a supplement to Cole's book, Underwater Explosions, which will be discussed later. The literature is well referenced.

"Behavior and Utilization of Explosives in Engineering Design and Biochemical Principles Applied to Chemical Medicine," Proceedings of the 12th Annual Symposium American Society of Mechanical Engineers, New Mexico Section, March 1972. (Ref. 5)

The first part of this compendium includes a number of well-written papers on detonation of explosives and their utilization. Its value lies in good descriptions of explosive processes, how explosives accelerate materials, and how materials respond to intense explosive loading. Most of the papers are excellent, and well-referenced.

Doering, W. and Burkhardt, G., "Contributions to the Theory of Detonation," Translation from the German as Technical Report No. F-TS-1227-IA (GDAM A9-T-4G), Headquarters, Air Material Command, Wright-Patterson AFB, Ohio, May 1949, AD 78873. (Ref. 6)

Much of the German work during World War II on detonation of explosives, and shock transmission through air, water, and at interfaces between media is included. The treatment is very lucid, even in translation. Reference is, of course, almost exclusively to German work. One of its most useful aspects is the presentation of equations for predicting shock strengths on reflection from or transmission between different media.

DISCUSSION OF DESIGN MANUALS

There are available a number of manuals for prediction of explosion and impact loads on structures, and design of structures to resist such loads. Most are intended for use by structural engineers, and they concentrate heavily on presentation of design equations and graphs. A number of weapons effects can be predicted from information in most of the manuals.

U. S. Army Material Command, Engineering Design Handbook: Principles of Explosive Behavior, AMC Pamphlet AMCP 706-180, 1972. (Ref. 7)

This is one in an extensive series of Army design manuals. It includes very thorough, well-written, and well-referenced material on the detonation physics of explosives. It will not allow you to numerically predict many weapons effects, but it should give you a good understanding of the physical processes occurring when explosives detonate.*

"Fundamentals of Protection Design (Non-Nuclear)," Department of the Army Technical Manual, TM 5-855-1, Department of the Army, July 1965. (Ref. 8)

This was one of the first design manuals for protective structures. It was based on work by MIT and University of Illinois structural engineers, and includes some information useful in estimating weapons effects. Like some other manuals, a weakness is inclusion of only a bibliography, and not specific references. It has now been superceded by later manuals.

---

*The Army Engineering Handbook Series includes several other manuals which are very useful in predicting weapons effects, but they are classified and so do not qualify for our list.

"Suppressive Shields Structural Design and Analysis Handbook," U.S. Army Corps of Engineers, Huntsville Division, HNDM-1110-1-2, 1977. (Ref. 9)

Suppressive shields are structures (usually vented) designed to arrest fragments and attenuate blast and fireball effects for accidental explosions in munitions plants. This manual includes a number of topics which can be quite useful in estimating weapons effects, including prediction methods and data for free-field blast waves, blast loading of structures, internal explosion blast and gas pressure loads, and fragment impact on structures. Presentation is clear, and sources are well referenced.

Crawford, Robert E., Higgins, Cornelius, J., Bultmann, H., "The Air Force Manual for Design and Analysis of Hardened Structures," Report No. AFWL-TR-74-102, Contract No. F29601-74-C-0018, Civil Nuclear Systems Corporation, Albuquerque, New Mexico, October 1974, Second Printing October 1976. (Ref. 10)

This manual is intended for design to resist nuclear weapons effects, but it still contains material useful in estimating some nonnuclear effects. Th useful parts are those on air blast phenomena, and ground shock and cratering. The treatment of structural response and damage largely repeats that in Ref. 9 and 20. Referencing is extensive and good.

Structures to Resist the Effects of Accidental Explosions, Department of the Army Technical Manual TM 5-1300, Department of the Navy Publication NAVFAC P-397, Department of the Air Force Manual AFM 88-22, Department of the Army, the Navy, and the Air Force, June 1969. (Ref. 11)

This design manual is the "Bible" for most structural engineers involved in blast-resistant design in reinforced concrete. Its strengths are in presentation of detailed procedures for estimating blast loading for internal explosions, failure modes for reinforced concrete, structural elements, and design of reinforcing. Basic structural design procedures are identical to those presented earlier by MIT authors.

There are data and prediction methods for estimating free-field blast wave properties, internal and external blast loads on structure, fragment impact effects on structures, and blast effects on humans. Descriptions of blast loading and its effects are quite good. A weakness is complete lack of referencing, although there is a reasonably complete bibliography.

This manual is now being revised and updated. Unfortunately, the weaknesses in lack of referencing will not be corrected.

Baker, W. E., Westine, P. S., Kulesz, J. J., Wilbeck, J. S., and Cox, P. A., "A Manual for the Prediction of Blast and Fragment Loading on Structures," (1980), DOE/TIC-11268, U.S. Dept. of Energy, Amarillo, TX, Nov 1980. (Ref. 12)

This voluminous work is directed toward structural engineers who design blast-resistant structures for accidental explosions involving high explosives. Many graphs and equations, and many example problems are included. Topics covered are air blast from single and multiple high explosive sources, both bare and encased; blast loading of structures for internal and external explosions; cratering and ground shock for explosions in earth-covered structures; and a very detailed treatment of fragmentation and impact effects of fragments. General information is given on dynamic properties of construction materials and on methods for dynamic structural design. Referencing is thorough, and an extensive bibliography is also included.

DISCUSSION OF REFERENCE TEXTS

There are a number of reference texts which provide very useful information relating to nonnuclear weapons effects. But, very few give direct prediction methods for such effects. It is suggested that the reader study them primarily to try to understand the physics of the complex processes occurring, for information on computational and experimental methods, and as general background reading.

Zel'dovich, Ya. B., and Razier, Yu. P., Physics of Shock Waves and High-Temperature Hydrodynamic Phenomena, Vol. I, Academic Press, N.Y., 1966. (Ref. 13)

Zel'dovich, Ya. B., and Razier, Yu. P., Physics of Shock Waves and High-Temperature Hydrodynamic Phenomena, Vol. II, Academic Press, N.Y., 1967. (Ref. 14)

This two-volume work is a translation from the Russian. If you want to make a detailed study of the title topic, it is must reading. The treatment is very thorough, but also very readable. Reference to related work world-wide is thorough.

Johansson, C. H. and Persson, P. A., Detonics of High Explosives, Academic Press, London and New York, 1970. (Ref. 15)

"This is a thorough treatment of almost everything that is known about liquid and solid explosives. It should be the first source for anything you want to know. It also contains many excellent modern references." (W. C. Davis, in Ref. 5)

Cook, M. A., The Science of High Explosives, Reinhold, NY, 1958. (Ref. 16)

"Here we have many useful data, lots of phenomenology, and interesting pictures. Unfortunately, there is also a great deal of interpretation which is not accepted by other workers in the field, and a newcomer to the business has a hard time deciding what to believe and what to reject. My advice is to use it as a very valuable source of data, but to be careful about accepting the discussion and conclusions." (W. C. Davis, in Ref. 5)

Kinney, G. F. (1962), Explosive Shocks in Air, MacMillan, New York, New York. (Ref. 17)

For some years, this was one of the few readily available references on air blast waves. It evolved from a course taught by its author of the U. S. Naval Postgraduate School. But, the material is relatively superficial and does not at all reflect the breadth of experimental and analytical work which had been done before it was published. Literature citations are very limited. It has been supplanted by later and more comprehensive works.

Baker, W. E. (1973), *Explosions in Air*, University of Texas Press, Austin, Texas. (Ref. 18)

"Although this book will not satisfy all the requirements of either the casual, neophyte, or experienced investigator, it provides by far the most comprehensive treatment of the subject available in a single volume, and as such it offers something worthwhile to all. A good balance between theoretical and experimental approaches is maintained throughout the book with adequate mention of theoretical-experimental relationships and their importance to the understanding of the blast phenomena or solving practical explosion problems."

"Baker does a good job of describing many types of instrumentation in current use for laboratory or field applications. Mechanical, electromechanical, and piezoelectric gages are discussed. Mechanical, CRO, magnetic tape, and photographic systems and techniques for recording transducer output or blast phenomena directly are given adequate treatment."

"In light of the rapid changes in instrumentation available for researchers' use, it would have been well to devote a page or two to the requirements of a blast-measuring system. A curve showing frequency response requirements versus charge weight (or energy, the term Baker is prone to use) would have been quite helpful."

"The relatively large bibliography is a fine feature; the serious investigator is given guidance to sources in greater depth."

"All in all, Baker's Explosions in Air is a welcomed and noteworthy addition to a sparsely documented field." (J. F. Petes, book review)

Henrych, J. (1979), "The Dynamics of Explosion and Its Use," Amsterdam, Elsevier Scientific Publishing. (Ref. 19)

This book is a very useful reference work, but flawed. In some respects, it is encyclopedic, with coverage of many aspects of explosions of chemical high explosives and the effects of such explosions in air, water, and earth. Some treatment of nuclear explosions is also included. But, like an encyclopedia, coverage of some topics is shallow and does not reflect the depth of material available on these topics.

Topics which are well covered include the stress wave theory, detonations and close-in effects of explosions in high explosives, explosions in soils, underground blasting and cratering,

and response of elastic and elastoplastic structural elements to blast loading. Coverage of elastic vibrations of structures is particularly exhaustive. Topics covered in a more superficial manner include explosions in air, explosions in water, use of explosives in demolition and seismic effects of explosions. Scaling laws for explosions in air or water, which are essential to these topics, are barely mentioned.

As is probably natural for a book written in Czechoslovakia, references to work in eastern Europe and Russia are extensive, and the inclusion of such references is very valuable for western readers. But, many readily available references from the United States and other western world sources are lacking, and many of the references which are listed are now dated and superceded by later work. In general, there are too few references to work more recent than 1969.

The writing is clear and the exposition easy to follow, but in some instances, too much mathematical detail is included. We would have preferred to see less mathematical development and more experimental data verifying some of the theory.

In summary, this is a voluminous book containing much useful information on detonative explosions of chemical explosives, effects of these explosions, and a number of peripheral topics. But the reader is cautioned that the coverage is quite incomplete on some topics, and perhaps too detailed on other topics. References to good recent works in this field are also omitted.

Norris, C. H., Hansen, R. J., Holley, M. J., Biggs, J. M., Namyet, S. and Minami, J. V., *Structural Design for Dynamic Loads*, McGraw-Hill Book Co., NY, 1959. (Ref. 20)

This book first appeared as a set of course notes for a short course taught by MIT staff. Procedures carry over directly from an earlier U. S. Army Corps of Engineers manual. As with the Army manual, these methods reappear in many later manuals. It is an excellent introductory text for response of dynamically-loaded structures.

Biggs, J. M. (1964), *Introduction to Structural Dynamics*, McGraw-Hill Book Company, New York, New York. (Ref. 21)

This is an excellent introductory text for any engineer engaged in dynamic structural design. Biggs is one of the authors of the earlier Army Corps of Engineers manual, and Norris, et al. (Ref. 20). This book draws heavily on the earlier work, but adds considerable material. Presentation is very clear and understandable.

Baker, W. E., Cox, P. A., Westine, P. S., Kulesz, J. J., and Strehlow, R. A., *Explosion Hazards and Evaluation*, Elsevier Scientific Publishing Co., Amsterdam, 1983. (Ref. 22)

This new book discusses a variety of types of explosion sources, and presents methods for estimating air blast loads on and within structures,

some classes of fragment formation and impact effects, simplified and more complex methods of predicting structural response and damage from blast loading, and thermal radiation effects from nonnuclear explosions. Referencing is thorough, and there is an extensive bibliography. A number of example problems illustrate the prediction methods.

Goldsmith, W., Impact, The Theory and Behavior of Colliding Solids, Edward Arnold, Ltd, London, 1960. (Ref. 23)

This text gives very thorough coverage of the title topic, both theory and experiment. If you have any interest in the elastic and plastic processes involved when solids collide, you should have this book on your shelf (or desk). The references to the literature are as complete as you could hope to find. [In fact, the earliest reference starts, "Galilei, G.... (1638)." It seems unlikely that Professor Goldsmith missed any significant references to this topic between 1638 and 1960!]

Zukas, J. A., Nicholas, T., Swift, H. F., Greszczuk, L. B., and Curran, D. R., Impact Dynamics, John Wiley & Sons, New York, 1982. (Ref. 24)

In recent years, the power of new computers has allowed numerical solutions to the complex sets of differential equations, describing the impact, and resulting deformation and penetration processes occurring in high-speed impacts. Experimental methods have also advanced to allow some observation of the dynamics of these very fast processes. This book covers both of these aspects of high-speed impact quite well. If you are interested in modern technology in this field, you should get this book. Presentation is graphic and clear, and all sources are well referenced.

Backman, M. E., Terminal Ballistics, NWC TP 5780, Naval Weapons Center, China Lake, CA, Feb 1976. (Ref. 25)

This book is in reality a report, but it is included because of its direct applicability to nonnuclear weapons effects. It is a primer in ballistics, and as such does not go deeply into any topic. It should make good initial reading for the neophyte, but it should be quickly supplemented by more detailed references. The reference list in the report is quite limited.

Cole, R. H., Underwater Explosions, Princeton University Press, Princeton, NJ, 1948 (Reprinted by Dover Publications, 1965). (Ref. 26)

This is an example of a reference which is truly unique in a field. Cole's book covered U.S. and British research, both analytic and experimental, on underwater explosions during World War II. There is no other comparable reference on this topic, and much of the material in it is as useful now as in 1948. Swisdak's compendium (Ref. 4) adds some newer work, but also relies very heavily on Cole's book. If you are interested in underwater explosions, you must get a copy of this book.

Baker, W. E., Westine, P. S. and Dodge, F. T., Similarity Methods in Engineering Dynamics, Hayden Book Co., New Rochelle, NJ, 1973. (Ref. 27)

The predecessor to this book was a set of notes for a short course on scale modeling of weapons effects. The book is expanded considerably beyond that scope, but it contains chapters on scaling of air blast waves and impact forces, scaling of dynamic elastic and plastic response of structures, scale modeling of penetration mechanics, modeling of rigid-body dynamics of structures, and scaling of cratering from buried explosions. The reference list is thorough.

There are a number of example problems, keyed to individual chapters.

CLOSURE

The limited list of broad references reviewed in this paper have, for the most part, proved very useful to staff members at Southwest Research Institute in prediction and evaluation of a number of conventional weapons effects, even though only a few of them were intended for that purpose. We have found that having a reference shelf with general, unclassified references of this kind is often far more valuable than having many file cabinets full of classified references.

Let us comment on the availability of the 27 general references on our list. Those which have an accession number for National Technical Information Services (NTIS) are readily available at a nominal cost, and we have given those numbers which we know. Procedures for obtaining the design manuals are often more difficult. You must usually contact the sponsor for the manual preparation and beg for a copy. Obtaining the newer reference texts in our list is not difficult, provided you are willing to pay the (sometimes outlandish) purchase price. Any published more than 10 years ago are probably out of print, and thus obtaining a copy can be quite difficult. Unfortunately, for a few very useful references such as Refs. 2 and 5, extra copies are now almost impossible to obtain, and you must rely on friendship with someone who happens to have access to a few spare copies.

REFERENCES

Compendia

1. White, M. T., (editor), Effects of Impacts and Explosions, Summary Technical Report of Division 2, National Defense Research Council, Volume 1, Washington, D.C., 1946, AD 221-586.

2. Annals of the New York Academy of Sciences, Volume 152, Article 1, "Prevention of and Protection Against Accidental Explosion of Munitions, Fuels and Other Hazardous Mixtures," October 28, 1968.

3. Swisdak, M. M., Jr., "Explosion Effects and Properties: Part I - Explosion Effects in Air," NSWC/WOL/TR 75-116, Naval Surface

Weapons Center, White Oak, Silver Spring, Maryland, October 1975, AD A018 544.

4. Swisdak, M. M., Jr., "Explosion Effects and Properties: Part II - Explosion Effects in Water," NSWC/WOL TR 760-116 Naval Surface Weapons Center, White Oak, Silver Spring, Maryland, Feb 1978, AD A056 694.

5. "Behavior and Utilization of Explosives in Engineering Design and Biochemical Principles Applied to Chemical Medicine," Proceedings of the 12th Annual Symposium American Society of Mechanical Engineers, New Mexico Section, March 1972.

6. Doering, W. and Burkhardt, G., "Contributions to the Theory of Detonation," Translation from the German as Technical Report No. F-TX-1227-IA (GDAM A9-T-4G), Headquarters, Air Material Command, Wright-Patterson AFB, Ohio, May 1949, AD 77863.

Design Manuals

7. U. S. Army Material Command, Engineering Design Handbook: Principles of Explosive Behavior, AMC Pamphlet AMCP 706-180, 1972.

8. "Fundamentals of Protection Design (Non-Nuclear)," Department of the Army Technical Manual, TM 5-855-1, Department of the Army, July 1965.

9. "Suppressive Shields Structural Design and Analysis Handbook," U.S. Army Corps of Engineers, Huntsville Division, HNDM-1110-1-2, 1977.

10. Crawford, Robert E., Higgins, Cornelius, J., Bultmann, H., "The Air Force Manual for Design and Analysis of Hardened Structures," Report No. AFWL-TR-74-102, Contract No. F29601-74-C-0018, Civil Nuclear Systems Corporation, Albuquerque, New Mexico, October 1974, Second Printing October 1976.

11. Structures to Resist the Effects of Accidental Explosions, Department of the Army Technical Manual TM 5-1300, Department of the Navy Publication NAVFAC P-397, Department of the Air Force Manual AFM 88-22, Department of the Army, the Navy, and the Air Force, June 1969.

12. Baker, W. E., Westine, P. S., Kulesz, J. J., Wilbeck, J. S. and Cox, P. A., "A Manual for the Prediction of Blast and Fragment Loading on Structures," (1980), DOE/TIC-11268, U.S. Dept. of Energy, Amarillo, TX, Nov 1980.

Reference Texts

13. Zel'dovich, Ya. B., and Razier, Yu. P., Physics of Shock Waves and High-Temperature Hydrodynamic Phenomena, Vol. I, Academic Press, NY, 1966.

14. Zel'dovich, Ya. B., and Razier, Yu. P., Physics of Shock Waves and High-Temperature Hydrodynamic Phenomena, Vol II, Academic Press, NY, 1967.

15. Johansson, C.H. and Persson, P. A., Detonics of High Explosives, Academic Press, London and New York, 1970.

16. Cook, M. A., The Science of High Explosives, Reinhold, NY, 1958.

17. Kinney, G. F., Explosive Shocks in Air, Mac-Millan, New York, NY, 1962.

18. Baker, W. E., Explosions in Air, University of Texas Press, Austin, TX, 1973.

19. Henrych, J., The Dynamics of Explosion and Its Use, Amsterdam, Elsevier Scientific Publishing, 1979.

20. Norris, C. H., Hansen, R. J., Holley, M. J., Biggs, J. M., Namyet, S. and Minami, J. Y., Structural Design for Dynamic Loads, McGraw-Hill Book Co., NY, 1959.

21. Biggs, J. M., Introduction to Structural Dynamics, McGraw-Hill Book Company, New York, NY, 1964.

22. Baker, W. E., Cox, P. A., Westine, P. S., Kulesz, J. J., and Strehlow, R. A., Explosion Hazards and Evaluation, Elsevier Scientific Publishing Co., Amsterdam, 1983.

23. Goldsmith, W., Impact: The Theory and Behavior of Colliding Solids, Edward Arnold, Ltd, London, 1960.

24. Zukas, J. A., Nicholas, T., Swift, H. F., Greszczuk, L. B., and Curran, D. R., Impact Dynamics, John Wiley & Sons, New York, 1982.

25. Backman, M. E., Terminal Ballistics, NWC TP 5780, Naval Weapons Center, China Lake, CA, Feb 1976.

26. Cole, R. H., Underwater Explosions, Princeton University Press, Princeton, NJ, 1948 (Reprinted by Dover Publications, NY, 1965).

27. Baker, W. E., Westine, P. S. and Dodge, F. T., Similarity Methods in Engineering Dynamics, Hayden Book Co., New Rochelle, NJ, 1973.

AD P001729

ANALYSIS OF CONTAINMENT RINGS FOR FLYWHEEL BURST PROTECTION

Charles W. Bert

School of Aerospace, Mechanical and Nuclear Engineering

The University of Oklahoma

Norman, Oklahoma

ABSTRACT

This paper is concerned with the analysis of Hertzian impact of a band-supported, thick-rim flywheel against an elastic containment ring. The following topics are addressed: consideration of probable failure mode of the flywheel, estimation of impact velocity, prediction of maximum conditions at contact, prediction of the maximum bending stress in the impulsively loaded containment ring, and sample calculation for a proposed containment ring.

INTRODUCTION

The functions of a containment shield for an automotive energy-storage flywheel system are:

1. Vacuum preservation
2. Protection against flywheel failure
3. Protection against external impact

Designing for the vacuum containment function involves a relatively simple static external-pressure vessel analysis. Furthermore, this function is independent of type, mass, and rotational speed of the flywheel. Thus, it will not be discussed further here.

Designing for protection against flywheel failure has certain similarities to rotor-burst-protection shields for turbine engines. The latter problem has been relatively extensively investigated; see, for instance [1-3]. In comparison, almost no attention has been directed toward flywheel containment [4], except for [5] which appeared subsequent to completion of the work described herein. Thus, in this work, attention is concentrated on this problem, with particular reference to the benign failure characteristics encountered in spin tests on band-supported, graphite-epoxy rim flywheels [6]. The present work can be considered to be a correction and extension of preliminary work reported in Section 4 of [7].

Protection against external impact is undoubtedly important in automotive applications, in connection with a head-on collision, for instance. However, the extent of the collision which must be borne by the automobile's chassis and that which

must be taken by the flywheel containment depends considerably upon the detail design of the specific vehicle concerned. Thus, consideration of this aspect of containment will not be discussed further.

METHODOLOGY OF ANALYSIS

The philosophy upon which this analysis is based is analogous to that used by Timoshenko for impact on straight beams [8] and by Yang [9] for impact on plates and shallow spherical shells. The analysis consists of the following steps:

1. Consideration of probable failure modes
2. Estimation of worst-case initial conditions (impact velocity) from elementary whirling theory and other considerations
3. Prediction of maximum impact force, contact stress, and contact time from Hertzian contact theory
4. Prediction of maximum bending stress from impulsively-loaded ring theory
5. Selection of suitable material and thickness for containment rings (sample calculation)

PROBABLE FAILURE MODES

In all of the spin tests previously mentioned, the flywheel rim remained intact. This is in contrast to turbine disks and other metallic rotating disks, which generally fail in three large pie-shaped fragments. It is not definitively known at this time whether this difference is due primarily to the differences in material (filamentary composite vs. monolithic), stress state (essentially uniaxial in a ring versus highly biaxial in a disk), or both.

The types of failure encountered in the tests of Ref. [6] were either shaft failure at the necked-down breakaway portion of the shaft or band failures. The former failure is merely a test-facility protective device and probably would not be desirable or even feasible in vehicular applications. Thus, primary concern here is with band failure, which may be due to either excessive tension or compressive buckling. In either case the failure may be quite sudden. However, there is a question as to how many bands would fail. If the rim was in an out-of-plane tilting mode at the

time of failure, it might be expected that only bands on either the top or the bottom would fail. This would induce a tilting type action which would not be the worst case to contain, since the impact with the containment shield would be oblique rather than normal (radial). However, preliminary calculations reported in [10] indicated that buckling, say in the top bands, and tensile failure in the bottom ones would occur at almost the same tilt angle. Thus, it is plausible that even under tilting action both top and bottom bands could fail. Of course, in the case of an in-plane translational whirling, the top and bottom bands would be exposed to identical conditions and thus would be expected to fail simultaneously and result in normal (radial) impact.

When a band fails, in say tension, on one side of the hub, depending upon the hub design, it may or may not carry through to its continuation on the opposite side of the hub. In one of the flywheel designs, this depends upon the frictional or mechanical splaying restraint at the hub. In the other design, if one band fails, the remainder may or may not remain effective.

ESTIMATION OF IMPACT VELOCITY

To estimate the maximum distance from the center of the rim to the center of the hub, the following approximate equation of motion for forced synchronous whirling of a single-degree-of-freedom system is used:

$$m_r \ddot{r} + (b/\omega)\dot{r} + Kr = m_r e \omega^2 \cos \omega t \qquad (1)$$

Here, m_r = mass of rim, r = radial displacement of rim center, b = material damping factor for the band material, K = in-plane spring constant of the entire band subsystem, e = initial eccentricity of rim, ω = rotational speed, t = time, and a dot denotes differentiation with respect to time.

The amplitude of the general solution of equation (1) is given by

$$\bar{r} = m_r e \omega^2 / [(K - m_r \omega^2)^2 + b^2]^{\frac{1}{2}} \qquad (2)$$

The maximum amplitude at resonance ($\omega^2 = K/m_r$) is

$$\bar{r}_{max} = (K/b)e \qquad (3)$$

However, for $K = 1.239 \times 10^5$ lb/in. and $m_r = 0.043$ lb-sec^2/in., this is predicted to occur at a speed of $(60/2\pi)(1.239 \times 10^5/0.043)^{\frac{1}{2}} = 51,260$ rpm, which is well beyond the design maximum operating speed of 32,000 rpm. At 32,000 rpm ($\omega = 3,351$ rad/sec), $b/K = 0.0172$, and $e = 0.010$ in., equation (2) yields $\bar{r} = 0.0064$ in. However, for more realistic design, based on the results of [11], a dynamic magnification factor of 1.0 will be used, i.e., $\bar{r} = 0.010$ in.

Under these conditions the peripheral velocity and radial acceleration of the mass center of

the rim would be

$$v_{tan} = \bar{r}\omega = (3,351)(0.010) = 33.5 \text{ in./sec or}$$
$$2.79 \text{ ft/sec}$$

$$a_r = \omega^2 \bar{r} = 112,000 \text{ in./sec}^2 \text{ or } 291 \text{ g's}$$

It is conservatively assumed that upon failure the bands offer no radial restraint and that there is a 0.028-in. radial clearance between the rim periphery and the inside of the containment housing. Thus, the radial velocity at impact, for a total travel $x = 0.028 - 0.010 = 0.018$ in., would be

$$v_r = (2 a_r x)^{\frac{1}{2}} = 63.5 \text{ in./sec}$$

Thus, the resultant impact velocity would have a magnitude of

$$v_o = (v_r^2 + v_{tan}^2)^{\frac{1}{2}} = 63.6 \text{ in./sec or } 5.30 \text{ ft/sec}$$

PREDICTION OF CONTACT CONDITIONS

To predict the contact displacement, force, and compressive (bearing) stress in the containment, the perfectly elastic Hertzian impact theory as developed by Goldsmith [12] is used. The containment parameters are denoted by subscript 1 and the rim ones by subscript 2. The inside surface of the containment is assumed to be perfectly cylindrical with an inside radius of 10.028 in. Thus, in the sign convention of Hertzian contact theory, $1/R_1 = 0$ and $1/\bar{R}_1 = -1/10.028$ in.

The flywheel rim is toroidally curved with these curvatures: $1/R_2 = 1/0.9474$ in.* and $1/\bar{R}_2 = 1/10.000$ in.

Since it is assumed that the principal axes of the rim and containment shield are aligned, Goldsmith's angle $\beta = 0$. Then the Hertzian geometric parameters A and B can be calculated simply as

$$A = (1/2)[(1/\bar{R}_1) + (1/\bar{R}_2)]$$
$$\qquad\qquad\qquad\qquad (4)$$
$$B = (1/2)[(1/R_1) + (1/R_2)]$$

Here, $A = 0.00140$ in.$^{-1}$ and $B = 0.428$ in.$^{-1}$. Thus, $A/B = 0.00265$ and by interpolating Goldsmith's [12] Table 5, page 87, one obtains factors $q_a = 14.7$ and $q_b = 0.370$. To obtain $q_c = 1.87$, it was necessary to extrapolate Goldsmith's values by plotting on log-log paper.

The contact force F is related to the contact displacement α as follows:

....

*The radius R_2 is calculated from the respective axial and radial semi-axes of the elliptical cross section of the rim (1.5 and 2.375 in., respectively; see Fig. A1 in [10]) as $(1.5)^2/2.375 = 0.9474$ in.

$$F = k_2 \delta^{3/2} = F_m \sin (1.068 \, v_0 t / \delta_m) \qquad (5)$$

where v_0 is the relative velocity at initial contact, t is time, and δ_m and F_m are the maximum values of the displacement and force, respectively:

$$\delta_m = (5 \, v_0^2/4k_1 k_2)^{2/5} \qquad (6)$$

$$F_m = k_2 \delta_m^{3/2} = 1.143 \, k_2^{2/5} \, v_0^{6/5}/k_1^{3/5} \qquad (7)$$

Here, the following additional parameters are defined as

$$k_1 = (1/m_1) + (1/m_2) \qquad (8)$$

$$k_2 = \frac{(4/3) q_k}{(\delta_1 + \delta_2)(A + B)^{1/2}} \qquad (9)$$

$$\delta_1 = (1 - \nu_1)/E_1 \; ; \quad \delta_2 = (1 - \nu_2)/E_2 \qquad (10)$$

where E is Young's modulus and ν is Poisson's ratio.

The total time of contact τ is given by

$$\tau = 2.9432 \, \delta_m/v_0 \qquad (11)$$

The contact area is an ellipse with semi-axes a and b:

$$a = q_a [(3F_m/4)(\delta_1 + \delta_2)/(A + B)]^{1/3} \qquad (12)$$

$$b = (q_b/q_a) a$$

The peak compressive stress developed is given by

$$\sigma_{cm} = (3/2)(F_m/\pi a b) \qquad (13)$$

DYNAMIC STRESS ANALYSIS OF CONTAINMENT RING

To determine the peak dynamic bending moment in the containment ring, the analysis by Mittal [13] is used. Mittal showed that for a circular ring subjected to a concentrated loading that is a half-sine pulse in time, i.e., equation (5), the maximum bending moment occurs at some value of time t, $0 < t < \tau$. For this time interval, the bending moment is given by

$$M = - (F_m/2)(E_1 I/\rho_1 A_r)^{1/4}(\tau/\pi)^{1/2}\{f(x)$$

$$- (1/2) \cos (\pi t/\tau) + (1/2) \sin (\pi t/\tau)]$$

$$+ (F_m \tau/2\pi)(E_1 I/\rho_1 A_r)(2.9303/R^3)$$

$$\cdot [t - (\tau/\pi) \sin (\pi t/\tau)] \qquad (14)$$

where $x = \sqrt{2t/\tau}$ and

$$f(x) = \frac{1 + 0.926x}{2 + 1.792x + 3.104x^2} \qquad (15)$$

Here, A_r = cross-sectional area of containment ring, I = rectangular area of moment of inertia of ring cross section about the appropriate centroidal axis, R = mean radius of containment ring. It is noted that equations (14) and (15) both differ slightly from those given by Mittal, since his paper had some obvious typographical errors.

SAMPLE CALCULATION

A sample calculation is carried out here for a containment ring of aramid fiber/epoxy matrix composite with $E_1 = 11.0 \times 10^6$ psi, $\nu_1 = 0.34$, $\rho_1 g = 0.050$ lb/in.^{3} and the Sandia flywheel rim of graphite fiber/epoxy matrix composite with $E_2 = 18.0 \times 10^6$ psi, $\nu_2 = 0.27$, $m_2 = 0.043$ lb-sec^2/in. The containment ring dimensions are an axial length of 3.00 in. and a radial thickness of 1.00 in. Thus, the containment ring has a mean radius of 10.528 in. and a mass

$$m_1 = 2\pi(10.528)(3.00)(1.00)(0.050/386)$$

$$= 0.0257 \; \text{lb-sec}^2/\text{in.}$$

Using equations (10), one obtains $\delta_1 = 2.56 \times 10^{-8}$ in.^{2}/lb and $\delta_2 = 1.64 \times 10^{-8}$ in.^{2}/lb. Then equations (8) and (9) yield $k_1 = 62.17$ in./lb-sec^2 and $k_2 = 89.62 \times 10^6$ lb/(in.)$^{3/2}$. From equations (6), (7), and (11), one gets $\delta_m = 0.00383$ in., $F_m = 21,200$ lb, and $\tau = 177 \times 10^{-6}$ sec.

Application of equations (12) yields a = 1.703 in. and b = 0.0429 in. Using these values in equation (13), one obtains $\sigma_{cm} = 139,000$ psi, which is an acceptable value for the Hertzian contact compressive stress in this material.

By examination of the numerical results given by Mittal [13] and some further calculations, it can be shown that the peak bending moment always occurs when $t/\tau = 0.72$. Then, application of equations (15) and (14) yield $f(x) = 0.2449$ and a peak moment $|M_m| = 21,600$ lb-in., respectively.

Finally, the maximum bending stress is given by

$$\sigma_b = 6|M_m|/BH^2 = 6(21,600)/(3.00)(1.00)^2 = 43,200 \; \text{psi}$$

This is a very reasonable tensile stress for aramid-epoxy, which has an ultimate tensile strength of 200,000 psi. However, it may be marginal on the compressive side of the bend.

It is noted that the calculated weight of the 1.0-in. thick aramid-epoxy containment ring is only 9.92 lb. It should be emphasized that this weight is equal to that of an aluminum containment ring 0.50 in. thick or a steel containment ring 0.177 in. thick.

DISCUSSION

In this section are discussed the implications of the numerous engineering approximations which have been made in the foregoing analysis in order to obtain relatively simple closed-form solutions.

The present analysis has been based upon Hertzian elastic contact theory, which in itself has some engineering approximations. However, relatively recent dynamic-contact experiments by several different investigators [14,15] have corroborated this theory. This was true even in the experiments of [14] which used impact condition that were chosen to maximize the effects of stress-wave energy dissipation. The question of the effects of material damping and localized yielding in the vicinity of contact were investigated by Chou and Flis [16] for the case of dynamic contact loading of straight beams. They concluded that these effects reduced the peak stresses only slightly. Thus, Hertzian theory should be slightly conservative, which, of course, is usually desirable for design purposes.

Perhaps the most questionable assumption used here is the use of isotropic-material contact stress theory. The theory could be improved, at the cost of considerable complexity, by combining anisotropic elasticity results for the point-loaded half-space from Lekhnitskii [17] in a manner analogous to Goldsmith's development of Hertzian dynamic contact for isotropic media [12].

There may be some question regarding the validity of using Mittal's thin-ring theory for a ring which has a 0.10 ratio of radial depth to inside ring radius. Although more accurate ring theory including transverse shear deformation and rotatory inertia is now available [18], the Morley theory used by Mittal has been shown to be adequate for thickness-to-radius ratios as high as 0.5 [19].

It should also be mentioned that the additional restraint provided by the end plates, located above and below the flywheel and necessary for vacuum preservation, has been neglected in the present analysis. Again, this is another factor which would provide additional structural integrity beyond that computed here.

Finally, it should be kept in mind that the present analysis has not addressed the problem of frictional heating due to the abrasive rubbing of the flywheel periphery against the inside of the containment ring.

REFERENCES

1. Chiarito, P.T., "Status of Engine Rotor Burst Protection Program for Aircraft," NASA Aircraft Safety and Operating Problems (Proc. of a conference held at Langley Research Center, May 4-6, 1971), NASA SP-270, 1971.

2. Wu, R.W. and Witmer, E.A., "Approximate Analysis of Containment/Deflection Ring Responses to Engine Rotor Fragment Impact," Journal of Aircraft, Vol. 10, No. 1, Jan. 1973, pp. 28-37.

3. Gerstle, J.H., "Analysis of Rotor Fragment Impact on Ballistic Fabric Engine Burst Containment Shields," Journal of Aircraft, Vol. 12, No. 4, Apr. 1975, pp. 388-393.

4. Bennison, R., "The Use of Composite Flywheels for Braking Energy Recovery in Road Transport Vehicles," Composites, Vol. 8, No. 3, July 1977, pp. 137-138.

5. Sapowith, A.D., Witmer, E.A., Curson, L.A., McElman, J.A., and Kaehler, R., "State-of-the-Art Review of Flywheel Burst Containment," Lawrence Livermore Laboratory Report UCRL-15257, May 15, 1980.

6. Reedy, Jr., E.D. and Street, H.K., "Composite-Rim Flywheels: Spin Tests," SAMPE Quarterly, Vol. 10, No. 3, Apr. 1979, pp. 36-41.

7. Bert, C.W., Kocay, C.A., Chen, T.L.C., and Busby, J.P., "Research on the Dynamics of Band-Supported Flywheel Systems," Sandia Laboratories, Report SAND78-7074, Feb. 1979.

8. Timoshenko, S.P., "Zur Frage nach der Wirkung eines Stosses auf einen Balken," Zeitschrift für Mathematik Physik, Vol. 62, No. 2, 1913, pp. 198-209.

9. Yang, J.C.S., "Impact on Plates and Shells," International Journal of Solids and Structures, Vol. 7, No. 5, May 1971, pp. 445-458.

10. Bert, C.W., Chen, T.L.C., and Kocay, C.A., "Critical Speeds and Natural Frequencies of Rim-Type Composite-Material Flywheels," Sandia Laboratories, Report SAND78-7049, Jan. 1979.

11. Chen, T.L.C. and Bert, C.W., "Whirling Response and Stability of Flexibly Mounted, Ring-Type Flywheel Systems," ASME Journal of Mechanical Design, Vol. 102, No. 2, Apr. 1980, pp. 369-378.

12. Goldsmith, W., Impact, E. Arnold (Publishers) Ltd., London, 1960, pp. 83-91.

13. Mittal, R.K., "Flexure of a Thin Elastic Ring Due to a Dynamic Concentrated Load," International Journal of Engineering Science, Vol. 14, No. 3, 1976, pp. 247-257.

14. Maiyshev, B.M., "Effect of Stress Waves on the Process of Collision Between Three-Dimensional Elastic Bodies," Mechanics of Solids, Vol. 8, No. 6, 1973, pp. 62-66.

15. Matsumoto, H. and Nakahara, I., "The Impact of an Elastic Cylinder on an Elastic Solid," Bulletin of the Japan Society of Mechanical Engineers, Vol. 21, No. 154, Apr. 1978, pp. 579-586.

16. Chou, P.C. and Flis, W.J., "Design Curves for Structural Response due to Impact Loading," Drexel University, _Proceedings of the AIAA/ASME/SAE 17th Structures, Structural Dynamics, and Materials Conference_, King of Prussia, PA, May 5-7, 1976, pp. 365-373.

17. Lekhnitskii, S.G., _Theory of Elasticity of an Anisotropic Elastic Body_, English translation of the 2nd. Russian edition, Mir Publishers, Moscow, 1981, pp. 147-151.

18. Kirkhope, J., "In-Plane Vibration of a Thick Circular Ring," _Journal of Sound and Vibration_, Vol. 50, No. 2, Jan. 22, 1977, pp. 219-227.

19. Morley, L.S.D., "Elastic Waves in a Naturally Curved Rod," _Quarterly Journal of Mechanics and Applied Mathematics_, Vol. 14, No. 2, 1961, pp. 155-172.

A RATIONAL APPROACH TO THE ANALYSIS OF STRUCTURES SUBJECTED TO UNDERGROUND BLASTS

S.F. Borg

Stevens Institute of Technology
Civil Engineering Department
Hoboken, New Jersey   07030

ABSTRACT

The two major data bases connected with underground blast effects on structures are utilized to obtain rational procedures for solving - approximately - the two fundamental engineering problems. The data bases are, 1) accelerogram records at points in the field affected by the blast and 2) isoseismal contour maps for the entire field affected by the blast. These then lead to analytic expressions and charts for the engineering problems, namely 1) damage assessment and 2) structural design/analysis.

INTRODUCTION

The theory and procedures to be described were developed during the course of earthquake engineering research. However, all the results obtained, suitably scaled, apply as well to the underground blast phenomenon. As is well known the earthquake mechanism has been likened, physically, to the equivalent of an underground explosion of enormous initial energy.

Thus, the presentation will utilize equations and charts that were obtained in studies related to earthquakes. But all the procedures, all the equations, all the charts apply as well for the underground blasts which are the topic of this symposium. The numerical values of the different terms will very likely vary from those obtained for earthquakes and used in this report. But the fundamental techniques are the same. In fact, underground blast phenomena afford an excellent means for checking the more comprehensive predictions which follow from the application of the theory to the earthquake event.

BASIC ASSUMPTIONS

This research is founded on three fundamental (and related) premises:

1) Underground blast engineering (hereafter designated as UBE) is a unique discipline in the overall field of applied mechanics, just as for example, elasticity and heat flow are separate and different. Therefore, UBE has its own particular invariants, parameters, equations, variables and similar quantities - and furthermore these should be very different from the other well-known terms and relations in applied mechanics.

2) The sources or fountain heads for all the quantities mentioned above (the invariants, parameters etc.) will be the two major observation banks (or experimental data or field data) of UBE, these being

a) The accelerogram which, physically, must be related in some fashion to the variation with time of ground surface energy at a point in the blast field.

b) The isoseismal contour map which, physically, must be related in some fashion to the variation with distance of the ground surface energy over the entire area affected by the blast.

Note, therefore, that proceeding from 1) to 2) above we are led directly to

3) namely, energy is the key element, the basic ingredient in the entire underground blast event, starting from its initiation (the explosion) and proceeding timewise and spacewise until its completion with the accompanying effect upon and response of structures.

The research - which will be reported elsewhere in its entirety (Ref. 1) covers every facet of the blast from its initiation (a blast mechanism) up to and including its effect on and the response of structures. New parameters, invariants, equations and similar relations are introduced and a complete unified, rational approximate theory of UBE is developed.

The theory is based upon reasonable mathematical, physical and technological assumptions, is dimensionally sound and represents logical, integrated over-all approaches to all facets of the blast event.

As in all engineering design applications, certain experimental (field) data must be obtained in order to establish "allowables" or equivalent terms. At this time only a limited fund of such quantities is available and the applications are limited in this respect. However, the entire development is "self-correcting" in the sense that as more and more data is collected and utilized, corrections and modifications to the working data can be made without difficulty until finally, the design relations, curves and charts will be established with sufficient accuracy so that ordinary engineering design offices can use them with a level of confidence suitable for engineering purposes. The author suggests that even at this time, there probably is sufficient data available (possibly in the classified files) to permit its use – at the appropriate approximate level.

In this report only that portion of the study dealing with damage to structures will be dealt with in detail and because of space limitations, only the results will be presented. The details are described elsewhere - as are the applications to the structural design and analysis phases of the problem.

THE ACCELEROGRAM INVARIANT AND PARAMETERS

A typical earthquake accelerogram is shown below, Fig. 1a. We assume that except possibly for scale, the underground blast accelerogram is similar. Hence the discussion which follows applies to UBE.
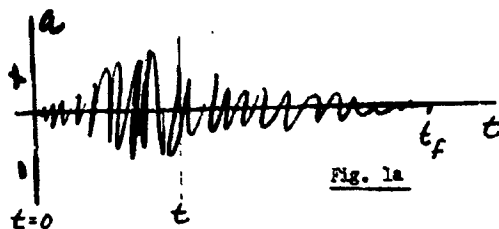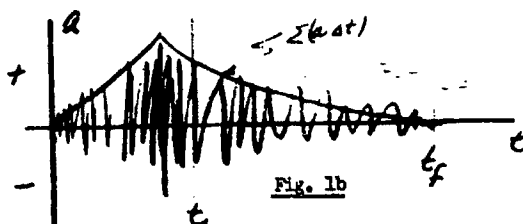

Fig. 1a

Fig. 1b

An analysis and study of a number of accelerograms, as well as physical considerations, suggest that $\sum_{t=0}$ (aΔt) and t are the important variables in this phenomenon, and in particular $\sum$ (aΔt)$_f$ and t$_f$ are the fundamental parameters, Fig. 1b.

A mathematical derivation leads to an invariant expression (the "acceleration index") which holds for "canonical" accelerograms, this being

$$\frac{\sum_{t=0}^{t}(a\,\Delta t)}{\sum_{t=0}^{t_f}(a\,\Delta t)_f} \cdot e^{0.12\left[1-\left(\frac{t_f}{6}\right)^{1.5}\right]} \qquad (1)$$

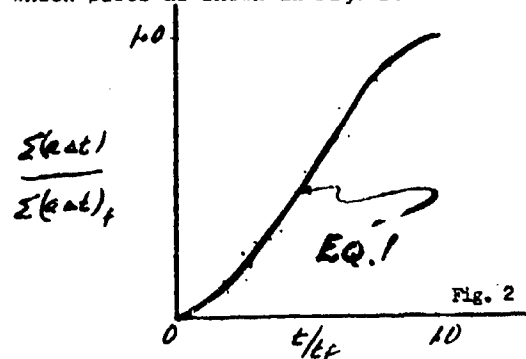which plots as shown in Fig. 2.

Fig. 2

The numerical values obtained in Eq. 1 apply to earthquakes. They probably differ for underground blasts. In any case, these values can be established without difficulty.

For those accelerograms that are not "canonical", typically as in Fig. 3, we
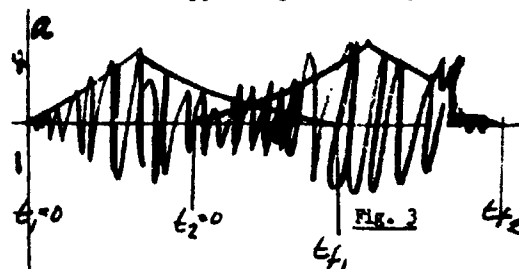
Fig. 3

can generally superpose 2 or more canonical accelerograms.

By utilizing an alternate, but equivalent postulated mathematical formulation, equating equal terms, and integrating we obtain an equation for the timewise variation of horizontal ground energy at the point where the canonical accelerogram was obtained, Eq. 2.

$$\frac{E_t}{E_{t_F}} = \frac{\left[\left(\frac{t_F}{t}\right)^{1.8} - \left(\frac{t_F}{t_i}\right)^{1.8}\right]}{1 - \left(\frac{t_F}{t_i}\right)^{1.8}} \qquad (2)$$

ε_t = surface horizontal energy per unit **ef**
fective area between the times t_i and t at
the accelerogram location.

ε_{tf} = same for $t \cdot t_f$

which plots as Fig. 4
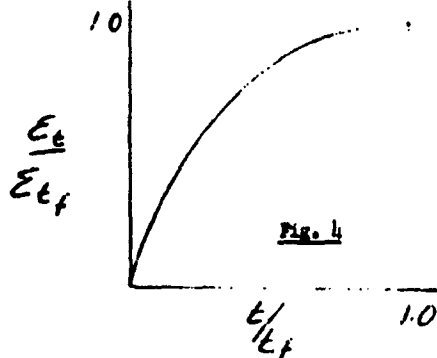
Fig. 4

In Eq. 2 also the numbers may be different for underground blasts.

For 2 or more superposed canonical records (Fig. 3) we superpose the energy expressions, Eq. 2, Fig. 4.

THE GEOLOGY AND MEASURES OF DAMAGE

Physically, we must assume that the "geology" of a region affects the ground behavior and structural response due to underground blasts. We assume, at this time, three different "geologies", designated as R_1, R_2, and R_3, to be defined following further study of this variable. It is conceivable that a smaller (or larger) number of separate geologies is required to account for all possible situations. In a general way, frequency of the acceleration is accounted for in this classification. These geological designations are used in the mathematical, physical and technical formulations throughout the research, as we shall see typically, in the present damage assessment portion of the study.

We assume "damage" is defined by an "Intensity Number," I, as given in a (possibly modified) Mercalli type Scale, cn an "isoseismal contour map". Fig. 5 shows such a map for an earthquake. Its form will be similar but the values may differ for an underground blast.

THE ISOSEISMAL INVARIANT AND PARAMETERS

An analysis and study of 28 earthquakes during the past 500 years, occuring all over the earth, as well as physical considerations, suggest that $\sum\limits_{s=0} (IS)$ and S are the important variables in this phenomenon and in particular that $\Sigma (IS)_f$ and S_f are
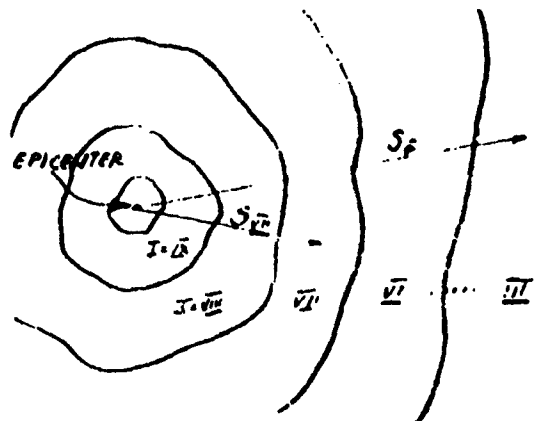
Fig. 5

the fundamental parameters.

A mathematical derivation leads to an invariant expression (the "iscseismal index") which holds for all 28 earthquakes, this being Eq. 3,

$$\frac{\sum\limits_{S=0}^{S}(IS)}{\sum\limits_{S=0}(IS)_f} = e^{2.0\left[1-\left(\frac{S_f}{S}\right)^{1/3}\right]} \qquad (3)$$

which plots as Fig. 6

Fig. 6

The author suggests that a similar equation and curve will hold for underground blasts - suitably modified, if necessary, for "geology".

By utilizing an alternate but equivalent postulated mathematical formulation, equating equal terms and integrating, we obtain an equation for the spacewise variation of horizontal ground energy over the

137

entire field affected by the earthquake, Eq. 4, which plots as Fig. 7.

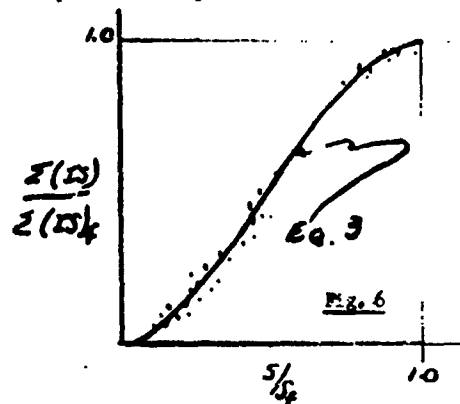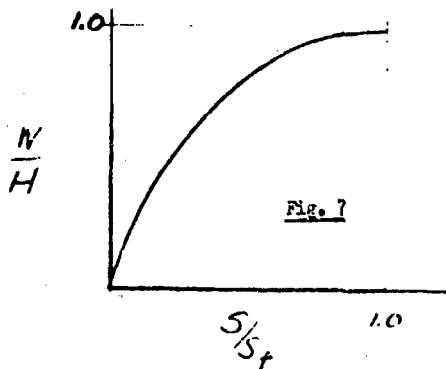$$\frac{W}{H} = \frac{\left[\left(\frac{S_f}{S_i}\right)^{1/3} - \left(\frac{S_i}{S}\right)^{1/3}\right]}{\left[\left(\frac{S_f}{S_i}\right)^{1/3} - 1\right]} \qquad (4)$$

W = total surface horizontal energy between the small radius S_i and the radius S.

H = same as above for S → S_f

Fig. 7

THE DAMAGE ASSESSMENT CURVES

In this theory, $\Sigma(a\Delta t)_f$ and t_f and $\Sigma(IS)_f$ and S_f are the key parameters in the rational underground blast analysis and must be included in all theoretical developments connected with the blast phenomena. Thus

A) Physically, $\Sigma(a\Delta t)_f$ and t_f must be connected with the damage of structures. A study of a limited number of earthquake accelerograms (corrected for direction) that had isoseismal maps for the same events leads to a preliminary damage (intensity) map as follows, Fig. 8, for earthquakes. A similar, suitably modified chart, should apply to underground blasts.

If we have a superposed accelerogram as in Fig. 3, the author suggests at this time that the separate $\Sigma(a\Delta t)_f$ and t_f values for each separate canonical envelope be added. Then use these sums in Fig. 8

B) Physically, $\Sigma(IS)_f$ and S_f must be related to the magnitude, M, and hence the energy, of the underground blast. For example, by using the 28 earthquakes we find Fig. 9, (and a similar representation will apply for the underground blasts) so that
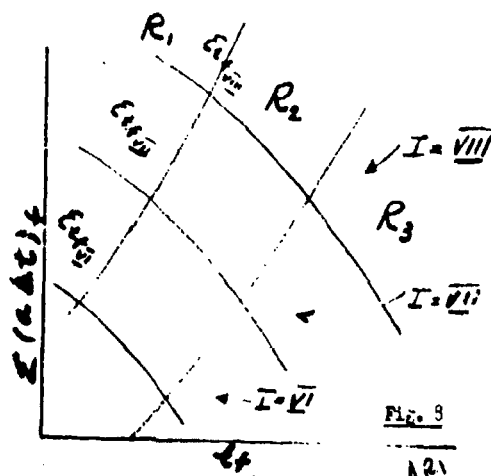
Fig. 8
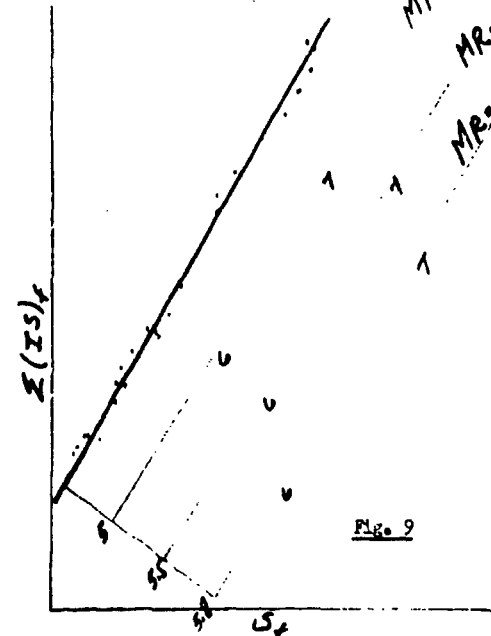
Fig. 9

C) using the equation given above and Fig. 9, for a given M and R we can determine $\Sigma(IS)_f$ and S_f and the corresponding isoseismal map may be computed and plotted, Fig. 10, from which the damage may be assessed.

THE STRUCTURAL DESIGN PROCESS

Very briefly (because of space limitations) - the structural design and/or analysis phase of the study utilizes the energy concept in conjunction with the accelerogram and isoseismal invariants and parameters previously described. The details are described in Ref 1e and 1f.

$$M =$$
$$R =$$
$$S_f =$$
$$\mathcal{I}(IS)_f =$$
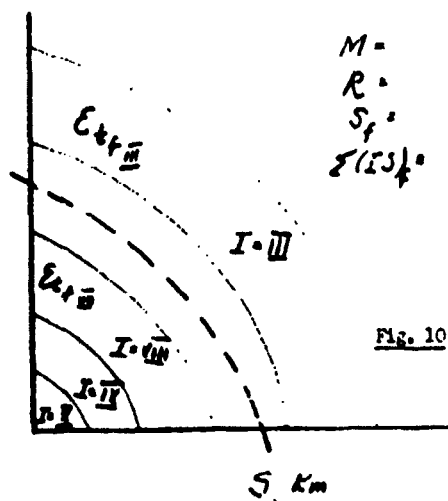
Fig. 10

In applying the method, symmetry and anti-symmetry are the basic tools used. A free-free form of vibration is assumed which requires the estimation of an "equivalent" length, ℓ. The energy to be absorbed by the structure requires the determination of an "effective area, a_e". Symmetrical and anti-symmetrical energy and vibrational configurations are utilized and the entire process leads to an approximate analysis that includes all of the variables that should enter into an underground blast analysis in a form that can be used by ordinary engineering design offices.

CONCLUSION

The design process, as in all engineering design, starts with specified or code or judgement design decisions. These could be, typically,

a) A specified canonical accelerogram or cluster cf canonical accelerograms with given separate $\mathcal{I}(a\Delta t)_f$ and t_f values and geology.

or

b) A given blast magnitude, efficiency and geology from which $\mathcal{I}(IS)_f$ and S_f are obtained.

or other similar data.

From these, using the equations and charts derived from this theory, we can determine all of the necessary UBE parameters required for the rational, analytical assessment of damage and for the structural design.

There is no doubt whatever, that every underground blast is different, in detail, from every other underground blast that has ever occurred, wherever it occurred.

But, by the same token, because the blast is a natural phenomenon, it must also be true that, overall, in the large, there are certain relationships or equations or parameters that are approximately common to all underground blasts.

These relationships or equations or parameters are here called the invariants of the blast phenomenon and the writer suggests that any attempt to obtain a rational, quantitative, scientifc theory for UBE must start with a consideration of these basic building blocks - the invariants.

To uncover these the research was guided strongly by physical-engineering-mathematical considerations founded on available earthquake tests and experiments which, initially, surfaced in the form of hypotheses. By extension the hypotheses permitted the derivations of new mathematical expressions which include those physical-engineering terms that must occur in UBE theory. These new expressions predict new phenomena which are capable of experimental check.

Should the new relations check out - with accuracy consistent with the observed data and sufficiently precise for engineering applications then one may with some confidence assume they represent an acceptable theory for the UBE event.

Closely related to the above is the fact that in all fields of applied engineering, an essential requirement for the engineer is the collection and tabulation of basic design information. This design data is generally subject to continuous adjustment and revision as additional experience or special conditions require. In structural engineering for example, we need data on (to name just a few items), wind loads, pile capacities, earth pressures, allowable steel stresses etc - data which to this day are being adjusted and revised as required by ongoing research. This data almost always can be determined only by performing laboratory or field tests and furthermore varies in form or content depending upon the applied engineering field considered.

As these experimental (i.e. field) data are collected, they become part of the inventory in the storehouse of design data and as they accumulate, the need for additional experimental values frequently diminishes and the applications (in design and/or analyses) can generally be made with greater accuracy and confidence.

In this new UBE theory, the necessary experimental refinements can be obtained by

analyzing experiments currently being routinely performed (i.e. the accelerogram and the isoseismal map) and/or by developing and performing other relatively simple exercises utilizing man-made blasts. In this way, the following terms will be evaluated more precisely, thereby permitting greater and greater accuracy as the accumulation of data continues:

    a) The efficiency, η, of the blast.

    b) The role of the "geology"

    c) The acceleration index invariant expression and the derived relations for pointwise - temporal variation of blast energy.

    d) The isoseismal index invariant expression and the derived relations for spacewise variation of blast energy.

    e) The effective length, ℓ

    f) The effective area, a_e

The design engineer, architect, specification or code writer, damage or safety engineer and other professionals who are concerned with rational scientific UBE analyses can use the new theory at the present time based upon available data and reasonable assumptions. Because of the limited available amount of the required accumulated experimental data (which is a common occurrence in any newly developed theoretical application in applied engineering) the amount of approximation involved and other possible limitations are uncertain. In order to increase the accuracy, the author recommends further continuing study, testing and refinement of the quantitative values for the uniquely UBE terms mentioned above in a) through f).

REFERENCES

1) S.F. Borg, "Earthquake Engineering - Damage Assessment and Structural Analysis", Wiley Heyden Publishing Company, London, England, in press.

    a) A Mathematical-Physical Model of a Deep-Focus Earthquake Mechanism, Eleventh Annual Modeling and Simulation Conference, Univ. of Pittsburgh, Pittsburgh, Pa. 15261. May 1-2, 1980. Also Technical Report ME/CE-79, Department of Mechanical Engineering (Civil Engineering), Stevens Institute of Technology, Hoboken, N.J., Nov. 1979.

    b) Accelerogram, Intensity, Damage - A New Correlation for Use in Earthquake Engineering Design, Seventh World Conference on Earthquake Engineering, Istanbul, Sept. 8-13, 1980. Also Technical Report ME/CE-791, Department of Mechanical Engineering (Civil Engineering), Stevens Institute of Technology, Hoboken, N.J., Dec. 1979.

    c) An Isoseismal-Energy Correlation for Use in Earthquake Structural Design, Seventh World Conference on Earthquake Engineering, Istanbul, Turkey, Sept. 8-13, 1980. Also Technical Report ME/CE-792, Department of Mechanical Engineering (Civil Engineering), Stevens Institute of Technology, Hoboken, N.J. Dec. 1979.

    d) Extended Analysis of Isoseismal-Magnitude-Intensity Index Correlations in Earthquake Engineering, Tech. Report ME/CE - 81-1, Department of Mechanical Engineering/Civil Engineering, Stevens Institute of Technology, Hoboken, N.J., May, 1981.

    e) Some New Approximate Procedures Relating to the Analysis of Structures Subjected to Earthquake Loadings - Part 1, Elastic Theory, Tech. Rept. ME/CE - 80-1, Department of Mechanical Engineering/Civil Engineering, Stevens Institute of Technology, Aug. 1980.

    f) Some New approximate Procedures Relating to the Analysis of Structures Subjected to Earthquake Loadings - Part II, Applications, Tech. Rept. ME/CE - 80-2, Department of Mechanical Engineering/Civil Engineering, Stevens Institute of Technology, Hoboken, N.J., Dec. 1980.

AD P001731

EXTREME DYNAMIC LOADING EFFECTS ON STEEL AND CONCRETE SHELL STRUCTURES

Yves Crutzen

Control Data Italia
Applications & Professional Services
Segrate(Mi), Italy

ABSTRACT

Using the modern computerized analysis, the special purpose computer program SLOOFSAN can be successfully applied for the evaluation of thin structure strength limits in presence of extreme dynamic loading phenomena. This program correctly solves wave-propagation-type of problems involving short transient (very rapid loading-time sequence) and including shock-wave response from impulsive loading (explosion or blast wave) and impact loading (missile impact). SLOOFSAN program is based on a finite element shell formulation using the Semiloof element and has been developed for transient dynamic non-linear analysis applying an efficient explicit direct time integration technique.

SLOOFSAN 3-D capabilities in the fields of structural safety assessment and anti-missile design are illustrated in the paper.

EXPLICIT DYNAMIC ANALYSIS USING SEMILOOF

The present formulation for the solution of complex shell problems in transient non-linear analysis is based on the construction of a very performing mechanical model with the use of advanced numerical techniques. The explicit solution strategy is preferred to a modal superposition procedure or an implicit direct time integration technique for the following reasons:

- the equations of motion are decoupled thanks to a mass-lumping process and are simply expressed i- term inertia, damping, internal and external vectors;
- the nodal accelerations, velocities and displacements are directly computed using central difference formulas;
- the internal force vector represents the keystone of the mathematical model because it solely contains all the information related to the structural stiffness and the non-linear material behaviour through the stress vector;
- the constitutive equations are easily implemented, in particular total stress-strain formulations of the explicit type. See e.g. Ref.(1).

- the geometrical non-linearities, due to large rotations, are trivially implemented using the convective coordinate technique;
- the program architecture is much more simple: no bandwidth problems, less computer storage, no assemblage nor inversion of any matrix, ease of programming;
- this strategy is more competitive for advanced vector processing, thanks to a complete vectorial formulation.

This technique of explicit time integration, in connection with numerically tested mass-lumping procedures, has been implemented in previous works of the author (2,3,8), for the more complex isoparametric shell element Semiloof developed by Irons (6).

The Semiloof dynamic model for steel and concrete thin shells has nodal masses and inertia moments obtained by lumping techniques, explained in Ref. (2), and can be represented as a system of discrete nodal masses interconnected by means of springs representing the internal forces and moments. Any spring stiffness may vary from high values to very small ones when plasticity and any other material disintegration process take place in the finite element.

The modelling of reinforcement is obtained by adding layers of steel bars at the upper and lower shell surfaces. These steel membranes undergo the same total strains as concrete until the reinforcement bars buckle when concrete locally crushes. Concrete thickness and steel reinforcement percentage may vary from an element to another and the reinforcement may be different at the upper and lower surfaces within one element.

Prestressing may be included in the concrete by giving an initial prestrain in the reinforcement. The static stresses due to prestressing or dead weight may be carried out using the transient program SLOOFSAN in a kind of dynamic relaxating mode, as illustrated for example in Ref. (3).

The material non-linearities, dealt with in this paper, include a plasticity model for ductile materials like steel, based on:

- experimentally observed monoaxial yield stress vs plastic strain relationship;
- the concepts of Von Mises' stress, Drucker's postulate, isotropic hardening and plastic energy dissipation.

For reinforced concrete, the following inelastic behaviours are included:

- cracking of concrete in tensile regime. The model is based on the concept of zero tensile strength, or small tensile strength, before the appearance of the first crack. A stress redistribution takes place when a crack strain is defined perpendicular to the new crack, in agreement with Mohr's circle. See e.g. Ref.(3);
- elasto-plastic formulation for concrete in compression. Based on the well-established theory of plasticity, the ascending and descending parts of the stress-strain curve are quite simulated, as shown for example in Fig. I. Crushing of concrete is defined by the post-peak strain softening behaviour;
- a new explicit biaxial stress-strain relationship for concrete in compression has also been incorporated in SLOOFSAN because it reproduces quite well the inelastic dilatancy of concrete near failure (4). This general constitutive equation, developed by Cedolin et al (I), is obtained by expressing the secant bulk and shear moduli of elasticity as non-linear functions of the first two invariants of the strain tensor only;
- concerning the steel reinforcement, plasticity is encountered in tension as well as in compression. Moreover, local steel buckling in compressive regime, when concrete crushes, is simulated by deleting the compressive contribution of the reinforcement to the internal force vector.
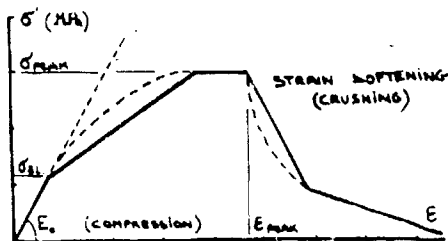
The proposed mechanical model permits to follow very accurately the progressive plastification of steel shells or the cracking propagation of concrete thin structures within each finite element in the mid-surface and across the thickness.

As a consequence, the complete disintegration of reinforced concrete shells is created by concrete cracking, concrete crushing, steel plasticity, local steel buckling, which represent the major four factors computed directly through the internal force vector.

The present material models for concrete do not yet take into account of the sensitivity of concrete to some parameters like stress history or strain rate. Experimental research into concrete behaviour under dynamic load is urgently needed in order to use the results from computer program with more confidence.

EXPLOSION / STRUCTURE INTERACTION

The advanced computer program SLOOFSAN permits to illustrate some extreme dynamic loading condition acting on thin metal structures. A cylindrical steel panel is submitted to impulsive loading (initial velocity) which is supplied by an explosive sheet in contact with the metal. Fig. 2 shows 1/4 model of the panel using only 20 Semiloof elements. High membrane and bending wave propagation effects occur in the cylinder together with a rapid plasticity extension.
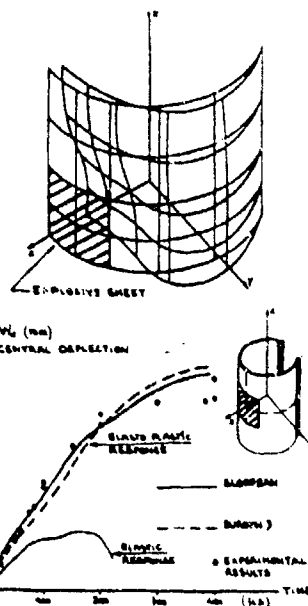

FIG.1 :

STRESS-STRAIN CONSTITUTIVE LAW FOR CONCRETE

FIG.2 : CYLINDRICAL PANEL UNDER IMPULSIVE LOADING (EXPLOSION)

The deformed shape of the cylindrical panel
shows how the impulsive motion involves very lar-
ge displacements and rotations. The highly non-
linear response of the central deflection versus
time is quite different from the elastic linear
response. Excellent agreement with numerical and
experimental results, given in Ref. (5), is ob-
tained.

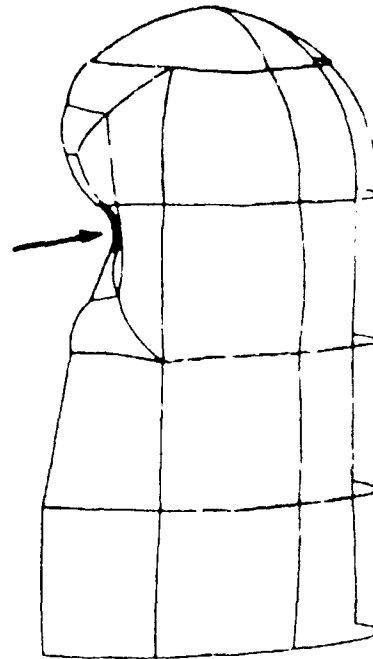## SOFT-MISSILE / STRUCTURE INTERACTION

The described numerical technique based on
explicit dynamic analysis using a shell formula-
tion is particularly suited to handle highly non-
linear problems of soft-missile impact on large
concrete structures. Using the Semiloof element,
relative coarse meshes are defined for the nu-
clear reactor containment building impacted by
an aircraft. The computer program SLOOFSAN per-
mits an accurate determination of the partial da-
mage of the local impacted area as well as the
overall behaviour of the remaining structure un-
der the induced vibrations. The impact of a civil
aircraft (Boeing 707-320) on the dome and the la-
teral wall of the reactor containment has been
already presented in a previous paper by the au-
thor (3).

For the complete 3-D problem of the reactor
building loaded laterally, the effects of incor-
porating the dead weight or a little tensile
strength for concrete on the dynamic structural
response are shown in Fig. 3. The values for the
maximum horizontal displacement obtained in li-
near and non-linear analysis are very close to
the response values published by Rebora et al (7)
where a more complex concrete model and solid
brick elements have been utilised. In Fig. 4, the
deformed shape and the crack pattern during the
aircraft impact are illustrated. Concerning the
crack propagation, radial cracks appear first du-
ring loading at the interior surface around the
impacted area. Than, radial and circumferential
cracks appear at the exterior surface as well as

DEFORMED MESH

CRACK PATTERN

REACTOR BUILDING ANALYSIS	SLOOFSAN (CR)	REBORA (CR)
LINEAR ELASTIC (8)	4.03/4.08	3.32
NON-LINEAR (CRACKING) σt=5.5 MPa (.)	4.47	4.29
NON-LINEAR (CRACKING) σt=0.0 (.) + DEAD WEIGHT	7.21	-
NON-LINEAR (CRACKING) σt=0.0 (.)	9.13	-

(.) : CONCRETE TENSILE STRENGTH : σt
(8) : TWO MESHES USED

FIG.3 : HORIZONTAL DISPLACEMENT DUE TO AIRCRAFT
CRASH (AT POINT 1)
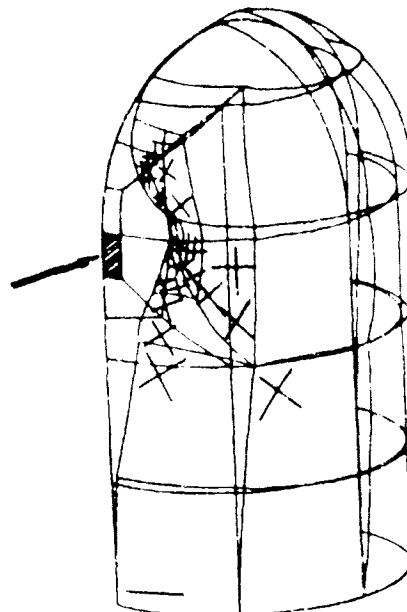
FIG.4 : NUCLEAR REACTOR BUILDING
UNDER SOFT-MISSILE (AIRCRAFT) IMPACT

through cracks in the impact zone. A tangential crack appear also at the containment base after the impact. SLOOPSAM analysis is fulfilled with the complete knowledge of the principal stresses in every place of the structure in both the concrete and the steel reinforcement. In this calculation, only multiaxial cracking appears without any concrete crushing nor steel yielding.

CHIMNEY COLLAPSE CAUSED BY AIRCRAFT COLLISION

The dynamic response of a tall chimney impacted by different aircrafts (military and civil) is studied using the present 3-D shell model. The scope of using the shell formulation is to examine the effects of all the non-linearities incorporated in SLOOPSAM and to understand the dynamic failure modes obtained by an explicit time integration approach. The aircraft loading functions for the military aircraft (Phantom F-4E) and the civil aircraft (Boeing 707-320) are defined in Fig.5.

A preliminary linear elastic analysis for the Boeing crash shows a well-known deflection mode with a maximum horizontal deflection at the top H of 5 m. , as shown in Fig. 6.a .

A complete different deflection shape is obtained, in Fig. 6.b , for the non-linear impact of the same civil aircraft. Due to this fast transient phenomena, only the impacted area is completely damaged with local bending failure mode at the top but without any loss of bending rigidity at the chimney base. Large rotations and horizontal displacements are observed at the top (H greater than 45 m.)

For the faster military aircraft collision, a more severe disintegration of reinforced concrete with a more pronounced shear failure mode is obtained, as shown in Fig. 6.c . The deflection at the top H exceeds the 40 m.
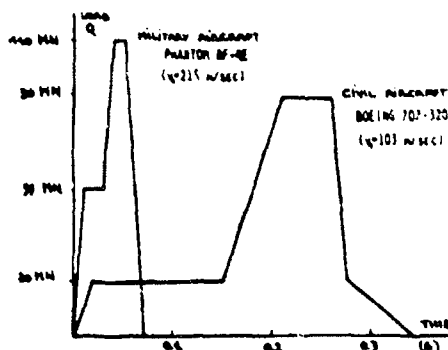
These highly non-linear analyses do not terminate when the finite elements start to be distorted, as shown in Fig. 6, but the analysis can be carried on until the internal resisting force vector vanishes completely in the impacted area, in presence of a total material disintegration . For the present structural behaviour simulation, all the disintegration factors (concrete cracking, concrete crushing, steel yielding, local steel buckling) have been encountered.

Unfortunately, no particular post-processor was available to correctly visualize the real local chimney collapse. Because, with the use of the present explicit non-linear dynamic analysis, the nodal points with their mass and velocity but without resisting forces (or springs connecting all of them together), are moving away and down (gravity field) like in the reality.
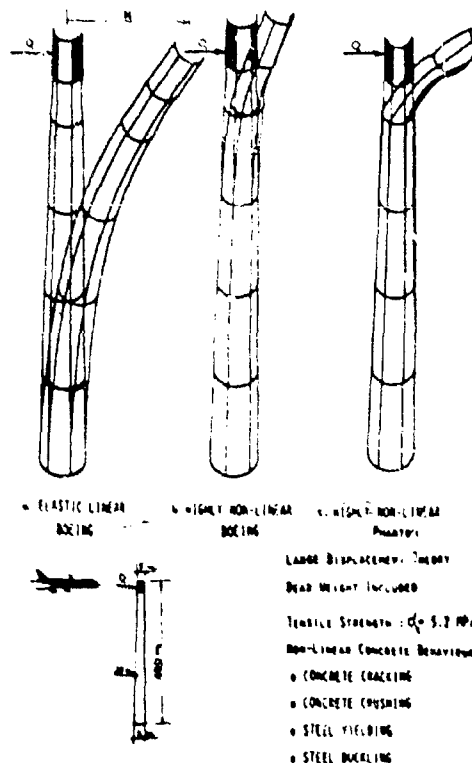

F16.6 : CHIMNEY COLLAPSE CAUSED BY AIRCRAFT IMPINGEMENT

F16.5 : AIRCRAFT LOADING FUNCTIONS

144

REFERENCES

1. Cedolin,L., Mulas,M.G., "Biax al Stress-Strain
   Relation for Concrete",J. of the Engineering
   Mechanics Div., ASCE, submitted for public.

2. Crutzen,Y., 'Non-Linear Transient Dynamic Ana-
   lysis of Thin Shells using the Semiloof Finite
   Element", Doctoral Thesis, Brussels Univ.,1979

3. Crutzen,Y.,Reynen,Y.,Villafane,E., "Concrete
   Structure Strength against Soft-Missile Impact
   ",Proceedings of RILEM-CEB-IABSS-IASS Inter-
   association Symposium,BAM,Berlin, June 1982.

4. Crutzen,Y., "Impact Damage in Reinforced Con-
   crete Shell Structures",ASCE-EMD Specialty
   Conference, Purdue Univ.,Lafayette, May 1983.

5. Donea,J., Giuliani,G., Halleux,J.P., "Predic-
   tion of the Non-Linear Dynamic Response of
   Structural Components using Finite Elements",
   Nucl. Eng. & Design,vol37, 1976.

6. Irons,B., Ahmad,S., "Techniques of Finite E-
   lements", Wiley & Sons, 1980.

7. Rebora,B., Zimmermann,Th., Wolf,J.P., "Dynamic
   Rupture Analysis of Reinforced Concrete Shells
   ",Nucl. Eng. & Design,Vol 37, 1976.

8. Reynen,J.,Crutzen,Y., "Explicit Dynamic Analy-
   sis with Semiloof",Proceedings of the Interna-
   tional Conference on Finite Element Methods ,
   Shangai, China. August 1982.

145

FRACTURE DIAGNOSIS IN STRUCTURES USING CIRCUIT ANALOGY[1]

Mehmet Akgun[2], Frederick J. Ju[3], and Thomas L. Paez[4]

The University of New Mexico
Albuquerque, New Mexico 87131

ABSTRACT

The paper uses the Kirchhoff's equations for the T- and Π-circuits to analogously simulate the beam vibration. Structures formed by straight beam segments can then be simulated by electrical meshes formed by T- or Π-circuits. In the paper the analogous circuits are also developed for the cracked beams. The natural frequencies of the circuits thus yields the natural frequencies of the structures with or without crack. In the inverse application, the change in frequencies leads to the location and assessment of the fracture damage of the structure.

The paper developed, specifically for the Π-circuit, a formalization of establishing the characteristic matrices. The standardized format makes it possible for adaptation to computer programming. An estimate of the algorithm is included for comparison of its advantage in the speed of computation.

1.0 Introduction

The diagnosis of fracture damage in structures may involve two steps: The first is the detection of the presence of damage, and the second is the determination of the location and intensity of the fracture [1][5]. The first step requires monitoring of some variables associated with the structure. The second is related to a quantitative interpretation of the first. In this paper the variables to be monitored are the first few modal frequencies of the structure. The data on changes of frequencies are used for the estimation of the location and the intensity of the fracture damage. The classical modal shape of beam oscillation is employed to discretized the mathematical model, which is analogous to the circuit equations describing the T- or Π-circuits.

Keropyan and Chegolin [2] surveyed the work done on electrical analogies for solving problems

in statics and dynamics of elastic structures. Their approach to frameworks with sideway involves either an iterative or a three-step procedure in solving the horizontal displacement of girders and is analogue-computer-oriented. In this paper, a modified and improved approach is developed, that is readily formalized and adaptable to digital programming. When the method is applied to free vibration of multi-story multi-span frame structures with or without cracks, natural frequencies of the analog circuit, hence modal frequencies of the frame with or without crack, can be determined by exciting the circuit with a variable frequency excitation, and by establishing the excitation frequencies at which response is maximum. Analytically this corresponds to finding zeros of a determinant. Multi-cell structures and structures with crack will be illustrated in the application.

2.0 Circuit Analogies

The classical modal shape $y(\xi)$ of a single section of a straight beam is:

$$y(\xi) = A\cosh\beta\xi + B\sinh\beta\xi + C\cos\beta\xi + D\sin\beta\xi \quad (1)[6]$$

where $\beta^4 = \rho\omega^2 L^4/EI$, ρ the lineal density, ω the modal frequency, L the beam element length, (EI) the beam stiffness and ξ the dimensionless length such that the two end points are $\xi_1 = 0$ and $\xi_2 = 1$. The set of slopes (y_1', y_2') and shears (V_1, V_2) can be expressed in terms of the set of resisting moments (M_1, M_2) and deflections (y_1, y_2) as follows:

$$
\begin{Bmatrix} y_1' \\ y_2' \\ V_1 \\ V_2 \end{Bmatrix} =
\begin{bmatrix}
-\dfrac{\overline{LS}}{ET} & -\dfrac{\overline{LT}}{ET} & -\dfrac{\overline{S'}}{L} & \dfrac{\overline{T'}}{L} \\
\dfrac{\overline{LT}}{ET} & \dfrac{\overline{LS}}{ET} & -\dfrac{\overline{T'}}{L} & \dfrac{\overline{S'}}{L} \\
\dfrac{\overline{S'}}{L} & -\dfrac{\overline{T'}}{L} & \overline{PS} & \overline{PT} \\
\dfrac{\overline{T'}}{L} & -\dfrac{\overline{S'}}{L} & -\overline{PT} & -\overline{PS}
\end{bmatrix}
\begin{Bmatrix} M_1 \\ M_2 \\ y_1 \\ y_2 \end{Bmatrix} \quad (2)
$$

---

[6]Numbers in parentheses denote the equations in this paper.

where $\bar{P} = EI \beta'/L^3$, $\bar{S} = (\coth \beta - \cot \beta)/2\beta$, $\bar{T} = (\csc \beta - \operatorname{csch} \beta)/2\beta$, $\bar{S}' = \beta(\coth \beta + \cot \beta)/2$, $\bar{T}' = \beta(\csc \beta + \operatorname{csch} \beta)/2$. The first two equations in (2) can be written as

$$
\begin{aligned}
y_1' &= (Z + Z_0) M_1 - Z_0 M_2 + E_1 \\
y_2' &= Z_0 M_1 - (Z + Z_0) M_2 + E_2
\end{aligned}
\bigg\}
\quad (3)
$$

where $Z = -(\bar{S} + \bar{T})L/EI$, $Z_0 = LT/EI$, $E_1 = (\bar{T}'y_2 - \bar{S}'y_1)L$ and $E_2 = (\bar{S}'y_2 - \bar{T}'y_1)/L$. Equations (3) are the Kirchhoff's equation for the active three terminal network shown in Figure 1. In this electromechanical analogy, moment and slope (M, y') are analogous to the electrical current and voltage, respectively. The coefficients, Z and E, are respectively the impedance and the potential source. The negative impedance shall pose no difficulty in the theoretical development. The natural frequencies, hence the modal frequencies of the analog frame, can be determined by exciting the circuit with a variable frequency excitation, and by establishing the excitation frequency at which response is maximum. With reference to Figure 1, a simple cantilever beam problem can be illustrated. The left part of the T-circuit is shorted, resulting in $y_1' = 0$, corresponding to the built-in end. The potentials E_1 and E_2 are computed based on $y_1 = 0$ and $V_2 = 0$ the last equation of (2). At modal frequency when a constant amplitude voltage of y_2' is input, M_2 diverges. The analysis becomes one to compute the zeros of the network impedance function $Z_{22} = y_2'/M_2$.

Modeling the cracked section in a beam shall follow the method of fracture hinge [1]. The crack is mechanically represented by a torsional spring of spring constant κ. Slope is thus discontinuous at the cracked section ($\Delta y' = M_c/\kappa$). Such discontinuity in the circuit analogy is represented by a voltage source of magnitude M_c/κ. The two parts of the beam, divided by the cracked section are each represented by a T-circuit as shown in Figure 2. The other continuity conditions are satisfied.

When the first two equations in (2) are inversed, we have this:

$$
\begin{Bmatrix} M_1 \\ M_2 \\ V_1 \\ V_2 \end{Bmatrix}
= \frac{EI \beta^2}{L^2}
\begin{bmatrix}
\frac{L}{\beta}S & \frac{L}{\beta}T & S' & -T' \\
\frac{L}{\beta}T & -\frac{L}{\beta}S & -T' & S' \\
S' & T' & \frac{\beta}{L}P & -\frac{\beta}{L}P' \\
T' & S' & \frac{\beta}{L}P' & -\frac{\beta}{L}P
\end{bmatrix}
\begin{Bmatrix} y_1' \\ y_2' \\ y_1 \\ y_2 \end{Bmatrix}
\quad (4)
$$

where $S = (\cosh \beta \sin \beta - \sinh \beta \cos \beta)/\alpha$, $T = (\sinh \beta - \sin \beta)/\alpha$, $P = (\cosh \beta \sin \beta + \sinh \beta \cos \beta)/\alpha$, $S' = \sinh \beta \sin \beta/\alpha$, $T' = (\cosh \beta - \cos \beta)/\alpha$, $P' = (\sinh \beta + \sin \beta)/\alpha$, $\alpha = \cosh \beta \cos \beta - 1$. The first two equations in (4) can be rewritten as

$$
\begin{aligned}
M_1 &= (G + G_0) y_1' - G y_2' + I_1 \\
M_2 &= G y_1' - (G + G_0) y_2' + I_2
\end{aligned}
\bigg\}
\quad (5)
$$

where $G = (S + T) EI \beta/L$, $G_0 = -TEI \beta/L$, $I_1 = (S'y_1 - T'y_2) EI \beta^2/L^2$, and $I_2 = (S'y_2 - T'y_1) EI \beta^2/L^2$. Equations (5) are the Kirchhoff's current equations for the active three terminal network shown in Figure 3. In this electromechanical analogy, moment and slope (M, y') are analogous to the electric current and voltage, respectively. G and T denote the admittances and the current sources, respectively. The negative admittance poses no difficulty in the theoretical development.

A single cantilever beam problem can be illustrated with reference to Figures 3 and 4. The left port of the π-circuit is shorted, resulting in $y_1' = 0$, corresponding to the built-in end. This yields the circuit in Figure 4. The current source I_2 is expressed in terms of the node voltage y_2, based on $y_1 = 0$ and $V_2 = 0$. The node equation produces $S - S'^2/P = 0$ which is the characteristic equation for the cantilever beam. It must be noted that this analysis does not hold for the clamped-clamped beam since α defined above is itself the characteristic equation for the clamped-clamped beam.

Similar to the T-circuit analogy, slope is discontinuous at the cracked section ($\Delta y' = M_c/\kappa$), giving rise to two more unknown slopes. Such discontinuity is represented in the analog circuit by an admittance of magnitude $-\kappa$. The two parts of the beam, divided by the cracked section, are each represented by a π-circuit as shown in Figure 5. The other continuity conditions are satisfied.

3.0 General Two-Dimensional Frame Structure

In a generic model of a two-dimensional multi-storied frame, for which there are n-stories and m-spans (thus m + 1 anchors), the analogous circuit network contains $n(2m + 1)$ interconnecting T-circuits. If there is a crack on any girder or any column, the number of T-circuits will increase by one. The magnitude of computation for modal frequencies involves principally the inversion of two matrices of orders $(3nm - n + 1)$ and (n) respectively.

In representing beam-frame structures, π-circuits corresponding to individual columns and girders joining at right angles are interconnected such that boundary conditions at the analog-frame joints are observed. Kirchhoff's current law is written in terms of the node voltages which correspond to the angles of rotation at the frame joints. Under free vibration the coefficient matrix must be singular, and zeros of its determinant yield modal frequencies of the frame structure. Order of the matrix is equal to the number of frame joints. For each crack introduced in one of the beam elements, order increases by two.

Order of the matrix involved for an n-story, m-span frame is thus $n(m + 1)$; $n(m + 1) + 2$ if there is a crack on any girder or column. The node equation can be established as $(\underline{U} - \underline{X}^T \underline{Z}^{-1} \underline{X}) \underline{y}' = 0$ where $\underline{X}$ is n by $n(m + 1)$, and $\underline{Z}$ is of order n $(n + 1$ by $n(m + 1) + 2$, and of order n + 1 respectively in the presence of a crack). The coefficient matrix $(\underline{U} - \underline{X}^T \underline{Z}^{-1} \underline{X})$ is symmetric. A step-by-step schematic procedure will now be described to compute the entries of the individual matrices without drawing any equivalent circuit. Reference will be made to Figure 6 which illustrates a two-dimensional frame with and without crack. For simplicity $m = 1$, $n = 2$, and uniform properties are assumed. With reference to Figure 6, each beam element is identified by a number. The numbering order begins at the left lowest column, proceeds up through the columns on the same line in n stories, returns back to the second anchor, proceeds up vertically, and in that order. Once the columns are finished, girders on each floor are numbered progressively from left to right starting with the first floor and continuing on with the upper floors. Quantities related to a beam element such as S, T, S', etc. are subscripted by the number of the element. The node is numbered by the column under the node. If there is a crack on a column (girder), the original number of the element refers to the upper (right) side of the column (girder) which is now represented by two beam elements. The lower (left) side is numbered following the largest number in the scheme. Due to discontinuity of slope at a crack, two new nodes are created on each side of the crack. In Figure 6b, cracks are represented by conductances $-1/\beta\theta_k$, where $\theta_k = EI/L\kappa_k$ is the sensitivity parameter [1] based on characteristic length L. The following steps will be presented in two parts:

3.1 Frame Without Crack (Figure 6a)

As a guidance $\underline{y}'$ and $\underline{y}$ vectors are arranged as $\underline{y}' = \{y_1 \ y_2 \ y_3 \ y_4\}^T$, $\underline{y} = \{y_1 \ y_2\}^T$ where y_1 and y_2 are the horizontal displacements of nodes 1 and 3, and 2 and 4, respectively.

1) To establish $\underline{U}$:

   a) diagonal entries u_{ii} corresponding to y'_i will be the sum of S values of the elements adjoining at the node i.

   b) off-diagonal entries u_{ij} will be T_k if ith and jth nodes are adjacent and kth beam element links them. Otherwise, $u_{ij} = 0$. Due to symmetry, $u_{ij} = u_{ji}$.

2) To establish $\underline{Z}$:

   a) diagonal entries z_{ii} will be the sum of β_k values of all the girder elements in the ith floor plus the sum of P values of all the columns adjoining at the ith floor, where β_k can be expressed in terms of β of the reference element as, $\beta_k = e_k\beta$.

b) off-diagonal entries $z_{i,i+1}$ will be negative of the sum of P' values of all the columns joining ith and i+1st floors. $z_{ij} = 0$ for $j > i + 2$ and $z_{ij} = z_{ji}$. $\underline{Z}$ is hence a tri-diagonal symmetric matrix.

3) To establish $\underline{X}$:

$\underline{X}$ is partitioned into m + 1 square submatrices of order n each. Namely,

$$\underline{X} = [\underline{X}^1 | \underline{X}^2 | \ldots | \underline{X}^{m+1}].$$

   a) diagonal entries $x_{ii}^k = S'_{n(k-1)+i} - S'_{n(k-1)+i+1}$, $i = 1,\ldots,n - 1$ and $x_{nn}^k = S'_{nk}$. Referring to Figure 6a, x_{ii}^k for the kth "wall", wall denoting the union of all the columns on the same line, is equal to S' value of the column under the node $n(k - 1) + i$ minus S' value of the column above the same node.

   b) off-diagonal entries $x_{i,i+1}^k = -T'_{(i-1)n+i+1}$ for $i = 1,2,\ldots,n - 1$. $x_{ij}^k = 0$ for $j \geq 2$ and $x_{ij}^k = -x_{ji}^k$ for $i \neq j$. $\underline{X}^k$ are thus tri-diagonal matrices. Referring to Figure 6a, $x_{i,i+1}^k$ is equal to the negative of the T' value for the column above node $n(k - 1) + i$.

$\underline{X}^T \underline{Z}^{-1} \underline{X}$ is thus in the form

$$\underline{X}^T \underline{Z}^{-1} \underline{X} = \begin{bmatrix} \underline{U}_{11} & \underline{U}_{12} & \cdots\cdots & \underline{U}_{1,m+1} \\ \underline{U}_{12}^T & \underline{U}_{22} & & \vdots \\ \vdots & & \ddots & \vdots \\ \underline{U}_{1,m+1}^T & & & \underline{U}_{m+1,m+1} \end{bmatrix}$$

(6)

where $\underline{U}_{ij} = (\underline{X}^i)^T \underline{Z}^{-1} \underline{X}^j$ are symmetric matrices of order n.

Based on the above procedure, the following matrices are obtained for the frame in Figure 6a:

$$\underline{U} = \begin{bmatrix} S_1 + S_2 + S_5 & T_2 & T_5 & 0 \\ T_2 & S_2 + S_6 & 0 & T_6 \\ T_5 & 0 & S_3 + S_4 + S_5 & T_4 \\ 0 & T_6 & T_4 & S_4 + S_6 \end{bmatrix}$$

(7)

$$\underset{\sim}{Z} = \begin{bmatrix} \beta_5 + P_1 + P_2 + P_3 + P_4 & -P'_2 - P'_4 \\ & \\ -P'_2 - P'_4 & \beta_6 + P_2 + P_4 \end{bmatrix} \quad (8)$$

$$\underset{\sim}{X} = \begin{bmatrix} S'_1 - S'_2 & -T'_2 & \vline & S'_3 - S'_4 & -T' \\ & & \vline & & \\ T'_2 & S'_2 & \vline & T'_4 & S'_4 \end{bmatrix} \quad (9)$$

3.2 Frame With Cracks (Figure 6b)

y' and y vectors are now given as $y' = \{y'_1\ y'_2\ y'_3\ y'_4\ y'_7\ \overline{y}_7\ y'_8\ \overline{y}_8\}^T$, $y = \{y_1\ y_2\ y_7\ y_8\}^T$ where y_7 and y_8 are the deflections at the two cracks. Node equations corresponding to nodes which are not adjacent to a cracked element will remain the same relative to the previous case. The new matrices will be of the form

$$\underset{\sim}{U}_c = \left[\begin{array}{c|c} \underline{U} & \underline{A} \\ \hline \underline{A}^T & \underline{B} \end{array}\right], \quad \underset{\sim}{Z}_c = \left[\begin{array}{c|c} \underline{Z} & \underline{C} \\ \hline \underline{C}^T & \underline{D} \end{array}\right],$$

$$\underset{\sim}{A}_c = \left[\begin{array}{c|c|c|c|c} \underline{X}^1 & \cdots & \overline{X}^{m+1} & \underline{E}_1 & \underline{E}_2 \\ \hline \underline{F}_1 & & \underline{F}_{m+1} & \underline{H}_1 & \underline{H}_2 \end{array}\right] \quad (10)$$

where barred matrices are modified forms of Equations (7)-(9). ith row in $\overline{\underline{U}}$ is unchanged relative to $\underline{U}$ if the ith node is not adjacent to a cracked element. ith row in $\overline{\underline{Z}}$ remains the same if there is no crack on any column adjoining with the ith floor. $\overline{\underline{X}}^k$ is the same as $\underline{X}^k$ if there is no crack on the kth wall. $\underline{F}_k = 0$ if there is no crack on the kth wall and on any of the girders adjacent to the kth wall.

Following the procedure in Part 3.1, the submatrices for the frame in Figure 6b are obtained as

$$\underline{U} = \begin{bmatrix} S_1 + S_2 + S_8 & T_2 & 0 & 0 \\ T_2 & S_2 + S_6 & 0 & T_6 \\ 0 & 0 & S_3 + S_5 + S_7 & 0 \\ 0 & T_6 & 0 & S_4 + S_6 \end{bmatrix} \quad (11)$$

$$\underline{A} = \begin{bmatrix} 0 & 0 & T_8 & 0 \\ 0 & 0 & 0 & 0 \\ T_7 & 0 & 0 & T_5 \\ 0 & T_4 & 0 & 0 \end{bmatrix},$$

$$\underline{B} = \begin{bmatrix} S_7 - M_4 & M_4 & 0 & 0 \\ M_4 & S_4 - M_4 & 0 & 0 \\ 0 & 0 & S_8 - M_5 & M_5 \\ 0 & 0 & M_5 & S_5 - M_5 \end{bmatrix} \quad (12)$$

where $M_k = 1/\beta\theta_k$.

$$\underline{Z} = \begin{bmatrix} \beta_5 + \beta_8 + P_1 + P_2 + P_3 + P_7 & -P'_2 \\ -P'_2 & \beta_6 + P'_2 + P_4 \end{bmatrix}, \quad \underline{C} = \begin{bmatrix} -P'_7 & 0 \\ -P'_4 & 0 \end{bmatrix} \quad (13)$$

$$\underline{D} = \begin{bmatrix} P_4 + P_7 & 0 \\ 0 & P_5 + P_8 \end{bmatrix}, \quad \overline{\underline{X}}^1 = \underline{X}^1, \quad \overline{\underline{X}}^2 = \begin{bmatrix} S'_3 - S'_7 & 0 \\ 0 & S'_4 \end{bmatrix} \quad (14)$$

$$\underline{E}_1 = \begin{bmatrix} 0 & 0 \\ T'_8 & 0 \end{bmatrix}, \quad \underline{E}_2 = \begin{bmatrix} T'_7 & -T'_4 \\ -T'_5 & 0 \end{bmatrix}, \quad \underline{F}_1 = \begin{bmatrix} -T'_7 & 0 \\ 0 & T'_4 \end{bmatrix} \quad (15)$$

$$\underline{F}_2 = 0, \quad \underline{H}_1 = \begin{bmatrix} S'_7 & -S'_4 \\ 0 & 0 \end{bmatrix}, \quad \underline{H}_2 = \begin{bmatrix} 0 & 0 \\ S'_8 & -S'_5 \end{bmatrix} \quad (16)$$

The frequency analysis applied to a two-story single-span frame with six equal length elements and with data of relative changes of 0.010 and 0.015 in the first two frequencies respectively yields, under the assumption of presence of single crack, four possible damage pairs: $(\theta_1, e_7) = (0.108, 0.906)$, $(\theta_2, e_7) = (0.182, 0.816)$, and due to symmetry, $(\theta_3, e_7) = (0.108, 0.906)$, $(\theta_4, e_7) = (0.182, 0.816)$, where e_7 indicates relative crack location measured from the lower end of each column. The crack is thus on one of the columns. In order to determine the actual damage pair within symmetry, relative change in the third frequency is required. (θ_1, e_7) and (θ_2, e_7) would produce relative changes of 0.0074 and 0.0155 respectively in the third natural frequency. It may be argued that if the relative change in the third frequency could not be measured, then it must be small and thus (θ, e_7) or (θ, e_7) is the likely damage pair.

4.0 Conclusions

Use of circuit analogy in computing model frequencies of a two-dimensional multi-story frame with or without cracks on it has been developed into a formalized method. The method enables the study of effect of cracks on modal frequencies of frame structures, as well as determination of the

location and intensity of a crack, given suffi-
cient number of modal frequency changes. Computa-
tion of modal frequencies of an n-story m-span
frame with k cracks on it requires finding zeros
of a determinant of order $n(m + 1) + 2k$. In the
finite element method, using generally required
twenty elements per basic beam segment, there are
$40 n(m + 1)$ nodes each with two degrees of free-
dom. The size of computation savings is almost
40-fold. However, using circuit analogy in deter-
mining the location and intensity of a crack may
involve $n(2m + 1)$ computations of zeros of a
determinant of order $n(m + 1) + 2$.

References

1. Ju, F. D., Akgun, M., Paez, T. L., Wong,
    T. E., "Modal Method in Diagnosis of Fracture
    Damage in Simple Structures," ASME 103rd
    Winter Annual Meeting, November 14-19, 1982,
    Phoenix, Arizona, Practical Applications of
    Mechanical Vibration, ASME publication,
    November 1982.

2. Keropyan, K. K. and Chegolin, P. M., Electri-
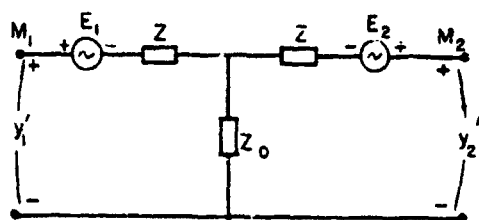   cal Analogies in Structural Engineering,
    Edward Arnold, Ltd., 1967.

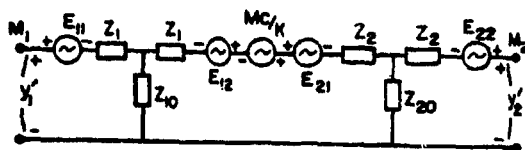Figure 4. Analog circuit for a cantilever beam.
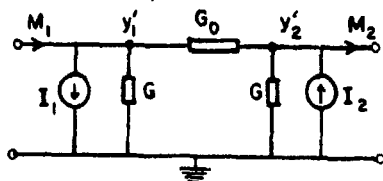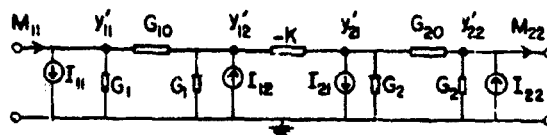

Figure 5. Fracture circuit.

Figure 1. T-Circuit.
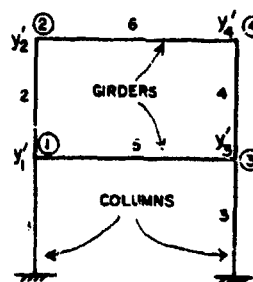
Figure 6a. Two-story, single-span frame
without crack.

Figure 2. Fracture CKT.
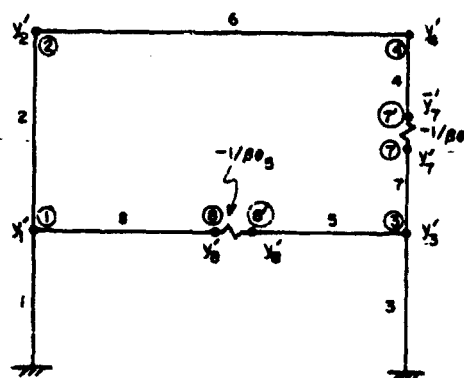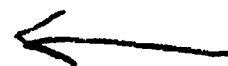

Figure 3. π-Circuit.

Figure 6b. Two-story, single-span frame
with two cracks.

DYNAMIC LOADING: MORE THAN JUST A DYNAMIC LOAD FACTOR

W. Karthaus and J.W. Leussink

Prins Maurits Laboratory TNO
P.O. Box 45, 2280 AA Rijswijk
The Netherlands

ABSTRACT

The response of a simply supported beam to uni-
form blast loading is determined by using the
normal-mode technique. Especially for short load
durations the higher modes become important. The
rotary inertia and shear force deformation have
to be taken into account. At short load durations
high peaks of shear force appear near the supports
immediately after loading.

1. INTRODUCTION

In literature such as TM 5-1300 [1] and Biggs
[2] the starting points for the design of explo-
sion resistant constructions are the static
shapes of deflections of the construction parts
and the static force distribution.
For the dynamics usually a dynamic load factor
is introduced. Experiments show clearly, how-
ever, that dynamics is more than just statics
multiplied by a DLF. Plates that are simply sup-
ported at two opposite edges and would collapse
in the middle in the event of static loading,
appear to collapse close to the supports some-
times when exposed to a uniformly distributed
explosion load.
Apparently not only the amplitude, but also the
shape of the deflection, shear force, and bending
moment diagrams are influenced by the loading
rate and the duration of the load.
To get more fundamental insight in the dynamics
of explosion loaded plates a theoretical study
has been performed of the behaviour of an ideal-
ized simply supported elastic beam.
The beam will be subjected to an uniformly distri-
buted blast load, i.e., the time variation in the
load is the same at any point x.
The blast load is simplified by a peak triangular
pulse of variable duration.

2. BERNOULLI-EULER BEAM

It is obvious to start with a simple prismatic
flexural beam that has uniform density ρ and has
constant stiffness EI. The governing equation of
motion during elastic response is the following
well-known equation [3]:

$$EIW''''(x,t) + \rho A \ddot{W}(x,t) = q(x,t) \qquad (1)$$

This equation takes into account transverse in-
ertia and bending deformation. To solve this
equation we use the normal-mode technique [3].

Express the transverse motion $W(x,t)$ as the product
of a time function $G(t)$ and a displacement function
$F(x)$. For free transverse vibration (i.e.,
$q(x,t) = o$) each displacement function $F(x)$ des-
cribing one of the normal modes of the beam gives
a solution if $G(t)$ is chosen as a periodic function
with a period that corresponds to the mode under
consideration.

Thus $F_n(x) = \sin \frac{n\pi x}{1}$ and $G_n(t) = A_n \sin\omega_n t +$

$+ B_n \cos\omega_n t \qquad n = 1,2,3,\ldots$

with $\omega_n^2 = n^4\pi^4 \frac{EI}{\rho Al^4}$ which gives for $W(x,t)$:

$$W(x,t) = \sum_{n=1}^{\infty} \sin \frac{n\pi x}{1} (A_n \sin\omega_n t + B_n \cos\omega_n t) \qquad (2)$$

A particular solution of eq. (1) can be found by
splitting up the load function $q(x,t)$ in function
corresponding to the normal modes as well:

$$q(x,t) = \sum_{n=1}^{\infty} q_n(x,t) = \sum_{n=1}^{\infty} \sin \frac{n\pi x}{1} Q(t) \qquad (3)$$

The complete solution of eq. (1) can be found by
combining the calculated responses for every
$q_n(x,t)$.
The constants A_n and B_n are established from the
initial conditions. When the displacement $W(x,t)$
is known the bending moment $M(x,t)$ and shear force
$D(x,t)$ can be calculated by the following equations

$$M(x,t) = - EI W''(x,t) \text{ and } D(x,t) = M'(x,t) \qquad (4)$$

Calculations have been made for several response
durations [4]. Interesting responses are found for
the extreme values of the triangular load, namely
the step load and the impulse load.
Results of the step load are as follows:
As for the deflection, the bending moment and the
shear forces, the maximum values are dominated by
the 1st mode response. Immediately after loading the
influence of the higher normal modes are percept-
ible, but the corresponding response values are small.
Results of the impulse load are as follows:
The deflections can be calculated and have the
shapes as illustrated in Fig. 3. The bending moment
calculations yield quite whimsical results, which
cannot be clarified. The influence of the higher
modes is very apparent.
For the impulse load it appears not to be possible
to calculate the shear force. The series for the
shear force does not converge.

As a result of the calculations it can be said that
for long load duration the first normal mode domi-
nates the beam response i.e., for response calcu-
lations methods as given in [1] and [2] are useful.
For very short load durations deflections can be
calculated, but the calculation of bending moments
yields doubtful results. High natural modes have
to be taken into account, which mean that the in-
fluence of rotary inertion and shearing deformation
cannot be neglected.
To enable the calculation of the beam response for
short load duration a more complicated equation
of motion is needed.

3. TIMOSHENKO BEAM

An equation of motion that takes into account the
influence of rotary inertia and shearing deform-
ation is given by Timoshenko [3]. Fig. 1 shows a
free body diagram of a beam element.

$$T = \rho A \ddot{W} dx \qquad (5a)$$
$$R = \rho I \ddot{\Psi} dx$$

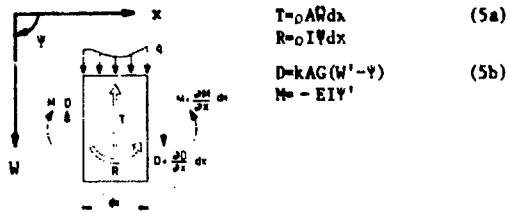$$D = kAG(W' - \Psi) \qquad (5b)$$
$$M = -EI\Psi'$$

Fig. 1. Free body diagram of beam element

The equations of motion are derived from the equi-
librium equations for forces and moments which
after filling in the relation (5a) and (5b) result
in

$$EIW'''' + \rho A\ddot{W} - \rho I\left(1 + \frac{E}{kG}\right)\ddot{W}'' + \frac{\rho^2 I}{kG}\dddot{W} = q - \frac{EI}{kAG}q'' + \frac{\rho I}{kAG}\ddot{q} \qquad (6a)$$

and

$$EI\Psi'''' + \rho A\ddot{\Psi} - \rho I\left(1 + \frac{E}{kG}\right)\ddot{\Psi}'' + \frac{\rho^2 I}{kG}\dddot{\Psi} = q' \qquad (6b)$$

Parameters W, Ψ, D and M are functions of x and t.
To establish W(x,t), D(x,t) and M(x,t) we have to
solve eq. (6a) and (6b). And here again the normal-
mode technique described before is used. The deter-
mination of the frequencies of the normal modes
produce two sets of natural frequencies' (see Fig.2).
This means that for each value of n there are two
different frequencies. Analysis of the nature of-
the types of motions corresponding to these two
sets of frequencies show [4] :
The lower frequencies in the first set describe
mainly the bending part in the response and the
higher frequencies in this set describe mainly the
shear part in the response. Generally speaking this
set of frequencies describes the transverse motion
of the response.
The second set of frequencies originates from the
coupling term for rotary inertia and shear force
deformations in the equation of motion. The combi-
nation of this set to the response is equal for
bending and shear but the corresponding displace-
ments for shear and bending are always opposite in

phase. This results in a more longitudinal type of
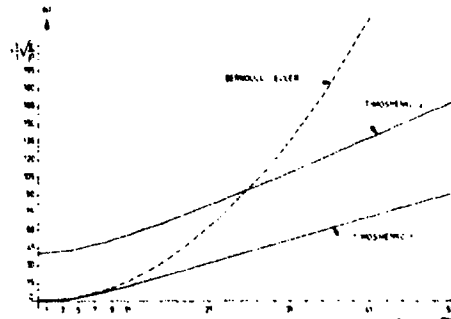motion in the beam response.

Fig. 2. Natural frequencies as function of n [4].

From Fig. 2 it is seen that for the Timoshenko beam
the frequencies of the higher modes are proportio-
nal to n, the number of the mode, instead of n^2 in
case of a Bernoulli-Euler beam. This means a better
chance for determining the impulse response, including
shear force, because the series will converge better.
Response calculations [4] for the impulse load
yield the deflection, bending moment and shear
force diagrams shown in Fig.3.
The parameter values used in the computation are:

$$E = 30.10^9, \quad \rho = 2400, \quad \nu = 0,2, \quad K = 0,845, \quad \frac{l}{n} = 20.$$

The deflection is given for time steps $\Delta t = \frac{1}{200}T_1$
where T_1 is the duration of the first mode.
The bending moments and shear forces are given for
$t = 1,6.10^{-5} T_1$, $0,0006 T_1$, $0,005 T_1$ and $0,0185 T_1$
respectively.
Letter n denotes the number of natural frequencies
that are taken into account. As unit for the scale
is chosen the maximum value of deflection, moment
and shear force respectively when only the first
mode is taken into account.
Worth noting in Fig. 4 are in the first place the
high shear force peaks at the supports immediately
after loading and secondly the disturbances in
shear force and moments that run from the supports
to the middle of the beam. The velocity at which
these peaks travel is about 2075 m^{-1} [4], which
equals the Rayleigh wave velocity calculated from

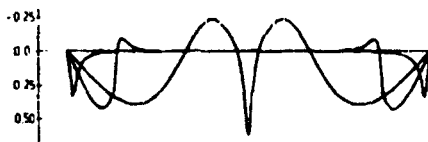$$\frac{1,14\nu + 0,862}{1 + \nu} \sqrt{\frac{G}{\rho}} \qquad [5]$$

with $G = 1,25.10^{10}$
$\nu = 0,2$
$\rho = 2400$

This is a very promising result because a velocity
of the order of the transverse wave velocity is
expected.

DEFLECTION   n = 41

00
0075
0.15

BENDING MOMENT   n = 251

-0.25
0.0
0.25
0.50
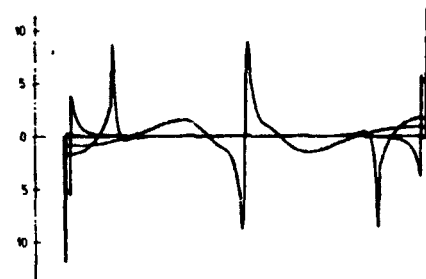
SHEAR FORCE   n = 2501

10
5
0
5
10

Fig. 3. Deflection, bending moment, shear
force diagrams

4. DISCUSSION OF THE RESULTS

Questions that remain are: what is the influence
of the damping on the results, and how close is
this approximation to reality.
Damping: Especially for the shear force calcula-
tions which need a high number of natural frequen-
cies [4] damping may be an important factor. The
important peak values at the supports, however,
appear immediately after loading so that damping
does not have any influence here yet. In the middle
of the beam the peak values may be a bit lower as
a result of the reduced influence of the higher
modes (Material damping in concrete - 0,01 for all
frequencies [6]).
Validation of the theories: The validity of the
theories are judged on the basis of an example.
Suppose a semi-infinite elastic beam having a cir-
cular cross-section with radius a. For the wave
velocity c of a harmonic disturbance placed at the
beginning of the beam an exact solution for v=0,29
is available (known as the theory of Pochhammer and
Chree [7]). The wave velocity is also established
with both the Bernoulli-Euler and Timoshenko
theory.

The wave velocity appears to be dependent on the
frequency of the disturbance. The Bernoulli-Euler
theory yields one dispersion relation, Timoshenko
two, one for each frequency set, and Pochhammer-
Chree give an infinite number of dispersion rela-
tions.
The results are presented in Fig. 4. It shows the
dispersion relations of Bernoulli-Euler and Timo-
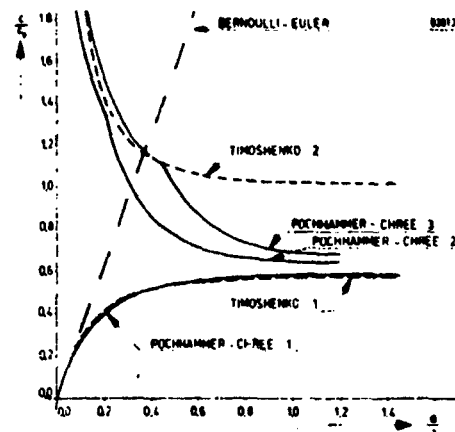shenko and three of the Pochhammer-Chree relations.

Fig. 4. Wave velocity as function of wave length

From Fig. 4 we learn the following:
a. For increasing frequency values the B-E wave
velocity reaches infinity. This means that high
frequency disturbances are transmitted instant-
iously. Only very low frequencies coincide with
the first P-C curve.
b. The first P-C and first T wave velocity curves
coincide and have as asymptote the Rayleigh
wave velocity [4].
c. The second T-curve envelopes the other P-C
curves and has as asymptote the longitudinal
wave velocity C_0 (velocity of sound).

It can be concluded from this exercise that:
1. BE-theory gives proper solutions for dynamic
loads that are governed by low frequency compo-
nents.
2. T-theory can be applied in all cases. The meas-
ure in which this theory is exact is determined
by the contribution of the second frequency set
to the solution.

Calculations with the Timoshenko-theory applied to
simple beams show that the response is mainly de-
termined by the first frequency set. The influence
of the second frequency set is strongest in the
determination of the shear force. The difference
in maximum shear force values calculated with or
without the second frequency set, however, is less
than 4 percent

5. CONCLUSIONS

a. For load durations $t_d > T_1$ the first mode is
   governing the response. Methods for response
   calculations as given in [1] and [2] can be used.

b. For load duration $t_d < T_1$ higher modes have to
   be taken into account.

c. For very short load durations $t_d \ll T_1$ very high
   modes become important in the beam response.
   Rotary inertia and shearing deformation have to
   be taken into account.

d. For short load duration peaks in shear force
   appear near the supports. These peaks are a
   qualitative explanation of the deviating fail
   behaviour mentioned in the introduction.
   To be able to design for these high shear force
   peaks it is necessary to know the material be-
   haviour under extreme deformation rates.

e. Thanks to the aid of the computer the analytic-
   al solution derived earlier leads readily to
   surprising results, which with the finite ele-
   ment methods which are frequently applied at
   present cannot or can hardly be determined.

LITERATURE

[1] TM 5-1300, Structures to resist the effects
    of accidental explosions, 1969.

[2] Biggs, J.M.
    Structural Dynamics
    McGraw-Hill Book Company, 1964.

[3] Timoshenko, S. c.s.
    Vibration problems in engineering
    4th ed. John Wiley and Sons.

[4] Leursink, J.W.
    Respons van een dynamisch belaste ligger.
    Analyse op basis van eigentrillingsvormen.
    M.Sc.Thesis, University of Technology, Delft.
    June 1983.

[5] Achenbach, J.D.
    Wave propagation in elastic solids,
    North-Holland Publishing Company, 3rd ed. 1980.

[6] Koten, H. van
    Structural damping
    Heron, vol. 22, 1977, no. 4.

[7] Abramson, H.N., Plass, H.J., Ripberger, E.A.
    Stress wave propagation in rods and beams.
    Advances in Applied Mechanics, 1958.

THE EFFECTS OF INDIRECT-FIRE MUNITIONS
ON FRAMED STRUCTURES

Bruce L. Morris
and
Patrick H. Zabel

Southwest Research Institute
San Antonio, Texas

ABSTRACT

This paper reports an effectiveness evaluation of the use of indirect-fire munitions against steel- and reinforced concrete-framed structures in an urban environment. Effects include collapse of columns due to lateral blast loads, crushing of columns by vertical blast loads, response of interior and exterior walls to blast and fragments, response of personnel to blast overpressures and wall debris, and the formation and location of rubble caused by the detonations of these munitions.

"TYPICAL" STRUCTURES

Two "typical" office/hotel structures, each 200 ft by 200 ft in plan and ten stories tall, were designed using reinforced concrete or steel structural frames. Columns were spaced at 20-ft centers in each direction with a floor-to-floor height of 12 feet, and the designs were governed by References 1 and 2 for the concrete and steel structures, respectively. While the required column sections vary through the height of the structure, the first-floor members are considered typical of all stories for ease of presentation. For the steel structure, the corner, exterior wall and interior columns are W8x67, W12x106 and W14x211 sections, respectively. The concrete corner column is 12 in. square with 5.08 sq. in. of steel reinforcement, the exterior columns are 16 in. square with 10.2 sq. in. of steel, and the interior columns are 22 in. square with 15.2 sq. in. of steel.

COLUMN RESPONSE TO LATERAL LOADS

An explosion between building floors will produce a lateral load and deflection on the columns between those floors. If the permanent deformation of the column, Δ, is great enough, the dead and live structural loads, P, will cause collapse of the column because of its inability to resist the now-combined axial load and moment produced by the deflection. The critical, mid-height deflection of the steel sections was calculated from

$$\Delta = \frac{1.18 M_p}{P} \left(1 - \frac{P}{P_y}\right)$$

where the moment capacity, M_p, was determined for the weaker axis. The reinforced concrete columns were analyzed using conventional interaction diagrams. These critical deflections are summarized in Table 1.

TABLE 1. CRITICAL MID-HEIGHT LATERAL DEFLECTIONS

Column Location	Deflection (inches)	
	Steel Column	Concrete Column
Corner	5.4	6.9
Exterior	5.8	10.7
Interior	7.7	12.6

The response of any of these columns to a lateral, time-varying load is dependent upon both the peak pressure or force and on its duration (impulse). Isodamage curves (relating the peak pressure and impulse required to provide the critical deflections of Table 1) were generated for a point load at mid-height of each of the six column types. Since a blast does not produce a true point load, the pressures were assumed to act over an area equal to the exposed width of the column squared. These curves are displayed in Figure 1. A pressure/impulse pair falling above and to the right of a curve will produce a mid-height deflection greater than that specified in Table 1, while a pair below and to the left will produce a smaller deflection. The curves for the steel columns reflect bending about the weaker axis of the section.

All of the munitions selected for evaluation (the 105 mm HE M1, the 155 mm HE M107, the 8-in. HE M106 and the 4.2 in. mortar HE M329A1) are capable of producing the required minimum impulses shown in Figure 1, but the required stand-off distance from the loaded surface of the column is at most six inches. A blast this close to the column requires some means to assure detonation of the shell at that location, but no such mechanism exists. A direct hit is then the only way to destroy a column. The likelihood or probability of achieving a direct hit on the selected columns by any of the munitions above is, at best, a function of the probable errors (a round-to-round variation for a fixed aim point) in both range and deflection. References 3 through 6 provide these data for a chosen range of fire of 5000 meters. The number of rounds required to achieve a 0.95 probability of hit on a single column was calculated and results are presented in Table 2. It must be pointed out that these results assume that there are no nearby buildings which would interfere with incoming rounds and that the walls and upper floors of the structure under attack do not shield the interior columns. We also assume that none of the projectiles are duds. None of these conditions
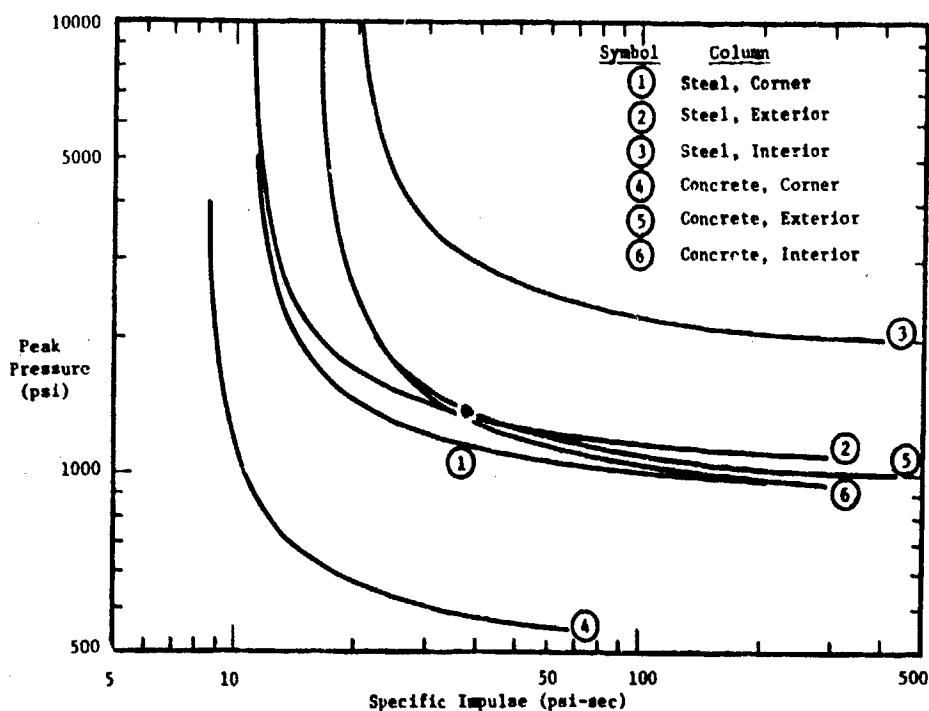
Figure 1. Isodamage Curves

TABLE 2. NUMBER OF SHELLS REQUIRED FOR A 0.95 PROBABILITY
OF HIT ON A SINGLE COLUMN*

Shell	Steel Columns			Concrete Columns		
	Corner	Exterior	Interior	Corner	Exterior	Interior
105 mm	586	403	355	403	355	236
155 mm	564	393	324	393	324	233
8-inch	276	188	157	188	157	113
4.2" Mortar	6240	4340	3608	4340	3603	2603

would exist in a real structure and with real pro-
jectiles; therefore, the number of shells required
would be much higher than those shown in Table 2.

COLUMN RESPONSE TO VERTICAL LOADS

An artillery round detonating between floors of
a framed structure will produce vertical loads on
the columns supporting the floor slab and beams near
the detonation point. These vertical loads are the
result of the reflected pressure from the shell and
of the quasi-static pressure buildup in the room in
which the explosion occurs. Venting through windows
is treated. This quasi-static pressure is a strong
function of the volume into which the explosion pro-
ducts expand, and this volume is determined by the
strength of the internal walls (weaker walls will
be destroyed by the initial blast and will cause a

lower qua.i-static pressure as the gases expand in-
to adjacent rooms). While the columns immediately
under the detonation will likely crush, the columns
which support them are protected somewhat in that
the maximum load which they must resist is limited
to the carrying capacity of columns above them. Ex-
tensive structural collapse from an internal detona-
tion is thus possible but will not be discussed fur-
ther because of the many unknowns which affect the
pressure loadings.

RESPONSE OF INTERIOR AND EXTERIOR WALLS
TO BLAST AND FRAGMENTS

Exterior walls of framed structures serve pri-
marily as an environmental shield and are not part
of the load-carrying system of the building. They
range in thickness from a heavy brick-and-block com-

bination to relatively light panels of glass, metal or other material. Interior walls range from nominal dry-wall construction to 4 in. hollow tile and plaster. Reference 7 has given an average room size for these structures of 13 ft by 20 ft. If one of the previously listed rounds detonates in the center of such a room, any of the above walls will be removed by the resulting initial blast and/or quasi-static pressure. There is the possibility, however, that the very early-time failure of light interior walls would sufficiently increase the volume into which the quasi-static pressure expands that the heavy exterior wall may stand after the detonation of a 105-mm round.

The 105 mm, 155 mm and 8 in. HE shells depend upon fragmentation for a major portion of their effectiveness against personnel. The Gurney equation (Reference 8) predicts initial fragment velocities of 2950 ft/sec, 3320 ft/sec and 3570 ft/sec for these shells, respectively. An average fragment weight of 90 grains is typical. Fragments of this weight and the above velocities can perforate a wall consisting of a total of two inches of plaster and still have a residual velocity greater than that required to penetrate winter clothing (References 9 and 10). These fragments also have the capability to perforate up to three or more drywall partitions and still pose a severe threat to personnel in other rooms. However, the floor slabs form an effective shield protecting personnel on adjacent floors from fragments.

RESPONSE OF PERSONNEL TO BLAST OVERPRESSURE

The blast overpressure from a detonating shell can kill or injure nearby personnel through any of several mechanisms: primary blast (damage to air-containing tissues of the lungs), secondary damage (impact by objects which are accelerated by the blast), tertiary effects (whole body translation and impact on rigid surfaces), and eardrum rupture. Secondary damage will not be considered further. Researchers at the Lovelace Foundation (References 11 and 12) have developed pressure versus duration lethality curves for humans due to primary blast damage. These curves suggest that the initial blast at a distance of 10 ft from any of the selected munitions is below the threshold for lung damage, but the quasi-static pressure from the 8-in. shell in a 20 ft x 13 ft room will result in less than 1% survival and the 155 mm shell will result in less than 10% survival. Personnel have a 98% or greater chance of survival from primary lung damage due to blast from the 105 mm or 4.2 in. mortar HE shells.

Blast overpressure and impulse serve to produce whole-body motion and, if rigid impact surfaces are assumed, an impact velocity of 10 ft/sec represents a "mostly safe" level (References 12, 13 and 14). The method developed in Reference 15 indicates that the velocity imparted to a 154-lb (70 kg) person is much less than this "mostly safe" level.

Hirsch (Reference 16) has concluded that there is a 50% rupture probability of eardrums of exposed personnel at an overpressure of 15 psi, and Refer-

ence 13 supports this value for "fast" rising over-pressures with durations of from 0.003 to 0.4 seconds. The threshold for eardrum rupture occurs at 5 psi. The direct blast from a 155 mm, 8-in. or 4.2-in. mortar shell in the 20 ft by 13 ft room exceeds the level for 50% eardrum rupture as does the quasi-static pressure from the 105 mm round. It must be observed that all of these blast effects or injuries are in addition to the more lethal fragmentation effects of the munitions.

PERSONNEL RESPONSE TO DETONATION DEBRIS IMPACT

The impact and point detonation of an artillery shell on the outside of a brick building wall will probably produce brick-size fragments in the room behind the wall. The velocity of these fragments is dependent on the amount of explosive in the shell, and the velocities for a 6.2-lb brick can range from 138 ft/sec to 300 ft/sec for 105 mm and 8 in. shells, respectively. The probability of death (P) from projectile-induced trauma to the thorax has been given in Reference 17 as

$$P = \frac{1}{1 + \exp[\alpha + \beta \ln(MV^2/WD)]}$$

where M = projectile mass, grams
  V = velocity of projectile, m/sec
  D = projectile diameter, cm
  W = mass of target animal, kg
  α = 34.90
  β = -4.39.

Combining the above brick mass and velocity with a 70-kg human target, the 105 mm, 155 mm and 8-in. shells all provide a probability of death greater than 0.95 for a person struck by such a projectile. There are, however, a very few such projectiles, and the probability of being hit by one is small.

FORMATION AND LOCATION OF RUBBLE

Sustained artillery and aerial bombardments of World War II produced enormous quantities of building rubble from the collapse of the load-bearing brick wall structures which were prevalent at the time. Today's framed structures do not have the amounts of material available to convert to rubble if one agrees that the floor slabs of the structures will not be destroyed and that entire structures should not collapse. Shell detonations in the center of a room behind the building exterior walls will probably (as shown earlier) rupture those walls and propel the brick or other material pieces into the street below. The maximum ground range for a brick or block piece coming from the top floor of our "typical" building is approximately 25 feet. A 10-story, heavy clad structure (brick and block exterior walls) will have around 38% of its exterior surface covered by glass (Reference 7), and the in-place volume of the wall materials is 39 ft³ per foot of street frontage. If a 1.3 expansion factor is used to include the effects of partly broken blocks and if the total exterior wall were blown out from the structure, the rubble volume would be 51 ft³ per foot of building frontage. Each 13 ft by 10 ft room wall section must be removed individually. The

resulting rubble pile should be triangular in shape, extending 25 feet from the building base and approximately 4 ft deep at the building wall.

The debris from a light clad structure (glass, metal or other thin material exterior walls) can consist of a number of relatively large-in-area, thin panels. These walls have an average thickness of 6.7 in. (Reference 7), of which 4.1 in. is light, non rubble-producing insulation. The expected ground range impact distance is difficult to predict because of lifting or sailing effects on the panels, and the expected rubble depth should be less than one foot. Such walls would produce trash instead of rubble. Trash would not be an effective barrier to vehicular travel.

These rubble distribution patterns are based on wall failure under the effects of the direct blast from a shell detonating at room center. If a super quick fuze mode shell hits the outside wall, the debris will be blown into the building and will not contribute to the rubble in the street below. If the wall should fail under the quasi-static rather than initial blast loading, the debris velocities and ground impact distances would be slightly greater because of the increased impulse imparted to the wall materials.

SUMMARY

The above analyses have shown that modern, framed buildings should not suffer severe structural damage or collapse under the effects of the indirect fire munitions considered. The exterior and interior walls can be destroyed on a room-by-room basis, and personnel in the rooms on the same floor are not afforded any real protection against the normal fragmentation of the rounds. The rubble produced by artillery bombardments of urban areas should not seriously hamper vehicular traffic in the streets.

ACKNOWLEDGEMENT

REFERENCES

1. Building Code Requirements for Reinforced Concrete, ACI 318-63, American Concrete Institute, 1963.

2. Specification for the Design, Fabrication and Erection of Structural Steel for Buildings, American Institute of Steel Construction, 1963.

3. Firing Table (FT), 105-AS-2, "Cannon, 105 mm Howitzer, M103, on Howitzer, Light, Self-Propelled, 105 mm, M108, Firing Cartridge, HE, M1...," (Charge 4, Table G), November 1967.

4. FT 155-AM-1, "Cannon, 155 mm Howitzer, M185, on Howitzer, Medium, Self-Propelled, 155 mm, M109A1,...," (Charge 4G, Table G), September 1972.

5. FT 8-Q-1, "Cannon, 8-inch Howitzer, M201, on Howitzer, Heavy, Self-Propelled, 8-inch M110A1, Firing Projectile, HE, M106," (Charge 4G, Table G), January 1976.

6. FT 4.2-H-2, "Mortar, 4.2 inch: M30, Carrier, 107 mm Mortar: M106A1 and M106 Firing Cartridge, HE, M329A1...," (800 mils w/Extension, Table E) August 1968.

7. Ellefsen, Richard and L. E. Wicks, "Characteristics of Urban Terrain," NSWC Tech Report TR 79-224, June 1979.

8. Gurney, R. W., "The Initial Velocities of Fragments from Bombs, Shells and Grenades," Report No. 648, Ballistic Research Laboratory, September 1947.

9. Butler, Stanley C., "Ballistic Limits of Tissue and Clothing (Addendum to BRL Tech Note 1645)," AMSAA Technical Report No 230, July 1978.

10. Sperrazza, J. and Kokinakis, W., "Ballistic Limits of Tissue and Clothing," BRL Technical Note No. 1645, January 1967.

11. Bowen, I. E., et al, "Estimate of Man's Tolerance to the Direct Effects of Air Blast," DASA 2113, October 1968, AD 693-105.

12. White, C. S., et al, DNA 2738T, July 1971, AD 734-208.

13. White, C. S., "The Scope of Blast and Shock Biology and Problem Areas in Relating Physical and Biological Parameters," Annals of the New York Academy of Science, Vol 152, Art 1, pp 89-102, October 1968.

14. Clemedson, C. J., et al, "The Relative Tolerance of the Head, Thorax and Abdomen to Blunt Trauma," Annals of the New York Academy of Science, Vol 152, Art 1, pp 187+, October 1968.

15. Baker, W. E., et al, "Workbook for Predicting Pressure Wave and Fragment Effects of Exploding Propellant Tanks and Gas Storage Vessels," NASA CR-134906, July 1975.

16. Hirsch, A. E., "The Tolerance of Man to Impact," Annals of the New York Academy of Sciences, Vol 152, Art 1, pp 168-171, October 1968.

17. Handbook of Human Vulnerability Criteria, Chapter 9, "Projectile-Induced Blunt Trauma," Special Publication EB-SP-76011-9, Edgewood Arsenal, May 1976.

MODELS FOR DAMAGE DIAGNOSIS IN SDF STRUCTURES

Ming-Liang Wang[1], Thomas L. Paez[2], and Frederick Ju[3]

The University of New Mexico
Albuquerque, New Mexico 87131

ABSTRACT

In structural engineering it is imperative to design each system to survive the inputs anticipated over the design life of the structure. Strong motion inputs cause systems to execute nonlinear responses, and during strong motion responses structures accumulate damage. Therefore, the capability to model nonlinear response and to assess the damage level in a structure is essential for optimal design.

Techniques for the diagnosis of damage in inelastic structures have been developed. The dissipated energy in mechanical systems is taken as a measure of damage accumulation. Two models for the simulation of damaged structural response have been developed. The objective of this study is to use these models to estimate the amount of energy dissipated due to a strong motion input.

The results show that structural damage can be predicted, even in the presence of measurement noise.

1. Introduction

The ultimate goal of the structural engineer is to design structures to survive preestablished environments. Structures subjected to strong motion inputs respond inelastically and accumulate damage. This damage accumulation may lead to failures. Therefore, in an accurate analysis of structural behavior, nonlinear response as well as the potential for damage accumulation must be considered. In this investigation, it is assumed that the dissipation of energy is related to the accumulation of damage.

To assess damage accumulation, a model describing structural behavior is required. This model is characterized by its parameters. In order to determine the parameters of a system, measured input and response data can be used with

a structural identification procedure. In this study the least squares approach is used to identify the parameters of damaged systems using simulated measured input and response data. In order to make the simulated data realistic the ideal input and response are first generated, then measurement noise is added to the signals.

Two models for the simulation of inelastic single-degree-of-freedom (SDF) structural response are proposed. The first is a higher order linear ordinary differential equation with constant coefficients. The second is a second-order linear ordinary differential equation with time varying coefficients. Methods for the identification of the parameters of these systems are presented in this paper.

The differential equation governing the response of an inelastic SDF system is a second-order ordinary differential equation with hysteretic stiffness term. Some recent investigations (e.g., Reference 1) have used a higher order linear model to simulate the behavior of the actual system because the hysteretic character of the response of an inelastic system can be approximately matched by the hysteresis in the response of a higher order linear system.

It is known that a structure subjected to an extreme environment displays a response with time dependent characteristics. Particularly, a structure executing an extreme response can display diminishing stiffness and variable damping. The investigation summarized in Reference 2 demonstrates this behavior.

As damage accumulates in a structural system, its strength diminishes. It is assumed that dissipated energy is a measure of structural damage. As the energy dissipated by a system increases, the residual strength decreases. The basis for this assumption is established in Reference 3.

The objective of this study is to demonstrate that the two models described above can be used to simulate the response of a damaged structure. The relative merits of each model are discussed. The results of some numerical experimentation using simulated data are presented. These investigate the feasibility and accuracy of the models.

[1]Research Assistant, Dept. of Civil Engineering
[2]Associate Professor, Dept. of Civil Engineering
[3]Professor, Dept. of Mechanical Engineering

2.0 Parameter Identification for Structural Models

The differential equation governing the response of an SDF system is

$$m\ddot{z} + u = f , \qquad (1)$$

where m is the structural mass, z is the displacement response, dots denote differentiation with respect to time, f is the forcing function, and u is the restoring force. This equation models the response of an actual system. When the system response is nonlinear, u(t) is a complicated function reflecting the hysteretic character of the system. In this study, two models will be developed to simulate the behavior of a hysteretic system. These are equivalent linear models.

2.1 Higher Order Linear Model

The first model to be considered is a higher order linear equivalent model. It is assumed that the restoring force in Eq. 1 is governed by the equation

$$\sum_{j=0}^{M} c_j u^{(j)} = c_{M+1} \dot{z} + z , \qquad (2)$$

where c_j, $j = 0,\ldots,M + 1$ are constants characterizing the model; a superscript (j) refers to the jth time derivative of the quantity it follows; and M reflects the order of approximation of the linear system to the actual system. The objective of the analysis is to use measured data to identify the parameters in the model. Once this is done, the energy dissipated in the system during structural response can be evaluated.

The following procedure is used to perform the parameter identification for the higher order linear model. Combine Eqs. 1 and 2 in the following way. Solve Eq. 1 for u, then take derivatives of the resulting expression. Use these in Eq. 2. The result is

$$\sum_{j=0}^{M} c_j(f^{(j)} - m z^{(j+2)}) = c_{M+1} \dot{z} + z . \qquad (3)$$

Since the parameter identification is to be carried out in the frequency domain, Fourier transform Eq. 3. Evaluate the modulus squared on both sides of the equation; the result is

$$\left| \sum_{j=0}^{M} c_j((i\omega)^j F(\omega) - m(i\omega)^{j+2} Z(\omega)) \right|^2$$

$$= \left| (c_{M+1}(i\omega) + 1) Z(\omega) \right|^2 . \qquad (4)$$

This equation is assumed to govern the response amplitudes in the frequency domain. If 1) the system under consideration were linear, 2) all measurements were noise free, and (3) all Fourier transforms were exact, then measured data could

satisfy Eq. 4. But Eqs. 1 and 2 are meant to model nonlinear systems; noise is practically always present in physical signals, and the discrete Fourier transform is often used in practical analyses. Therefore, measured data will not generally satisfy Eq. 4. An error term, $\epsilon(\omega)$, must be added to Eq. 4 to establish equality. This yields

$$\epsilon(\omega) = \left| \sum_{j=0}^{M} c_j((i\omega)^j F(\omega) - m(i\omega)^{j+2} Z(\omega)) \right|^2$$

$$- \left| (c_{M+1}(i\omega) + 1) Z(\omega) \right|^2 , \qquad (5)$$

where $F(\omega)$ and $Z(\omega)$ are the Fourier transforms of the measured input and response signals. The optimum model parameters are those which minimize the error, in some sense.

Define the square of the model error as follows.

$$\epsilon^2 = \int_{\omega_a}^{\omega_b} \epsilon^2(\omega) \, d\omega . \qquad (6)$$

ω_a and ω_b are frequencies which band the characteristic frequency of the SDF system. The system constants, c_j, $j = 0,\ldots,M + 1$, are those whose values satisfy the sequence of equations

$$\frac{\partial \epsilon^2}{\partial c_j} = 0 , \qquad j = 0,\ldots,M + 1 . \qquad (7)$$

These constants are optimal in a least squares sense.

In this investigation computations involving two specific cases, where M = 0 and M = 1, were performed. The governing equations (Eq. 3) in these cases are second and third order differential equations, respectively. In all cases, a search procedure can be used to solve Eqs. 7. In the cases where M is small, approximate analyses can also be executed.

When M = 0, the constants c_0 and c_1 must be evaluated. An approximate analysis can be carried out (Reference 3) where small-valued cross terms are neglected. Then the solution of Eqs. 7 can be evaluated in closed form. Numerical investigations have shown the approximate analysis to be quite accurate in this case.

When M > 1 approximate analyses of Eqs. 7 can still be performed, but more accurate results are obtained using an exact search procedure. In the present study an iterative Newton-Raphson approach was used to find the solution of Eqs. 7. Other techniques, including gradient search techniques, can also be used to solve Eqs. 7. Numerical examples have shown that the analysis described here can be executed.

Some numerical examples, solved using the techniques developed in this section, are summarized in Section 3.0.

2.2 Time Varying Linear Model

The second model for inelastic system response is a time varying linear model. It is assumed that the restoring force in Eq. 1 is governed by the equation

$$u(t) = c(t) \dot{z} + k(t) z , \qquad (8)$$

where $c(t)$ is a time varying damping and $k(t)$ is a time varying stiffness. The specific forms used to represent $c(t)$ and $k(t)$ are given below.

$$c(t) = (1 + \alpha t) c_0 . \qquad (9)$$

$$k(t) = (1 + \beta t) k_0 . \qquad (10)$$

α, c_0, β, and k_0 are constants. As in the previous analysis, the objective is to use measured data to identify the parameters in the model. Once this is done, the energy dissipated in the system during structural response can be evaluated.

The following procedure is used to perform the parameter identification for the time varying linear model. It is assumed that the parameters α and β are relatively small compared to one. Then the perturbation method can be used to express the response. The response is assumed to be approximately

$$z(t) = z_0(t) + \alpha z_\alpha(t) + \beta z_\beta(t) . \qquad (11)$$

This expression can be used, along with Eqs. 8, 9, and 10, in Eq. 1 to obtain the governing differential equation. The coefficients of the terms 1, α, and β can be established, and equated to zero, to obtain the sequence of governing equations

$$m\ddot{z}_0 + c_0\dot{z}_0 + k_0 z_0 = f , \qquad (12a)$$

$$m\ddot{z}_\alpha + c_0\dot{z}_\alpha + k_0 z_\alpha = -c_0 t \dot{z}_0 . \qquad (12b)$$

$$m\ddot{z}_\beta + c_0\dot{z}_\beta + k_0 z_\beta = -k_0 t z_0 . \qquad (12c)$$

Since the parameter identification is to be carried out in the frequency domain, Eqs. 11 and 12 must be Fourier transformed. The results are

$$Z(\omega) = Z_0(\omega) + \alpha Z_\alpha(\omega) + \beta Z_\beta(\omega) \qquad (13)$$

$$(-m\omega^2 + ic_0\omega + k_0) Z_0(\omega) = F(\omega) \qquad (14a)$$

$$(-m\omega^2 + ic_0\omega + k_0) Z_\alpha(\omega) = c_0(Z_0(\omega) + \omega Z_0'(\omega))$$
$$(14b)$$

$$(-m\omega^2 + ic_0\omega + k_0) Z_\beta(\omega) = -ik_0 Z_0'(\omega) \qquad (14c)$$

where $Z(\omega)$, $Z_0(\omega)$, $Z_\alpha(\omega)$ and $Z_\beta(\omega)$ are the Fourier transforms of $z(t)$, $z_0(t)$, $z_\alpha(t)$ and $z_\beta(t)$; and primes denote differentiation with respect to frequency.

Equations 14 can be solved sequentially and used in Eq. 13 to obtain an approximate expression for the Fourier transform of the response. The modulus of the resulting equation can be evaluated to obtain

$$\left| Z(\omega) \right| = \left| [1 + \alpha c_0(H(\omega) + \omega H'(\omega))\right.$$
$$- ik_0\beta H'(\omega)] H(\omega) F(\omega)$$
$$\left. + (\alpha c_0\omega - ik_0\beta) H^2(\omega) F'(\omega) \right| \qquad (15)$$

where

$$H(\omega) = [(k_0 - m\omega^2) + i(\omega c_0)]^{-1} . \qquad (16)$$

This equation is assumed to govern the response amplitudes in the frequency domain. Measured data will not generally satisfy Eq. 15 for the reasons discussed following Eo. 4. An error term $\epsilon(\omega)$, must be added in Eq. 15 to establish equality when measured data are used. Let $Z^{(m)}(\omega)$ be the modulus of the Fourier transform of the measured response. Then,

$$\epsilon(\omega) = \left| Z(\omega) \right| - \left| Z^{(m)}(\omega) \right| , \qquad (17)$$

where $Z(\omega)$ is the expression obtained when the Fourier transform of the measured input is used on the right side of Eq. 15.

The optimum model parameters can be determined, in a least squares sense, by minimizing the square of the model error. The square of the model error is

$$\epsilon^2 = \int_{\omega_a}^{\omega_b} \epsilon^2(\omega) \, d\omega . \qquad (18)$$

ω_a and ω_b are frequencies banding the characteristic frequency of the SDF system. The error is minimized when the model parameters are chosen to satisfy

$$\frac{\partial \epsilon^2}{\partial \alpha} = 0 = \frac{\partial \epsilon^2}{\partial c_0} = \frac{\partial \epsilon^2}{\partial \beta} = \frac{\partial \epsilon^2}{\partial k_0} . \qquad (19)$$

These equations can be solved simultaneously using a search procedure. In this study an iterative Newton-Raphson approach was used to solve Eqs. 19. Other search techniques could also be used.

Some numerical examples were solved using the technique developed in this section. One of these is summarized in Section 3.0.

2.3 Computation of Dissipated Energy

It was stated in the introduction that the energy dissipated in a structure is a measure of the damage accumulated in the system. The energy dissipated in a structure can be calculated in the process of computation of the structural response. Once the parameters of a structural system have been identified the restoring force can be calculated using either Eq. 2 or Eq. 8. The formula for dissipated energy is

$$F_D = \int_{z(-\infty)}^{z(\infty)} u(z) \, dz \ , \tag{20}$$

where $u(z)$ is the restoring force as a function of displacement, and $z(-\infty)$ and $z(\infty)$ are the displacements at the times minus and plus infinity. A change of variables can be made in the above expression to obtain

$$E_D = \int_{-\infty}^{\infty} u(z(t)) \, \dot{z}(t) \, dt \ . \tag{21}$$

In the numerical solution of Eq. 1, z, $\dot{z}$, z, and u are determined at each time step. The energy dissipated can be incrementally computed using these values.

3.0 Numerical Example

Two numerical examples are solved in this section using the approaches established in Section 2. In both examples the parameters of an SDF system are identified. The higher order linear model of Section 2.1 and the time varying linear model of Section 2.2 are used. The parameters of the higher order linear model are identified for the cases where $M = 0$ and $M = 1$. Once the model parameters are identified, the method of Section 2.3 is used to calculate the energy dissipated in each model.

The input used in this study is an oscillatory random function with decaying exponential amplitude. The input is modeled by the expression

$$f(t) = e^{-at} \sum_{j=1}^{N} c_j \cos(\omega_j t - \phi_j) \ , \qquad 0 \le t \le T \ . \tag{22}$$

a is the amplitude decay rate of the input; N is the number of harmonic components in the input; c_j, $j = 1,...,N$ are the input amplitudes; ω_j, $j = 1,...,N$ are the frequencies where the input has power, ϕ_j, $j = 1,...,N$ are mutually independent uniform random variables distributed on the interval $(-\pi, \pi)$. The input is an approximately normally distributed, nonstationary random process. The parameters of the input used in the examples are listed in Table 1.

Table 1. Parameters of the Forcing Function

$a = 0.1 \qquad N = 50$

$c_j = 10.0 \ , \qquad j = 1,...,50$

$\omega_j = (1.8 + 0.008 \, j) \, \pi \ , \qquad j = 1,...,50$

The input generated using these parameters is shown in Figure 1.

In each example a different SDF system was analyzed. In the first example a linear system was considered. In the second example a nonlinear hysteretic system was used. The system parameters are listed in Table 2.

Table 2. System Parameters

Example 1	Example 2
m = 1.0	m = 1.0
c = 1.26	c = 1.26
k = 39.48	k = 39.48
E_D = 11028	k_y = 0
	D = 4.0
	E_D = 8225

m, c, and k are the mass, damping, and elastic stiffness. k_y and D are the yield stiffness and yield level of the inelastic system. The actual response of the inelastic system is shown in Figure 2. The energy dissipated during each response is given in Table 2.

It is assumed that noise may be present when the input and response are measured. To simulate this, the generated input and response are modified by the addition of white noise. A ten percent noise-to-signal ratio was used in the examples. The noisy input and inelastic response of Example 2 are shown in Figures 3 and 4.

The parameters of the higher order linear model ($M = 0$ and $M = 1$) and the time varying linear model were identified using the input and the responses, described above, in a computer program (Reference 3). The parameter identification was performed using both the noise-free and noisy signals. The results of the computations are given in Tables 3, 4, and 5. The model responses are compared to the actual response in Figures 5, 6,

Table 3. Linear Model Parameters (M = 0), Energy Dissipated

	Noise-Free Case Actual Response:		Noisy Case Actual Response:	
	Linear (ex. 1)	Nonlinear (ex. 2)	Linear (ex. 1)	Nonlinear (ex. 2)
c_0	40.0	34.6	39.2	32.0
c_1	1.28	1.75	1.37	1.95
E_D	10720	7700	10900	6476

Table 4. Linear Model Parameters (M = 1), Energy Dissipated

	Noise-Free Case Actual Response:		Noisy Case Actual Response:	
	Linear (ex. 1)	Nonlinear (ex. 2)	Linear (ex. 1)	Nonlinear (ex. 2)
c_0	39.2	30.3	34.3	32.0
c_1	1.28	3.95	2.98	2.60
c_2	0	0.07	0.05	0.02
E_D	11090	7598	11710	6803

Table 5. Time Varying Linear Model Parameters, Energy Dissipated

	Noise-Free Case Actual Response:		Noisy Case Actual Response:	
	Linear (ex. 1)	Nonlinear (ex. 2)	Linear (ex. 1)	Nonlinear (ex. 2)
α	0	0.0010	~0	0.011
c_0	1.27	1.71	1.29	1.54
β	0	-0.0079	~0	0.0026
k_0	39.3	40.3	38.4	32.8
E_D	10741	8186	10929	7016

and 7 for Example 2 (where the actual response is nonlinear).

The results show that all models match the actual response quite well. Especially, the peak response in each model matches the actual peak response well. Of course, the linear models do not permit permanent set; therefore, the final displacement of each model is in error. Using displacement response as a criterion, the third order and time varying models appear to provide the best results. Using dissipated energy as a criterion, the time varying model provides the best result.

4.0 Summary and Conclusions

The objective of this study was to develop approximate linear models for the simulation of inelastic system response and the measurement of damage accumulation in a structure. It was assumed that energy dissipated is related to the accumulation of damage. The model parameters were identified, then the energy dissipated during a strong motion was calculated. The displacement response and the energy dissipated in each model were compared with the displacement response and energy dissipated in the actual structure.

Three basic models were considered in this study. These are second- and third-order linear models with constant coefficients, and a second order linear model with time-varying parameters. The frequency domain approach was used in all the parameter identification computations.

The results of the numerical examples lead to the following conclusions.

1. Linear and nonlinear hysteretic SDF systems can, in some respects, be accurately modeled using second- and third-order linear differential equations with constant coefficients, and a second-order linear differential equation with time-varying coefficients. The models provide accurate simulations when displacement response and energy dissipated criteria are used.

2. The frequency domain approach can be used to identify model parameters of all three models when the force and response measurements are noisy.

3. The second-order model with time-varying coefficients provides the best simulation of system response and energy dissipated among the three models considered.

Acknowledgement

References

1. Wen, Y. K., "Stochastic Response Analysis of Hysteretic Structures," Proceedings of the Speciality Conference on Probabilistic Mechanics and Structural Reliability, ASLE, Tucson, Arizona, January 1979.

2. William H. Townsend and Robert D. Hanson, "Reinforced Concrete Connection Hysteresis Loops," Reinforced Concrete Structures in Seismic Zones, ACI Publication SP-53, 1974.

3. Wang, M. L., Paez, T. L. and Ju, F. D., "Mathematical Models for Damageable Structures," The Bureau of Engineering Research, The University of New Mexico, Albuquerque, NM, February 1983.
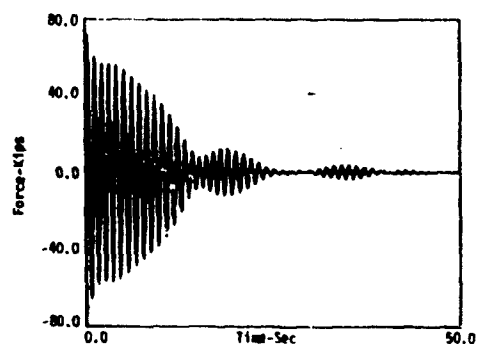

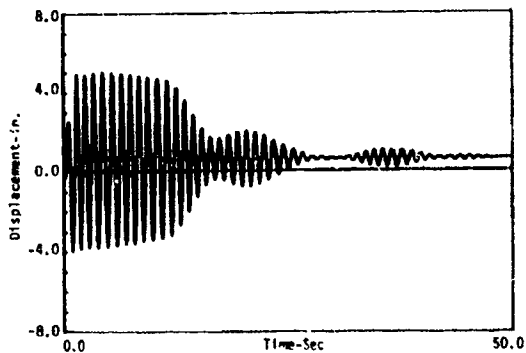Figure 1. Signal used to simulate actual input.

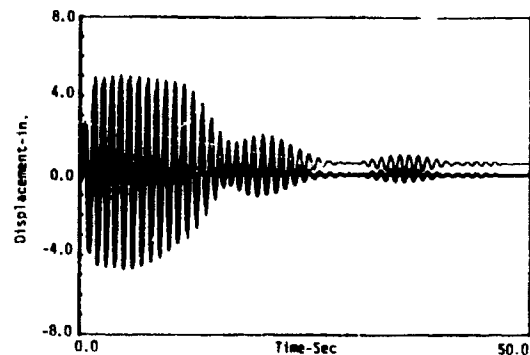Figure 2. Signal used to simulate actual displacement response.

Figure 3. Input force plus noise.

Figure 4. Displacement response plus noise.
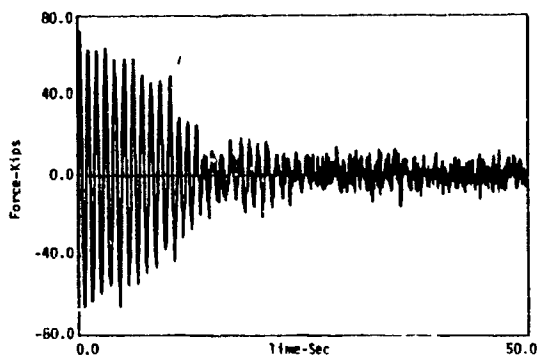

Figure 5. Comparison between actual response (thin line) and model (M = 0) response (thick line).
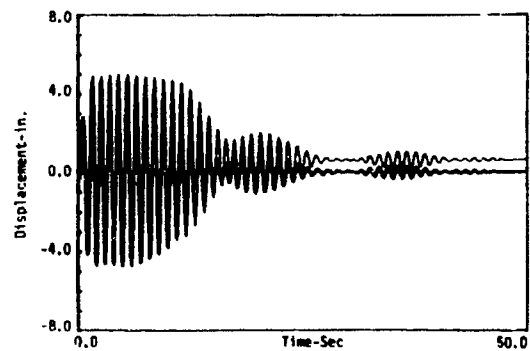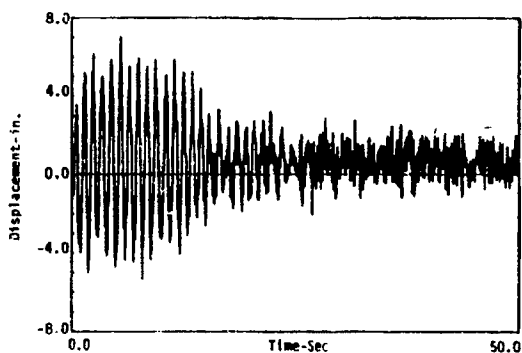

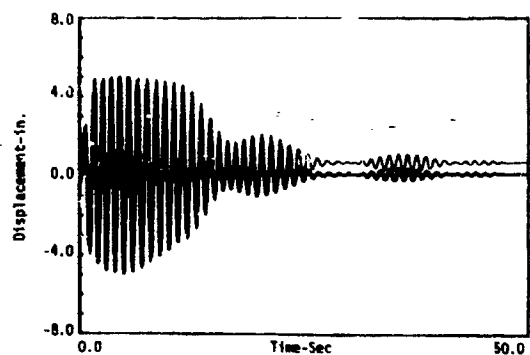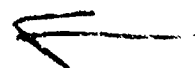Figure 6. Comparison between actual response (thin line) and model (M = 1) response (thick line).

Figure 7. Comparison between actual response (thin line) and model (time varying parameter) response (thick line).

164

TODAY'S CONSTRAINTS DRIVE AMMO MAGAZINES UNDERGROUND

W. A. Keenan and J. E. Tancreto

Naval Civil Engineering Laboratory
Port Hueneme, California

ABSTRACT

Aboveground magazines for storage of ammunition are increasingly difficult to accommodate within constraints imposed by explosives safety, physical security, survivability, and fleet operational requirements. The Navy has developed an alternative design concept, called a chimney magazine. The chimney magazine consists of a box for weapons storage, two chimneys for access to storage, a horizontal sliding door over each chimney, a blanket of soil over the box, and a straddle trailer to retrieve and transport weapons. The concept dramatically increases the physical security and survivability of storage and dramatically decreases the encumbered land area without compromising explosives safety requirements for noncommunication of explosions, damage to storage from explosions, and protection of life and property in inhabited areas from blast, ground shock, and debris. It is concluded the chimney magazine offers high potential of being a cost effective concept to meet DOD requirements for tomorrow's ammo depot.

INTRODUCTION

Ammunition storage magazines comprise the largest investment of real property inventory at shore activities supporting the Naval ammunition logistics system. The traditional magazine design is an aboveground, arch- or box-shaped structure bermed with soil. The soil berm, 2 feet deep over the roof, extends horizontally beyond the walls where it slopes down over three sides of the structure. The fourth side is a vertical headwall with doors for horizontal access to storage. The design concept is perennial, dating back almost to the discovery of gun-powder.

Safety is achieved by separation distance. Freedom from risk of sympathetic detonation between magazines is achieved by providing a minimum separation distance between magazines. Freedom from risk of damage to contents from explosions in other magazines is achieved by blast hardening headwalls and doors. Safety of unrelated areas outside the magazine depot is achieved by providing sufficient separation distance to limit the risk of injury and damage from blast, fragments and debris caused by an inadvertent explosion. For 350,000 pounds Net Explosive Weight (NEW) of storage per magazine, the required separation distance to unrelated areas exceeds 3,524 feet and encumbers over 896 acres of land.

PROBLEM

The existing concept for ammo storage encumbers large areas of valuable real estate - at a time when the Navy is already faced with a rising cost of land acquisition (which is sometimes not available at any price), shrinking supply of buildable land, and increasing encroachment by the private community. Further, aboveground magazines provide limited physical security - at a time when both the terrorist threat and the arms, ammunition and explosives requiring secure storage are increasing. The problem is particularly acute at coastal activities and certain installations in Europe. Faced with this dilemma, the Naval Civil Engineering Laboratory (NCEL) is developing technology and concepts for alternative solutions. The goals are new design concepts for ammo storage, maintenance, testing and transfer facilities which are affordable and also meet explosives safety, physical security, survivability, and fleet operational requirements.

SOLUTION

A new design concept for ammo storage magazines is illustrated in Figures 1 and 2. The
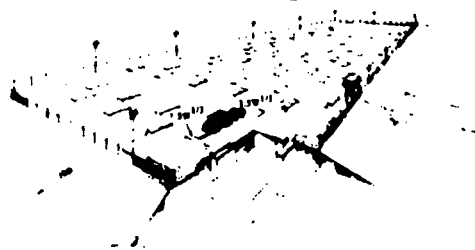

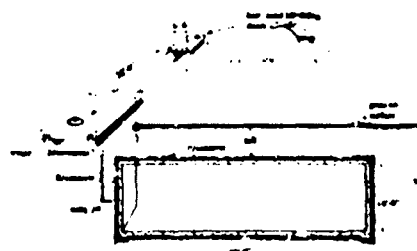Figure 1. Ammunition depot of chimney magazines.

Figure 2. Interior of chimney magazine.

magazine depot has a flat surface. The minimum spacing between magazines in any direction is about $1.50W^{1/3}$, where W is the NEW limit of any magazine. This is the minimum spacing allowed by DOD explosives safety standards to prevent explosion communication between underground storage chambers. For W = 300,000 pounds NEW, the minimum spacing between magazines would be 100 feet, compared to 84 feet ($1.25W^{1/3}$) side-to-side spacing and 402 feet ($6W^{1/3}$) front-to-rear spacing required by DOD safety standards for aboveground, earth-covered, box-shaped magazines.

Essential elements of the design concept are a rectangular-shaped box for weapons storage, two chimneys for access to storage in two bays, a horizontal sliding door over each chimney, a blanket of soil over the storage box, and a straddle trailer to retrieve and transport weapons.

Storage Box: Ammunition is stored in a large box-shaped structure constructed of conventional reinforced concrete. Many magazines in the current Navy inventory are arch-shaped structures but studies of the present and projected types and mix of Navy weapons call for a box-shaped structure for maximum space utilization. Interior dimensions of the box are about 70 x 70 x 18 feet high. The box has two storage bays, separated by two reinforced concrete columns designed to safely support the roof loads (Figure 3). The entire box is designed to safely resist dead plus live loads. Effects from an explosion in an adjacent magazine are not expected to dictate the design loads – the effective mass of the roof slab plus the soil above it should be sufficient to safely absorb the blast energy from explosions in other magazines. The rated storage capacity of the box is about 300,000 pounds NEW.
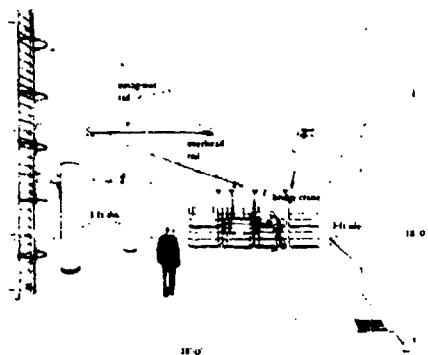
Chimney Access: Access to storage is through a reinforced concrete chimney cast monolithic with the storage box, as shown in Figure 2. A chimney is located at one end of each bay to service storage in its bay. Interior horizontal dimensions of the chimney are about 28 x 6.5 feet to allow easy access to the largest containerized weapon and palletized unit of ammunition in the projected Navy inventory. The chimney extends about 12 inches above the elevation of the soil blanket. The chimney extension above the ground surface serves

as a curb to prevent surface water from entering the chimney and to force alignment of a straddle trailer over the chimney.

An interior view of the chimney is shown in Figure 3. The floors of the chimney and box are at the same elevation. Each chimney has a personnel access-escape ladder and a floor drain leading to a sump pit. The area of the vertical wall common to the chimney and storage box is open for ease in moving weapons between the chimney and box.

Sliding Door: Each chimney in the magazine depot supports a horizontal sliding door, as shown in Figures 1, 2 and 4. The door, constructed of massive concrete and steel, is designed to safely resist the blast overpressure from an explosion in an adjacent magazine. It also is expected to meet minimum requirements of a high-security door to provide a minimum delay time for forced entry. Further, the mass and construction of the door can provide a much longer delay time to a larger spectrum of terrorist attack scenarios, compared to conventional hinged and hanging vertical doors common to aboveground magazines.
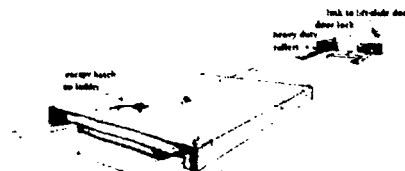

Figure 4. Blast-resistant, high-security sliding door over chimney.

The door consists of two leafs. Each leaf has heavy-duty rollers that ride on the chimney curb and set in groves when the door is either open or closed. The mass and mechanical system of the door is such that only the straddle trailer can operate the door. A circular hatch in one door leaf allows for personnel access via the chimney ladder.

Bridge Crane: Pallets of bombs or gun ammunition and metal containers of missiles, torpedos or mines are transported between the storage bay and its chimney by a bridge crane, illustrated in Figure 3. The bridge crane, one in each bay of the storage box, rides the full length of the storage bay on two overhead rails fastened to the ceiling of the storage box. All cargo in a bay is serviced by its own bridge crane; no cargo passes across the column line of the storage box. Metal containers are fastened to their spreader bar and lifted by a hoister (mechanical or electrical) connected to the bridge crane. Transport of pallets is similar except the pallet is lifted by metal forks that reach under the pallet like "stacker" blades. The overhead rails in the chimney area span the width of the chimney to ledge supports on the far wall of the chimney. When not in use, the overhead rails in the chimney area swing back into the storage box to allow unobstructed flow of cargo up and down the chimney.

Design of the cargo handling system in the storage box is extremely critical to acceptance by field personnel and safety authorities. Maintainability, availability, simplicity and reliability of operation are paramount. The bridge crane concept is no panacea - alternative cargo handling systems must be studied.

Soil Blanket: The soil blanket forms a flat surface over the entire magazine depot (Figure 1). The depth of soil over each storage box is the key to explosives safety performance and reduction in encumbered land area. Given an inadvertent explosion involving the entire rated NEW capacity of the magazine, the soil blanket serves three very important functions.

First, the soil blanket must provide sufficient mass to limit shock waves reaching the atmosphere to those escaping from the two chimneys - not through the roof. Thus, the roof must not breach and offer a major escape route for shock waves before internal pressures have decayed sufficiently. Given the desired performance, the far-field blast environment will be significantly less than that from the same explosion in an aboveground magazine. Consequently, the required separation distance to unrelated areas, e.g., inhabited facilities, is significantly less than that required for an aboveground magazine.

Secondly, the soil blanket serves to reduce the maximum possible strike range of concrete debris missiles significantly below that from an aboveground magazine. The logic is as follows. The total shock plus gas impulse applied to the roof slab plus soil cover must equal the charge in their momentum. Therefore, the initial launch velocity of concrete debris missiles is directly proportional to the total mass of the roof slab plus soil cover per unit area of roof slab. Thus, doubling the soil depth reduces the launch velocity of concrete debris missiles by almost one-half. Finally, reducing the debris launch velocity by one-half happens to reduce the maximum possible strike range of debris missiles by a factor of four. Thus, the maximum possible strike range of debris is inversely proportional to the square of the soil depth, approximately.

Third, the mass of the soil blanket substantially reduces the threat of forced entry into the magazine via the roof, which is a concern for standard aboveground magazines.

Simply stated, the soil blanket allows the Navy to release land normally encumbered by explosives safety arcs and to significantly enhance the physical security and survivability of storage. The cost-benefit of this strategy depends upon the cost of soil fill (or excavation as the case may be) and the value of Navy real estate. Based on the high value of coastal real estate and the extent of encroachment by the private community, a cost-benefit analysis is expected to show that the Navy can easily justify today's market price of straddle trailers and the extra soil fill and/or excavation associated with chimney-magazines.

Straddle Trailer: Pallets of ammunition and containers of weapons are moved to and from the storage box, via the chimney, and transported over land in the straddle trailer shown in Figures 1, 5 and 6. The straddle trailer is a rubber-tire vehicle

with a steel frame superstructure and a timber bed or platform. The platform is allowed to be raised or lowered by means of a motor-driven winch attached to the trailer frame. The lift capacity of the straddle trailer is about 20 tons.
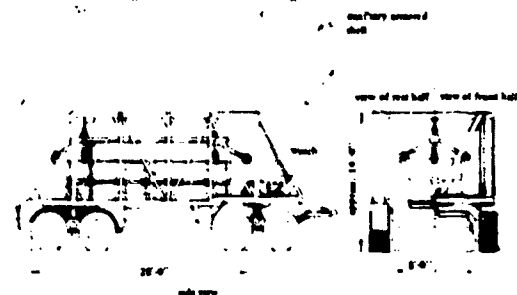

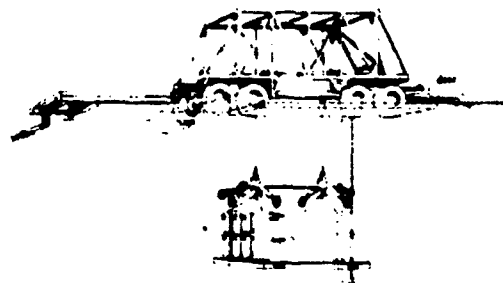Figure 5. Straddle trailer for retrieving ammo from magazine and over land transport.

Figure 6. Straddle trailer lowering its platform with ammo load down chimney.

The straddle trailer passes cargo into and out of the storage box as follows. To retrieve cargo, the straddle trailer is first drawn into position over the chimney. The chimney curb assures alignment. Next, the trailer winch is used to lift-and-slide open both leafs of the chimney door. The mass and mechanical system of the door allows only the straddle trailer to open the chimney door - physical security is thus assured. The trailer platform is then lowered down the chimney to its floor. Guide wheels above the trailer platform assure alignment of the platform in the chimney and prevent sparks from friction. Should the trailer winch malfunction, safety against freefall of the platform is assured by a dog-ear ratchet guide fastened to each wall of the chimney. A probe under the platform sounds a bell on the trailer and gears down the winch when the platform is within 6 inches of the chimney floor.

Once the platform rests on the chimney floor, the overhead rail extensions in the storage-box are swung out into position across the chimney. This allows the bridge crane to position its cargo on the platform. The platform loaded, the overhead rails are swung back out of the chimney. The trailer winch now raises the platform up the chimney and automatically locks it into position on the straddle trailer. During the lift operation, the dog-ear ratchet operates in reverse to prevent possible free fall of the platform and its cargo.

The trailer winch is then operated to close and lock the chimney door. Locked and loaded, the straddle trailer is pulled away by a vehicle to its final destination.

The physical security of ammunition during transportation is an ever increasing concern. The straddle trailer can be easily outfitted with a "SAFEPOT" type armored shell to provide required levels of physical security for special weapons. The armored shell would be optional equipment.

At a transfer point, the platform of the straddle trailer is raised or lowered to the deck elevation of the other vehicle, e.g., rail boxcar, or platform, e.g., deck of pier, to facilitate transfer of the cargo.

The straddle trailer and vertical access to storage are counter to tradition, i.e., horizontal access to magazine and forklift trucks for cargo handling. But vertical passage of ammunition is not new to the Navy – all ammunition ships pass cargo vertically into magazines located below deck. Further, the straddle trailer is not new – the agriculture industry in California has used straddle trailers for years to retrieve produce in the field and haul it over the highway to processing plants. Thus, the straddle trailer is a reliable concept that has already been debugged. Given deployment of the concept, the straddle trailer would become as common and popular as forklift trucks are today at Naval Ordnance Activities. Transportation of all ammunition within the confines of the Navy base would be by a single type of equipment – the straddle trailer.

The acquisition cost of the straddle trailer is not cheap – but neither is a forklift truck. The estimated cost of a straddle trailer is $100,000 without an armored shell. The cost of a forklift truck is about $80,000.

PERFORMANCE

Major performance goals are achieved with a chimney magazine. Physical security and survivability of storage increase dramatically. Encumbered land area decreases dramatically. Both benefits are achieved without degrading the level of explosives safety and without substantial increases in the construction cost. Achievement of these goals stems from the application of new NCEL technology to the design and predicted performance of a chimney magazine. Among the technologies are criteria for the external blast environment from confined explosions, the effects of semi-frangible covers on the blast environment inside structures containing explosions, the effects of internal explosions on the dynamic response of soil-covered structures, and the delay time of facilities and their components to forced entry. Based on NCEL technology, the following is a gross overview of the predicted safety performance of a chimney magazine from an internal explosion.

Safety From Blast: Given an explosion of magnitude W(lbs NEW) inside a chimney magazine having a volume V(ft^3) with vertical chimneys having a total vent area, A(ft^2), the peak incident blast overpressure, P_{so} (psi), at ground range R(ft) from the chimney is:

$$P_{so} = 290 \left(\frac{A}{V^{2/3}}\right)^{0.401} \left(\frac{W}{V}\right)^{0.0025} \left(\frac{R}{W^{1/3}}\right)^{-1.490}$$

$$\ldots\ldots(1)$$

Note that P_{so} at any R depends on not just W but also other parameters related to the design of the chimney magazine, i.e., A and V.

Consider the specific chimney-magazine design shown in Figure 7. For this particular design, A = 360 ft^2 and V = 97,600 ft^3. Now, if the safe inhabited building distance, IBD(ft), is defined to be the ground range R(ft) where P_{so} = 1.20 psi maximum for W < 100,000 lb NEW and P_{so} = 0.90 psi maximum for W > 250,000 lb NEW (current DOD safety criteria for inhabited buildings) then it follows from Equation 1 that the scaled safe inhabited building distance for the chimney magazine is:

For W < 100,000 lb NEW,

$$IBD/W^{1/3} = 23.8 \text{ ft/lb}^{1/3} \qquad (2a)$$

For W > 250,000 lb NEW,

$$IBD/W^{1/3} = 29.3 \text{ ft/lb}^{1/3} \qquad (2b)$$

For a standard aboveground magazine, DOD safety criterion requires:

For W < 100,000 lb NEW,

$$IBD/W^{1/3} = 40.0 \text{ ft/lb}^{1/3} \qquad (3a)$$

For W > 250,000 lb NEW,

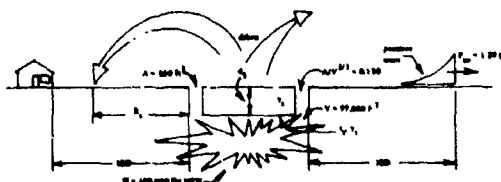$$IBD/W^{1/3} = 50.0 \text{ ft/lb}^{1/3} \qquad (3b)$$

Figure 7. Design parameters for a chimney magazine and the safe separation distance from blast and debris.

Comparing Equations (2) and (3), IBD for this particular chimney magazine is 41% less than IBD for a conventional aboveground magazine, regardless of W! More importantly, the encumbered land area is reduced by 65%, regardless of W! Note that the encumbered land area could be reduced even further by reducing the chimney area, A. However, doing so will increase the blast environment inside the box which, in turn, will increase the depth of the soil blanket required for adequate containment of explosion effects. The cost-benefit of further reductions in IBD needs to be studied.

It is important to understand that the vertical chimney is a key feature of the chimney magazine concept. Vertical venting of explosion effects is necessary to achieve a large reduction in the encumbered land area. Horizontal access tunnels – the alternative – would encumber more

168

land area (and the construction cost would be higher for horizontal access tunnels vice vertical access chimneys).

Safety From Debris: The safe distance from debris is derived from the principle of conservation of energy and the flight dynamics of a missile. Referring to the soil blanket in Figure 7, the scaled total impulse of gas plus shock pressures inside the magazine is $i_T/W^{1/3}$ (psi-msec/lb$^{1/3}$). The soil-blanket thickness over the roof is d (ft). The mass density of the soil blanket is γ_s (lb/ft^3). The reinforced concrete roof slab has a thickness t_r (ft) and a mass density γ_r (lb/ft^3). From the principle of conservation of energy and flight dynamics of a missile, the maximum possible strike range of debris missiles is:

$$R_s \le \frac{0.334\,(i_T/W^{1/3})^2\,W^{1/3}}{(\gamma_s d_s + \gamma_r d_r)^2}$$ (4)

Equation (4) is approximate but conservative. It neglects energy lost in breaking the missile free from the chimney magazine and energy dissipated by tumbling and air drag during missile flight. Further, it assumes that the debris missile is launched from the magazine at the critical launch angle producing the maximum possible strike range.

Safety From Ground Shock: The soil blanket in a chimney magazine is thicker than in an aboveground magazine. The added soil mass increases the confinement of an internal explosion. This increased confinement increases the ground shock at any distance to a level above that from the same explosion in an aboveground magazine. However, inhabited building distance from a chimney magazine, IBD = 23.8W$^{1/3}$ to 29.3W$^{1/3}$, exceeds minimum safe distance requirements of NAVSEA OP-5 by a factor of about two. Thus, ground shock is not expected to present unacceptable risk of damage to inhabited buildings.

The ground shock applied to an adjacent chimney magazine spaced at 1.5W$^{1/3}$ will also be greater. NAVSEA OP-5 requires a minimum separation distance of 1.5W$^{1/3}$ between underground storage magazines to prevent explosive communication and 3.5W$^{1/3}$ in sandstone (5W$^{1/3}$ in granite) to prevent damage to stored ammunition. But the difference between the shock propagation characteristics in sandstone and soil should more then compensate for reduction in the separation distance from 3.5W$^{1/3}$ to 1.5W$^{1/3}$ for chimney magazines. Thus, ground shock is not expected to cause sympathetic detonation between chimney magazines or damage to storage in an adjacent magazine. Should this prediction be incorrect, the "whiskey bottle" concept can easily be deployed to dissipate ground shock energy to safe levels.

Safety Criteria: Operational requirements are expected to dictate the value of A, V and W for the chimney magazine. In this case, the value of land, cost of soil fill, cost of excavation and the elevation of the water table will dictate the most cost-effective thickness of the soil blanket over the storage box. However, a cost-benefit analysis is expected to show the soil-blanket thickness should be such that the maximum possible strike range of debris, R_s, never exceeds the safe inhabited building distance for blast.

$$R_c \le IBD$$ (5)

Combining Equations (2b), (4) and (5), preliminary design criterion for soil blanket thickness required for safety against both blast and debris ($R_s \le IBD$) is:

$$d_s = \frac{0.1195\,(i_T/W^{1/3})\,W^{1/6} - \gamma_r t_r}{\gamma_s}$$ (6)

Solution of Equation (6) has led NCEL to the limits of existing explosion effects technology – large uncertainties exist in today's technology for predicting $i_T/W^{1/3}$ for the range of parameters characteristic of a chimney magazine. Prediction error in the component of $i_T/W^{1/3}$ resulting from internal gas pressures is believed to be small. But prediction error in the scaled impulse resulting from shock pressures, the other component of $i_T/W^{1/3}$, is believed to be large. The large uncertainty in the shock impulse applied to the roof slab stems primarily from lack of knowledge about close-in effects of a large charge density (W/V = 3.1 lb NEW/ft^3) and a thin pancake-shaped charge (representing 300,000 pounds NEW of bombs on pallets stacked two-high and uniformly spaced over the entire floor area). Further, large uncertainties exist on the extent and effects of the crater on the maximum debris range. Data from field tests planned for FY84 should reduce these uncertainties. For the interim, NCEL believes it has bracketed the value for a chimney magazine where W = 300,000 lbs NEW, γ_r = 150, t_r = 1.25 and γ_s = 120. Based on computer analysis, extrapolation of test data and engineering judgment,

$$10 < d_s \le 20 \text{ ft}$$ (7)

COST-BENEFIT

The cost-benefit of a depot of chimney magazines depends upon the increase in construction costs relative to the value of all benefits derived. One added cost is the extra soil fill and/or excavation required for a chimney magazine. One benefit is the value of land freed from large safety arcs. A gross estimate of this cost-benefit and description other benefits follows.

MCON Cost: The structural cost ($/ft^2) for a chimney magazine is estimated to be about the same as for a conventional, box-shaped, reinforced concrete, missile storage magazine (aboveground magazine). The quantity of reinforced concrete in the chimney magazine is about 39% greater than in an aboveground magazine having the same floor area. This increase stems primarily from the two chimneys, the greater ceiling height, and a thicker roof slab (because of the higher dead load from the deeper soil cover – even though the blast loads from an adjacent magazine will be less).

But other cost components will be less. The structural and mechanical costs of the doors in the chimney magazine should be less because the total area of openings is less (two doors at 28 x 6.5 feet vice two doors at 28 x 12 feet in an aboveground magazine), the clear span of the door is less, and the applied blast load from explosions in adjacent magazines is less. Further, the chimney magazine requires no blast hardened headwall and doors to protect contents from explosions in adjacent magazines, no reinforced concrete pilasters to support the door from being blown-in, no headwall extensions to support the soil berm, no elevated platform forward of the headwall for transferring cargo and no complicated electrical trolley system to open doors. The designer need only be instructed to provide a water-tight, reinforced-concrete box with two chimneys that safely supports a prescribed depth of soil cover. Knowledge of blast resistant design is not required.

One measure of the cost-benefit is the difference between the MCON costs of a chimney magazine and an aboveground magazine, divided by the total acres of land unencumbered by use of the chimney magazine. This ratio ($/acre) is the price the Navy is paying to unencumber land by using chimney-magazines. This cost-benefit ratio is shown in Figure 8 as a function of depth of size, depth of excavation, and thickness of soil blanket (10 and 20 feet). The curves assume a depot with a square array of magazines.
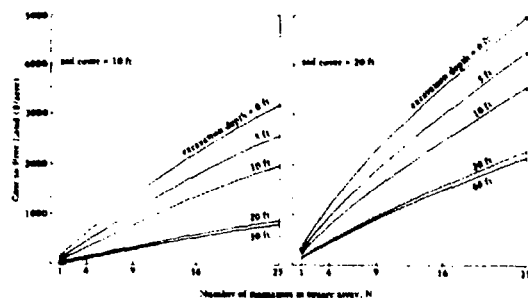
Figure 8. Cost benefit of chimney magazines relative to above ground box magazines.

Figure 8 assumes the aboveground magazines are spaced at $1.25W^{1/3}$ side-to-side and $6.0W^{1/3}$ front-to-back, and are covered with 2 feet of soil cover. Encumbered land includes the depot area and all land within the confluence of 50 ft/lb$^{1/3}$ measured from the skin of any magazine.

The chimney magazines are spaced at $1.5W^{1/3}$ side-to-side and front-to-back. The depth of soil cover over the chimney magazines for the left and right set of curves (Figure 8) is 10 and 20 feet, respectively.

Unit costs are based on a survey of cost data for Southern California. Both depots are based on the structure costing 150 $/ft^2 floor area, fill 4 $/yd^3 and excavation 3 $/yd^3. Aboveground magazines are assumed to require no excavation, and no fill under their elevated floor and loading platform.

The curves illustrate major savings would be realized at most Navy installations, based on the

"cost of freed land." For example, a depot of 9 chimney magazines with 10 feet of soil cover (vice 9 aboveground magazines) frees Navy land for other uses at an effective cost of between 310 and 1,350 $/acre, depending on the depth of excavation allowed by the water table. In other terms, the MCON cost of the nine-magazine depot would increase by 5 to 20% based on an MCON cost of 150$/ft^2 for an aboveground depot. Actually, the effective cost is much less than this because all the benefits are not included – and many of these are significant. In any case, Figure 7 shows that the chimney magazine offers a very cost-effective scheme to "purchase" land.

Total Benefit: Other benefits of a chimney magazine, in addition to a major reduction in encumbered land area, are the following: Major increase in level of physical security, increase in survivability, reduction in plutonium (for special weapons) that could escape to atmosphere, increase in environmental control, greater concealment, less logistics burden (the haul distance is reduced 41% and one piece of equipment does all the work), standardization of design, a solution for depots in Europe (where 69% of the floor area of existing magazines cannot be utilized because explosives safety arcs would encumber inhabited buildings), and a scheme to increase the buildable land area at Navy bases by using unbuildable land as the source of fill for the depot. Regarding physical security, a chimney-magazine depot designed to store 300,000 pounds NEW per magazine offers secure storage for special weapons. Given an inadvertent explosion, the chimney magazine offers almost complete containment because of the low NEW associated with special weapons. Given a mix of conventional and special weapons stored in a chimney-magazine depot, the "shell game" applies – no one knows which magazines (and which Navy Activity) have the special weapons. Further, the labor cost for special security forces is much lower.

FUTURE WORK

The chimney magazine is only a concept, but work is underway to refine its cost-benefit and verify its predicted performance, given an explosion equivalent to 300,000 lb NEW in small-scale structures. In view of the anticipated resistance to any changes from the traditional concept for ammo storage, the authors welcome any opinions regarding the utility of the chimney-magazine concept for tomorrow's ammo depots.

BIBLIOGRAPHY

1. Naval Sea Systems Command. NAVSEA OP-5: Ammunition and explosives ashore, volume 1, 4th revision. Washington, D.C.

2. Civil Engineering Laboratory. Technical Report R-828: Blast environment from fully and partially vented explosions in cubicles, by W. A. Keenan and J. E. Tancreto. Port Hueneme, Calif., Nov 1975.

3. _____. Technical Report R-878: Design criteria for soil cover over box-shaped ammunition

magazines, by W. A. Keenan (NCEL) and L. C. Nichols
(WPNSTA Concord). Port Hueneme, Calif., May 1980.

4. Naval Civil Engineering Laboratory. Technical
Memorandum M-51-82-08: Design criteria for fran
gible covers in ordnance facilities, by
W. A. Keenan and J. E. Tancreto. Port Hueneme,
Calif., Oct 1982.

171

SWEDISH DESIGN MANUAL FOR PROTECTIVE STRUCTURES

Bengt E Vretblad & Göran B Svedbjörk

Royal Swedish Fortifications Administration, Eskilstuna, S-631 89 Sweden

ABSTRACT

The design of Swedish military hardened concrete structures is based on different manuals among those RSFA publ Bk 25. This publication gives design values for three different classes of structures A-C where e g different degrees of deformations are accepted. The paper describes the design procedures, according to the manual, with respect to fragment penetration.

BACKGROUND

During the early seventies the Swedish manual for the design of concrete structures exposed to non-nuclear weapons effects was revised by the Royal Swedish Fortifications Administration (RSFA). The revision which was outlined by Dr Håkan Sundquist, at that time by the RSFA, resulted in RSFA Publ nr 25 in 1973. This manual has been updated in 1977, /1/.

CLASSES OF STRUCTURES

An elastic design of structures exposed to weapons effects will often result in conservative and uneconomical solutions. While some structures have to be intact after being subjected to blast and fragments other might sustain different degrees of damages without their primary function of protection being violated.

For this reason hardened structues are organized in classes A, B and C according to /1/.

Class C is for structures to give survival to people in it accepting damages to the structure itself and to installations in it. Spalling from fragments is accepted on every 3rd square meter of exposed walls and a small risk of penetration is accepted.

Class B structures may have permanent deflections not greater than 3% of the span. Spalling may occur on every 10th square meter and the risk of penetration is reduced compared to Class C structures.

Class A structures are to fulfill requirements for Class B structures and are also to be secure for gasoverpressure after exposure to blast and fragments. This often leads to an elastic design.

The requirements for the different classes of structures are put together in Table 1.

CLASS OF STRUCTURE	PERMANENT DEFLECTION	RISK OF SPALLING (FROM FRAGMENTS)	RISK OF PENETRATION (FROM FRAGMENTS)
A	NO	$0.1 \ m^{-2}$	MINOR
B	$\leq$ 3% OF SPAN	$0.1 \ m^{-2}$	MINOR
C	YES	$0.3 \ m^{-2}$	SMALL

Table 1

PENETRATION

The manual is based on the fragmentation concept given by Mott & Linfott in /2/. According to this reference the number of fragments with a mass greater than m_0 is given by

$$N(m_0) = \frac{m_c}{2K^2} e^{-\frac{\sqrt{m_0}}{K}}$$

where m_c is the mass of the case and K a constant depending on the geometry and the fragmentation of the bomb.

This gives the fragment density, ϱ, on a wall at a distance R from the bomb

$$\varrho(m_0, R) = \frac{C}{2\pi R^2} \cdot N(m_0)$$

C a distributing factor to be 1 with a uniform distribution of fragments in all directions. In /1/ C is taken equal to 2 giving credit to the increased density of fragments perpendicular to the axis of the projectile for a vertical wall and a vertical projectile.

The maximum fragment mass for a certain fragment density can then be calculated with bombweight and bomb geometry given for different distances. This is illustrated in Table 2 for a 500 kg GP bomb.

FRAGMENT DENSITY	DISTANCE (m)			
(m^{-2})	5	10	15	20
0.01	0.89	0.65	0.52	0.44
0.1	0.51	0.33	0.24	0.19
0.3	0.36	0.22	0.15	0.11

Table 2. Maximum fragment mass (kg) at different distances from a 500 kg GP bomb and for different fragment densities.

The wall thickness, d, has been calculated according to $d = 2.7 \cdot 10^{-4} \cdot v \sqrt[3]{m_0}$

where v is the velocity of a fragment at the wall. Table 3 gives d for Class B structues ($\varrho = 0.3$) for different bombs.

BOMB	DISTANCE			
	5 m	10 m	15 m	20 m
1000 kg		0.50	0.45	0.40
500 kg	0.45	0.40	0.35	0.30
250 kg	0.40	0.32	0.30	0.25
100 kg	0.30	0.25	0.20	0.20

Table 3. Wall thickness (m) for Class B structures with GP bombs at different distances.

By this method the minimum thickness of a structural element can be determined. Additional requirements e g from bending and shear actions of course might make greater thickness necessary.

CONCLUSIONS

The concept adopted in RSFA publ Bk 25 for classification of structures has proved to be very useful. The method for calculating minimum thickness of concrete elements with respect to fragments and penetration has shown to be a versatile instrument for design engineers.

REFERENCES

/1/ PUBL NR 25 Bk/1973/1977 Anvisningar för dimensionering av armerade betongkonstruktioner som skydd mot verkan av konventionella vapen inom närmissområde (Manual for the design of reinforced concrete structures against non-nuclear weapons effects in the close range). Fortifikationsförvaltningen. Stockholm 1979. (In Swedish)

/2/ Mott, N F & Linfoot, E H, A Theory of Fragmentation. MOS-AC3348, 1942.

DESIGN OF UNDERGROUND SHELTERS
INCLUDING SOIL-STRUCTURE INTERACTION EFFECTS

Felix S. Wong and Paul Weidlinger

Weidlinger Associates
Menlo Park, California and New York, New York

ABSTRACT

Soil-structure interaction significantly affects the loads acting on buried shelters subjected to nearby explosions. Recent research has improved our understanding of this complex phenomenon and led to a new design method for buried shelters. This method recognizes the coupling between dynamic response of a buried structure and the loading exerted on it by the neighboring soil. It is simple to use, inexpensive and sufficiently accurate for most underground shelter designs.

DYNAMIC SOIL-STRUCTURE INTERACTION

Dynamic soil-structure interaction involves very complex wave mechanics. The process is a coupled phenomenon, i.e., the motion and deformation of the structure depends on the loading acting on it, and the loading, in turn, is affected by the structural motion and deformation. This is illustrated in Fig. 1. A buried slab is impinged by a one-dimensional stress wave propagating in soil. Since the soil is assumed elastic, the free-field stress wave propagates unattenuated until it encounters the slab (dashed line in the figure). If the slab is assumed fixed, the pressure loading on
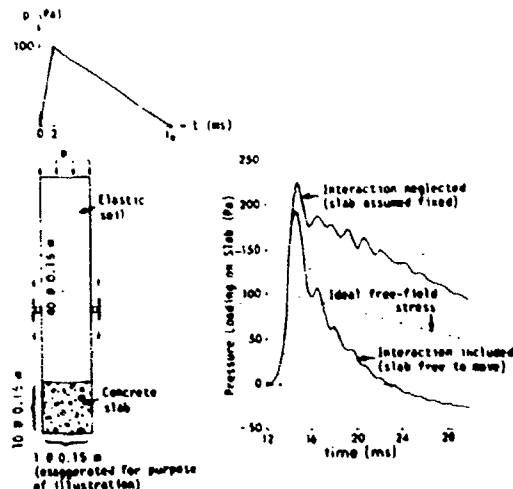

Fig. 1. Beneficial effect of dynamic soil-structure interaction in reducing loading on buried structures, one-dimensional illustration.

the slab is equal to the incident plus the reflected soil-stress waves, or twice the free-field stress. This is the assumption used in most prevalent shelter designs. In reality, the slab moves as a result of the soil loading, and this leads to significant reduction in the loading, as Fig. 1 indicates.

INTERACTION ALGORITHM

While the beneficial effect of soil-structure interaction is well-known, it has not been integrated in the structural design process because of the complex nature of the interaction phenomenon, and the lack of an efficient design procedure which includes this effect. Recent research at Weidlinger Associates with the aid of analytical and numerical methods indicates that, for impulsive loading of shallow-buried shelters, the interaction is governed mainly by the velocity of the structure relative to the velocity of the free-field soil particles. The loading is considered impulsive when the effective duration of the free-field ground shock pulse is comparable to the fundamental period of the major deformation mode of the structural element of interest. A shelter is shallow-buried when the depth-of-burial is of the order of the span of the structural element of interest. Under these conditions, the generalized plane-wave interaction algorithm

$$\sigma_{int} = \sigma_{ff} + \rho c \, (v_{ff} - \dot{x}) \qquad (1)$$

(σ_{int} denotes the interaction loading, σ_{ff} the free-field stress, $\dot{x}$ the velocity of structure, v_{ff} the free-field particle velocity and ρc the soil impedance) provides a good approximation to the actual interaction loading. This algorithm leads to a new design method for underground shelters which is simple to implement and provides a better and more consistent estimate of the effect of dynamic soil-structure interaction at little additional expense.

DERIVATION OF DESIGN PROCEDURE

Consider the design of the roof slab of a buried rectangular shelter against a top threat (Fig. 2). Suppose the design is pursued using the beam equation

$$\mu \frac{\partial^2 x}{\partial t^2} - EI \frac{\partial^4 x}{\partial s^4} = \sigma_{int} \qquad (2)$$

where μ is the mass density per unit length, EI the bending rigidity, x the lateral deflection of the beam, and σ_{int} is the interaction loading exerted

by the soil on the roof. Substituting Eq. (1) for σ_{int} gives

$$u\frac{\partial^2 x}{\partial t^2} + \rho c\frac{\partial x}{\partial t} - EI\frac{\partial^4 x}{\partial s^4} = \sigma_{ff} + \rho c v_{ff} \qquad (3)$$

Note Eq. (3) is a beam equation similar to Eq. (2), with a loading function which depends only on the free-field environment. Hence, the design procedure can be divided into two uncoupled parts: definition of the free-field environment, and the design of the beam subjected to an equivalent (free-field) loading. The effect of dynamic soil-structure interaction is included explicitly in the beam model in the form of viscous damping.
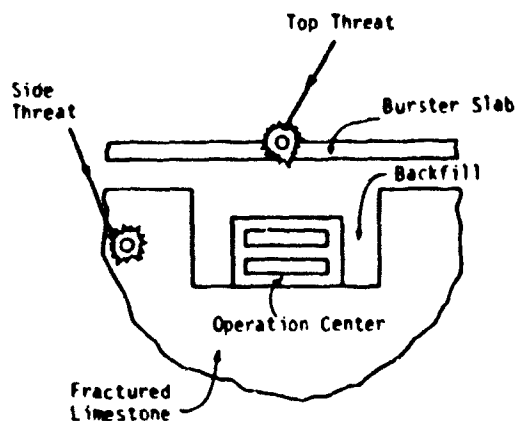
Fig. 2. Buried shelter subjected to top and side munition attacks.

It is easy to generalize the above derivation. The equation of motion of a shelter can be represented as

$$L(x) = \sigma_{int} \qquad (4)$$

where x is the structure displacement and $L(\cdot)$ the differential operator. The use of the simplified soil-structure interaction algorithm in the equation of motion gives

$$L(x) = \sigma_{ff} + \rho c \ (v_{ff} - \dot{x})$$

or

$$L(x) + \rho c\dot{x} = \sigma_{ff} + \rho c v_{ff} \qquad (5)$$

Again, the forcing function is a function of the free-field environment only. The structural system on the lefthand side of the equation is the original system $L(x)$ with the added damping term $\rho c\dot{x}$ to represent the interaction effects.

A new design procedure is developed based on Eq. (5). This is illustrated in Fig. 3. The structural model (numerical or otherwise) is modified to include the interaction damping. The equivalent free-field loading is then applied to the bare structure. Other than these changes, the design procedure is identical to the prevalent procedure for unburied shelters.
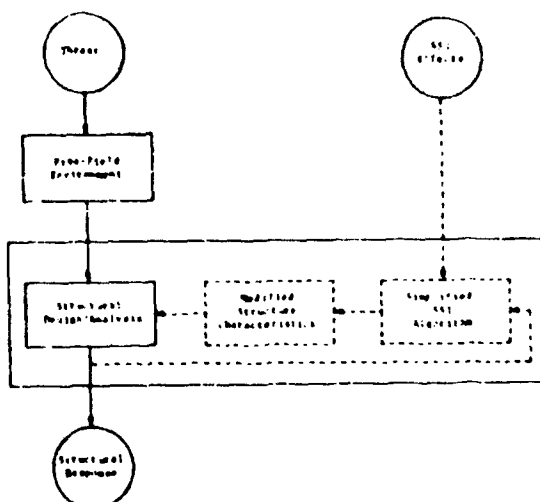
Fig. 3. New design procedure with simplified soil-structure interaction (SSI) algorithm.

VERIFICATION

The accuracy of the new design procedure depends on the validity of Eq. (1). Based on extensive comparisons of the design results with detailed finite element soil-structure analysis results, the new design method is found to yield good approximations under the conditions specified for Eq. (1), i.e., impulsive loadings and shallow-buried shelters. Fig. 4 is representative of the results obtained. The interaction loadings on the midspan of the roof of a buried shelter are obtained using the direct coupled finite element method and the new design method with a beam model to represent the roof. They are compared in the figure. The comparison is excellent despite the fact that the free-field loading is non-planar. This is because the intensity of the soil stress decays rapidly with distance from the source and at midspan where the loading is most severe, the interaction is approximately planar. This is often the case for conventional weapons.
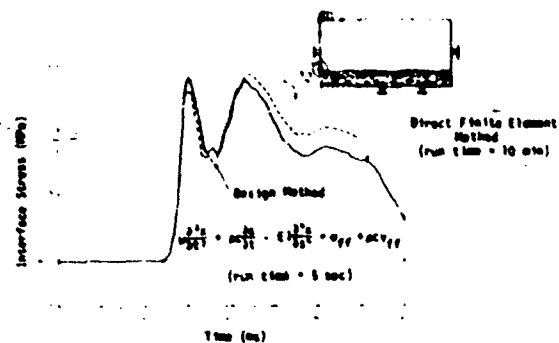

Fig. 4. Comparison of interface stress at midspan of an 18 m roof, direct finite element calculation versus design method.

175

The same design procedure has been used for inelastic soil-structure systems; the impedance coefficient, ρc, is represented as a function of the soil stress at the interface in accordance with the inelastic stress/strain relationship of the soil. Tensile interaction loading should also be limited to reflect the limited tensile strength of the soil-structure interface. The algorithm as outlined has been incorporated in computer programs commonly used in structural design, e.g., SAP and STRUDL.

CONCLUSION

Soil-structure interaction effects are properly accounted for only by considering wave propagation in the model. The cost and complexity of an explicit wave analysis often deter a designer from including the beneficial effect of soil-structure interaction on the design. A new design procedure based on an approximate interaction algorithm has been developed, which greatly simplifies the supporting analysis. It allows the designer to obtain an excellent estimate of the peak interaction loads on the structure with little additional cost or labor compared to a conventional procedure. It is also compatible with any reasonable structural model the designer chooses to evaluate candidate designs.
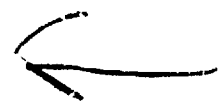
GAS PRESSURE LOADS FROM EXPLOSIONS WITHIN VENTED AND UNVENTED STRUCTURES

W. E. Baker
J. C. Hokanson
E. D. Esparza
N. R. Sandoval

Southwest Research Institute
San Antonio, Texas

ABSTRACT

Gas pressures from explosions within enclosures, as opposed to shock loads, can be the dominant loads causing structural failure. This paper reviews test results and prediction methods for gas pressures for many types of internal explosions including high explosives, high explosives plus combustibles, gas mixtures and dust suspensions.

INTRODUCTION AND BACKGROUND

For explosions in enclosures involving high explosives, solid propellants, high explosive with combustible materials in contact, or combustible mist, dust, or gaseous explosive mixtures, the long-duration gas pressures caused by confinement of the products of the explosions can be the dominant loads causing structural failure. These quasi-static pressures are determined by the total heat energy in the explosive and/or combustible source, the volume of the enclosure, the vent area and vent panel configuration, the mass per unit area of vent covers, and the initial ambient conditions within the enclosure.

Previous analytic work, similitude analysis, and numerous experiments have addressed several aspects of this problem and provided a good data base for more general predictions. Ref. 1 collates much of this information for gas pressure parameters for bare high explosive detonations in enclosures with open vents, while Ref. 2 includes analytic predictions of these parameters for similar explosions with covered vents with various masses per unit area. Maximum pressures for gas and dust combustible mixtures initiated in unvented and vented enclosures are reported in Ref. 3 and 4. Most recently, test data for gas pressures in a sealed structure from high explosives surrounded by combustible liquids and solids are reported in Ref. 5.

Tests of solid propellants burned in vented structures are reported in Ref. 6 and 7. Ref. 6 also includes derivation of a scale modeling law for pressures for this situation. Scale modeling of dust and gas explosions in enclosures is inherent in work in Ref. 3, while a more thorough law for vented dust explosions appears in Ref. 8.

In this paper, the authors will review the literature and present methods for predicting internal gas pressure loads under the following conditions: 1) bare high explosive detonations in structures with open vents, 2) high explosive plus combustible explosions in closed structures, and 3) gas and dust explosions in closed and vented structures. The predictions will be based on graphs and/or numeric fits to scaled parameters from appropriate similitude analyses.

GAS PRESSURES FOR INTERNAL HE EXPLOSIONS

The loading from an explosive charge detonated within a structure consists of two phases. The initial phase consists of several high amplitude, short duration, reflected pressure shocks. This phase of the loading is very geometry dependent, with the highest loads generally occurring on the surfaces nearest the charge. On each reflection, the shock strength is attenuated until at some point the internal pressure has settled to a slowly decaying level. This is the quasi-static pressure loading phase. This phase is characterized by essentially uniform pressures throughout the structure at any point in time. The rate of quasi-static pressure decay is a function of the vent area, structure volume and the nature of the explosive source.

A typical pressure trace obtained during an internal explosion in a vented structure is shown in Figure 1. Traditionally (Ref. 9), the peak quasi-static pressure is established by fitting a smooth line through the data beginning at the end of the pressure trace and extending back towards time zero, the time of charge ignition. This line is shown in Figure 1 as a solid line. The peak P_{qs} is then taken as the intersection of the fitted line and a vertical line at time zero (shown as a dotted line in the figure). This point is labeled A in Figure 1. For a vented structure, a more appropriate technique has been suggested (Ref. 1, 5). This method is applied by drawing a ramp increase in pressure extending from time zero, which follows the base of the pressure shocks. This line is shown as a dashed line in Figure 1. The intersection of the ramp pressure increase with the line fitted through the pressure decay is the peak quasi-static pressure. This point is labeled B in the figure. For explosions inside sealed enclosures, points A and B will have nearly the same ordinates, whereas for explosions with increasing vent areas, the difference in ordinates between points A and B increases.

In Ref. 1, a very complete analysis of gas pressures from internal explosion data was presented. The authors performed a similitude analysis to
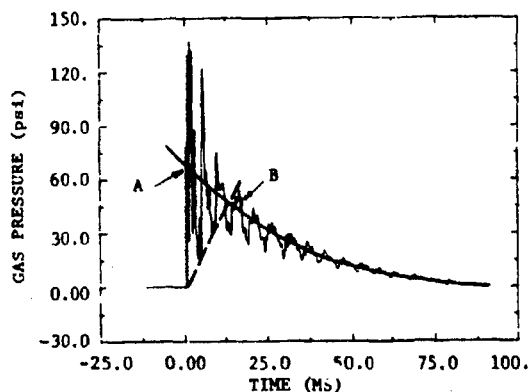
Figure 1. Typical Pressure Record from an Internal Explosion in a Vented Structure

Figure 2. Peak Quasi-Static Pressure as a Function of the Charge Weight to Enclosure Volume

determine the functional form of the quasi-static pressure, as a function of the physical parameters pertaining to the problem of an internal explosion inside a vented structure. Based on this analysis, the following equation was derived:

Peak Quasi-Static Pressure:

$$\log \bar{P}_{QS} = 0.30759 + 0.51815 \log (W/V) -$$
$$0.150534 [\log (W/V)]^2 + 0.31892 [\log (W/V)]^3 +$$
$$0.10434 [\log (W/V)]^4 - 0.14138 [\log (W/V)]^5 + \tag{1}$$
$$-0.019206 [\log (W/V)]^6 + 0.021486 [\log (W/V)]^7$$

Equation (1) was the result of curve fits to 177 experiments. Figure 2 presents the curve fit together with the measured data. One approximation was made in the analysis of the test data. The explosive energy contained in any high explosive is directly proportional to the explosive mass. As it turns out, the charge energy-to-explosive mass ratio for most explosives is nearly the same. For convenience, the analysis performed in Ref. 1 utilized the charge mass, rather than the charge energy.

Based on the results of the analysis of the internal explosion data, the authors of Ref. 1 found that the peak quasi-static pressure was independent of the vent area, but dependent on the charge weight-to-structure volume ratio.

GAS PRESSURES FOR HE PLUS COMBUSTIBLES

Recently (Ref. 5), a series of experiments was conducted in which various combustible materials were placed in varying degrees of contact with high explosive charges. The object of the tests was to determine whether the combustible materials could contribute to the quasi-static pressure development within a sealed enclosure. The combustible materials investigated in this effort are listed in Table 1. In every case, the high explosive was 0.992 lb of PBX-9404. All of these experiments were conducted in the same enclosure, so the only parameter not held constant was the combustible

Table 1. Combustible Materials and Configurations Tested*

Series	Material	Configuration
1	Polycarbonate	A 67.6 gm polycarbonate disk was attached to the end of a cylindrical ($\ell/d=1$) charge.
2	Polycarbonate and Aluminum	A 135 gm aluminum casing surrounding the side of a cylindrical charge. A polycarbonate disk covered one end of the charge.
3	50/50 Mix of DMF and Acetone	A spherical charge was submerged in 5 oz of the fluid.
4	Polycarbonate	Two polycarbonate hemispheres were attached to opposite poles of the charge. The total polycarbonate weight was 48.25 gm.
5	50/50 Mix of DMF and Acetone	Five 1 oz containers of the fluid were equally spaced on a circle 36 in. in diameter around the charge.
6	Low density polyethylene	Polyethylene beads suspended in an epoxy base, and formed into a four-sided box, centered on the charge. The weight of the box was 273 gm.

*The explosive was 0.992 lb of PBX-9404. Test Series 1 and 2 utilized cylindrical charges, while the remaining tests utilized spherical charges. The charge location was the same in all experiments.

configuration. Note that the P_{qs} for a bare 0.992 lb PBX-9404 charge is 48.7 psi. In every case, the addition of combustible materials in near contact with the HE charge increased the quasi-static pressure, in some cases dramatically.

The degree of quasi-static pressure enhancement produced by a combustible is related to the heat energy content of the material. This is shown in Figure 3 where the excess P_{qs} (the P_{qs} produced by the combustible plus the HE, less the P_{qs} produced by the HE alone.) is plotted as a function of the combustible energy content. The combustible energy content is defined as the mass of combustible times the appropriate heat of combustion from Table 2. As seen in Figure 3, the enhancement in the quasi-static pressure increases uniformly with increasing combustible energy, as long as the combustible is in intimate contact with the charge. The only point not following the general trend of the data corresponds to the series of tests in which the combustible fluid was dispersed a large distance from the charge.

The phenomenon of quasi-static pressure enhancement produced when combustible materials are placed near HE sources has only been recently discovered. The effect has been observed for a variety of combustible materials, but no variations in charge to combustible mass, charge type, structure volume, or degree of venting have been tested. The implications of the data accumulated so far are that quasi-static loading calculations should include estimates of contributions from the burning of combustible materials whenever such materials are expected to be in intimate contact with HE sources.
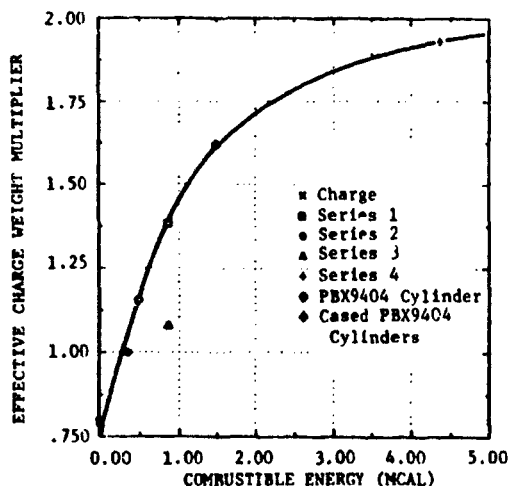
Figure 3. Excess Quasi-Static Pressure (psi)

GAS AND DUST EXPLOSIONS IN CLOSED AND VENTED CHAMBERS

Many accidental explosions occurring in industry involve the ignition within enclosures of combustible mixtures of gases with air, or suspensions of combustible dusts in air. Such mixtures ignited in the open do not cause blast waves or significant pressure waves, but instead generate only transient fireballs as flame fronts progress at rather low rates (meters per second) through the combustible mixtures.

But, when the combustible mixtures are ignited inside a sealed or vented enclosure, the confinement provided by the enclosure can allow significant pressure rises which can disrupt the structure. A typical pressure history for such an explosion within an unvented enclosure is shown in Figure 4.

The maximum rate of pressure rise $\frac{dP}{dt}$, and the maximum pressure P_m are determined by the reactivity of the particular material, the fuel-air ratio, the amount of material, and the volume of the enclosure. When the enclosure has a vent area, covered by a vent designed to open at pressure P_u, the pressure-time history is modified as shown in Figure 5. The amplitudes and times of the maxima P_1 and P_2 are functions of the gas flow dynamics through the vent, and either P_1 or P_2 may be the maximum pressure.

Table 2. Heat of Combustion for the Various Combustible Test Materials

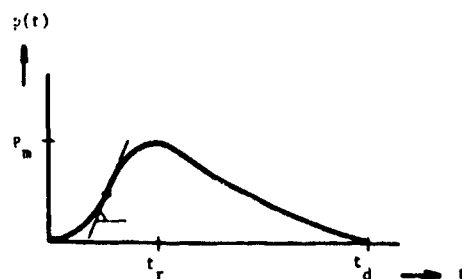| Material	Heat of Combustion (cal/gm)
PBX-9404	2369
Polycarbonate	7223
Acetone	7363
DMF	6259
Polyethylene	9400
Aluminum	7400

Figure 4. Schematic Overpressure-Time History in Confined Gas or Dust Explosions (Ref. 10)
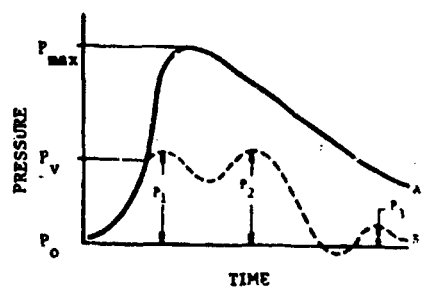

Figure 5. A Representation of a Pressure-Time History of an Unvented (Curve A) and Vented (Curve B) Deflagrative Explosion (Ref. 13)

The voluminous data and analyses in the literature (see Ref. 10) on the characteristics of these pressure histories can be condensed and presented in compact form based on similitude analyses

179

(Ref. 6 and 7). Bradley and Micheson (Ref. 11 and 12) present scaled upper limit curves for gas explosions in vented vessels. These are reproduced here as Figures 6 and 7. In these figures, the dimensionless terms are

$$\bar{A} = \frac{AK_d}{A_s} \quad , \quad \bar{S}_o = \frac{U}{a_o} \quad , \quad \bar{P}_m = P_m/c \qquad (2)$$

where A is vent area, A_s internal surface area, K_d discharge coefficient (≈ 0.6), U is gas velocity ahead of a flame front, a_o is ambient sound speed, P_m is maximum pressure and p_o is ambient pressure.
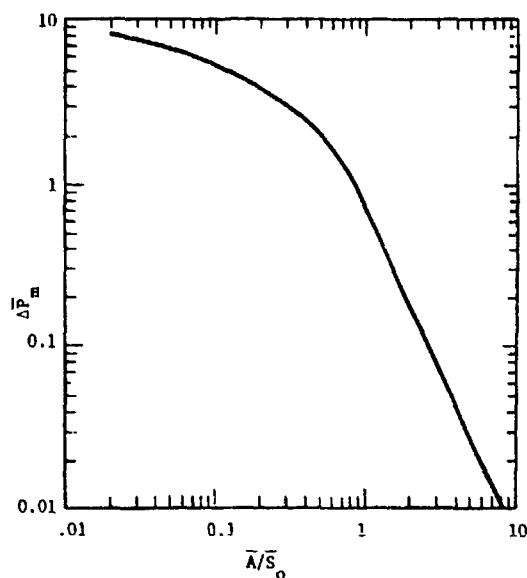
Figure 6. Safe Recommendations for Uncovered Vent Areas. Gaseous Explosions (Ref. 12)

For dust explosions, maximum pressures are also a function of the dust reactivity, and a scaled vent area. Figure 8 shows scaled plots of $\bar{P}_m$ for dusts of increasing reactivity, ST1 through ST3. Here $\bar{A}$ is defined somewhat differently, as

$$\bar{A}_v = (A/V^{2/3}) \qquad (3)$$

where V is volume of the enclosure.

In either gas or dust explosions of this nature, the dimensionless maximum pressure rate for a given combustible mixture is

$$\bar{P} = (\dot{P} V^{1/3}/a_o p_o) \quad . \qquad (4)$$

This scaling is consistent with Bartknecht's "cube-root law." (Ref. 3)
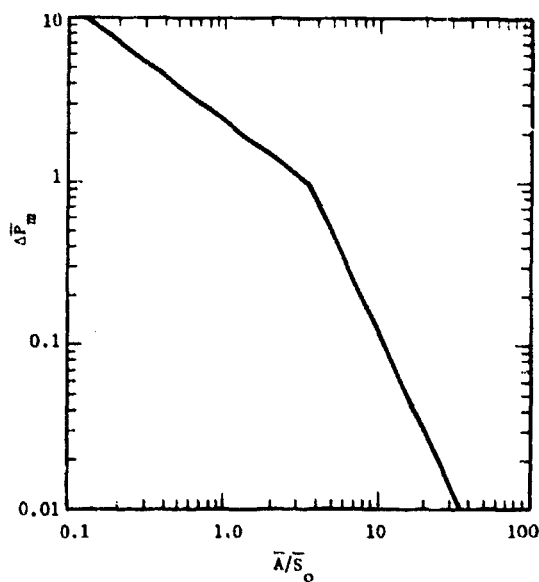
Figure 7. Safe Recommendations for Covered Vent Areas, Gaseous Explosions (Ref. 12)
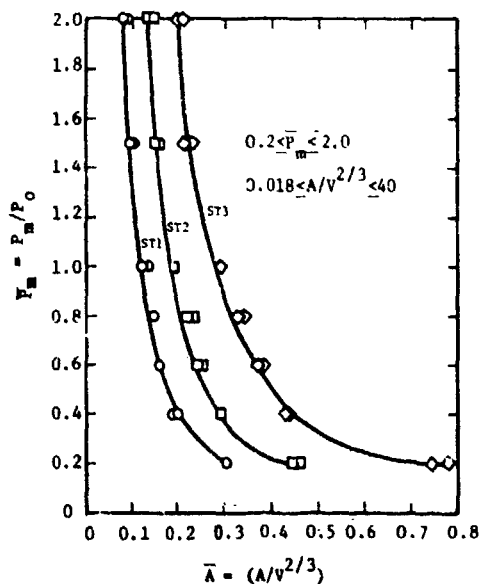
Figure 8. Scaled Maximum Pressures for Dust Explosions Versus Scaled Vent Area Ratio (Ref. 10)

It is also clear from Ref. 11 and 12 that the maximum pressures attainable within enclosures for gaseous explosions are remarkably constant for all

combustible gases, varying from about 8 atmospheres for natural gas to only 10.25 atmospheres for acetylene.

CLOSURE

Even though the material on gas pressures for explosions within enclosures which is summarized in this paper shows an extensive experimental and analysis base, there are still a number of significant data gaps which limit our ability to predict these pressures. These include at least:

o   Lack of data on pressures generated by HE-combustible combinations

o   Lack of data and validated analytic methods for effects of vent cover parameters for HE explosions

o   Lack of data for mixtures of combustible gases and dusts

o   Lack of data for dust explosions in real configurations, such as grain elevator galleries.

o   Lack of data for effects of vent cover parameters for gas and dust explosions.

Not all of these gaps are important to weapons effects analysts, but all are quite important in the explosives safety community.

REFERENCES

1.   W. E. Baker, C. E. Anderson, Jr., B. L. Morris, D. K. Wauters, "Quasi-Static Pressure, Duration and Impulse for Explosions in Structures," to be published in _Int. J. of Mech. Sciences._

2.   W. E. Baker, et al, "Manual for the Prediction of Blast and Fragment Loadings on Structures," DOE/TIC-11268, U.S. Dept. of Energy, Pantex Plant, Amarillo, TX, Nov 1980.

3.   W. Bartknecht, _Explosionen, Ablauf und Schutzmassnahmen_, Springer-Verlag, Berlin, Heidelberg, New York, 1978.

4.   P. Field, _Dust Explosions_, Elsevier Scientific Pub. Co., Amsterdam, 1982.

5.   J. C. Hokanson, E. D. Esparza, N. R. Sandoval, and W. E. Baker, "Effects of Combustibles on Internal Blast Loads in the Damaged Weapons Facility, Final Report for Phase IV," Final Report on P.O. F0913400 for Mason & Hanger - Silas Mason Co., Inc., Pantex Plant, Amarillo, TX, Oct 1982.

6.   J. L. Evans, R. Rindner, and W. Seals, "Explosive Hazards Tests for Establishing Hazards Classifications for M1 Propellant for Automated Single-Base Finishing Operations," Contractor Report ARLCD-CR-78014, U.S. ARRADCOM, Dover, NJ, Jan 1978.

7.   J. L. Evans and W. O. Seals, "Explosive Hazards Tests for Establishing Hazards Classifications for M1 Propellant for Automated Single-Base Finishing Operations - Part II," Contractor Report ARLCD-CR-80011, U.S. ARRADCOM, Dover, NJ, June 1980.

8.   W. E. Baker, J. C. Hokanson and J. J. Kulesz, "A Model Analysis for Vented Dust Explosions," _Proc. of the 3rd Int. Symposium on Loss Prevention and Safety Promotion in the Process Industries_, Basel, Switzerland, Sept 1980.

9.   C. N. Kingery, R. N. Schumacher, and W. O. Ewing, Jr, "Internal Pressures from Explosions in Suppressive Structures," BRL Interim Report Memorandum No. 403, Aberdeen Proving Ground, MD, 1975.

10.   W. E. Baker, P. A. Cox, P. S. Westine, J. J. Kulesz, and R. Strehlow, _Explosion Hazards and Evaluation_, Elsevier Scientific Publishing Co., Amsterdam, 1983.

11.   D. Bradley and A. Mitcheson, "The Venting of Gaseous Explosions in Spherical Vessels: I-Theory," _Combustion and Flame_, 32, pp 221-236, 1978.

12.   D. Bradley and A. Mitcheson, "The Venting of Gaseous Explosions in Spherical Vessels: II - Theory and Experiment," _Combustion and Flame_, 32, pp 237-255, 1978.

13.   E. J. Anthony, "The Use of Venting Formulae in the Design and Protection of Building and Industrial Plant from Damage by Gas or Vapor Explosions," _J. Hazardous Materials_, 2, pp 23-49, 1977.

STRUCTURAL RESPONSE OF RC-MEMBERS IN CASE OF IMPULSIVE LOADING
Failure Analysis in Bending and Shear

Cornelis van der Veen

Johan Blaauwendraad

Delft University of Technology, Delft, Holland

Rijkswaterstaat, Structural Research, Utrecht, Holland

ABSTRACT

Beams and one-way slabs subjected to impulsive loading are analyzed with aid of a numerical model, which is kept as simple as possible, and which is sufficient powerful to simulate real beam response. Therefor the beam is schematized as a system of rigid sections and elasto-plastic hinges which can account for hysteresis. The equations which hold for this discrete model are presented. They are solved by use of the systems dynamics language Dynamo.

In case of the application of an impulsive loading to a simply supported beam a very typical pattern of 'travelling' plastic hinges may occur, different to what is known from static loads.

In case of the application of an explosive load to a beam with clamped ends, the similarity with static results is much greater. In the example of the flat roof of a traffic tunnel however, the shear failure criterion is extremely dominant, yielding strongly reduced allowable peak values of the explosive loads.

PROBLEM STATEMENT

Increasingly more we need to examine the strength of rc-structures in case of dynamic loading. The load can be a local impact or more general some kind of distributed impulsive loading. This paper reports on a study which has been originated by questions whether or not to transport explosive liquified gasses through traffic tunnels of rectangular cross-section. Especially the roof slab of the tunnel is studied, and for this purpose a strip of 1 m width has been examined. So the study regards a beam type structure, and in fact the results have been more general purpose than strictly spoken was needed for traffic tunnels.

The understanding of the structural behaviour of rc-structures is increasing rapidly. Research of last ten years has yielded a fastly growing number of tools to analyse total structures or members. At least as far as static loading is concerned which increases monotonically. Progress is also being made for repeated static loading and cycling static loading, in which the problem of stress reversal has to be dealt with. A less covered area is the dynamic response of rc-structures. In this case all mentioned aspects of static loading play their role, but above that the equations of motions have to be integrated in the time domain. Authors feel that the present-day finite element programs have proven to be powerful in the field of nonlinear static analysis of elastic structures, and even for the nonlinear dynamic analysis of metal structures. Experience and expertise for the nonlinear dynamic analysis of rc-structures is still poor however. A number of problems arise simultaneously in that case, for instance the correct choise of failure criteria, a satisfactory formulation of the softening problem after cracking, and particularly the problem of numerically stable processes for the integration in time of the equations of motion in case of such specific nonlinear phenomena. Therefore the nowaday finite element programs may give rise to problems which are connected with the mathematical algorithms, rather than relevant for the structural problem which is being studied. Authors expect much futural improvement in this field, but for the time being a well-proven approach is preferred which yields immediately insight in the structural respons, whithout being troubled to much with numerical problems.

The adopted simple beam model is used to gain improved understanding of elasto-plastic flexural structural response in the case of a beam subjected to impulsive distributed loading. Two special cases are discussed in some detail. The first one is the response of a simply supported beam, and the second one is the behaviour of a clamped beam. The simply supported beam is of interest to explain experimental results. In experiments it has been found that beams which have been subjected to distributed load of short duration may not get plastic hinges or fail in the mid of the span, but at positions more close to the supports.

The clamped beam more or less reflects the situation of a strip which can be taken from a roof slab in a traffic tunnel. Now questions arise which reinforcement is optimal, and which capacity a beam has for severe combinations of dynamic moments and shear forces.

DESCRIPTION OF THE BEAM MODEL

To achieve the simple beam model which has been aimed at, two decisions were made. The first one regards the mechanical modelling of the beam. We used the well-known discrete model in which a continuous beam in bending is replaced by a set of rigid sections and flexible rotational hinges at the nodes where sections join together, fig. 1. The mass of the sections is lumped at the nodes,

and likewise the time-dependent distributed load on the sections. The length of the sections is y. The flexible hinges are modelled as elasto-plastic springs.

The second decision regards the integration of the equations of motion. In stead of once more writing a specific computer code, we profited by the available systems dynamics package Dynamo. This language facilitates the stepwise integration in time of any set of first-order linear or nonlinear differential equations. Though Dynamo has been developed at MIT for socio-economical time-dependent problems, it proved to be possible to use it in the engineering field as well. Be it, that structural plastic irreversal deformation had to be interpreted as some type of an economical delay!

The two decisions, to use the discrete beam model and to make use of Dynamo, are in fact just one decision. Due to the discrete model we are able to use Dynamo, because of the fact that this model description can yield first-order differential equations in a simple way.
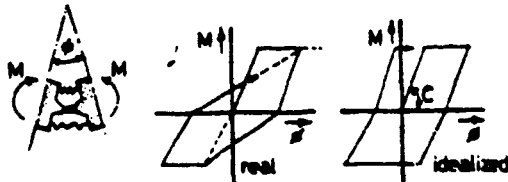
Fig.2 Elasto-plastic characteristics of the flexible springs.

We have to become more precise on the characteristics of the flexible springs in the discrete model. We will discuss the situation of a prismatic beam in which different percentages of top- and bottom-reinforcement can be used. First of all, it is important to describe hysteresis in an appropriate way, because of its strong damping action. In literature a v-ϕ diagram is used as is shown in the mid part of figure 2. This diagram is derived from the relation between the moment M and the curvature κ, for in fact ϕ is equal $y\kappa$, and the diagram holds for situations as occur with earthquakes during which cycling of the loads may last a number of seconds. In our case of a puls load or explosive loading one may expect that we do not run through the diagram a couple of times, but just one time due to strong plastic damping. After that the vibration will vanish elastically. This made us decide to use the more schematized M-ϕ diagram which is shown in the right-hand part of figure 2.
The stiffness C of the elastic branch is easily derived from the bending stiffness EI which holds for a rc-beam. We consider a part of the beam of length y and require that the discrete model yields

an equal angle ϕ as will occur in the real continuous beam when the same moment M is applied. From this we derive $M=C\phi$ in which $C=EI/y$.
The horizontal plateaus in the M-ϕ diagram are determined by the plastic bending moment which follows from the applied percentage of reinforcement. Also the ultimate value of ϕ and the inelastic rotation capacity ϕ_p must be determined.
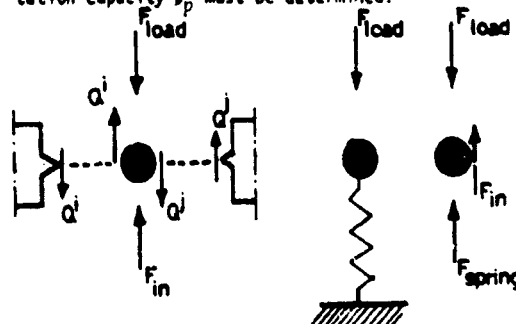

Fig.3 Each node of the discrete model can be considered as a mass-spring-system.

Each node of the discrete model can be considered as a mass-spring-system (fig.3). Three forces act on each node: F_{load} which is the external loading consisting of a static part F_{stat} and a dynamic part F_{dyn}, F_{in} due to the inertia of the mass, and F_{spring} which is the difference of the shear forces on both sides of a node. We introduce a for the acceleration of a node, v for the velocity of a node, w for the displacement of a node and m for the lumped mass. The integration process is as follows. Starting from known values $w(t)$, $v(t)$ and $a(t)$ at the beginning of a time step Δt, we calculate for each node using Euler's method the values $w(t+\Delta t)$ and $v(t+\Delta t)$ at the end of the time step by

$$w(t+\Delta t)=w(t)+\Delta t.v(t) \wedge v(t+\Delta t)=v(t)+\Delta t.a(t) \quad (1)$$

From the new values w we successively calculate for each node j

$$\phi^j=(-w^i+2w^j-w^k)/y \quad \rightarrow \quad M^j=C^j\phi^j \quad (2)$$

$$Q^i=(M^i-M^j)/y \quad \wedge \quad Q^j=(M^j-M^k)/y \quad (3)$$

$$F^j_{spring}=Q^i-Q^j \quad (4)$$

Herewith a new value $a(t+\Delta t)$ is calculated for each node: $a(t+\Delta t)=(F_{load}-F_{spring})/m \quad (5)$ which facilitates to use (1) again for the next time step. The scheme has to be adapted sligthly for a node at a clamped edge; equation (2) has a modified form in that case. The scheme implies that we have known values at $t=o$ for the quantities w,v and a, which are derived from the boundary conditions at that time. If the bending moment M^j from (2) exceeds the value of the plastic moment, this value is taken. Also specific attention is given to unloading processes and the related hysteresis, which will not be discussed here.

ULTIMATE STRENGTH AND ROTATION CAPACITY

The characteristics of the M-ϕ as were adopted in figure 2 presuppose that the beam has been designed in such a way that no failure in shear occurs before the plastic moment has been reached. It has also been adopted that the rotation capacity is not influenced by the presence of a shear force.

In genera¹ this is true because of the applied stir-
rup reinforcement in beams.
However, another situation applies for slabs, be-
cause of the absence of stirrups. So the strip which
can be selected from a tunnel roof -though being
treated as a beam- may behave in another way. In
that case a cross-section can fail for combinations
of a bending moment and a shear force in which the
bending moment is smaller than the plastic moment.
Brittle failure will be the case then. Or, in case
that the plastic moment can be reached, the rota-
tion capacity may be reduced. So, limitations on
strength and deformation.

As for the strength, shear failure strongly depends
on the relation of M and Qh, in which h is the ef-
fective depth of the beam. For different values of
M/Qh different failure mechanisms will occur, each
with its particular strength. In case of static
loads one normally differentiates in the following
modes:
-a shear crack grows from an existing bending crack
 (flexural shear failure);
-a diagonal crack in the web occurs due to tension
 stresses (tension shear failure).
We need not consider cases with diagonal crushing
which only might occur when stirrups are applied.
Neither we need view the case of failure in the
anchoring zone of the main reinforcement.

For static loads Rafla has proposed an appropriate
formula to estimate the flexural shear strength
of a beam. He derived the formula in a statistical
way from a large number of tests. We adapted the
5% lower boundary of all results for application
in dynamically loaded structures, yielding

$$\tau_{u,dyn} = \alpha_{dyn} \, f_{cc}^{\frac{1}{3}} \, \omega_0^{\frac{1}{3}} \, h^{-\frac{1}{4}} \quad (N/mm^2) \qquad (6)$$

Herein $\tau_{u,dyn}$ is the nominal shear stress which
has to be multiplied by the effective depth and the
width of the slab strip to find the shear force,
f_{cc} is the cube crushing strength, ω_0 is the per-
centage of reinforcement, and h is the effective
depth of the slab strip. The value α_{dyn} depends on
the relation of M and Qh:

$$\alpha_{dyn} = 0.9-0.03 \, M/Qh \qquad (7)$$

The other failure criterion for tension shear more
likely will occur for values of the bending moment
which are smaller than the flexural cracking moment
at which bending cracks come into being. For such
small moments (thus small values of M/Qh) no flex-
ural shear failure mechanism can develop. The ten-
sion shear failure will occur if the principle
tension stresses in the mid-plane of the strip ex-
ceed the dynamic tensile strength $f_{ot,dyn}$. There-
fore, a good approximation of τ_u at tension shear
failure reads

$$\tau_{u,dyn} = 0.67 f_{ot,dyn} \qquad (8)$$

The determination of the flexural cracking moment
can not be done very accurate however, because we
use average dynamic properties of the concrete.
Therefore we preferred to make the transition de-
pendent on the value of M/Qh. Rather arbitrarily
we decided to use the tension shear failure cri-
terion for values $M/Qh<0.75$ and the flexural shear
failure criterion for values of $M/Qh>1.75$. In be-
tween of these values a gradual transition has
been proposed from the one failure criterion to
the other.

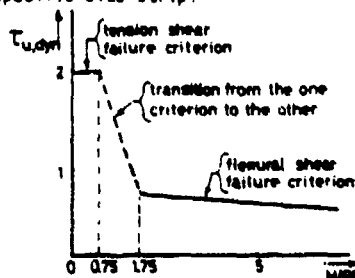Figure 4 shows the result of this decision for a
specific slab strip.

*Fig. 4 The failure envelope for the shear strength
in case of a particular concrete quality,
percentage of reinforcement, and depth of
the slab.*

We now concentrate on the deformation capacity. In
the case that no stirrups are applied, the shear
force must be partly transferred by the compression
zone of a cross-section. When a plastic moment
starts to occur, the compression zone will become
smaller for increasing curvature. However, in this
plastic case almost all shear force has to be trans-
ferred by the compression zone, due to large crack
widths. At certain deformation the compression zone
will have become so small that failure (by shear)
occurs. Hence the rotation capacity θ_{pQ}, which is
left over when a shear force is transferred, is
smaller than the rotation capacity θ_p which is at
disposal when no shear force occurs. The reduction
depends on the ratio of the present shear force Q
and the ultimate shear force Q_c, which anyhow can
be transferred by the concrete. This latter value,
holding before large shear cracks come into being,
can be calculated with aid of the Rafla-formula
(6) which has been adapted for dynamic conditions.
Figure 5 represents the adopted dependency of the
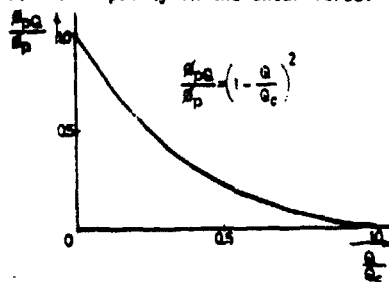rotation capacity on the shear force.

$$\frac{\theta_{pQ}}{\theta_p} = \left(1-\frac{Q}{Q_c}\right)^2$$

*Fig. 5 The rotation capacity θ_{pQ} decreases for an
increasing shear force Q.*

APPLICATION TO A SIMPLY SUPPORTED BEAM

In this application it is assumed that the beam
can not fail in shear. So it has been adopted that
sufficient shear reinforcement is applied.
The span is 15000 mm, the depth of the beam is
1200 mm and the width is 1000 m. Top and bottom
reinforcement percentage is 0.3%. The concrete
quality is B22,5 and steel quality is FEB 400.
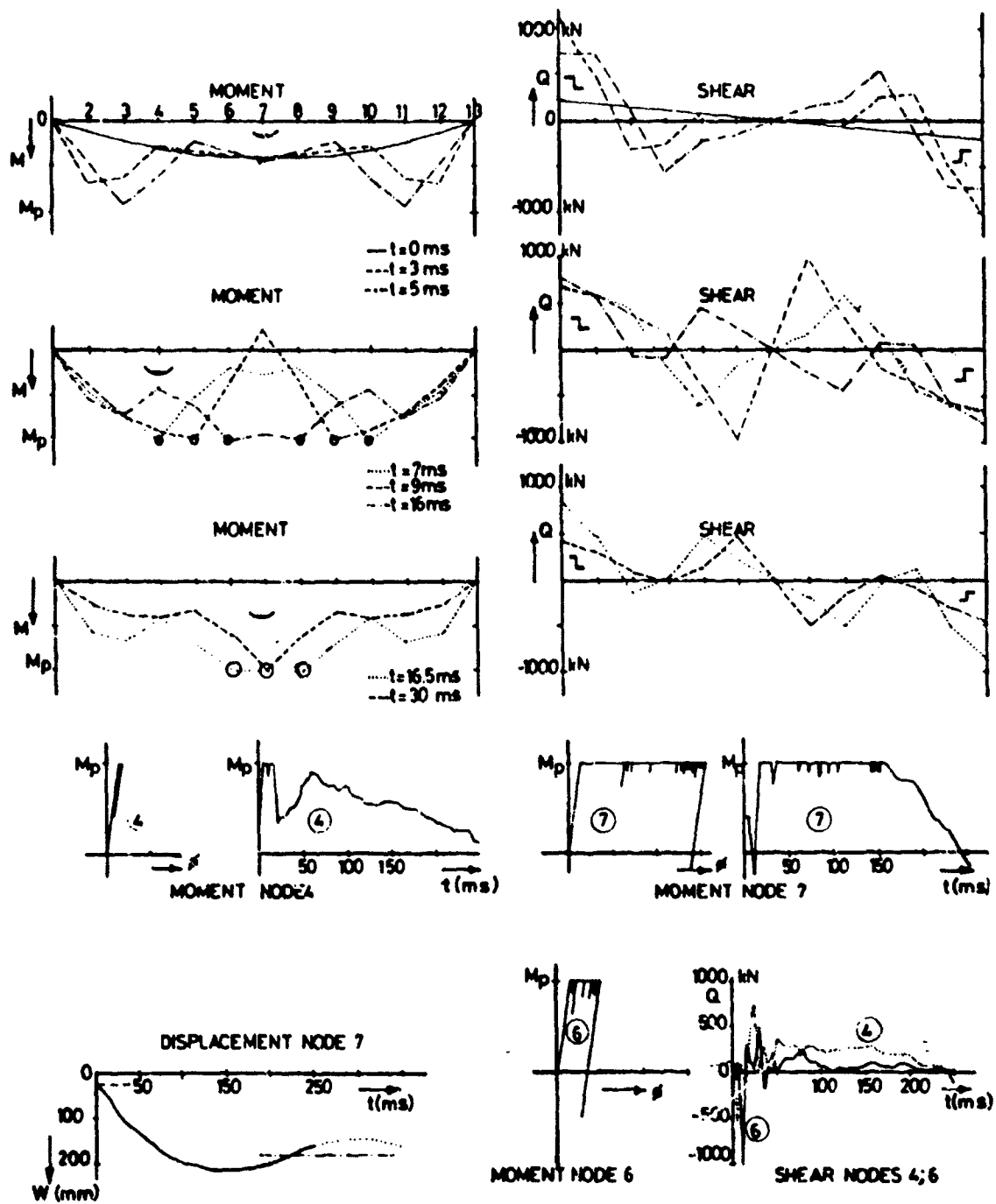For the concrete material we introduced

Fig.6 Typical response plots for an impulsive distributed load on a simply supported beam.

The span is modelled with 12 discrete sections, which implies that the length of a section is to be compared with the depth of the beam. The load in each node consists of an impuls 6 kNs at $t=o$. The lumped mass m in each node is 3600 kg, so the impulsive load yields an initial value of the velocity $v = 6000:3600 = 1.7$ m/sec. One could interpret the analysis as an experiment in which the beam falls freely from some height until it hits at time $t=o$ the two supports.

Results of the analysis are given in fig. 6. Herein the distribution along the span of the beam is shown for the moment M and the shear force Q for different times t. At small values of time t the beam hardly feels that the supports have been hit. Only at the end strong curvatures and thus moments occur. Also big shear forces appear in these parts of the beam. When time goes on the bending moment diagram changes of shape and the displacement diagram developes in an expected way. One can easily see that a wave of shear force travels through the beam. In total agreement with the development of the moment diagrams one also can note from the plots in fig. 6 that plastic hinges come into being at some distance from the supports and then "travel" to the mid of the span. Also some plots in the time domain of a displacement w, a moment M, and a shear force Q are shown in fig. 6. The alternating character is demonstrated once more in these plots. In the same figure it is shown for a couple of hinges which path has been run through in the elasto-plastic $M-\phi$ diagram. From this it appears that the beam after some time vibrates in an elastic way over its whole length.

In conclusion, it is felt that the runs made, have shown that the elasto-plastic discrete model is able to represent the main characteristics of the behaviour of a beam for impulsive loading in a satisfactory way. Though the real behaviour in detail may be slightly different, the global behaviour is modelled in an appropriate way. Available experimental data are confirmed by the results of the model. This holds at least in a qualitative sense, but also the quantitative information sounds profound.

APPLICATION TO BEAM WITH CLAMPED ENDS

We now consider a beam with clamped ends, which is representative for the response of the roof of a tunnel in which an explosion occurs. Fig. 7 shows the cross-section of a typical traffic tunnel as it is applied in the western part of the Netherlands. The pressure-time plot of the shock wave due to an explosion in a tunnel is shown in fig. 3. Herein P_{max} is the peak value of the pressure, which is expressed in bars (1 bar = 100 kN/m²), and t_d is the duration of the phase at which the pressure is present (positive phase). After $t=t_d$ suction may set in (negative phase). The pressure-time plot appears to be described accurately by the formula
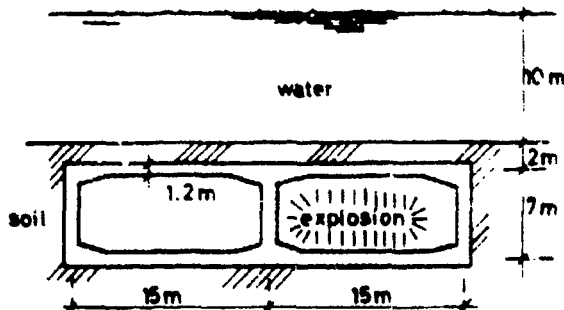
$$p(t)=P_{max}\left(1-\frac{t}{t_d}\right) e^{-\alpha\frac{t}{t_d}}$$

Fig.7 Example of a typical traffic tunnel in the Netherlands.

The coefficient α is a shape factor of the shock wave. In a tunnel its value can be set to 4. Dependent on the type of liquified gas, the peak value can be of the order of 10 bar up to 25 or 30 bar for the worst type. Tests in small scale tunnels show a positive phase duration t_d of about 50 ms. It is not quite clear which model law applies to determine the value of t_d in a real tunnel, but it should be expected that t_d may increase. Therefore we have examined the influence of three values of t_d, namely 50 ms, 100 ms and 150 ms.
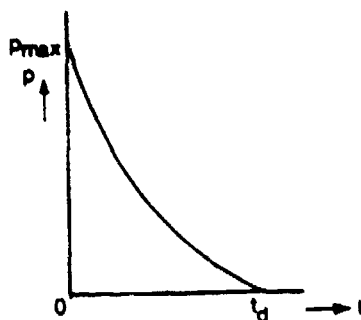

Fig.8 Pressure-time plot for an explosion in a tunnel.

Firstly we made an analysis of a beam with clamped ends, assuming that no failure due to shear will occur. The span is 15 m and the slab thickness 1.2 m. We started with a high percentage of main reinforcement at the top and bottom of the slab of 2.5%. This yields the following capacity of the beam, which is determined by exhausting the ultimate rotation capacity.

$\omega_o = 2.5\%$

t_d	P_{max} (rot. cap.)
50 ms	60 bar
100 ms	34 bar
150 ms	26 bar

We see that P_{max} reduces for increasing t_d. Though not exactly true, one can roughly say that the product of P_{max} and t_d is constant. Or said in another way, that the total impuls is more of less determining. In all three analyses plastic hinges come into being at the clamped ends and at mid span, in the same way as is found for a static load (so

different from what we experienced for a simply supported beam).

The analyses may produce insight and understanding, they have however no practical value because of too high shear forces. In slabs without shear reinforcement the allowable nominal shear stress τ_u is of the order 1 N/mm², and we have found values between 5 and 8 N/mm². So the real applicable P_{max} will be much lower.

To demonstrate the influence of the shear failure criterion, a new series of analyses have been then executed, for reinforcement percentages 0.7, 1.1, 1.8 and 2.5. Here we only present the results for $\omega_o = 1.1\%$.

t_d	$P_{max}(rot.cap.)$	$P_{max}(shear failure)$
50 ms	26 bar	7 bar
100 ms	14 bar	4.5 bar
150 ms	8 bar	3 bar

$\omega_o = 1.1\%$

We see that the application of the shear failure criterion strongly reduces the allowable P_{max}, as compared with the situation in which one just checks the exceedence of the rotation capacity. Roughly P_{max} decreases to one third. And for higher percentages of the reinforcement the reduction is still more severe.

An inspection of the results learns that even no plastic moments occur anymore, because of early shear failure. Whilst the moment diagram along the span is similar to the distribution which is found for a static load, the distribution of the shear force is quite different. Failure does occur rather close to the mid of the span in node 5 or 6! The analysis for $t_d = 150$ ms has also been carried out for the other percentages of reinforcement which have been mentioned before. Supprisingly enough, the allowable P_{max} in all cases was 3 bar. It is true, the allowable shear force does increase for an increasing percentage of reinforcement, but apparently also the acting shear force can become bigger, due to an increasing bending stiffness.

CONCLUSIONS

A discrete beam model consisting of rigid sections and flexible hinges is a powerful tool for better understanding of the elasto-plastic response of reinforced concrete beams which are subjected to impulsive loading. This is achieved thank to the fact that the governing equations of such a model are easily solved by the use of an available systems dynamics language Dynamo.

For simply supported beams impulsive load yields a moment distribution and shear forces which strongly differ from the ones which hold for simular static loads. Provided that no shear failure occurs, plastic moments can occur at positions along the span at some distant of the mid. The plastic hinges thereupon travel to the mid of the span.

In case of the examined beam with clamped ends (simulating a tunnel roof) the results are different. The moment distribution is more similar to the one which appears for static loads, but the shear force still differs, be it less than in a simply supported beam.

From this one can conclude that an idealization of a tunnel roof to a simple-mass-spring-system is accurate for the displacement and moments, but may be misleading for the value of the maximum shear force and the position along the span of its occurrence.

If no stirrups are applied a shear failure criterion has to be introduced, which strongly reduces the allowable load, and in most cases no plastic hinges will come into being anymore.

REFERENCES

1. Blaauwendraad, J; Methods and Possibilities for Electronic Analysis of slabs (in Dutch). De Ingenieur, Vol. 03, 7 Febr. 1969.

2. Pugh, A.L.; Dynamo II User Manual, 4th edition. The MIT press, 1972.

3. Monnier, Th.; The Moment-Curvature Relation of Reinforced Concrete, Heron, Vol. 17, no. 2, 1970.

4. Rafla, K.; Empirical Formula for the Calculation of the Shearcapacity of rc-beams, Part I (in German). Strasse, Bruecke, Tunnel, Dec. 1971, no. 12.

5. CUR-VB report 108: Plastic Hinges (in Dutch), Sept. 1982.

6. Walraven, J.C.; Shear Capacity of Reinforced Concrete Beams and Lightweight Concrete Beams without Shear Reinforcement, (in Dutch). Betononderzoek, Delft University of Technology, 1980.

7. Van der Veen, C.; Blaauwendraad, J.; Dynamic Elasto-Plastic Model for RC-members in case of Impulsive and Explosive Loading, Rijkswaterstaat, Structural Research, report no. 83-01, Utrecht, Holland (extended version of the paper; summary of thesis of C. v.d. Veen).

COMPARISON OF PREDICTIVE METHODS FOR STRUCTURAL RESPONSE
TO HE BLAST LOADS

Washington T. Char
Michael M. Dembo

US Army Corps of Engineers
Huntsville, Alabama

ABSTRACT

Numerous methods for predicting structure re-
sponse to airblast caused by HE explosions were
developed during the last twenty years. The rigor,
complexity and sophistication of the methods are
known to cover a wide spectrum. Some the less
complex but widely accepted methods are examined,
assessed, and discussed relative to their degree
of conservatism. To support their assessment,
the authors critically examined the structural
design parameters used in the predictive methods.

BACKGROUND

The Corps of Engineers, as the Army's
designer and builder of military facilities,
maintains a continuing interest in the technol-
ogy of the effects of weapons and explosions on
structures. The earliest design techniques were
related to projectile penetration and then came
the great interest in effects of nuclear weapons
including blast, shock, and other associated
effects. During World War II, there developed
relatively crude procedures usually "rule of
thumb" methods to estimate effects of accidents
at the many munitions and explosive manufacturing
facilities which we rapidly erected during the
period 1941-1945. In the last 30 years, problems
of design of structures to resist the effects
of HE explosions have been addressed on a more
rational basis.

Two of the most recent non-nuclear documents
reflecting the Corps' efforts are TM 5-1300,
Structures to Resist the Effects of Accidental
Explosions (1969), and HNDM-1110-1-2, Suppressive
Shield Design and Analysis Handbook (1977).
These documents, among other Corps references,
provide our basic guidance. However, the Corps
design activities have not been restricted to
these two documents.

Many methods conforming to other authorities
are also used. Some of the most frequently used
methods are: (1) ASCE Manual 42, (2) Air Force
Manual 500-8, (3) Defense Civil Preparedness
Agency (now Federal Emergency Management Agency)
Protective Construction, and other texts usually
associated with structural dynamics.

APPROACH

Our experience with HE explosions typically
centers on three basic types of airblast loading:
(1) pressure-time (triangular), (2) impulsive,
and (3) the combination of impulsive and pressure-
time loading as shown in Figure 1.

Accordingly, each of these loads was sepa-
rately included in the analysis. It was consid-
ered important that these loads be treated
separately in view of possible variances in con-
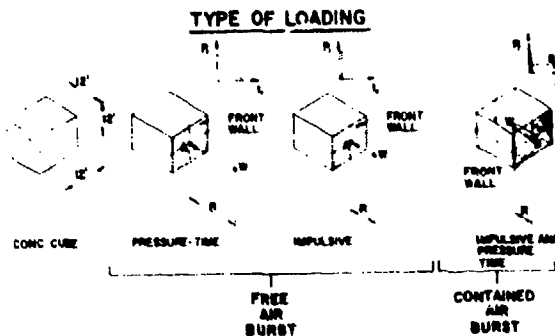servatism in the methods under the different
loading.

TYPE OF LOADING

Figure 1

Since reinforced concrete prevails among pro-
tective structures, we selected a reinforced
concrete wall as the structural element for our
assessment of the methods. After determining the
loads and the structural elements, we proceeded
with our analysis.

BEST AVAILABLE COPY

STRUCTURAL CAPABILITY

The two-way reinforced concrete wall in Figure 2 was designed for flexure as indicated by the main reinforcement. No shear calculations were made. For our purpose, it is assumed that shear may be adequately provided. Flexural strength and other structural properties are tabulated in Table 1. These were used as the basis for calculating deflection used in our comparison.
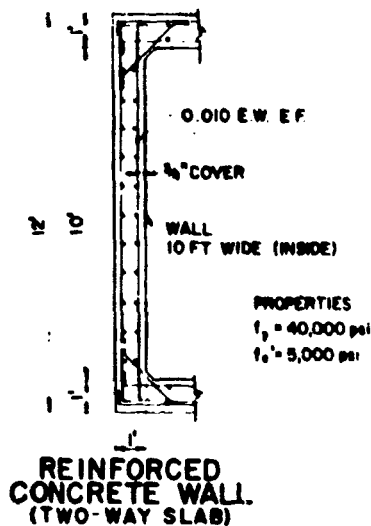
REINFORCED
CONCRETE WALL.
(TWO-WAY SLAB)
Figure 2

TRIANGULAR LOAD

A family of curves is plotted for the reinforced concrete wall to predict the wall deflection resulting from a triangular pressure-time load. Each curve represents a specific ductility ratio, u, hence deflection. See Figure 3.
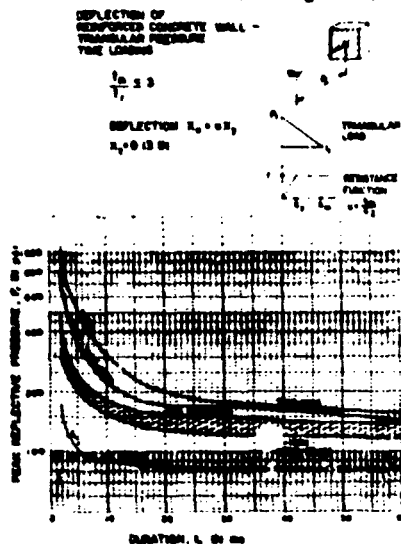
Figure 3

By locating the coordinate (t_d, P_r), the ductility ratio may be estimated by interpolating between the u's. For a ductility ratio, $u = 3$, two curves are shown; one for TM 5-1300 method and the other for the suppressive shield method. All the other methods previously discussed are distributed in the shaded band. A close observation indicates that the TM 5-1300 curve is more conservative than the others, because being on the lower side of the shaded band it has more restrictions on the limits of pressure and duration for the given ductility ratio, $u = 3$. The Suppressive Shield Handbook curve is less restrictive, allowing 25 percent higher pressures for the same duration and ductility ratio.

IMPULSIVE LOAD

When the wall is impulse sensitive from close-in explosions, deflections are also predictable. Based on the curves in Figure 4, the TM 5-1300 curve on the lower side of the shaded band is conservative because being on the lower side of the shaded band, it has more restrictions on the limits of the impulse for a given deflection. The Suppressive Shield Handbook curve is less restrictive allowing 20 percent higher impulse for the same deflection. Curves for the other methods are distributed within the shaded band.
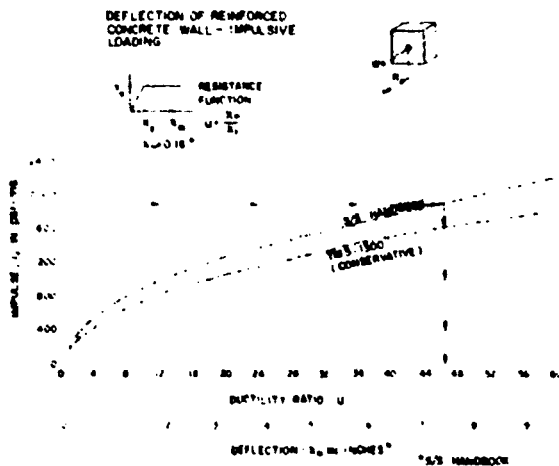
Figure 4

COMBINED LOAD

The combined load consists of an impulsive load followed by a prolonged gas pressure. A family of curves is shown in Figure 5 and each curve represents a specific ductility ratio, u.

After locating the coordinate (P_{gs}, i_r), the ductility ratio, u, can be estimated by interpolation between u's. The ductility ratio curve u = 3 for TM 5-1300 and the Suppressive Shield Handbook methods are shown. It can be demonstrated again that the TM 5-1300 curve on the lower side of the shaded band is more conservative than the Suppressive Shield Handbook curve on the upper side of the band. TM 5-1300 is more restrictive on the limits of impulse and gas pressure for a given ductility ratio, u = 3. The Suppressive Shield curve is less restrictive allowing 15 percent impulse or 30 percent higher gas pressure for the same ductility ratio.

DEFLECTION OF REINFORCED
CONCRETE WALL - COMBINED
LOAD
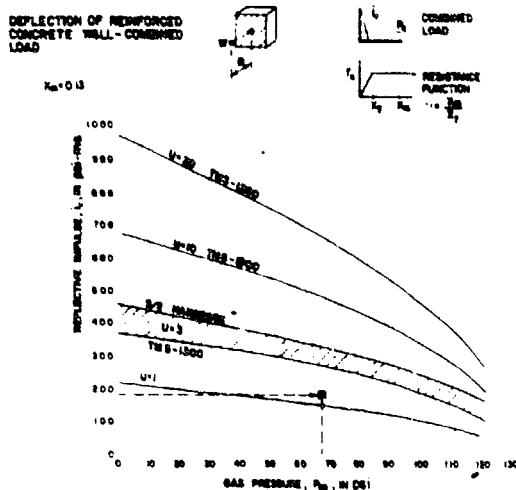
Figure 5

EXAMPLE

The charge weight, distance and load parameters are shown in Figure 6. These numbers provide an appreciation for the magnitude involved and an understanding of the curves. Applying load parameters on the wall, deflections are estimated by using Figures 3, 4, and 5. These examples are not restricted to any one method, i.e., both TM 5-1300 and Suppressive Shield methods are used below.

For the 8000# TNT at 100 feet, where P_r = 90 psi and t_r = 16 ms, select from Figure 3 (TM 5-1300 curve) approximate u = 1.4 or X_m = uX_o = 1.4 x 0.13 in. = 0.2 in. For the 512 lb. TNT at 10 feet, where i_r = 1920 psi-ms, select from Figure 4 (Suppressive Shield curve) X_m = 7.4 in.

For the contained 8 lb. TNT at 5 feet, where i_r = 184 psi-ms and P_{gs} = 64 psi, select from Figure 5 (TM 5-1300 curve) approximate u = 1.3 or X_m = 1.3 x 0.13 = 0.2 in. These deflections compare well with the calculated X_m in Table 1.

ASSUMPTIONS

Four factors influence the differences in the predictive methods; yield line assumption, moment of inertia, modulus of elasticity and stiffness. As expected, the variance within these factors are the basis for the differences in the predicted deflection.

YIELD LINE

In most two-way slab designs, the effective unit resisting moments are assumed to be uniformly distributed on the yield lines. In TM 5-1300, the effective resisting moment at the corners are reduced by one third. This reduction causes the TM 5-1300 method to be significantly conservative. See Figure 7.

TWO-WAY SLAB
YIELD LINE DISTRIBUTION OF MOMENTS
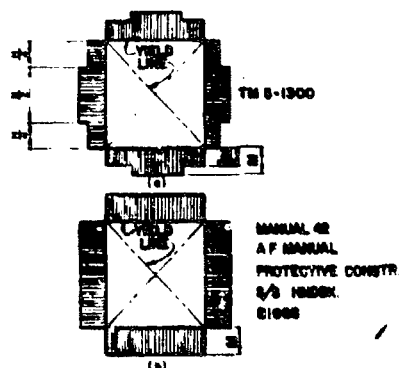
MOMENT OF INERTIA

The formulas for moments of inertia are shown in Figure 8.

FORMULAS FOR MOMENT OF INERTIA
(REINFORCED CONCRETE SLAB)

Figure 8

Appreciable difference in I_a appears when the slab thickness is small. This is attributable to the use of "T" in TM 5-1300 and "d" in the other methods.

MODULUS OF ELASTICITY

When 3600 psi concrete is specified, the E_c in Figure 9 is the same for all methods. See intersection of curves.

MODULUS OF ELASTICITY(CONCRETE)

$E_c = W^{1.5} 33 \sqrt{f_c'}$ TM 5-1300
A F MANUAL
S/S HNDBK.
BIGGS
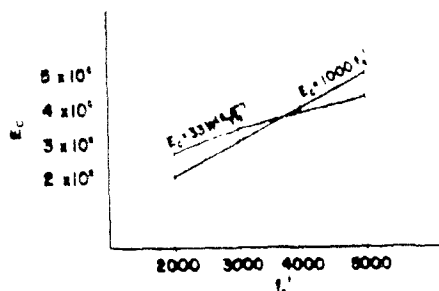
$E_c = 1000 f_c'$ MANUAL 42
PROTECTIVE CONSTR.

Figure 9

Since most concrete strength for airblast loads exceed 4000 psi, a difference in modulus of elasticity is unavoidable.

STIFFNESS

With the exception of protective construction and Manual 42, the equivalent stiffnesses are used. From our preceding example, the stiffness by Manual 42 is significantly higher as shown below:

Manual 42
Protective Construction
$$k = 807\left(\frac{E_c I_a}{L_a^4}\right)$$

Others
$$k = 605\left(\frac{E_c I_a}{L_a^4}\right)$$

DISCUSSION

The assessment on the relative conservatisms are based on airblast data from TM 5-1300 curves. The more recent data in the Suppressive Shield Handbook is significantly different. The difference in impulse is seen in Figure 10. TM 5-1300 is as much as 60 percent higher.
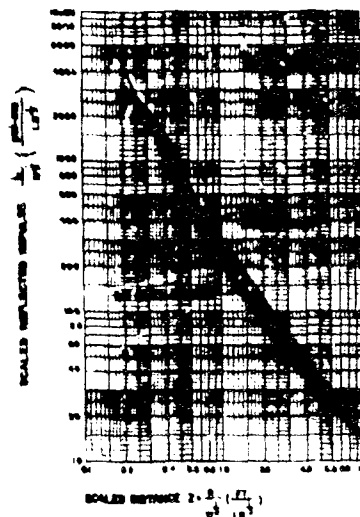
Figure 10

If the latest data were separately used in the Suppressive Shield Handbook method, the differences in conservatism between methods would be more pronounced.

We have examined the extremes in the predictive methods. Of the six methods, no comparison was made as to how how each related to the other in conservatism. The best basis for judgement is the comparison of deflections in Table 1.

In our examination of the methods, we assumed all methods are conservative. This assumption is supported by testing of full scale and model structures in previous Army programs associated with the development of Corps or Engineers manuals for hardened structures. Accordingly, we consider the assumption to be reasonable.

CONCLUSION

In assessing the relative conservatism of the methods, the focus was on both ends of the spectrum; the most conservative on one end and the least conservative on the other. We identified the TM 5-1300 method as the most conservative and the Suppressive Shield Handbook method as the least conservative.

Based on the maximum deflection, X_m, in Table 1, the order of conservatism beginning with most conservative to least conservative follows:
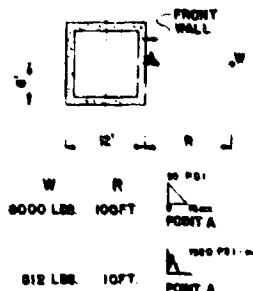
1. TM 5-1300

2. Manual 42

3. Protective Construction

4. Air Force Manual

5. Biggs

6. Suppressive Shield Handbook

In general, because of similarity, it would be more appropriate to group conservatism as follows: TM 5-1300 by itself as the most conservative; Manual 42, Protective Construction, and the Air Force Manual in the intermediate group; and Biggs and the Suppressive Shield Handbook as the least conservative group.

BIBLIOGRAPHY

1. TM 5-1300: Structures to Resist the Effects of Accidental Explosions, TM 5-1300, Department of the Army, Washington, DC, June 1969.

2. Manual 42: Design of Structures to Resist Nuclear Weapon Effects, ASCE Manual of Engineering Practice No. 42, American Society of Civil Engineers, New York, NY, 1964 edition.

3. AF Manual: Effects of Airblast, Cratering, Ground Shock and Radiation on Hardened Structures, AFSCM Manual 500-8, Department of the Air Force, Washington, DC, January 1976.

4. Protective Construction: Protective Construction, TR-20 (Vol 4), Defense Civil Preparedness Agency, Baltimore, MD, May 1977.

5. Suppressive Shield Handbook: Suppressive Shields, Structural Design and Analysis Handbook, F A-1110-1-2, US Army Corps of Engineers, Huntsville, AL, November 1977.

6. Biggs: Biggs, J. M., Introduction to Structural Dynamics, McGraw-Hill Book Company, New York, NY, 1964.

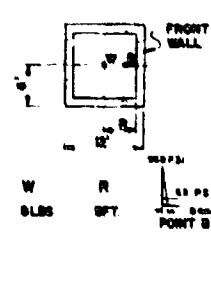**FREE AIR BURST**   **CONTAINED BURST**

Figure 6

Table 1

COMPARISON
(DESIGN PARAMETERS OBTAINED THROUGH DIFFERENT DESIGN METHODS)

METHOD / PARAMETER	TM5-1300	MANUAL 42	AF MANUAL	PROTECTIVE CONSTR	S/S HDBK	BIGGS
	970	700	66.0	70 0	60 0	60 0
	4.3×10⁵	5.0×10⁵	4.3×10⁵	5.0×10⁵	4.3×10⁵	4.3×10⁵
	1015	1370	1000	1370	1000	1000
T_m	6	6	6	6	6	6
	47,900	44,800	44,800	44,800	47,900	47,900
	132	149	149	149	194	199
ELASTIC DEFLECTION X m	013	011	016	011	016	016
X m-10	02	01	02	01	02	02
X m-10 IMPULSE	03	100	--	106	73	73
X m	02	—	—	02	02	—

RESPONSE OF A LINEAR STRUCTURE TO AN EXPONENTIAL PRESSURE PULSE

Franklin D. Maine

Naval Surface Weapons Center
White Oak, Silver Spring, Md. 20910

ABSTRACT

Explosion Dynamics is concerned with the response of structures to intense pressure loadings from shock waves. Most interactions that occur in practice are very complex, so that scaling laws are often employed to reduce the number of independent variables to a lesser number of dimensionless variables. Very often, this makes the results easier to interpret. Here, new similarity variables are introduced which lead to flatter response curves than those obtained previously.

The energy transfer from the fluid to the structure is treated by computation of the fluid work done on the structure and the increase in elastic energy stored in the structure.

INTRODUCTION

Underwater explosions produce a complex fluid-structure interaction at the surface of a submerged body. The pressure at the body surface is dependent not only on the shape of the body, but is modified by the induced motion of the body surface. In general, because of the non-linear behavior of the water, the surface pressure at any particular time will depend on the previous history of the motion of the surface.

This means the free field pressure from the explosion is modified not only by shock reflection from the body, but also by the particular path taken by the surface as it moves under the pressure loading.

This paper is concerned with the special case where the pressure modification from body surface motion is negligible. This usually occurs in the case of explosions in air. The structure is assumed to be a linear spring-mass system subjected to an exponential pressure load. A development of model laws for this case appears in Reference 1. In this paper, new similarity variables are introduced which give further insight into the dynamics of explosion induced motions of structures.

DYNAMICS OF A LINEAR STRUCTURE

The single degree of freedom spring-mass system is governed by the differential equation

$$\ddot{x} + \omega^2 x = P \exp(-t/T) \qquad (1).$$

where x is the displacement, $\ddot{x}$ is the acceleration, P is the peak pressure, t is the time, and T is the characteristic time of the pressure pulse. The natural frequency ω is given by

$$\omega = \sqrt{k/M} \qquad (2).$$

where k is the linear spring constant, and M is the mass of the body surface per unit area. The boundary conditions at $t = 0$ are

$$t = 0: \dot{x} = x = 0 \qquad (3).$$

where $\dot{x}$ is the velocity of the surface. The solution of this system is oscillatory with the maximum displacement xm reached at time tm.

It is convenient to introduce the following dimensionless variables:

$$\bar{x} = k\,x/P \qquad (4).$$

$$\overline{xm} = k\,xm/P \qquad (5).$$

$$\bar{T} = \omega\,T \qquad (6).$$

$$\bar{t} = \omega\,t \qquad (7).$$

$$\overline{tm} = \omega\,tm \qquad (8).$$

In terms of these new variables, the solution to Equation (1) that satisfies the boundary conditions given by Equation (3) is

$$\bar{x} = \frac{\bar{T}^2}{1 + \bar{T}^2}\left[\exp(-\bar{t}/\bar{T}) - \cos\bar{t} + (\sin\bar{t})/\bar{T}\right] \qquad (9).$$

The relationship between the exponential pressure loading and the resultant displacement of the structure is shown in Figure 1.

TIME OF MAXIMUM DISPLACEMENT

As indicated in Figure 1-A, the maximum displacement mm of the structure is reached at time tm when the velocity vanishes. Differentiation of Equation (9) leads to the expression

$$\bar{T} \exp(-\overline{tm}/\bar{T}) + \bar{T} \sin \overline{tm} + \cos \overline{tm} = 0 \quad (10).$$

The time at maximum displacement is shown in Figure 2 as a function of the characteristic loading time.

MAXIMUM DISPLACEMENT BASED ON PEAK PRESSURE

Substitution of $\overline{tm}$ into Equation (9) leads to the distribution of the maximum displacement function $\overline{mm}$ shown in Figure 3. The maximum displacement function, as defined by Equation (5), is the ratio of maximum displacement to the displacement that would occur under a static load equal to the peak pressure. A disadvantage of this definition is that it is independent of the shape of the pressure pulse. This produces the large variation in $\overline{mm}$ shown in the Figure 3. A flatter response curve can be obtained by basing the displacement on an average pressure exerted on the wall, rather than the peak pressure.

AVERAGE PRESSURE AND APPLIED IMPULSE

The definition of total impulse is

$$I = \int_0^\infty p(t)\,dt \quad (11).$$

For the exponential loading used here,

$$P = I/T \quad (12).$$

Because the total impulse includes the pressure loading applied to the structure after it has reached its maximum displacement, we introduce a new similarity variable, the applied impulse J defined by the shaded region in Figure 1-B. By fixing the upper limit of integration to the time of maximum displacement, the applied impulse is

$$J = \int_0^{tm} p(t)\,dt \quad (13).$$

From Figure 1-B, the average pressure, applied up to the time of maximum deflection, is

$$Pa = J/tm \quad (14).$$

For the exponential loading considered here, Equation (14) becomes

$$Pa = (P\,\bar{T}/\overline{tm})\{1 - \exp(-\overline{tm}/\bar{T})\} \quad (15).$$

MAXIMUM DISPLACEMENT BASED ON AVERAGE PRESSURE

A new displacement function analogous to Equation (5), but based on the average pressure instead of peak pressure is

$$mm^* = k\,mm/Pa \quad (16).$$

A plot of this function, showing the relatively flat response is shown in Figure 3. A quasi-static load with $\bar{T} = 1000$ will produce a maximum deflection that is 1.273 times larger than that produced by a impulsive load with $\bar{T} = .01$, if the average pressure Pa is the same for both loadings. In this comparison, the maximum deflection mm is not very sensitive to the shape of the pressure pulse.

PEAK AND AVERAGE PRESSURE FUNCTIONS

In Reference 1, a peak pressure function was defined as

$$\bar{P} = 2\,P/(k\,mm) \quad (17).$$

The denominator on the right represents the maximum elastic energy stored in the spring. This occurs at the time of maximum displacement. Here, an average pressure function is introduced in the form

$$Pa^* = 2\,Pa/(k\,mm) = 2/mm^* \quad (18).$$

This function gives the ratio of the average pressure to the average spring force. Plots of these pressure functions appear in Figure 4. The applied pressure function is relatively flat compared to the peak pressure function. This means that, over a wide range of values of the characteristic time of the pressure pulse, the ratio of average pressure to the maximum elastic energy stored in the structure is almost constant.

TOTAL AND APPLIED IMPULSE FUNCTIONS

In Reference 1, a impulse function was defined as

$$\bar{I} = I/(\omega\,M\,mm) = \bar{P}\,\bar{T}/2 = \bar{T}/\overline{mm} \quad (19).$$

Here, this is replaced by an applied impulse function defined as

$$J^* = J/(\omega\,M\,mm) = Pa^*\,\overline{tm}/2 = \overline{tm}/mm^* \quad (20).$$

As shown in Figure 5, J^* varies from 1.0 for impulsive loads to 1.571 for quasi-static loads.

The pressure function, total impulse function response curve from Equation (19) is shown in Figure 6. The curve is a hyperbola

extending to infinity along force and impulse
asymptotes. A corresponding applied pressure
function, applied impulse function response
curve from Equation (20) is also shown. The
latter curve is a small segment of a hyerbola
that gives the combinations of applied pressure
and applied impulse that produce the same
maximum displacement of the system.

ENERGY CONSERVATION

If viscous dissipation and radiation damping
from wall motion are neglected, the work done on
the structure by the fluid is converted directly
into kinetic energy of the structure and elastic
energy stored in the spring. If time is
measured from shock impingement with the
structure, the work done on the structure by the
fluid pressure up to the time of maximum
displacement is

$$W = \int_0^{tm} x\, p(t)\, dt \qquad (21).$$

where x is the surface velocity. A work
function is defined by the expression

$$W^* = W/(P\, xm) \qquad (22).$$

where the denominator is the fluid work done on
the structure by a static load equal to P. With
the aid of Equation (21), Equation (22) becomes

$$W^* = \frac{\overline{T}(1 + \overline{T}^2 - 2\, H\cos \overline{tm})}{2(\sin \overline{tm} - \overline{T}\cos \overline{tm} + \overline{T}\, H)} \qquad (23).$$

where

$$H = \exp(-\overline{tm}/\overline{T}) \qquad (24).$$

The fluid work function is shown in Figure 7.
As the pressure loading becomes more impulsive,
the work done by the fluid on the structure is a
smaller percentage of that produced by a quasi-
static load.

At any instant in time, the fluid work is in
equilibrium with the elastic energy stored in
the spring and the kinetic energy of the mass.
This can be expressed as

$$W = E + Q \qquad (26).$$

where the elastic energy is

$$E = k\, x^2/2 \qquad (27).$$

and the kinetic energy is

$$Q = M\, x^2/2 \qquad (28).$$

Equation (26) can be written in the form

$$G^* = E/W = 1 - Q/W \qquad (29).$$

After some manipulation, we obtain

$$U^* = \frac{[\sin \overline{t} - \overline{T}\cos \overline{t} + h\, \overline{T}]^2}{(1 + \overline{T}^2)(1 + h^2 - 2\, h\cos \overline{t})} \qquad (30).$$

This function is plotted in Figure 8 for
three values of the characteristic time ranging
from 0.1 to 1000. These curves correspond to
impulsive, dynamic, and quasi-static loads,
respectively. Each curve starts at zero time
and ends at the time of maximum deflection when
all the fluid work on the structure is stored as
elastic energy. For times between these two
endpoints, only a fraction of the fluid work
done on the structure is stored as elastic
energy. The balance, as indicated by Equation
(29), is stored as kinetic energy.

As the wall starts to move under the intense
pressure loading, most of the work done by the
fluid goes into kinetic energy. Only a small
percentage goes into elastic energy stored in
the spring. After the wall has reached its
maximum velocity, a greater percentage of the
work has been converted into elastic energy.
When the wall finally comes to rest at the
maximum displacement point, all the fluid work
is stored as elastic energy.

CONCLUSIONS

The response curves for a linear spring-mass
system have been modified by the introduction of
new similarity variables. The applied impulse
is defined as the impulse received by the
structure up to the time of maximum
displacement. Any impulse received after this
time does not have any influence on the
magnitude of the maximum displacement, and is
therefore neglected. An average pressure over
this time interval was also introduced to be used
in place of the peak pressure. This was chosen
because two different pressure loadings with the
same initial peak can have completely different
responses because their charactistic times are
different.

The response curves for the new functions
introduced here are fairly flat and do not
approach zero or infinity as when the loading
is static or very impulsive. A structure that
receives the same applied impulse from two
different pressure pulses will receive
approximately the same maximum deflection. This
cannot be said for two different pulses that
have the same total impulse.

A study of the energy transfer from the
fluid to the structure indicates the work done
by the fluid is initially transformed mostly
into kinetic energy. Later, after the structure
has reached its maximum velocity, a greater
percentage of the fluid work is stored as

elastic energy in the spring. When the structure has reached its maximum displacement, all the fluid work is stored in the spring as elastic energy. Any energy remaining in the pulse after the time of maximum displacement is irrelevant, and is essentially wasted, since it cannot have any influence on the maximum displacement.

It is expected that these results will be significantly modified when the pressure loading is changed by radiation damping produced by fluid-structure interaction. Even when the free field pressure is exponential, the actual pressure at the surface of the structure will no longer have that form of decay. This case, which applies to most underwater explosions, will be the subject of a future study.

REFERENCES

1. Baker, W. E., Westine, P. S., and Dodge, F. T., "Similarity Methods in Engineering Dynamics" (New Jersey: Hayden Book Co., Inc., 1973), pp.28-32.
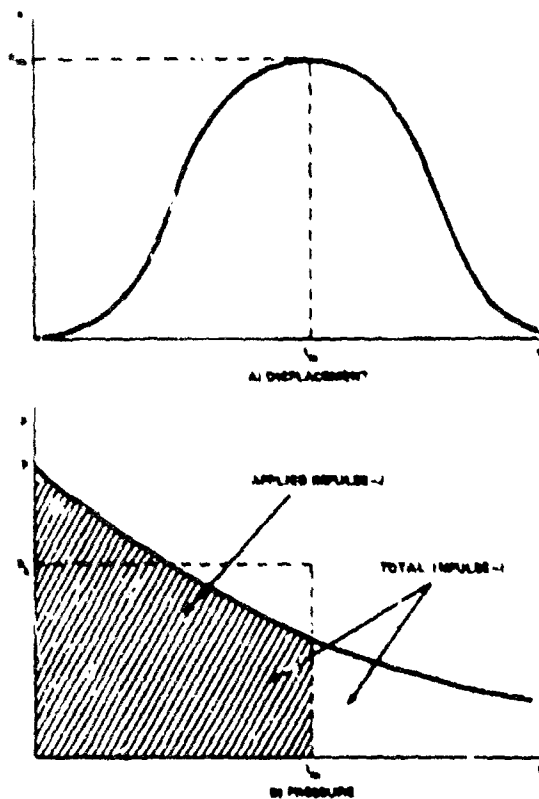
FIGURE 1. PRESSURE LOADING AND RESULTANT DISPLACEMENT
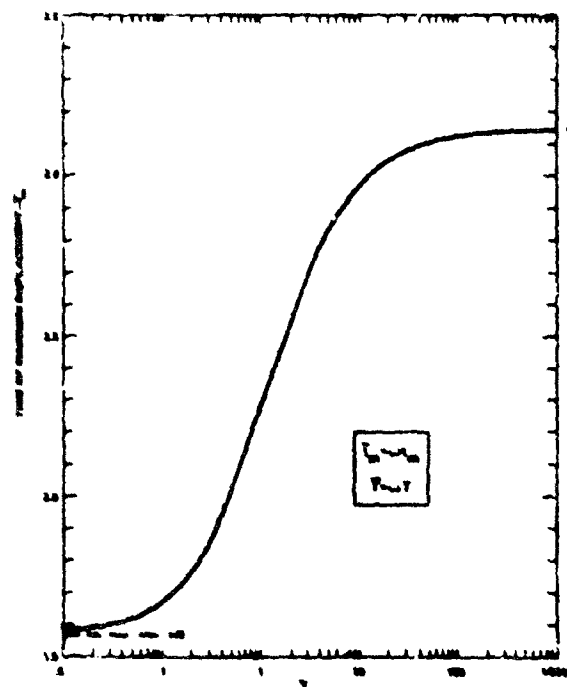
FIGURE 2. MAXIMUM DISPLACEMENT RESPONSE CURVES
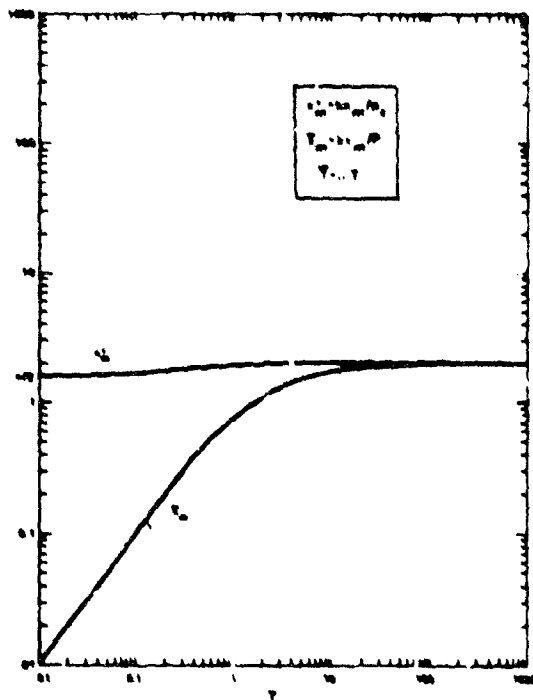
FIGURE 3. TIME OF MAXIMUM DISPLACEMENT RESPONSE CURVE
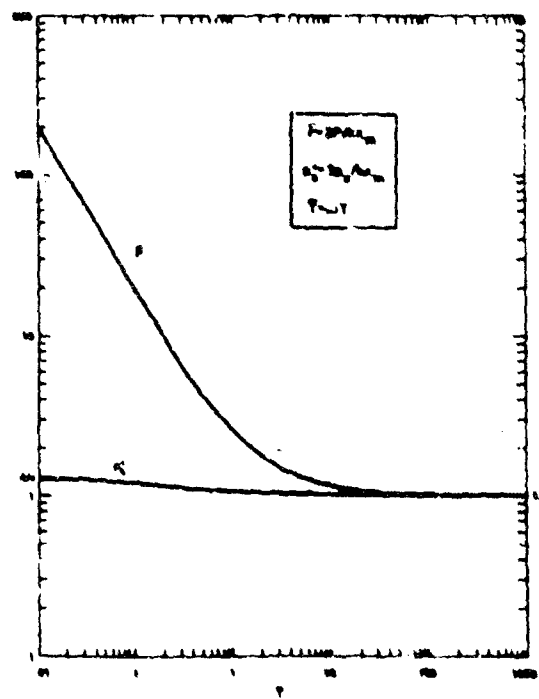
FIGURE 4. PRESSURE RESPONSE CURVE
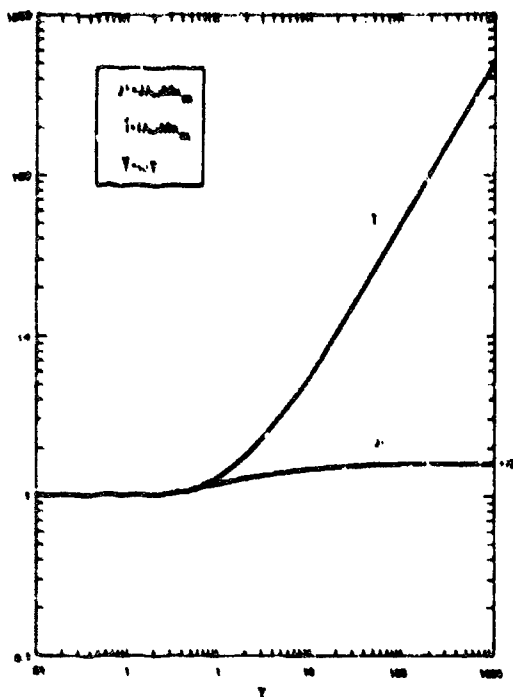
FIGURE 5. IMPULSE RESPONSE CURVES
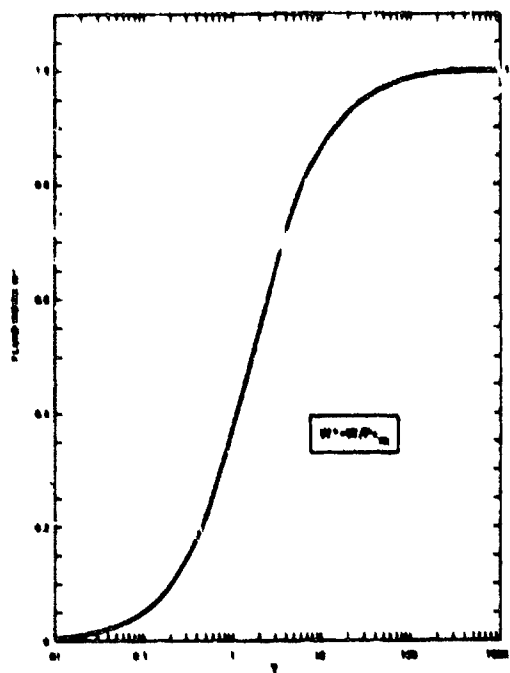
FIGURE 7. FLUID SIDE RESPONSE CURVE
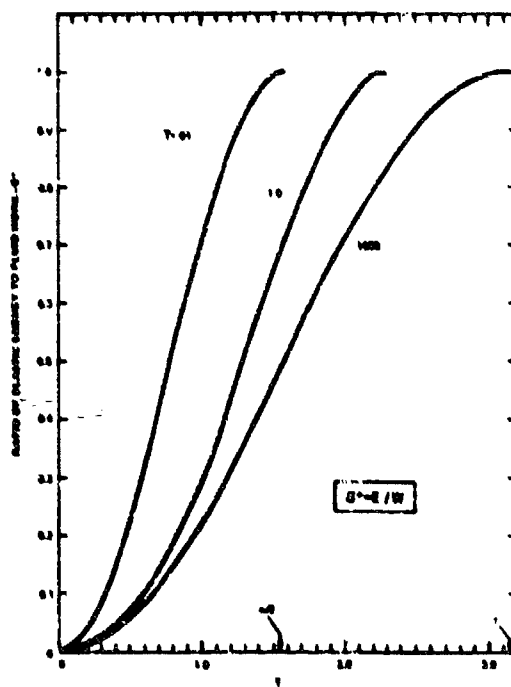

FIGURE 6. MODIFIED IMPULSE RESPONSE CURVES
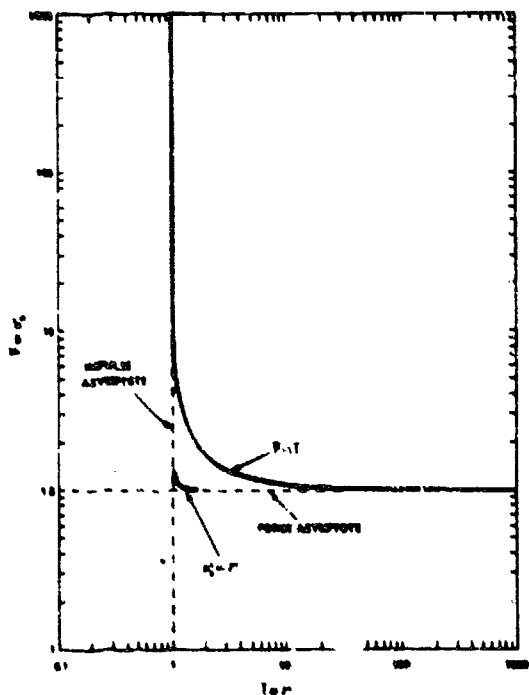
FIGURE 8. ENERGY TRANSFER DIAGRAM

THE USE OF STEEL FIBER REINFORCED CONCRETE IN CONTAINMENT AND EXPLOSIVE-RESISTANT STRUCTURES

Charles H. Henager

Battelle, Pacific Northwest Laboratories
Richland, Washington

ABSTRACT

The results of several investigations of steel fiber reinforced concrete (SFRC) under explosive loading are presented. Tests using high explosives were performed by the U.S. Corps of Engineers to compare reinforced concrete slabs using conventional concrete to similar slabs using SFRC. The conventional slabs were completely disintegrated. The slabs containing SFRC retained their integrity even though severely damaged. Similar results were obtained with explosive tests on slabs by Lawrence Livermore Laboratory, impact loading by a pendulum-type impact machine, ballistic impact by small arms fire, impulsive loading on beams and a drop weight impact test. Use of SFRC in a reactor containment structure is reviewed. Design aids and potential applications of SFRC for blast resistance in structures are listed.

INTRODUCTION

Probably the most outstanding improvements of steel fiber reinforced concrete over that of plain concrete are in its energy absorption characteristics and its resistance to impact and explosive loading. The advantage is not merely that of greater toughness, but the presence of fibers prevents the total disintegration and shattering of concrete associated with shock loads. With fibers, the cracks cannot extend without stretching and debonding the fibers. As a result, substantial energy inputs are necessary before complete fracture of the material can occur. A measure of the energy absorption properties or toughness of steel fiber reinforced concrete compared to plain concrete can be seen from the area under the load-deflection curves shown in Figures 1 and 2 [1]. Many tests show that the toughness of steel fiber reinforced concrete is an order of magnitude higher than that of plain concrete [2,3].

With explosive loading, steel fibers reduce the fragment velocity and the fiber reinforced slabs retain their integrity. This unique property of spall and shatter resistance, and the ability to retain the shape and integrity of structural elements and to hold them together can be vital in the design of certain types of structures. Because of these properties, random steel fiber reinforcement is well suited for use in beams or other structural elements subjected to impact.
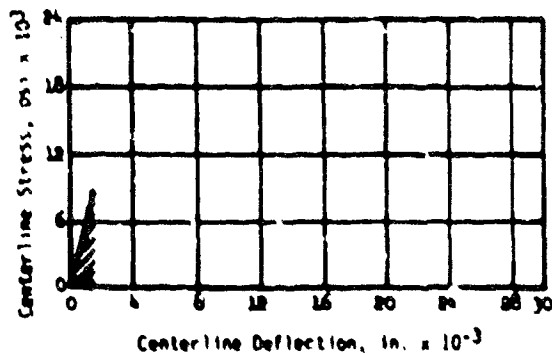

FIGURE 1. Load-Deflection Curve for 3-1/2 x 4-1/2 x 16 in. (89 x 114 x 406 mm) Plain Concrete Beam. Maximum Size Aggregate Used was 3/8 in. (9 mm) (Ref. 1, page 5).
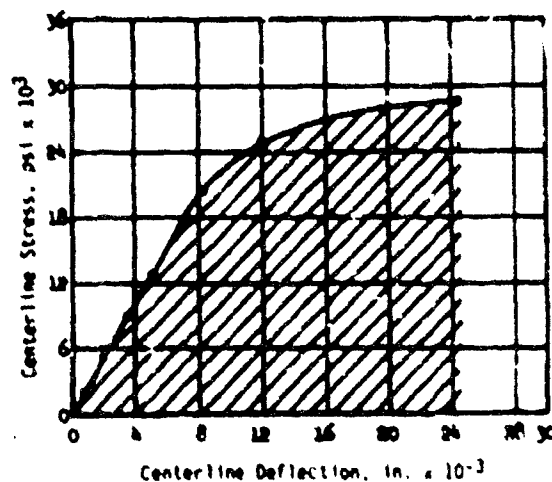

FIGURE 2. Load-Deflection Curve for 2 x 2 x 6 in. (50 x 50 x 150 mm) Fiber Reinforced Concrete Beam. Reinforcement was 1.96% by volume of .017 x 1-1/2 in. (0.43 x 38 mm) Steel Wire. Maximum Size Aggregate Used was 3/8 in. (9 mm) (Ref. 1, p. 5).

RESULTS OF EXPLOSIVE LOADING, IMPULSIVE LOADING AND IMPACT TESTING

Explosive Loading

Tests by Williamson [1] demonstrated that with explosive loading, a shock wave travels through a wall as a compressional wave and is reflected on the opposite face as a tensile wave which then causes spalling and disintegration of concrete. Williamson's tests have shown that while conventionally heavily reinforced slabs disintegrate completely under explosive loading, the inclusion of steel fibers in the concrete reduces the fragment velocity by up to 23 percent. More importantly, it causes the slabs to retain their integrity without producing secondary fragments of sufficient mass and velocity which might cause further damage. Figure 3 shows the effects of a 10 lb. (4.5 kg) charge of HE on a conventionally reinforced concrete slab while Figure 4 shows the effects on a reinforced concrete slab containing SFRC.

FIGURE 4. This Slab Was Similar to the One in Figure 3 Except That it Contained 1-3/4% by Volume of 0.017 x 1-1/2 in. (0.43 x 39 mm) Steel Fibers (Ref. 1, page 13).
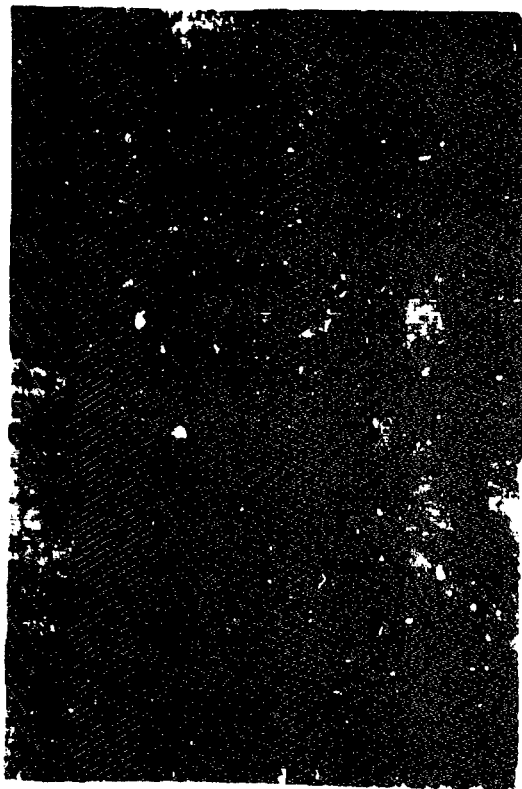

FIGURE 3. The Remains of a 32 x 32 x 4 in. (800 x 800 x 100 mm) Concrete Slab with Conventional Reinforcing After Explosive Testing with 10 lbs (4.5 kg) of HE (Ref. 1, page 12).
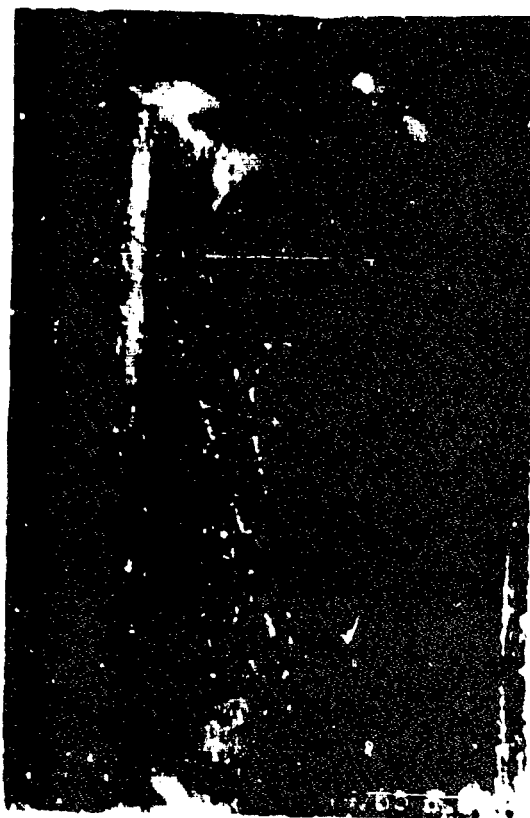
Full scale tests by Lawrence Livermore Laboratory [4] have also demonstrated the effectiveness of steel fibers in reducing the damage from high explosives. Figures 5 and 6 illustrate the effects of 49 lbs (22 kg) of high explosives on 5 ft x 5 ft x 18 in.(1.5 x 1.5 x 0.45 m) thick slabs with No. 8 (25 mm dia) Grade 60 reinforcing bars on 6 inch (150 mm) centers, each way, each face. The slab containing fibers used 0.010 x 0.022 x 1 in. (0.25 x 0.55 x 25 mm) cut sheet fibers at 1.25% by volume in a 7.5 sack, 3/4 in. (19 mm) maximum size aggregate mix designed for 4000 psi (28 MPa) at 28 days. The conventional concrete was similar, using 7 sacks, 3/4 in. (19 mm) aggregate, designed for 4000 psi at 28 days. Actual 28-day compressive strengths were 4300 psi (30 MPa) for the SFRC and 4513 psi (31 MPa) for the plain concrete.

FIGURE 5. Conventional Reinforced Concrete Slab Underside, After Test Shot (Ref. 4, p 32)

Impact and Impulsive Loading

Edgington, et al., [5] used a pendulum-type impact machine to evaluate 4 x 4 x 20 in. long (100 x 100 x 500 mm) specimens of steel fiber reinforced mortar and concrete made with different shapes and strengths of steel fibers. Maximum aggregate sizes were approximately 3/8 and 3/4 in. (9 and 19 mm). The impact resistance of the steel fiber reinforced concrete increased as the fiber content increased. Of four fiber types tested, a 0.20 in. (0.5 mm) diameter by 2 in. (50 mm) long, high tensile, crimped fiber proved most beneficial. Increases in impact resistance of more than 400 percent at a fiber content of less than 1-1/4 percent by volume were measured with this fiber. Ritchie and Al-Kayyali [6] found that steel fibers increased the impact resistance of lightweight concrete by as much as three times.

Sweby [7] has reported improved resistance of steel fiber reinforced slabs subjected to repeated drop ball tests. Failure in these tests was defined as occurring only when a hole was punched through the slab rather than by shattering of the slab into fragments.

The impact test recommended by the ACI in report ACI-544.2R-78, "Measurement of Properties of Fiber Reinforced Concrete", uses a 10 lb (4.5 kg) compaction hammer with an 18 in. (460 mm) drop to impact a 2-1/2 in. (64 mm) thick disc 6 inches (150 mm) in diameter. The number of blows to first crack and failure, or ultimate impact resistance, are recorded. Failure occurs when a crack opens enough to allow the sides of the disc to touch the surrounding stays. The ultimate impact resistance in number of blows is commonly 15 to 40 for plain concrete and ranges from about 40 to as high as 500 or more for 1 to 1.5 percent by volume of a deformed or crimped-end wire fiber [8].

FIGURE 6. Reinforced SFRC Slab, Underside, After Test Shot (Ref. 4, page 35).

Ballistic impact tests using small arms fire were conducted by Nkus and Williamson on SFRC domes and plate specimens [9]. Plate tests showed that 3 to 4 inch (75 to 100 mm) thick SFRC [1.5% by volume of 0.01 x 0.022 x 1 in. (0.25 x 0.55 x 25 mm) cut sheet fibers] resisted penetration from 30 caliber (7.62 mm) machine gun fire and M16 (7.62 mm) ammunition at 50 yards (46 m) with no spalling on the reverse side, whereas the same thicknesses of plain concrete were either penetrated, cracked through or showed spalling on the reverse side. A 4-1/2 inch-thick (115 mm) SFRC dome resisted all but 50 caliber (12.7 mm) machine gun ball ammunition and a 6 inch-thick (150 mm) dome resisted penetration by 50 caliber ammunition for a limited number of firings. The 50 caliber ammunition penetrated or shattered plain concrete plates 6 to 7 inches (150 to 175 mm) thick with a single impact.

Romualdi and Ramey conducted impulsive loading tests on concrete beams 4 x 6 x 72 in. long on a clear span of 63 inches (100 x 150 mm x 1.8 m, 1.6 m span)[10]. Twenty beams were tested, all with tensile reinforcing bars. Half used plain concrete and half used SFRC with 2% by volume of 0.006 in. dia. x 0.5 in. (0.15 x 13 mm) long brass-coated, cold drawn steel wire fibers. Three SFRC beams had no diagonal tension reinforcing (stirrups). All other beams had stirrups. A special spring-loaded apparatus was used to impulsively load the beams at the third points with sufficient force to cause failure. All dynamic tests were performed with an initial total spring load of 14,000 pounds (62,275 newtons).

Typically, the plain beams failed in compression and all load was lost at about 0.025 seconds. The SFRC beams, however, continued to support the load with diminishing oscillations until they stopped at some final residual load. The fiber beams, even though damaged considerably, were able to maintain their structural integrity. The residual loads carried by the fiber beams ranged from 4,900 to 11,900 lbs (21,800 to 53,000 newtons). The residual load carried by the plain reinforced beams was zero [10].

The three SFRC beams without web reinforcing were tested statically and failed in flexure, rather than in shear. An average shear stress of 444 psi (3 MPa) was calculated from the formula $\tau = P/bd$ from a maximum shear of 8,250 lbs (36,700 newtons). Also, in three of the SFRC statically tested beams, the tensile reinforcing bar broke, an unusual occurrence in concrete beams. This was because the SFRC concrete in compression at the top of the beam, maintained its integrity instead of crushing, providing a fulcrum around which the reinforcing steel could be continuously strained to a higher level.

The report concluded that:

1. Impulsive loading of the magnitude used in these tests does not cause sudden failure in the fiber reinforced beams such as the sudden failure observed in plain beams.

2. The internal resisting moment is significantly greater in the fiber beams and, therefore, permits the beams to absorb more energy. The beams retain their structural integrity and carry considerable residual load through a relatively large angular distortion.

3. In the event that the fiber concrete does fail in compression, the failure is not sudden but preceded by extensive deformation.

4. The increased tensile strength of the concrete permits the use of fiber concrete without special shear reinforcement.

CASE HISTORY - CONTAINMENT - DOUNREAY REACTOR ROOF

In 1972, SFRC was used in construction of a reactor roof at the UKAEA Fast Reactor at Dounreay, Scotland. Because of space limitations, it was desired to maintain a minimum depth for the roof slab. The resulting conventional shear reinforcement would have been difficult to locate and fix accurately and its use would have been unduly time consuming on the construction program. The solution was to use SFRC to replace the conventional shear reinforcement. The SFRC mix used 180 lbs/yd^3 (107 kg/m^3) of 0.020 x 1.57 in. (0.5 x 40 mm) deformed fiber in a 8.8 sack mix. A total of 208 yd^3 (159 m^3) was used.

DESIGN AIDS FOR CONTAINMENT OF NUCLEAR STRUCTURES

Two general articles on SFRC for reactor and spent fuel shipping cask design/construction are available [11,12]. Rammant [11] proposes a general theory for the elasto-plastic and cracked behavior of SFRC with reinforcing bars and describes a general finite element program which predicts crack propagation until failure of the structure. It also accounts for thermal cycling conditions. Advantages of the SFRC concrete are cited as resisting impact from brittle failures, increasing post-cracking load-carrying behavior, high energy absorption and improved seismic resistance. The fibers are not used to replace normal principal reinforcement but are used together with classical reinforcement. In the process, the safety factor for the structure is improved. In the case of anchorage zones in prestressed concrete construction, calculations indicated that steel fibers in the amount of 2.8 volume percent are as effective as the normal bar reinforcement and provide a stiffer anchorage zone.

Laug and Lührmann [12] devised and tested a high density steel fiber reinforced concrete to use for radiation shielding in a cask between an inner liner and outer steel shell. The concrete used magnetite, hematite, iron granules and steel fibers. The purpose of the steel fibers was to aid in resisting damage from the impact of a possible accident. The concrete weighed 3.99 kg/dm^3 (250 lbs/ft^3) and had a compressive strength of 5075 psi (35 MPa). The proportions of the mix and amount of fibers were not specified.

POTENTIAL APPLICATIONS FOR BLAST RESISTANCE IN STRUCTURES

Potential applications of SFRC reinforced structures to protect against blast or explosives include:

- The use of inflation-formed SFRC domes for aircraft protection or personnel protection. Domes of up to 150 ft (45 m) or more in diameter 50 ft (15 m) high and 3 inches (75 mm) thick are feasible. In the spherical shell portion, only SFRC is required. Reinforcing steel bars are used around openings and to tie into the foundation.

- Hardening of missile silos. The blast resistance of such structures would be enhanced by the energy absorbing capabilities and ductility of SFRC.

- Ammunition storage buildings. The reduced spalling of SFRC would reduce detonation of stored explosives by internally-generated missiles.

REFERENCES

1. Williamson, G.R., "The Use of Fibrous Reinforced Concrete in Structures Exposed to Explosion Hazards", Ohio River Division, U.S. Army Corps of Engineers, Misc. Paper No. 5-5, August 25, 1965.

2. Shah, S.P. and Rangan, B.V., "Fiber Reinforced Concrete Properties", Journal of the American Concrete Institute, February 1972, pp. 126-135.

3. Henager, C.H., "A Toughness Index of Fibre Concrete", RILEM Symposium 1978, Testing and Test Methods of Fibre Cement Composites, 1978, The Construction Press, Ltd.

4. Mullins, R.K. and Baker, C.F., "Interim Report on Use of Steel Fibers in Concrete Slab Construction to Resist Spall Caused by High-Explosive Blast Effects", Lawrence Livermore Laboratory Report UCID 18251, September 7, 1979.

5. Edgington, J., Hannant, D.J. and Williams, R.I.T., "Steel Fibre Reinforced Concrete", Current Paper CP 69/74, July 1974, Building Research Establishment, Garston, England.

6. Ritchie, A.G.B., and Al-Kayyali, O.A., "The Effects of Fibre Reinforcements on Lightweight Aggregate Concrete", Proceedings RILEM Symposium, Fibre-Reinforced Cement and Concrete, September 1975, pp. 247-256. Construction Press, Ltd., Lancaster, England,.

7. Swamy, R.N., "The Technology of Steel Fibre Reinforced Concrete for Practical Applications", Proceedings, The Institution of Civil Engineers, Part I, Design and Construction, Vol. 56, May 1974, pp. 143-159.

8. Schrader, E.K., "Impact Resistance and Test Procedure for Concrete", ACI Journal, Proceedings, Vol. 78, No. 2, March-April 1981, pp. 141-146.

9. Maus, D.J. and Williamson, G.R., "Ballistics Tests of Fibrous Concrete Dome and Plate Specimens", U.S. Army Construction Engineering Research Laboratory, Technical Report No. M-179, April 1976.

10. Romualdi, J.P. and Ramey, M.R., "Effects of Impulsive Loads on Fiber-Reinforced Concrete Beams", Carnegie Institute of Technology for Office of Civil Defense. Final Report on Contract OCD-PS-64-77, October 1965, 77 p.

11. Rammant, J.P., et al., "Steel Fibre Concrete, A Safer Material for Reactor Construction -- A General Theory for Rupture Prediction", Transactions of the 4th International Conference on Structural Mechanics in Reactor Technology, August 1977, Vol. H., paper H 5/4, 12 p.

12. Lauy, R. and Lührmann, A., "Suitability of a Special High Density Concrete as Material for Spent Fuel Shipping and Storage Casks", Proceedings of the 6th International Symposium on Packaging and Transportation of Radioactive Materials, PATRAM '80, Vol 1, November 1980. Editor H.W. Hubner, BAM, Berlin (West).

SIMULATION OF PRESSURE WAVES AND THEIR EFFECTS ON LOADED OBJECTS
Part I: Outlining the Problem, Description of the Simulation Device

Günter Hoffmann
Kersten Behrens

Fraunhofer-Institut für Kurzzeitdynamik, Ernst-Mach-Institut
7800 Freiburg, Fed. Rep. Germany

Abstract

Blast waves generated by detonations of HE or fuel-air-mixtures are characterized by their peak pressure and their overpressure phase duration, i.e. by two parameters. But normally unconfined fuel-air-mixtures will deflagrate generating a pressure time history of a quite different shape. In contrast there is a relatively slow pressure rise up to a peak value followed by a sudden decay into a suction phase the minimum value of which is of the order of the overpressure peak value. The overall duration of this pulse is comparatively long. For such a pulse there are more than two parameters necessary for a complete description. Despite the small peak pressure value these waves proved rather dangerous as numerous accidents have shown. Therefore it is desirable to get some insight into the destructive mechanism of these pulses. To be able to do that a special simulation device was developed which will be described.

1. Introduction

Blast waves generated by detonations of HE (High Explosives) or fuel-air-mixtures as e.g. FAE (Fuel Air Explosives) are characterized by their peak overpressure Δp and their overpressure phase duration t^+. Their pressure decay with time can be described by a FRIEDLANDER-function $p=\Delta p(1-t/t^+)e^{+(t/t^+)}$ for which only these two parameters are necessary. The same is valid for the pressure time history of the detonation of a fuel-air-mixture as Fig. 1 demonstrates. One gets very similar pressure pulses -one can say nearly identical ones at appropriate distances- if the mass of the charge of condensed explosive and fuel-air-mixture are in a certain relationship. Figure 1.1 shows the peak overpressure of blast waves generated by a small high explosive charge -that was in the example 62 g of Composition B- to be much higher and the overpressure phase duration to be much smaller than that one of an equivalent fuel-air-mixture at the same relative distance. In this example the fuel-air-mixture was a stoichiometric ethylene-air-mixture containing therefore 62 g of ethylene. If the distances to the hemispheric charges are chosen in such a manner
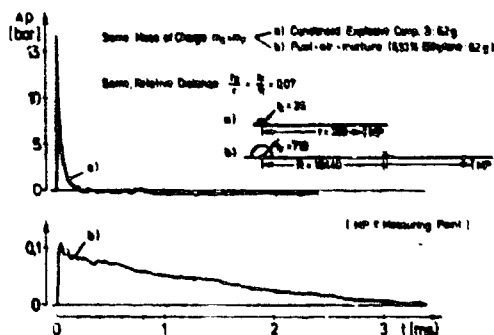
Picture 1.1
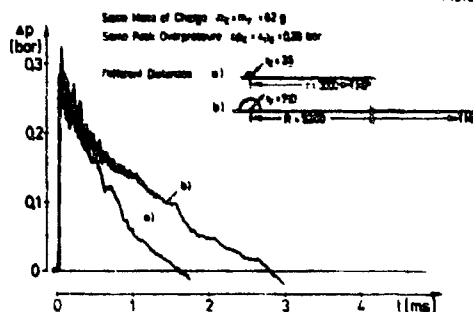
Picture 1.2
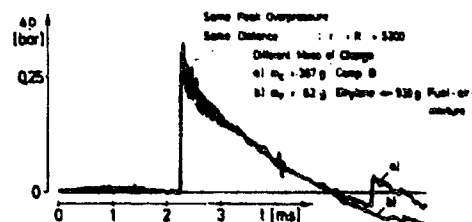
Picture 1.3

Fig. 1: Pressure Time History $\Delta p(t)$ of Detonating Condensed Explosive and Fuel-air-mixture

that the peak overpressures are the same,
the overpressure phase duration in the case
of the ethylene-air-mixture is twice the
corresponding value of the condensed explo-
sive as Fig. 1.2 illustrates. But if the
mass of the high explosive is six times
the mass of ethylene in the stoichiometric
fuel-air-mixture one gets no significant
differences between the pressure time his-
tories -for high explosive this is restric-
ted to the far field of lower pressures-
generated by Composition B or by the fuel-
air-mixture as it can be seen in Fig. 1.3.
This also can be shown in the normalized
$\Delta p/R_M$ -diagram and in the J_M/R_M-diagram of
Fig. 2. Since this diagram demonstrates
the overpressure distance relations and
the impulse distance relations to be almost
identical for Composition B and ethylene-
air-mixture in a relatively broad range
one can conclude the corresponding pressure
time histories of the blast waves to be al-
most identical tro, as was shown by Fig.1.3.
Thus as to the simulation aspect the pres-
sure time histories can be treated in the
manner, that means in both cases the same
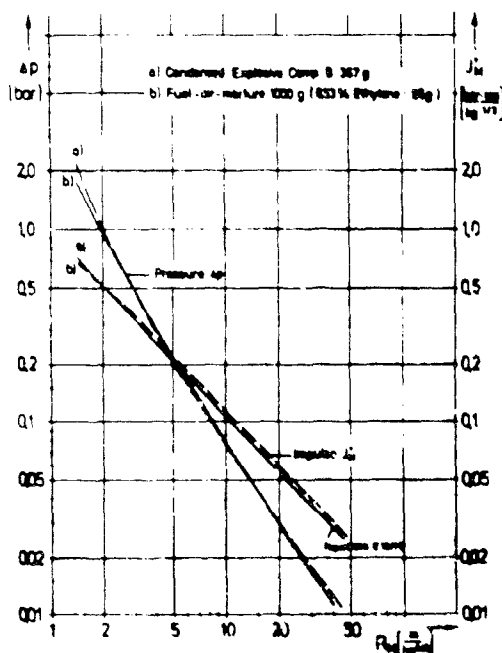well-known simulation facilities can be
used, e.g. shock tubes.

Fig. 2: Comparison of Peak Over-
pressure Δp and Impulse J^+
of a Blast Wave Generated by
Condensed Explosive and Fuel-
air-mixture

2. Outlining the Problem

If there is not a high ignition energy like
that of a detonator, normally an uncon-
fined fuel-air-mixture doesn't detonate, it
deflagrates. The same happens in the case
of ignition failure of FAE. Experiments as
well as calculations have shown that the
pressure time history of purely deflagra-
ting fuel air clouds are quite different
from those of detonating mixtures. On ac-
count of the quite different combustion
process there one finds also quite another
pressure time history. In contrast to the
detonation the energy conversion is slow:
The pressure distortion spreads only with
sound velocity and the overpressure rises
also slowly to its peak on account of the
expansion of the hot burned fuel-air-mix-
ture which compresses the surrounding pure
air. In the near field, out of the cloud
boundary, the pressure rises to a value
which is estimated not to be higher than
about 300 mbars because the flame velocity
is limited. If energy conversion is finish-
ed, i.e. if all reacting gas is burned, the
surrounding compressed air flows quickly
into the cloud like an implosion therefore
outside an underpressure is generated which
equalizes again slowly to the normal atmos-
phere pressure.

This deflagration mechanism results in a
more-parametric pressure time history as it
is shown in Fig. 3, diagram 3.1. This curve
was recorded at experiments [1] with small
methane air filled hemispheres. On account
of the small volume and therefore also low
flame velocity the peak pressure is also
very small, 3 mbars are measured; but its
duration is extremely long. From the begin-
ning to the end it takes about 400 ms, i.e.
t^+- 200 ms. This is very conspicuous in
comparison with the detonation: a slight
rise and a sudden decay to an underpres-
sure peak and a suction phase with a dura-
tion of the same order of that one of the
overpressure. The corresponding times are
nearly the same, i.e. t^+=t_- or I^+= I_-, resp.

Calculations which OPPENHEIM [2] had done
for larger balloons resulted in the same
feature of the curve as one can see in dia-
gram 3.2: For a balloon of 50 m in diame-
ter Δp~ 100 mbars by nearly the same pres-
sure duration in the same relative distance
of r/r_M = 5. GIESBRECHT et. al.[3] came on
the basis of their experiments and calcula-
tions with bursting vessels to the conclu-
sion that a real gas cloud explosion in a
factory cannot generate a peak pressure
which exceeds the value of about 0.3 bar
and a maximum duration of overpressure of
about 200 ms. That is considered as an up-
per limit and it is obvious that there are
variations depending on the cloud size and
shape as well as on the kind of fuel and
its concentration distribution. Also it is
evident that the deflagration pressure time

history is defined by more than two parameters: e.g. rate of pressure rise, peak over- and underpressure, serval durations as pressure rise time, pressure changing time, duration of underpressure.
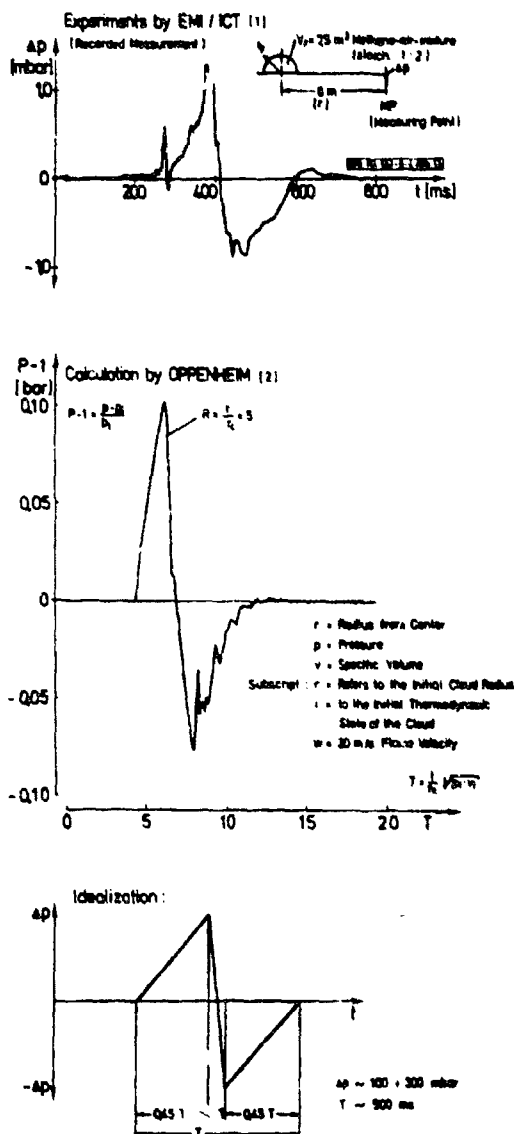

Fig. 3: Pressure Time History of a Deflagration

These waves proved sometimes rather dangerous too despite of the fact that their peak pressure values are much smaller than those of detonations as numerous accidents espe-

cially in chemical plants have shown in the past and as e.g. some ones mentioned in [3] . Therefore it seemed to be desirable to get some insight into the destructive mechanism and potential of this kind of pressure pulses. For this purpose the pressure time history was very approximately simplified to a shape shown in diagram 3.3 of Figure 3. For the further considerations and in the beginning of the experiments it seemed allowable to reduce the number of characteristic parameters to two as in the case of detonatively driven blast waves. In the mentioned idealized curve the parameters are coupled in such a manner that $\Delta p_- = \Delta p^+$, in the experiments $\Delta p_- = -0.8 \cdot \Delta p^+$ or $\Delta p_- = -1.3 \Delta p^+$ respective, and the pressure rise times $(0 \to \Delta p^+ , \Delta p_- \to)$ are each 45 % from the total duration T and the rest of 10 % remains for the pressure-changing-time.

An experimental set-up to investigate the effects of deflagrative pressure waves on hit structures could consist of non-scaled free-field gas explosions. But there are some considerable difficulties applying this method. First of all in order to get pressure values in the desired range one would have to handle fuel-air clouds or balloons of up to 50 m diameter. That needs a lot of space, time and not at last much safety requirements. The second difficulty arises from the fact that deflagration is a stochastic process due to turbulences and distribution of concentration thus leading to bad reproducibility of the generated pressure waves. This would require a great number of tests in order to get reliable results by means of statstics.

3. Description of the Simulation Device

To avoid these handicaps a simulator had to be found and developed which should permit to approximate the afore-mentioned idealized deflagrative pulse as accurate as possible including the possibility of parameter variations within a broad range. After experimenting with a modified shock tube, slowly burning gun-powder or a compressed air driven piston in a tube the solution was found to be a two-chamber-facility. With the help of Fig. 4 the construction principle shall be explained: The simulator consists of a both-end-closed tube with constant diameter which is separated pressure-tightly by a wall -with an open squared section in the middle into two equal-volumic chambers. At the edges are the supports for the areal (two-dimensional) specimen. A measuring girder contained displacement transducers fixed also at the specimen. Pressure gages were also mounted in the walls of each chamber. In the end cover of chamber 1 is a small opening, in that one of chamber 2 a port of larger diameter, both closed by a mem-

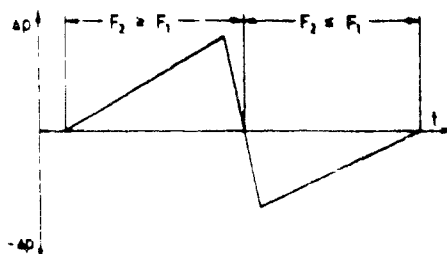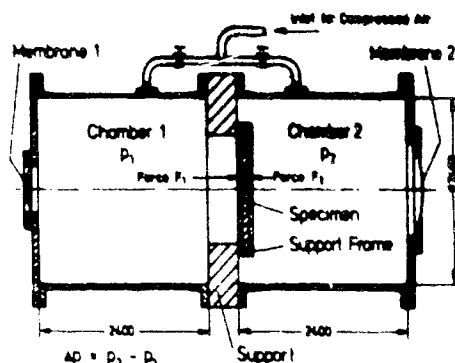brane. Both tube sections can be filled simultaneously with compressed air.

Fig. 4: Construction Principle of a Deflagration Simulator

At the beginning of the experiment both chambers are filled up to a pressure which is twice the wanted peak-pressure, i.e. should the peak over- or underpressure rise up to 100 mbars the filling pressure must be 200 mbars. No bending or deflection forces, which would break the specimen are acting on it, because they are balanced: $F_1 = F_2$. At the time t = 0 the membrane of chamber 1 consisting of plastic or steel sheets is destroyed by a small HE-charge. Air leaves through the port and likewise pressure decreases. That means on the other hand the difference pressure between both chambers rises and a corresponding force $F_1 - F_2$ is working in the direction to chamber 1 deflecting the specimen. If the pressure in chamber 1 arrives at half of its maximum value, i.e. the peak overpressure of the deflagration pulse (in the example 100 mbars), membrane 2 will be opened. On account of the large opening this chamber empties very quickly, therefore the acting force de-

creases. The pressure decay overtakes that one of the other chamber; in the overtaking moment the point is achieved where the pressures are equal to each other; in the difference pressure time history it means the passing of the t-axis and end of simulating the overpressure part. Off from this moment the force acting direction reverses until chamber 2 is exhausted. Then the underpressure peak is simulated, but in chamber 1 pressure decay is going on, i.e. the force F_1-F_2 in direction to chamber 2 becomes smaller until it is 0, when chamber 1 is exhausted.

Thus it is possible to simulate the effects of a deflagration wave on an areal structure by reversing the forces. Considering the load it is the same as if forces are acting first from one side then from the other side or at the same side changes over- to underpressure respectively. By a skilful choice of the port diameters in the cover plates which can be calculated by the formula of De Saint-Vena `/Wantzel $(w^2 = 2 g \times/(\times-1) P_{1w} [1-(P)P_1)]exp(\times-1)w)$ and by a convenient adaption of the chamber volumes as well as by coordinating of the time for opening the membranes the mentioned parameters could easily be influenced. By this method there is given a very good reproducibility.

In the upper part of Fig. 5 is shown the simplified pressure time history and that one achieved by the simulation device. The agreement is very good. In the lower part of this figure the deflection of a glass pane loaded with this pressure is plotted.

There are three curves: the straight one gives the experimentally found deflection, the dotted one is the result of a linear calculation and the cross-line is that one of a non-linear calculation using the equation

$$F = d_1 \cdot \ddot{y} + d_2 \cdot \dot{y} + d_3$$
with $F = K_L a^2 P(t)$; K_L = load factor
   a = side length of the pane
$d_1 = K_M m$ P(t)=acting force
d_2 = damping constant K_M=mass factor
$d_3 = K_L R(y)$ R(y)=restoring force

Significant differences between experiment and calculation are only found in the simulated suction phase, because the pressure time history in this part was not sufficiently to approximate with a tolerable effort. The best agreement was found in the pressure changing phase, (what also was best to calculate).
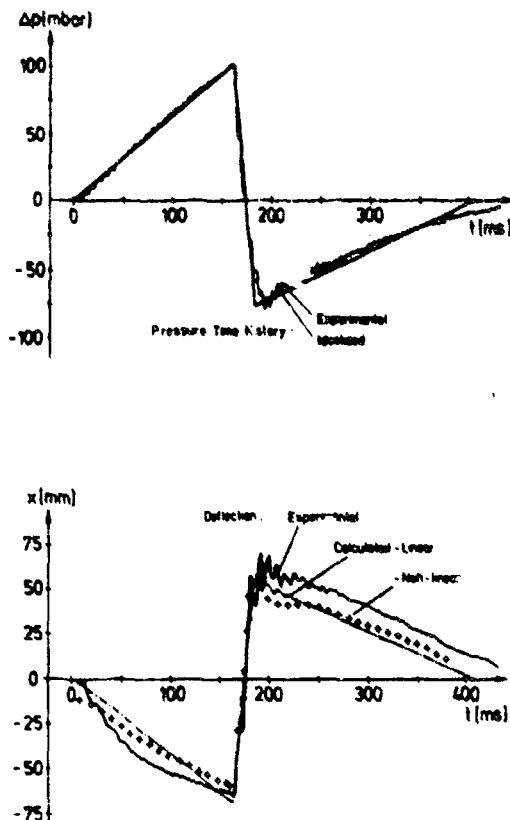
Fig. 5: Loading and Deflection Time
History at a Glass Pane [4]

Fig. 6: Views of the Deflagration
Simulator [4]

In the beginning of the experimental phase a small simulation set-up was installed with tubes of 1 m in diameter. As its working was successful and on account of scaling effects a bigger one with tubes of 2.4 m in diameter was built. This one is shown in Fig. 6. The upper picture gives a view to the chamber with the big discharge opening. On account of the available membrane sizes and for better handling the orifice contains three openings. The lower picture shows the entrance door through which the specimens were brought in and which contains two small discharge ports.

A great advantage of this simulation facility is that the same specimen under the same supporting conditions can be loaded statically as well as dynamically In the first case it is only necessary to fill the chamber 2 very slowly with compressed air. Thus it is very easy to compare the dynamic and static behaviour of a specimen without changing its position on the supports. In this way it is also possible to ascertain the restoring force which is
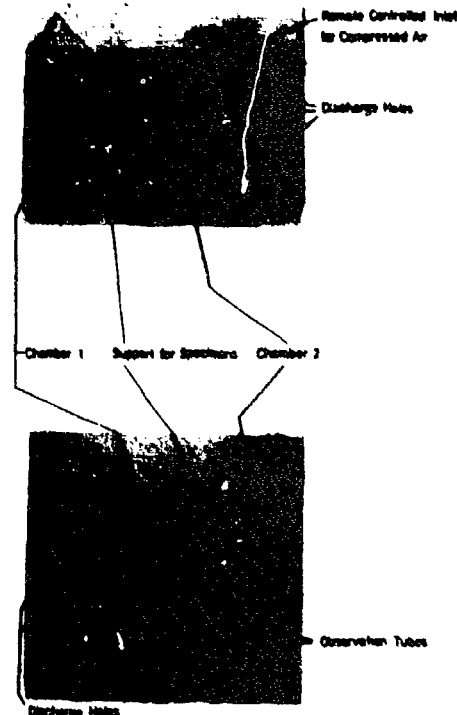
By a small variation of the device it is also possible to simulate the blast waves of a detonation within a certain, a little bit restricted extent. Chamber 1 must be minimized to the smallest volume that is possible. In an extreme case this may be not more than the volume between the specimen and the membrane vaulted by the compressed air, Fig. 7.

Then one finds a very sudden rise of the acting force in chamber 2. The rise time will take a time of about 3 to 5 ms. That is surely more than the infinitely steep rise of a blast wave. But it is acceptable for a specimen with a very long duration of its natural motion, since then there is only a negligible influence on the dynamic behaviour. This is mostly found by specimens with a heavy mass like walls of concrete. In Fig. 8 is plotted the calculated displacement of reinforced concrete plates versus time.

The dotted line shows that case when the pressure rise takes t_1 = 2.5 ms, the straight line when the rise is infinitely

steep. In the upper couple of curves the reinforcement consists of steel bars in the lower of glassfiber bars. It can be seen that the duration of natural motion is more than one order longer than the time for the pressure rise.
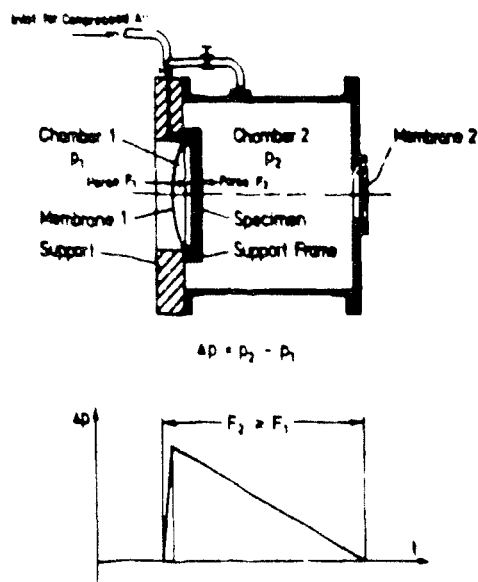
Fig. 9 shows two pressure time histories. In the upper one is shown the simulation of a pressure wave with a very long duration as it may be caused by a nuclear explosion. This is achieved when the membrane port of chamber 2 remains closed or if it is very small one gets a slight decay since the compressed air can escape only slowly. The curve below shows a simulated blast wave as it might be generated by a conventional weapon. Then a large opening will be necessary in the coverplate. It is obvious therefore that the pressure decay can easily be manipulated by the width of the opening.
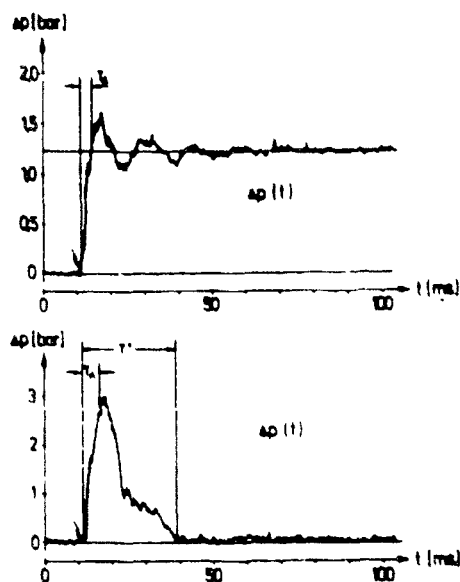

Fig. 7: Construction Principle of a Detonation Simulator

Fig. 9: Pressure Time Histories at Experiments with a Detonation Simulator

Fig. 8: Calculated Deflection Time Histories for Different Pressure Rise Times

SIMULATION OF PRESSURE WAVES AND THEIR EFFECTS ON LOADED OBJECTS
Part II: Experiments and Calculations; Destruction Curves

Karsten Behrens
Günter Hoffmann

Fraunhofer-Institut für Kurzzeitdynamik, Ernst-Mach-Institut
7800 Freiburg, Fed.Rep. Germany

Abstract

Experiments to investigate the response of model panes and model brick walls to deflagrative pressure pulses were carried out in the deflagration simulator described in part 1 of this paper.

Calculations based on a one-degree-of-freedom oscillator model were compared with the test results. They led to a set of curves in the scaled pressure impulse plane from which isodamage or destruction curves were derived for the specific objects under investigation. These curves differ from the well known P-I-curves for objects under blast load conditions in that the curves for deflagrative loading split up into two branches in the region of small impulses. This is due to the significant underpressure phase of the deflagrative pulse which causes resonance effects in the response of the loaded object.

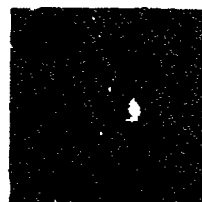## 1. Experiments

Test objects were

- panes of the size 50 x 50 x 0.3 cm^3 and 100 x 100 x 0.6 cm^3 with three different support conditions at the edges (simply supported, clamped by a metal frame, and fixed by permanently plastic putty)

- masonry walls (131 x 131 x 6 cm^3) made of 1:2 scaled model bricks (Fig. 1.1) fixed at the edges by steel u-shaped frames and clamping devices (Fig. 1.2). These walls should model a simple structural component of an industrial building frame shown in Fig. 2.

The load consisted of approximated static loading, i.e. very slow pressure rises (slope of pressure rise of about 10^{-3} bar/s) until rupture occurred and deflagrative loads. The peak overpressure varied from 30 mbar to 200 mbar in the case of loading the panes and it was always above 230 mbar for the masonry walls. Total pressure pulse times were in the range from 10 ms up to 750 s thus including the natural periods

(10 ms to 28 ms) of the objects under investigation at the lower limit and approximating static loadings at the upper limit of the time interval.

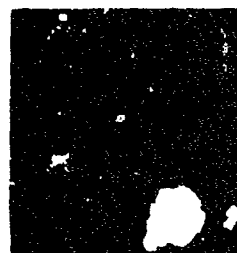Fig. 1: Specimen of the Model Masonry Slab and Comparison of Bricks

Fig. 2: Examples for Masonry in Steel Skeletons at a Workshop-Hall

The essential quantities measured during an experiment were the difference pressures at the test objects and the deflections in the middle of the square plates as function of time (see Fig. 5 of Part 1). In the case of static loads the combinations of measured pressure time histories with deflection time histories result in experimental restoring functions some examples of which are shown in Fig. 3.

The curves in diagram 3.1 and diagram 3.2 respectively are the functions for small panes with fixed edges and masonry walls. All of them are nonlinear. The increasing
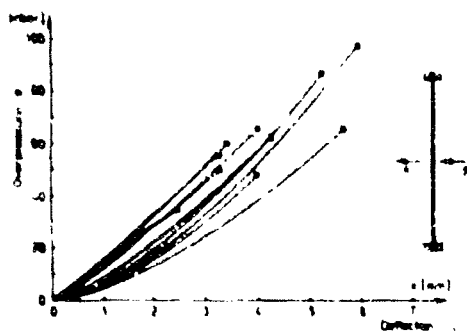
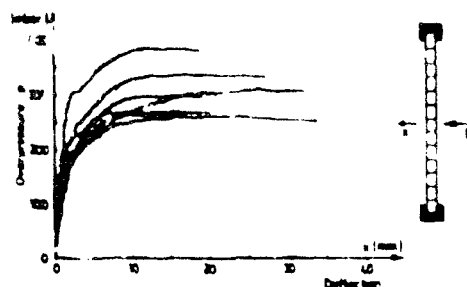Diagram 3.1   Glass Panes with Clamped Edges

Fig. 3: Static Load Deflection
Curves of Glass Panes and
Masonry Slabs

slope in the case of the panes is due to
membrane stresses at larger deflections.
The scatter in the slopes of the curves is
an effect of not completely reproducible
clamping of the panes - it is significantly
reduced when the edges are only simply
supported. But of course there is still a
considerable scatter of about 25 % in the
resistance to rupture of the panes. Dia-
gram 3.2 shows the masonry walls to be
almost linear elastic at small deflections
and plastic at larger deflections. Scatter
is essentially due to scatter in the mate-
rial properties. The restoring functions
were needed for the calculation of the be-
low-mentioned destruction curves.

In the case of short deflagrative loading
dynamic effects could be observed. To give
an example it should be mentioned that in
certain cases of deflagrative loading of
the small panes rupture occurred in the
underpressure phase at pressures of appro-
ximately -54 mbar and deflections of -8 mm.
Peak overpressures and the corresponding
maximum deflections were +83 mbar and +7 mm
respectively. Pressure pulse durations
were 100 ms and 77 ms.   The time it took
to change from peak overpressure to peak
underpressure was 10 % of the pulse dura-
tion and therefore it was in the range of
the natural period of the panes (10 ms).

This means that obviously resonances had
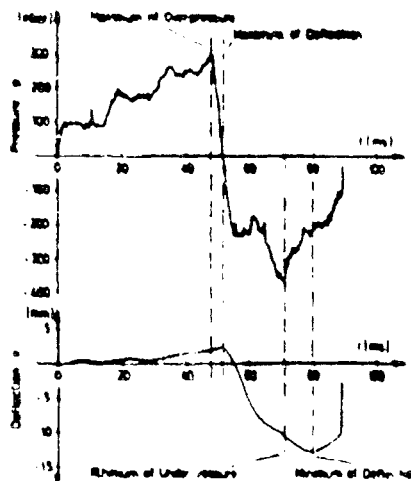occurred.

Fig. 4: Recorded Pressure and Deflection
Time Histories of Masonry Slabs
(Dynamic Load)

Another example for dynamic effects is
illustrated in Fig. 4. Diagram 4.1 re-
presents the pressure time history of the
load while diagram 4.2 shows the correspon-
ding deflection time history of a masonry
wall. There is a definite delay between
pressure maximum (minimum) and deflection
maximum (minimum) which is caused by the
inertia of the wall. The minimum deflection
is about 6 times larger than the maximum
deflection while the relation of pressure
minimum to pressure maximum is about 1.3:1.

The wall was not destroyed though some
cracks had formed. These cracks having a
width of some tenth's of millimeters and
therefore being coloured by black ink for
visualization purposes are shown in Fig. 5.
At the front side there are the typical
diagonal cracks and at the rear the cracks
are parallel to the edges. In this context
the front side of the wall is that side on
which the overpressure acts at the begin-
ning of the pressure pulse, which meant
the wall in Fig. 5 being bent away from the
chamber 2 during the overpressure phase
and being bent towards the chamber 2 during
the underpressure phase. Keeping this in
mind one can conclude from Fig. 5 that the
cracks must have formed as a result of the
underpressure phase which is plausible
considering the deflections of Fig. 4.

Finally Fig. 6 gives an illustration of a
destroyed pane and a destroyed masonry
wall. For these objects destruction was
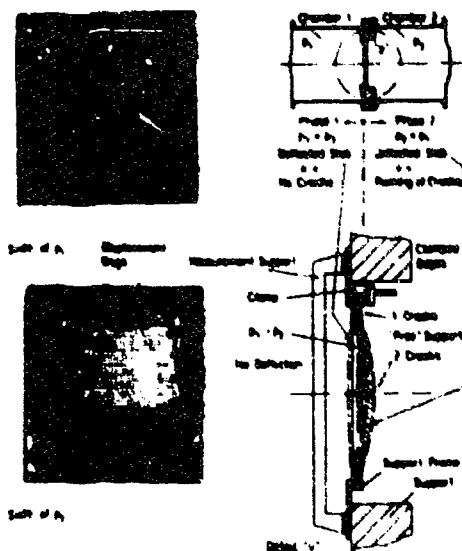defined as complete fragmentation, which

Fig. 5: Formation of Cracks by
Dynamic Pressure-Loading

may be self-evident in the case of the
brittle panes but which may be differently
defined for other objects depending on
their purpose, e.g. cracks may be toler-
able considering the stability of a shelter
but they are not acceptable if gas tight-
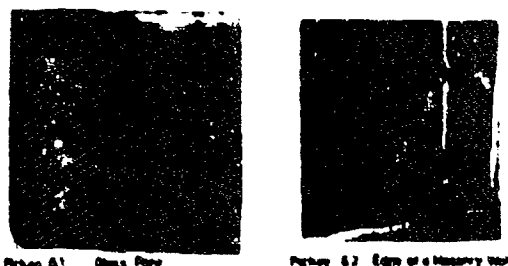ness is of interest.

Fig. 6: Destroyed Specimens

2. Calculations

It is well known from structural dynamics
that a one-degree-of-freedom system can
be used to describe the gross behaviour
of simple structural elements such as
plates with sufficient accuracy. Consider
the equation of motion

$$m\ddot{x} + R(x) = F(t)$$

where x is the displacement of the mass m,
$\ddot{x}$ is the acceleration, $R(x)$ is a restoring
force and $F(t)$ is the time-dependent ex-
ternal force acting on the mass m. In this
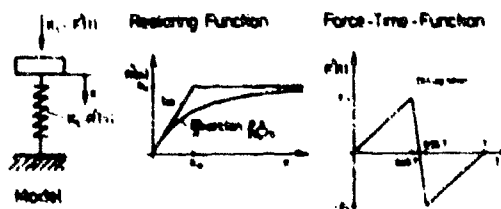
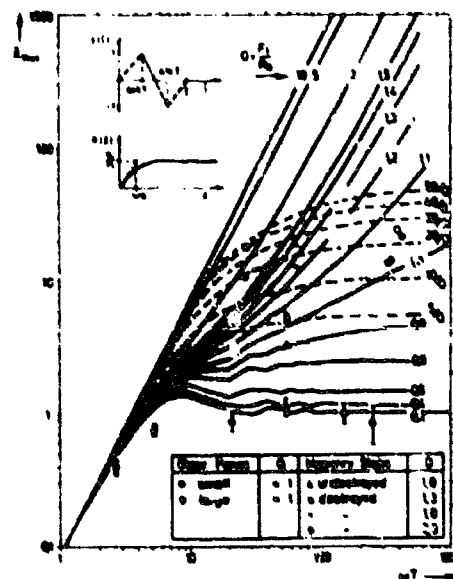equation damping is omitted.

Fig. 7: Simplified Model for
Calculation

Fig. 8: Deflection Maxima in the
1. Period of Oscillation

The reasons for neglecting damping are dis-
cussed extensively by Baker et.al [7].
Equating the work done by the external
forces, the kinetic and the potential en-
ergy of the model and the real system
respectively yields transformation factors
for the mass m°, restoring force R° and
external force F° of the physical system
such that the following relations hold [8].

$$m = K_M m^\circ, \quad R = K_L R^\circ, \quad F = K_L F^\circ$$

With respect to the previously shown re-
sistance functions of the masonry walls

the restoring force R^* is approximated by the arctan-function:

$$R^* = \frac{2R_0}{\pi} \arctan \frac{\pi x}{2R_0/k}$$

and the external force F^* is assumed to be the simplified deflagrative pulse (see Fig. 7).

Applying the following transformations

$$\bar{t} = \omega t = \sqrt{\frac{x_L}{F_m} \cdot \frac{k}{m^*}} \, t \qquad \text{time}$$

$$Q = \frac{F_1}{R_0} \qquad \text{force}$$

$$\bar{x} = \frac{x}{F_1/k} \qquad \text{displacement}$$

one finally gets the nonlinear dimensionless second order differential equation

$$\ddot{\bar{x}} + \frac{1}{Q} \frac{2}{\pi} \arctan \left(\frac{\pi}{2} Q\bar{x}\right) = f(\bar{t})$$

This equation is in the limit for $Q \to 0$ a linear equation since

$$\lim_{Q \to 0} \frac{1}{Q} \frac{2}{\pi} \arctan \left(\frac{\pi}{2} Q\bar{x}\right) = \bar{x}$$

Hence for small Q it should approximate the response of the above-mentioned panes the resistance functions of which did not deviate too much from linear functions.

Solving the equation by numerical methods (4th order RUNGE-KUTTA-method, initial conditions $\bar{x}_0$, $\dot{\bar{x}}_0 = 0$) for a certain normalized pulse $f(\bar{t})$ the duration of which is $\bar{T}$ an oscillating displacement $\bar{x}$ as a function of the time $\bar{t}$ is obtained.

Only the first period of this oscillation is of interest since actually damping will attenuate the deflections of physical structures in later cycles. Hence one can consider the maximum displacement $\bar{x}_{max}$ and the minimum displacement $\bar{x}_{min}$, both taken from the first period of oscillation as the quantities which are essential for the response and the eventual failure of a structure.

Performing the calculations for different pulse durations $\bar{T}$ one obtains $\bar{x}_{max}$ and $\bar{x}_{min}$ as functions of $\bar{T}$ with $Q = F_1/R_0$ as a parameter [6]. Fig. 8 shows a plot of the function $\bar{x}_{max}(\bar{T})$. The normalized deflection function for $Q = 0.2$ is almost identical with the curve for a linear restoring force. A comparison of the calculated deflections for small Q with the experimental points for the panes shows a relatively good agreement. Addi-

tionally to the displacement curves the broken lines represent curves with different constant multiples of the normalized elastic displacement $\bar{x}_{E1}$ as parameter (definition of $\bar{x}_{E1}$ see Fig. 7. Since $Q = F_1/R_0$ and $R_0 = kx_{E1}$ one gets $\bar{x}_{E1} = 1/Q$).
In the experiments with masonry walls the slabs were fragmented at deflections approximately as large as the wall thickness [5]. This corresponds to 20 to 30 times the elastic displacement x_{E1} of the walls. Fig. 8 illustrates the corresponding experimental points to be in vicinity of the dashed curve with parameter $30 \, \bar{x}_{E1}$.

Fig. 9 shows the curves $\bar{x}_{min}$ as functions of the normalized pulse duration with Q as parameter.
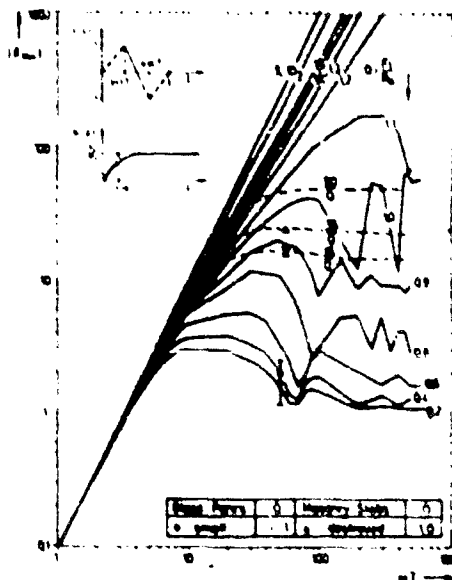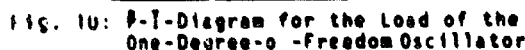

Fig. 9: Deflection Minima in the 1. Period of Oscillation

According to those curves significant resonances should occur. The normalized test values for the destroyed masonry walls are in the range of 15 to 25 times the elastic displacement, that is, in the approximate range of wall thickness. Following the procedures described in [9] one can use the normalized diagrams of Fig. 8 or 9 to calculate dimensionless (P-I)-diagrams. Since the total impulse of the assumed simplified deflagrative pulse is equal to zero one can consider the impulse of the positive phase I^+ which together with the peak force completely characterizes the deflagrative pulse.
Using the following relations

$$P = 2 \frac{F_1/k}{x_{max}} = \frac{2}{\bar{x}_{max}} \quad \text{for the peak force}$$

and

$$I^* = \frac{1}{2} \frac{I}{\bar{x}_{max}} \quad \text{for the positive impulse}$$

Fig. 10: P-I-Diagram for the Load of the One-Degree-o -Freedom Oscillator

Glass Panes	Q	Masonry Slabs	Q
o small	= 1	▲ undestroyed	1.0
● large	= 1	● destroyed	1.3
		●	1.8
		●	2.3

one obtains the curves of Fig. 10 which is simply a somewhat different presentation of the curves of Fig. 6.

Finally one can replot the fragmentation curve introducing the physical parameters of the walls to obtain the dimensional P-I-representation of the curve shown in Fig. 11. It must be noted that the pressures and impulses of this diagram are the quantities acting on the wall which means that they are normally reflected pressures and impulses. Assuming reflection factors of 2 for both quantities as in the acoustic limit of blast waves one could easily get the corresponding P-I-diagram for the incident waves. The dashed part of the curves indicates that this range of the solution is of no physical meaning since under-

pressure phase and overpressure phase should be of the same magnitude according to the assumptions. It may even be doubted that there exist reflected deflagrative pressure pulses having a peak pressure value close to one bar and still being symmetric. The deflagrative cloud experiments known to the authors which are essentially small scale experiments give no indications of peak pressure values above 300 mbar. (GIESBRECHT et. al.) [3]

Masonry	destroyed	undestroyed
Overpressure ⌐——⌐	● ●	▲
Underpressure ⌐----⌐	▲	▲

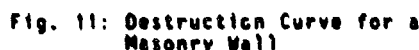Fig. 11: Destruction Curve for a Masonry Wall

Fig. 11 clearly illustrates the effects of the underpressure phase on the loaded object. There is a region of resonances between the two branches of the destruction curve in which deflagrative pulses should destroy the walls (objects) by their underpressure phase but not by the overpressure loading. For reasons of comparison a third curve based on the calculations of MAYR-HOFER and THOR [10] for blast loaded elastic-plastic objects is plotted in Fig. 11. In the static loading range the effects of a blast wave and a deflagrative wave of the same reflected peak overpressure and the same reflected positive impulse are equal. In the range where resonance to deflagrative loading occurs the deflagrative wave may destroy the objects while the blast wave does not.
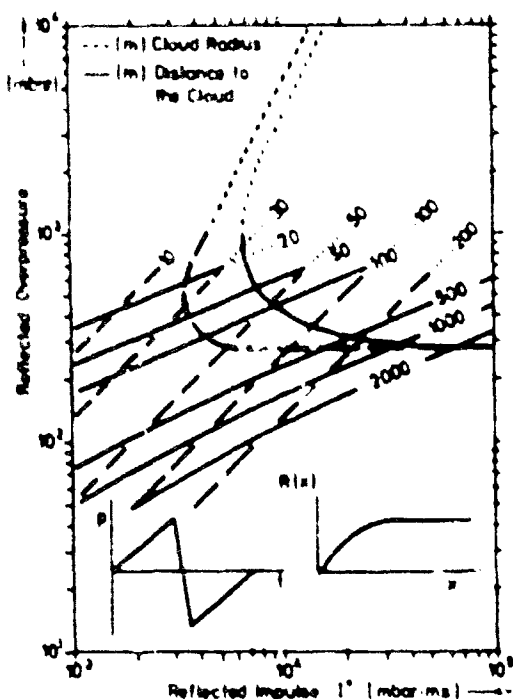
Fig. 12: Destruction Curve for Masonry
Walls and P-I-Relation for De-
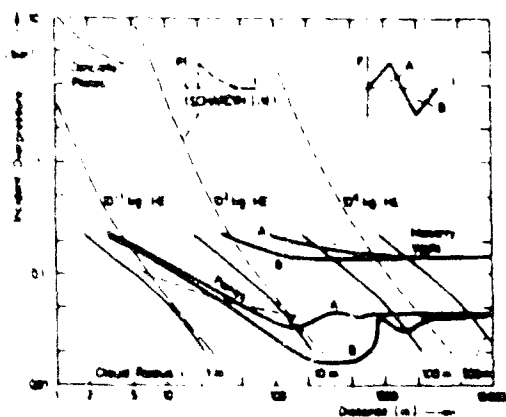flagrating Clouds (12), Flame
Speed 20 m/s)

Fig. 13 Destruction Curves (Solid Lines:
Overpressure Distance Relations
according to Oppenheim (2) Flame
Velocity 20 m/s)

Finally one can combine the destruction
curve of the P-I-diagram with the over-
pressure-distance relations for exploding
clouds. Since there are only a few experi-
ments on a small scale basis with deflagra-
ting clouds and since therefore the pres-
sure and impulse distance relations are not
really kr_n for deflagrating clouds as a
first approach to the problem the corre-
sponding relations calculated by OPPENHEIM
et.al. are taken. Assuming a laminar flame
speed of 20 m/s and reflection factors of
2 the straight lines in Fig. 12 represent
the OPPENHEIM pressure-impulse-relations
for constant cloud radii and constant
distance respectively. Reflected pressures
and impulses above and to the right of the
destruction curve will rupture the wall
and it can easily be seen at which cloud
radius and at which distance from the cloud
the fragmentation could occur.

Another representation for destruction
curves was developed by SCHARDIN (11) for
numerous blast loaded objects. Again based
on OPPENHEIM's (2) calculations for de-
flagrating clouds and assuming the flame
speed to be 20 m/s as above one gets in
this kind of representation the destruction
curves of Fig. 13. Pressures and impulses
in this diagram are the incident quantities
and the destruction curves for panes and
walls are derived from the corresponding
P-I-diagrams assuming reflection factors
of 2.

References:

1) Behrens, R., Schneider, H.
Druckaufbau und Flammenaus-
breitung bei der Deflagration
von Explosionsstoff/Luft/Ni-
Gemischen
ICT/EMI-Bericht
RS 100-86-4, April 77

2) Kuryla, J., Cohen, L.M.
Oppenheim, A.K.
Numerical Study of Blast Waves
Generated by Explosive Clouds
Interim Report University of
California, Berkeley
1976

3) Giesbrecht, H., Hess, K.,
Leuckel, W., Maurer, B.
Analyse der potentiellen
Explosionswirkung von kurz-
zeitig in die Atmosphäre frei-
gesetzten Brenngasmengen
Teil 1: Chem.Ing.-Tech.52/80
Teil 2: Chem.Ing.-Tech.53/81

4) Behrens, K., Hoffmann, G.,
Langhein, H.
Untersuchungen des Bruchver-
haltens von Glasplatten bei
Belastung mit deflagrativen
Druckwellen
Ernst-Mach-Institut, Freiburg
E 24/80, Dez. 80

5) Behrens, K., Langhein, H.
Deflagrative Belastung von
Modellorgansmauern
Ernst-Mach-Institut, Freiburg
E 8/81, Aug. 81

6) Behrens, K., Langhein, H.
Thar, H.J.
Verhalten von plattenförmigen
Objekten unter deflagrativer
Belastung
Ernst-Mach-Inst., Freiburg
E 16/81, Sept. 81

7) Baker, W.C., Cox, P.A.,
Westine, P.S., Kulesz,J.J.
Strehlow, R.A.
A Short Course on Explosion
Hazards Evaluation
Southwest Research Institute
Course Notes SRI (1979)

8) Norris, C.H., Hansen, R.J
Structural Design for Dynamic
Loads
McGraw-Hill, N.Y. (1959)

9) Baker, W.C., Westine, P.S.,
Dodge, F.T.
Similarity Methods in
Engineering Dynamics
Hayden Book Comp., Rochelle
Park, N.J. (1973)

10) Mayrhofer, Chr., Thar, H.J.
Dyn. Response of Fibre and
Steel
Reinforced Concrete Plates
under Simulated Blast-Load.
Proc IASS-Interess. Symp.
Concrete Structures under
impact and impulsive Loading
Editor Plank,R., BAM,
Berlin 1982

11) Schardin,H., Molitz, H
Schärer, H.
Wirkungen von Spreng-und
Atombomben auf Bauwerke Zivil-
ler Luftschutz Nr 12 (1954)

RESPONSE OF STRUCTURES TO DETONATIONS IN SAND

Bengt E Vretblad

Royal Swedish Fortifications Administration, Eskiltuna,   Sweden

ABS

Tests made at RSFA have known how the pressure on
the wall of a structure from deconations of ex-
plosives in sand depends not only on the explosive
and its distance to the wall but also on the pro-
perties of the wall (e g mass and stiffness). The
paper gives data from these tests and a suggested
procedure for design of walls in buried structures
exposed to detonations effects. The procedure is
based on an energy-absorption concept.

BACKGROUND

Many data on shock waves in sand generated by
explosives can be found in literatue. Most of
these however are freefield data of limited value
to the engineer to design structures in sand to
withstand the effects of detonations.

Some sources e g /1/ and /2/ give peakpressure and
impulse density on an infinitely rigid wall. A
pressure increase factor of 2.0 and an impulse
increase factor of 2.6 are suggested relative to
the corresponding freefield values.

Ordinary structures are more or less compliant
when exposed to loads. This is true also for
hardened structures. In order to get a better
understanding of the effects on different struc-
tures from explosives in sand a research program
was started at the RSFA a couple of years ago.
Responsible for this program is Staffan A Hultgren.
Results have been published in /3/ and /4/.

PROBLEM AND TEST DEVICE

The problem can be identified from figure 1. A
rigidly supported wall is exposed to a detonating
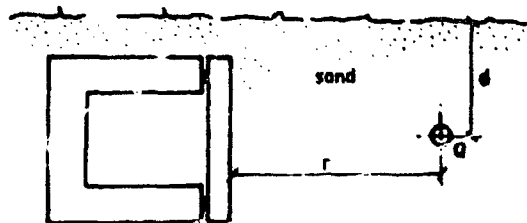charge, Q , at a distance, r, and with a depth of
burial, r

Figure 1. Concept

The behaviour of walls with different sizes and
different designs for different values of these
parameters are studied.

The basic parameters in' uencing the structural
behaviour of a wall exposed to a dynamic load are
its mass and stiffness.

To facilitate a study of these parameters a test
device according to figure 2 was designed where the
mass and stiffness of the front could be varied
independently. The front consisted of a 0.34 m dia-
meter circular disc supported by a horisontal
movable axis on ball bearing and by a helical
spring all within a 295 kg   18 m long steel cylin-
der.

The mass of the disc was varied from 5.2 to 105 kg
and springs were used with springconstants ranging
from 0.1 to 1.2 MN/m.

The pressure against the disc and its acceleration,
velocity and displacement were measured.

The pressure measured on the disc is then compared
with the inertial pressure and the pressure
corresponding to the spring force.

The inertial pressure can be calculated from the
measured acceleration using Newtons 2nd law of
motion. The spring force is equal to measured de-
flection multiplied by the spring constant.

A comparison between these three pressure components
is given for different masses in figure 3. Mass and
stiffness both contribute to the pressure. While
the inertia forces develop momentarily the forces
from the spring develop as the deflection increases.

Conclusively more mass constitutes a shorter rise-
time for the pressure.

It should be pointed out, that the duration of the
pressure indicates that not only the mass of the
disc but also parts of the mass of sand between
the charge and the wall contribute to the structural
behaviour.

From figure 3 is clear, that the pressure is de-
pendant on the properties of the wall and also that
the duration of the pressure exceeds by far the
fundamental period of the wall. Neither the pressure
nor the impulse is therefor well suited for design

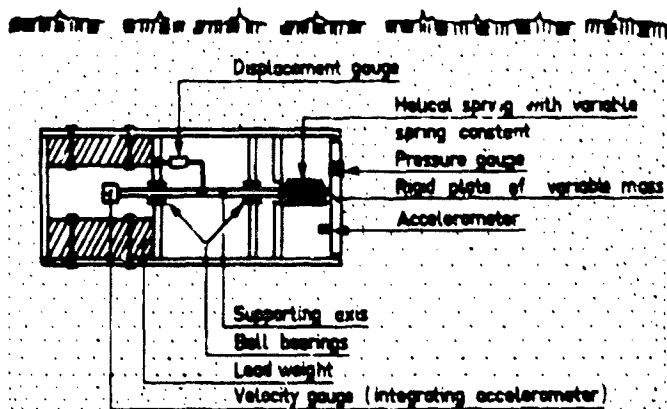purposes. For this reason an energy-concept has
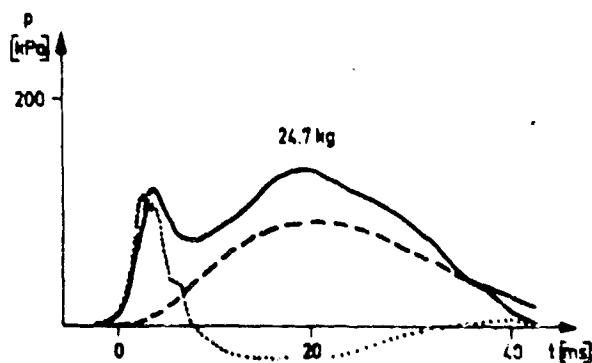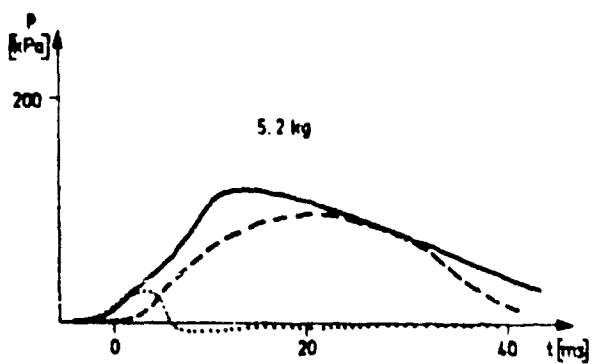been adopted.

Figure 2. Test device

Figure 3. Wall pressure components. Wall stiffness = 0.5 MN/m.

WALL TESTS

The initial test series with the device in figure 2 was followed by tests where walls supported along the four edges were examined. Concrete walls in scale ≈1:3 and in full scale with different thicknesses and different amounts of reinforcement were tested. Absorbed energy by the wall-slab when deforming was calculated according to yield-line theory. A straight linefit to calculated values gives the specific energy per unit area of the slab to

$$E_*/Q^{1/3} = 1040 \ (r/Q^{1/3})^{-4.74} \quad Mm/(m^2 \cdot kg^{1/3})$$

The idealised deformation of the slab is shown in figure 4. The formula for Ea shows, that the distance, r, is highly significant for the energy. This means also that the energy density is unevenly spread over the slab. The parts of the slab near the supports are more remote from the charge than the midpoint. Conclusively they will be exposed to a lower density. The specific energy can be averaged over the slab by integrations in an iterative procedure giving a factor ζ.

Table 1 gives data for the concrete walls tested. It also gives the specific energy, Ea, calculated using the averaging factor ζ. Ea is given as a function of the specific distance in figure 5. The equation for the straight line is:

$$E_a/(\zeta \cdot Q^{1/3}) = 1540 \ (r/Q^{1/3})^{-5.53} \quad Mm/(m^2 \cdot kg^{1/3})$$

Two of the tests were made in compacted sand while the other were made in loose sand. This difference in compaction did not give any significant differences in the test results.
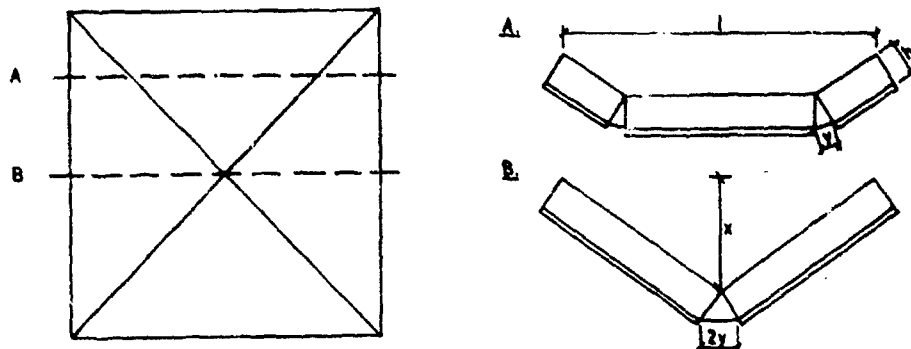

Figure 4. Slab with yield lines. Elevation and sections.

r m	Q kg	$r/Q^{1/3}$	l m	h m	Reinf ratio %	x mm	Compaction	$E_a/(\zeta \cdot Q^{1/3})$ kNm/(m² · kg^{1/3})
1.26	1	1.26	0.73	0.04	0.94	12	-	0.33
1.00	1	1.00	"	"	"	39	-	1.18
0.79	0.5	1.00	"	"	"	37	-	1.65
0.59	0.2	1.00	"	"	"	24	-	1.87
1.26	2	1.00	"	"	"	56	-	1.25
1.00	1	1.00	"	"	"	42	-	1.28
2.15	10	1.00	1.8	0.13	0.54	56	-	1.76
"	"	1.00	"	"	"	54	Yes	1.76
"	"	1.00	"	"	1.0	29	-	1.76
1.70	"	0.79	"	"	"	67	-	4.92
2.71	"	1.26	"	"	0.54	16	-	0.45
1.70	"	0.79	"	0.28	0.54	34	-	5.27
"	"	"	"	"	"	42	Yes	6.50
1.36	"	0.63	"	"	1.0	44	-	18.6
2.15	"	1.00	"	0.13	0.30	128	-	2.20

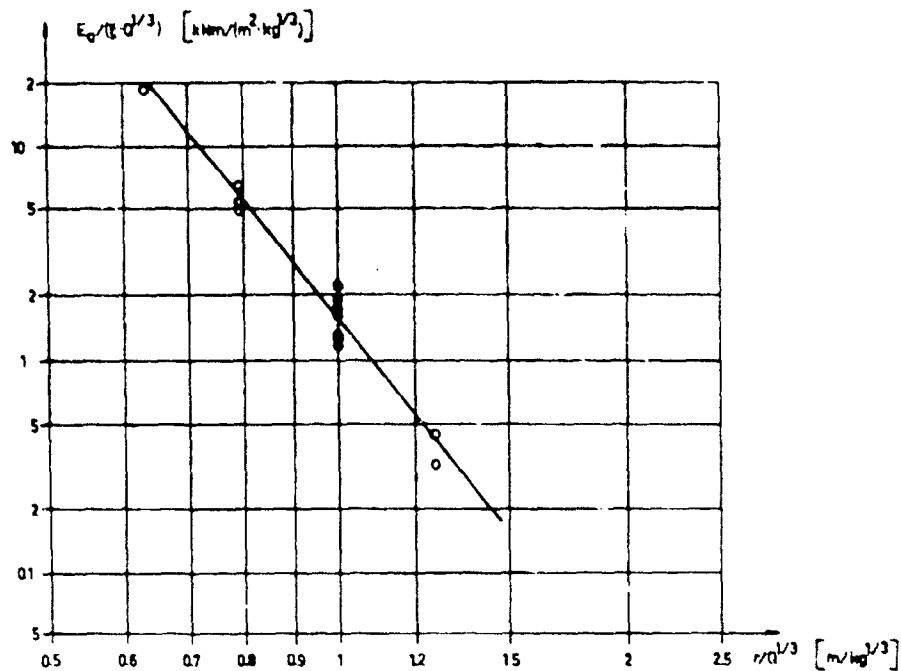Table 1. Data for the tested concrete walls.

Figure 5. Specific energy vs specific distance for walls tested.

The equation for E_a can be used for design purposes. With the energy transmitted to the wall from the detonation calculated with this equation the design engineer then has to find dimensions of the wall and reinforcement in it so that this energy can be absorbed without deformations exceeding permitted values.

The equation so far is based on data within the interval 0.63 to 1.26 for the specific distance, $r/Q^{1/3}$, and with the charge on the axis of symmetry of the wall.

In order to check the formula outside these limitations some more tests have been performed. In these tests the shape of the deformed wall is analyzed using photogrammetric methods. Figure 6 shows as an example a plot of the deformed shape of a slab after test. The measured deflections can be used for a more sophisticated calculation of the energy-absorption in the wall than with the model in figure 4.

Preliminary results from these tests support the using of the equation for E_a for design purposes.

CONCLUSIONS

The tests performed on concrete walls exposed to effects from detonating charges in sand support the use of the energy-absorption concept, outlined in the report, for design purposes.

REFERENCES

/1/ Schall, R, über Druckwellen bei Sprengungen Sand und sandigen Boden, Nobel Heft, p.76. Mai 1960.

/2/ Effects of Impact and Explosion. - Summary Technical Report of the National Defense Research Committee. Washington D.C., 1946.

/3/ Hultgren, S A, Response of Buried Model Structures to Buried TNT-Explosions in Sand. Proc 6th International Symposium on Military Applications of Blast Simulation. Cahors,1979.

/4/ Hultgren,S A, Response of Reinforced Concrete Walls to Buried Explosions in Sand. Proc 7th International Symposium on Military Applications of Blast Simulation, Medicin Hat, 1981.
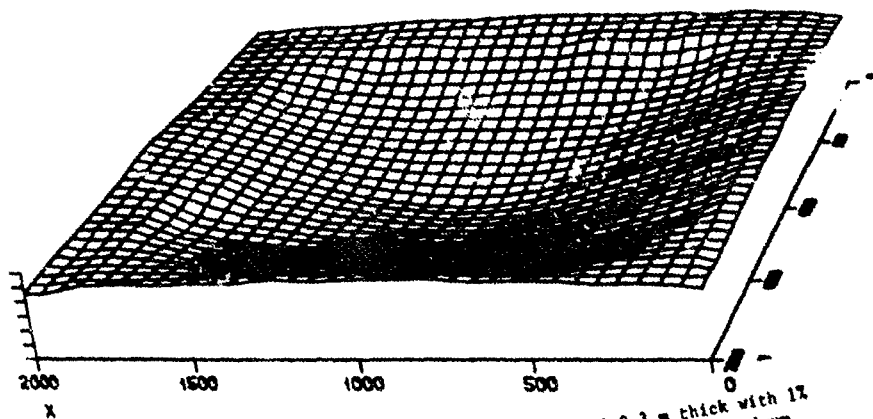
Figure 6. Example of deformed shape of 1.8 by 1.8 m wall 0.3 m thick with 1% reinforcement ratio exposed to a 50 kg detonation at 3 m distance. Maximum deflection appr. 0.1 m.

AD P001747

EFFECTS OF BARE AND CASED EXPLOSIVES CHARGES ON REINFORCED CONCRETE WALLS

Hansjörg Hader

Ernst Basler & Partners
Consulting Engineers
8029 Zurich / Switzerland

ABSTRACT

This paper represents a summary of an extensive investigation concerning the local effects of bare and cased explosives charges on reinforced concrete walls. The investigation includes a literature search as well as several test series. As a main result, charts for the prediction and comparison of the effects of bare and cased explosives charges are developed.

The most important conclusion is that cased charges result in *perforation of reinforced concrete walls* at distances up to ten times larger than bare charges of the same weight. Vice versa, given the charge weight and the distance, the wall thickness required to avoid perforation is up to three times larger for cased charges than it is for uncased charges. Hence, it becomes evident that simulating local effects of weapons with bare charges - as often done for practical reasons - may lead to considerable underestimation of the actual effects.

1. INTRODUCTION

In this paper the damage to reinforced concrete slabs from bare explosives charges and weapons detonating at or near such slabs is discussed.

Is this topic still of such interest as to give rise to a detailed investigation? The need for reliable data on the effects of explosives charges and weapons detonating close to walls is not new. However, it becomes of immediate interest in connection with some actual defense and safety problems.

As an example, a small free-standing ammunition magazine is shown in Figure 1. The ammunition stored therein might explode or otherwise be damaged by a hostile attack. In the course of analyzing survivability chances, the probable circular error (CEP) of the relevant weapons has to be compared with the size of the target area. But the virtual target area strongly depends on the distance to the building at which a detonating grenade or bomb can destroy the wall and possibly initiate a detonation

of the stored ammunition.

As another example, a safety problem within an ammunition factory can be mentioned. This was, in fact, the actual problem which stimulated our investigation (Figure 2). The question was whether or not a dividing wall, designed to withstand an uncased charge of 10 kg of TNT, could protect a workshop piece from a detonating HE grenade of calibre 155 mm containing 6.8 kg of explosives.

Some data referring to these problems can be found in various handbooks and in the literature. Information, however, as to which cases are really referred to, is generally rather poor. In particular, it is not possible to make a distinct comparison between the effects of bare and cased charges. On the other hand, it was clear to us from a few earlier tests that casing does affect the resulting damage significantly.

With the purpose of improving our knowledge concerning this problem, an investigation was performed, including the following three steps:

- Existing data were gathered from earlier tests and from literature. A number of 87 tests was evaluated with respect to information regarding this problem.

- Three complementary test series including a total of 46 tests were conducted in order to allow for a systematic variation of parameters.

- Design charts, both for bare charges and cased charges, have been developed and compared to each other. Moreover, an extensive collection of photographs has been published. This might give a better insight into the actual phenomena than any theoretical model.

As the most important conclusion it has been recognized that cased charges can produce perforation of reinforced concrete walls, if detonating at distances of up to ten times larger from the wall than uncased charges of the same weight. In the case of the above-mentioned ammunition magazine, the distance from which a projectile or bomb detonating above ground can destroy an outer wall, determines

the size of the virtual target area. Thus, it is essential to realize the big difference in the destructive range of bare and cased charges.

In the case of the dividing walls in an ammunition factory, the wall designed to withstand 10 kg of uncased TNT proved to be inadequate for the 155 mm HE grenade. The grenade representing a cased charge of only 6.8 kg of explosives required a wall thickness of more than twice as much.

2. DEFINITION OF DAMAGE CATEGORIES

Damages on a reinforced concrete wall from near-by explosions may vary from minor cracks up to complete perforation. Figure 3 shows an overview of characteristic damages. For the assessment of the protection provided by a wall, damage effects at its back are most relevant. Three damage categories have been defined for the evaluation of the tests and other data:

Damage Category 0: No relevant damage at the back

Damage Category A: Moderate up to heavy spalling at the back

Damage Category B: Complete, open perforation

These categories are rather wide and do not represent a sophisticated system, but this grouping facilitates the placing of the observed individual damages in the groups themselves. These damage categories allow to draw conclusions with respect to the lethality of persons exposed behind a wall, or for a detonation's propagation to stored ammunition. Since such considerations usually have to be based on pragmatic approaches, a more detailed classification of the damage categories would not be useful.

3. COMPILATION OF THE EVALUATED TESTS

Number and type of test	Explosives Quantity	Distance r	Thickness of slab t
Bare Charges			
Own tests: 31	0.013 - 10 kg	0 - 1 m	0.1 - 0.4 m
From literature: 65	0.06 - 227 kg	0 - 1.2 m	0.09 - 1.1 m
Cased Charges			
Own tests: 15	0.37 - 6.86 kg	0 - 5 m	0.1 - 0.4 m
From literature: 22	0.2 - 22 kg	0 - 4 m	0.1 - 1.2 m

Using all 133 tests as data base, the variation of the following parameters has been investigated:[4]

- Size of explosives charge; for explosives other than TNT, the TNT-equivalent for corresponding peak overpressure has been used.
- Charge weight to total weight ratio for cased charges
- Shape of charge
- Distance from center of charge to slab surface
- Thickness of concrete slab
- Reinforcement u (weight per volume)
- Concrete compression strength
- Damage category 0, A or B

In a couple of tests, additional parameters have been investigated such as initial velocity of wall-debris, their travel distance and mass. Furthermore, data from 12 earlier tests with bombs and grenades located at the wall surface below ground (i.e. tamped charges) have been included.

5. RESULTS OF THE INVESTIGATION

The previously mentioned tests have been evaluated systematically and design charts have been developed showing wall thickness versus scaled distance for the different damage categories. It was found that limited variation of concrete strength, reinforcement and charge to total weight ratio for cased charges did not strongly affect the results. But the observed damage was considerably more severe when the reinforcement of the concrete was less than a threshold value of about 50 kg/m³. On the other hand, the extent of damage attenuated for cased charges if the weight of the casing was less than 40 % of the total weight.

In Table 4 the parameter limits for the succeeding design charts are given. Selecting data from tests which meet these limits allows to obtain clear results.

Figure 5 shows the design chart for bare explosives charges. In this chart the two axes are the scaled wall thickness and the scaled distance of the charge from the wall respectively. The lower line represents the threshold between perforation and spalling. The upper line correspondingly represents the limit between the spalling category and the one for minor damage. The two threshold lines are parallel in this log/log-plot, i.e. they are separated by a constant factor. Regarding the wall thickness, the factor between the beginning of perforation and spalling at the back is always two for bare charges.

Figure 6 shows the corresponding plot for cased
charges, i.e. grenades and bombs. The threshold
between the different damage categories is again
quite sharp. There is one particular data-point
from an older test with 50 kg bombs shown, which
does not fit into its category. At a scaled dis-
tance of 1.5 $m/kg^{1/3}$ only minor damage was report-
ed, whereas the chart indicates that spalling or
perforation should occur. Next to this point, at a
scaled distance of about 1.6 $m/kg^{1/3}$ a test with a
heavily cased 105 mm HE projectile produced perfo-
ration slightly above the threshold line. The ana-
lysis of the test has led to the conclusion that
damage to reinforced concrete walls from cased
charges is dominated by the impact of fragments,
particularly at large scaled distances. Of course,
the ratio of net explosives charge weight to total
weight is important for the damage of light cased
charges in the transition range between bare and
cased charges. This parameter has not been studied
in more detail yet.

All data shown in Figure 6 are based on tests with
non-tamped grenades and bombs. A comparison with
data from tamped cased charges shows good agreement
for weapons which have contact with the exposed
wall. Tamping has, therefore, only little effect on
the damage produced by cased charges with wall con-
tact.

In Figure 7 the damaging effects of bare and cased
charges are compared. For a given wall thickness,
the distance required to avoid perforation is four
to ten times larger for cased charges than it is
for uncased charges of the same explosive weight.
Vice versa, given the charge weight and the dis-
tance, the wall thickness required to avoid perfo-
ration is up to three times larger for cased than
for uncased charges. Hence, it becomes evident that
simulating local effects of weapons with bare char-
ges - as often done in tests for practical reasons
- may lead to a considerable underestimation of the
actual effects. Figure 8 gives a visual impression
of the damage produced by two different types of
charges placed at the same distance from a rein-
forced wall.

This investigation was sponsored by the Defense
Technology and Procurement Group, TA 6, of the
Swiss Federal Department of Defense. The results
including numerous pictures from tests are pub-
lished in the following reports which are available
upon request:

- Amt für Bundesbauten: "Sprengversuche an Beton-
  wänden", Ernst Basler & Partners, B 922.10,
  February 1980

- Gruppe für Rüstungsdienste, TA 6: "Sprengversu-
  che an Betonplatten", Ernst Basler & Partners,
  B 3113-1, June 1981

- Gruppe für Rüstungsdienste, TA 6: "Lokale Scha-
  denwirkungen an Betonplatten durch Sprengladun-
  gen", Ernst Basler & Partners, B 3113.10-1,
  Sept. 82

Example: Target Areas for Different Damage Categories

Target Area for Direct Hit (Penetration)

Target Area for Perforation
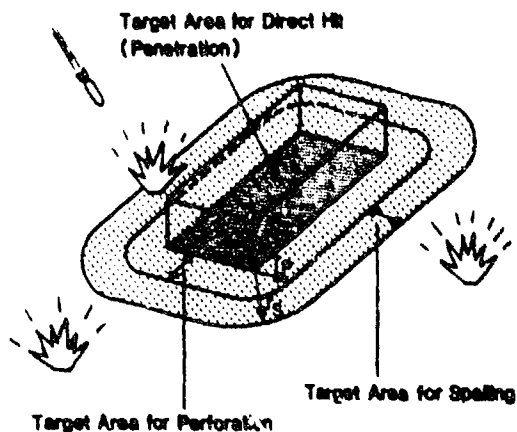
Target Area for Spalling

Figure 1: Assessment of target-area for above-ground building for different damage categories as a basis for estimating the probability of survival for a given type of attack.
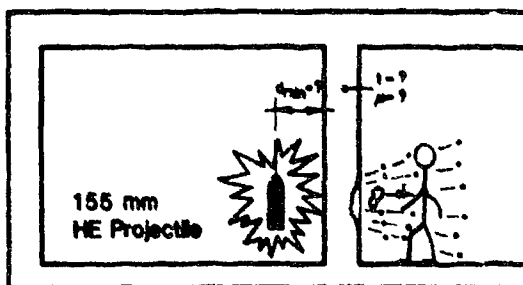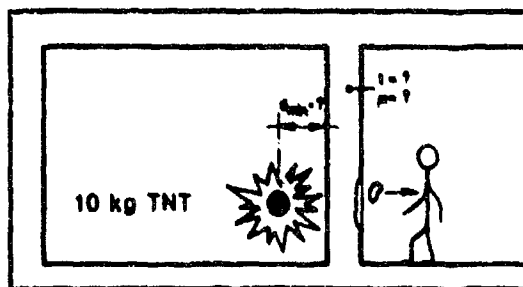
10 kg TNT

155 mm HE Projectile

Figure ?: Example: Design of a Dividing Wall in an Ammunition Factory

Definition of Damage Categories

Distance of Explosion from Wall		Characteristic Damages	Defined Damage Category
		No relevant damage, cracks or. small crater	O
		crater, deflections and cracks	
		Spalling on back	A
		Heavy spalling on back	
		Perforation	B
		Heavy Perforation	

Figure 3: Definition of Damage-Categories

Range of Explosives Charges Covered by Design Charts

Charge Weight

- Uncased Charge   0.01 kg – 200 kg
- Cased Charge, net   0.3 kg – 30 kg

    Total Weight   0.5 kg – 50 kg

Charge Weight Ratio   13 % – 60 %

Distance from Target   contact up to 1 m/kg$^{\frac{1}{3}}$

Thickness of Concrete Slab   t   0.1 m – 1.2 m

Reinforcement β 50 kg/m^3 – 150 kg/m^3

Concrete Strength β_w 20 N/mm^2 – 55 N/mm^2

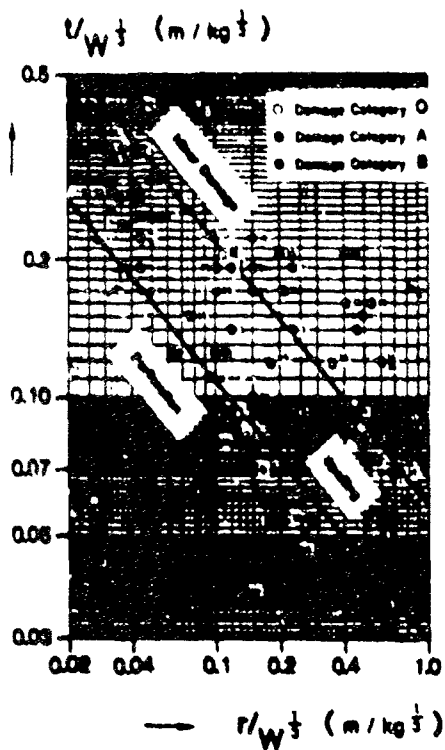Figure 4: Range of Parameter Covered by Design Charts

224

Figure 5: Damage to Reinforced Concrete Walls caused by Detonation of Uncased Explosives Charges

($r/W^{1/3}$ = Scaled Distance;

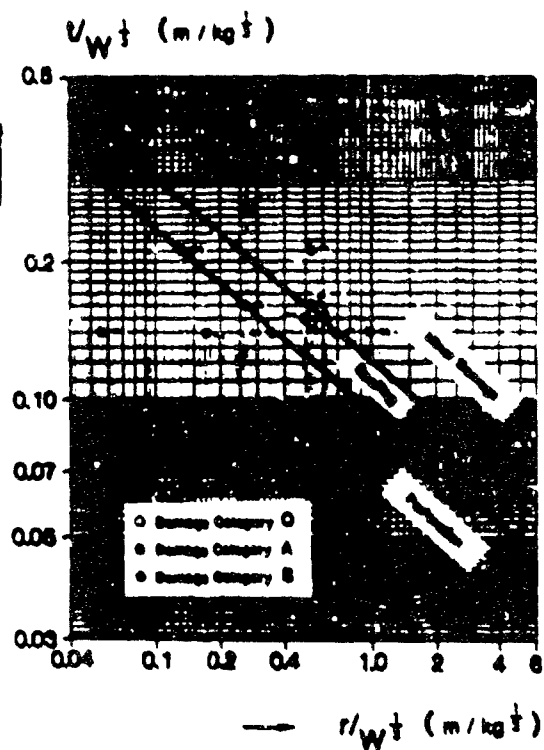$t/W^{1/3}$ = Scaled Wall Thickness)

Figure 6: Damage to Reinforced Concrete Walls caused by Detonation of Cased Explosives Charges

($r/W^{1/3}$ = Scaled Distance;
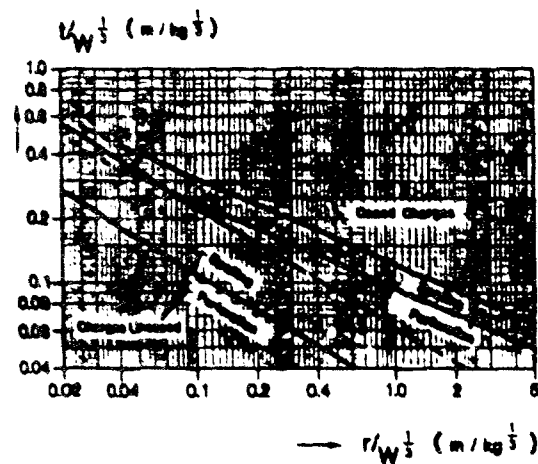
$t/W^{1/3}$ = Scaled Wall Thickness)

Figure 7: Comparison of Damage Caused by Uncased and Cased Explosives Charges

228

Before Test   # After Test

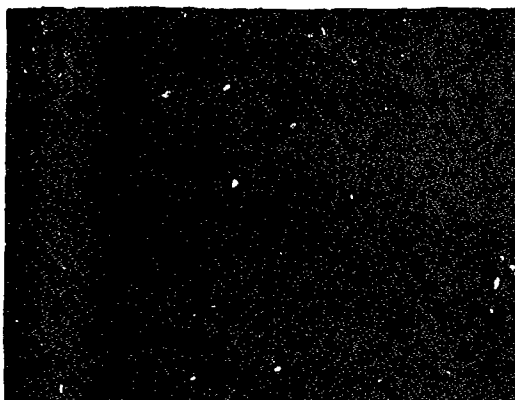**Bare Charge**   10 kg TNT
                   Distance r = 0.5 m
                   Wall Thickness t = 0.3 m   Back of exposed wall shows minor cracks

Cased Charge   15.5 cm (6.85 kg TNT)
                   Distance r = 0.5 m
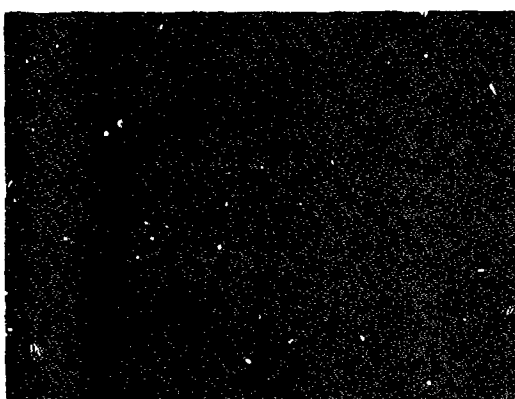   Wall Thickness t = 0.3 m   Exposed wall completely destroyed

Figure 8:   Visual comparison of the effects of bare and cased charges

226

TESTS AND EVALUATIONS OF CLOSE-IN DETONATIONS

Maj F.O. Kropatschek

Federal Armed Forces for Studies and Exercises, FRG

Abstract

Some close-in detonation tests conducted in the FRG are described and methods to determine the loading caused by blast and fragmentation are mentioned. After establishing the load the local damage effects are explained theoretically. The problem of determining the blast load caused by cased cylindrical charges as well as the question of pressure waves caused by fragmentation is mentioned. Finally the question of scaling fragmentation effects is considered.

1. Introduction

Late in 1981 and in summer 1982 Federal Armed Forces Office for Studies and Exercises - Special Infrastructure Tasks Division - did some experimental work concerning upgrading of underreinforced concrete walls of semihardened structures against a given threat (Ref. 5 and 6). This test series seems to be a good experimental baseline for the subject I am going to deal with. However, I am not going to talk about the different upgrading systems we tested and we finally recommended. This can be taken from the references given above. But what makes this series so important for us is the fact that we have been forced to identify the damage mechanism against which we tried to provide protection. Thus, I am going to present the tests performed on walls without upgrading only, totalling 6 shots out of about 25. 5 of these 6 shots were cased tests and 4 of the 6 shots were conducted with a cased weapon.

One of the structures which was tested is shown in Fig. 1. The clear height of the wall was 1.75 m. The percentage of the vertical reinforcement was 0.085% for walls No. 3 and 4 and 0.17% for walls No. 1 and 2 with a steel quality of 500/550 N/mm² and 420/500 N/mm² respectively, according to German Standards. The concrete compressive strength was about 25N/mm² for the first test and 40N/mm² for the other tests.

2. Brief Description of the Tests

Fig. 2 shows a test with 26.6 kg C4. Using an equivalent weight factor of 1.3 the scaled distance was 0.44m/kg^1/3. As it can be seen the wall was breached over an area of about 1.5 m width and 60 cm height. The first spalling layer was about 10 to 12 cm thick.

Fig. 3 shows another test with an uncased weapon. In this case 30 kg TNT were used. This results in a scaled distance of 0.46m/kg^1/3. Besides a scabbing crater on the outside and some smaller cracks on the inside no further damage was observed.

Fig. 4 shows a test with a cased weapon. In this case the charge weight was the same as in test No. 2. The difference in result is significant. However, it should be considered that the casing had a square cross section. The wall was breached over an area of about 2.10 m width and 60 cm height.

Fig. 5 shows a test similar to test No. 3. However, in this case the casing had a circular cross section and the explosive consisted of 26.6 kg PETN. Using an equivalent weight factor of 1.3 the scaled distance was the same as in shot No. 1. The wall was also breached. The reason for not obtaining a clearly localized breach might be that the wall acted like a cantilever because of the fact that the entrance opening was a weak point in the load-bearing system. The spalling layer had a thickness of about 10 cm.

Fig. 6 shows the result of the same test with a smaller weapon. The charge weight was 5.5 kg PETN. With this the scaled distance became about 0.46 m/kg^1/3. The damage was a limited spall down to a depth of about 15 cm. The spalling layer had a thickness of about 7 cm. The area of damage was about 60 cm wide and 40 cm high.

Fig. 7 shows the result of a full scale test with a MK83. The charge weight was 202 kg Tritonal which results in a scaled distance - using 1.0 as equivalent weight factor - of about 0.51 m/kg^1/3. The damage was a limited spall down to a depth of about 10 cm within an area of about 2.5 m by 40 cm.

Table 1 gives a summary of the test data.

As all tests showed more local effects than overall reaction I am going to deal with the local damage only.

3. Theories

3.1 Loading of the Wall

A comparison of tests No. 2 and No. 3 (though with a square casing) and No. 4 proves that the contribution to the total load applied to the wall by fragmentation cannot be neglected. Changing one parameter only - i.e. adding a case - the damage to the wall increases from almost no damage on the inside to a total breach of the wall.

The same fact was also determined in Ref. 2. Fig. 4 shows a summary of the work which was done for that report and shows a comparison of the extent of damage for cased and uncased charges. Using this graph there is a fairly good agreement with the results. Only the full-scale test (No. 6) and the test using C4 (No. 1) do not match. Test No. 6 should have yielded a breach instead of spalling. However, the deviation is not too drastic. The result of test No. 1 does not match at all. According to the graph the result should have been spalling only; instead we got a breach.

It should be noted that this graph is strictly based on test results and thus certain limitations have to be observed. No variation of e.g. concrete quality, percentage of reinforcement, casing thickness etc. is considered. However, the tendency of an increased damage when having fragmentation is also shown by this graph.

Thus, the conclusion is that for further calculations a combined loading caused by blast as well as by fragmentation has to be considered.

3.2 Pressure-Time History for a Cylindrical Charge

Due to the lack of reliable data to calculate the pressure-time history for cylindrical charges one has to use other procedures. One possibility might be to use the graphs for hemispherical charges - e.g. Ref. 7 - which give fairly good results. However, as it will be shown later on it is important to have a good description of the pressure with respect to the time.

An extended research work concerning this topic was performed in Germany and is described in Ref. 8. However, some of the conclusions - especially the recommended tables - are partially misleading. Therefore they have to be revised which will be done within the next couple of months. In addition to this some work will be done to compare cased and uncased cylindrical charges.

As there is no further theoretical or experimental work available to my knowledge, one has to rely on these experimental data. However, very little data are available for the weapon/structure configuration considered in

this paper, i.e. a scaled distance of about 0.5 m/kg$^{1/3}$ (1.0 ft/lb$^{1/3}$).

The problem of measuring data within this range is that we are still in the region of the fire ball and in addition - if fragmentation is involved - very heavy damage is to be expected especially to the gages directly opposite the charge on the wall.

Because of all these difficulties I am going to use a modified experimental pressure-time history using a free field measurement and multiplying it by the reflection factor recommended in Ref. 7.

A summary of all pressure data used for further consideration is given in Fig. 9. Ref. 5 shows that there is almost no difference between an exponential and a triangular type of pressure distribution if spalling is concerned. Thus, for further calculations the triangular pressure pulse - as shown in Fig. 9 with dotted lines - is used.

3.3 Load by Fragmentation

In addition to the blast load the fragmentation contributes a considerable portion to the total load applied to the wall. The most appropriate way available at this time to calculate this load seems to be the one described in Ref. 1 which is supposed to be a revised version of the corresponding chapters in Ref. 7. However, some research work is under progress in Germany to investigate the loading caused by fragmentation. But, because it is very difficult to find an answer due to the influence of statistical effects and the question of scaling fragmentation this investigation may very well take a long time.

Thus, using Ref. 1 we can calculate the general fragmentation parameters like
    fragmentation distribution,
    total number of primary fragments,
    initial velocity,
    area of impact assuming a certain angle of propagation.

After that the fragments are grouped according to their weight. For each group we can calculate
    average fragment weight,
    impact velocity,
    arrival time,
    number of fragments hitting the area considered,
    penetration depth,
    duration of penetration assuming that the fragment is decelerated linearly from its impact velocity at the surface to zero at a calculated penetration depth,
    pressure applied to the construction member resulting from the penetration.

Summarizing all fragmentation groups one gets a pressure-time history caused by fragmentation only.

We have been using a computer program for the procedure described above. So we got a representative pressure-time history as shown in Fig. 10.

It should be considered that this load is strictly based on theoretical considerations

and that it represents a statistical average.
However, at the present time it seems to be
the most appropriate way to solve the problem,
though it needs to be verified by experimental
work.

3.4 Combined Impulse

The combined pressure-time histories for tests
No. 4, 5, and 6 are shown in Fig. 11 and give
a general view comparing both pressure pul-
ses.
In any case the blast load hits the structure
first. Thus, as it will be shown later on the
fragments are hitting a possibly weakened
structural member.
It can also be seen that the load caused by
fragmentation is heavily dependent on the
standoff distance. Though in all three tests
considered in this chapter the scaled dis-
tance - and with this the peak blast pres-
sure - is the same, the pressure peak as well
as the arrival time and the duration of the
pressure pulse caused by fragmentation vary
considerably. Ref. 4 gives some parameters
for scaling the penetration processes. Ob-
viously in this case some of the boundary
conditions are violated. Certainly the shape
and weight of the fragments vary as well as
the impact velocity.
More research work has to be done to investi-
gate the problem of scaling the loading cau-
sed by fragmentation.

3.5 Spalling Mechanism

The most common theoretical solution for cal-
culating spalling effects is described e.g.
in Ref. 5. The principles of the calcula-
tions are to reflect the pressure wave after
letting it travel through the structural mem-
ber to the free inner surface. The magnitude
of this reflected wave - a tensile wave -
might be sufficient to produce fractures near
the surface. Ref. 5 gives a graphical method
of solution as well as an analytical one. For
a combined blast-fragmentation impulse it
might be more appropriate to use the graphical
one.
However, some assumptions have to be made to
simplify the calculation. At first, at the
free surface normal reflection will be con-
sidered only. Second, a change of the dura-
tion of the pressure wave will be neglected.
Third, a certain attenuation will be con-
sidered which is assumed to be about 10% due
to material properties and geometrical confi-
gurations.
To calculate the thickness of the spalling
layer as well as the spalling velocity it is
necessary to know the tensile strength of the
material of the structural member. As the tests
dealt with in this paper were conducted
against concrete targets the dynamic tensile
strength of concrete has to be determined.
This is a difficult problem because of the
fact that concrete is a very inhomogeneous ma-
terial. Though there is a procedure to deter-
mine the concrete tensile strength the results
are at least questionable.

Thus, one commonly assumes a static tensile
strength of about 10% of the compressive
strength. As shown in Fig. 12 - taken from
Ref. 9 - the dynamic compressive strength is
dependent on the loading rate. For these tests
one has to assume a pressure rise time which
will be in the range of about 0.05 msec. Thus,
based on a peak pressure of about 400 bar =
5690 psi the rate of stress is about 10^5. With
this, we are outside the range given in the
graph and one has to extrapolate. The increase
of the static tensile strength will be about
350%. With this the tensile strength becomes

$$r_s = 0.1 \cdot 250 \cdot 3.5 = 87.5 kp/cm^2$$

for test No. 1 and

$$r_s = 0.1 \cdot 500 \cdot 3.5 = 175 kp/cm^2$$

for tests No. 2 to 6.
However, by calculating the spalling effects
one has to observe that the limit velocity of
the concrete is not exceeded. The amount of
this limit velocity is about 15 m/sec. If this
value is exceeded the concrete will be blown
out and a breach will be the result.

4. Application of the Theory

Assuming a triangular pressure distribution
within the wall as mentioned above one gets
the pressure wave/structure configuration as
shown in Fig. 13 e.g. for test No. 4. As can
be seen, the damage mechanism caused by the
blast wave takes place first and after that
the pressure wave caused by fragmentation hits
a weakened wall. This fact explains the in-
crease of damage by cased charges. To calcu-
late the dimensions of the pressure wave, i.e.
especially the length, a seismic velocity for
concrete of about 3400 m/sec was assumed.
With the formulas given in Ref. 5 one can
easily calculate the thickness of the spalling
layers as well as their velocities. Because of
the fact that the rise time for the pressure
waves is assumed to be zero the thickness of
the different spalling layers is equal and the
velocity decreases by a fixed amount for each
layer. Table 2 gives a general view of all
tests calculated. The results agree fairly
well with the test results. However, in no
case the calculated spalling velocity exceeds
the limit velocity as mentioned above.
This table also shows that scaling of fragmen-
tation effects is very questionable. Though all
tests were conducted using the same scaled
distance the peak load as well as the effect of
the fragmentation varied considerably.
In a final step we have several possibilities
for calculating the damage process going on. A
most appropriate way is to consider the inside
wall reinforcement acting as a membrane almost
like a spall plate. However, one main problem
in considering a membrane type reaction of the
reinforcement is that we have to assume a suffi-
cient embedment length. This might be very
questionable especially as in the tests dealt
with in this paper the weapon was placed at the
footing of the wall which apparently might be a

weak point in the structural design. Unfortunately the time does not allow to go into more detail concerning this calculation procedure.

5. Conclusion and Recommendations

To my knowledge there is at present no better way of theoretically solving the problem of a close distance detonation.

However, because this is a very common threat configuration in standard conventional weapons effects design much more research - theoretically and experimentally - should be performed to get a better knowledge in this area. Some work is under way e.g. within the US Air Force supported by the US Army Waterways Experiment Station and we will have some more tests within the next year in Germany.

However, it should be mentioned that, though the tests described in this paper, produced considerable damage in some cases, we found a very easy-to-construct and cheap method to upgrade the wall by means of berms or concrete slabs. The main objectives of those upgrading systems is to cut the peak of the blast pressure and prevent the fragments from hitting the wall by means of an elastic and compressible design.

References

1. Healey, J. et al   "Primary Fragments Characteristics and Impact Effects on Protective Barriers" Picatinny Arsenal Technical Report 4903 December 1975

2.   "Grundlagen für die Sicherheit bei der Verarbeitung und Lagerung von Explosivstoffen - Sprengversuche an Betonplatten - Zusatzversuche vom Mai bis Oktober 1980" Gruppe für Rüstungsdienste Fachstellen und Forschung/Technische Abteilung 6 B 3113 - Juni 1981

3. Kinslow, R.   "Spallation Resulting from High Velocity Impacts" US Army Mobility Equipment Research and Development Command Report No. 2179 - May 1976

4. Canfield, J.A. and Clator, I.G.   "Development of a Scaling Law and Techniques to Investigate Penetration in Concrete" US Naval Weapons Laboratory Technical Report No. 2057 - August 1966

5. Loos, G.   "Quick Look Report - Explosive Tests on Underreinforced Model Structures in INCIRLIK an MEPPEN" Amt für Studien und Übungen, Bereich Sonderaufgaben Infrastruktur WV-TB-82-01 - January 1982

6. Kropatscheck, M.   "Summary Report - Explosive Tests on Underreinforced Model Structures at Proving Ground 91 of the Federal Armed Forces of Germany at MEPPEN August/September 1982" Amt für Studien und Übungen der Bundeswehr, Bereich Sonderaufgaben Infrastruktur WV-TB-82-12 - December 1982

7.   "Structures to Resist the Effects of Accidental Explosions" Department of the Army Technical Manual TM 5-1300 - June 1969

8. Gürke, G. et al   "Blastparameter bei der Oberflächendetonation von Explosivstoffzylindern, Ernst-Mach-Institut E 6/82 - März 82

9. Pahl, H.   "Ingenieurmäßiges Bemessungsverfahren gegen die Wirkung von Kontaktdetonationen an Stahlbetonbauteilen" Infrastrukturstab der Bundeswehr WV-TB-78-18

Test No	weight of explosive	type of explosive	equivalent weight factor	cased / uncased	thickness of casing	diameter of casing	scaled distance	vertical reinforcement	concrete compress. strength
	kg				mm	mm	$m/kg^{1/3}$	%	N/mm^2
1	26.6	C4	1.3	uncased	-	-	0.46	0.085	25
2	30	TNT	1.0	uncased	-	-	0.48	0.17	30
3	30	TNT	1.0	cased	6	230 square	0.48	0.17	30
4	26.6	PETN	1.3	cased	6	200	0.46	0.085	30
5	5.5	PETN	1.3	cased	5	105	0.46	0.085	30
6	202	Tritonal	1.0	cased	9	360	0.51	0.3 about	30

Table 1: Summary of testdata

Test No	$0.9 \cdot P_{so}$		time of arrival		assumed duration		thickness of spalling layer		spalling velocity 1. layer	
	blast	fragmentation	blast	fragmentation	blast	fragmentation	blast	fragmentation	blast	fragmentation
	bar	bar	msec	msec	msec	msec	cm	cm	m/sec	m/sec
1	234	-	0.55	-	0.075	-	4.77	-	4.39	-
2	-	-	-	-	-	-	-	-	-	-
3	277	-	0.75	-	0.175	-	18.78	-	4.58	-
4	360	396	0.4	0.8	0.2	0.15	16.53	11.27	6.29	7.12
5	360	495	0.25	0.5	0.15	0.13	12.46	7.81	6.29	9.41
6	360	288	0.8	1.4	0.3	0.3	41.32	20.99	6.29	4.63

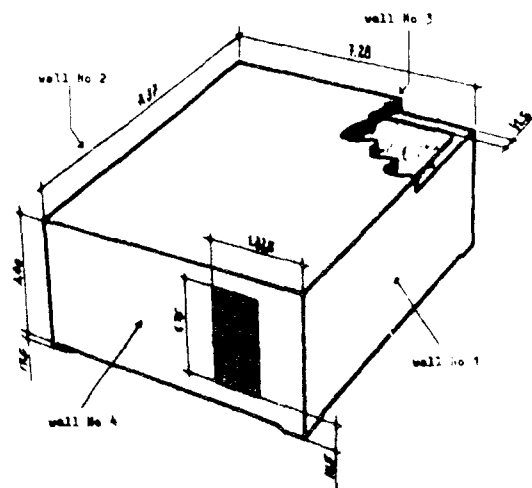Table 2: Calculation results for spalling effects

Fig 1:

Example for Modelstructure
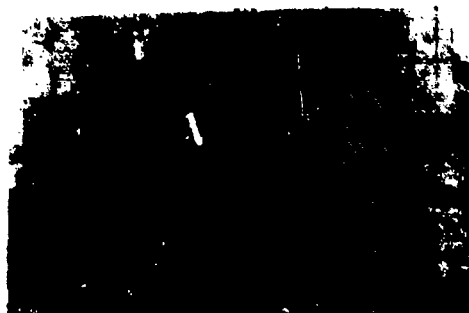(used in Test No 2 to 5)

Fig 2a Test No1 - outside damage

Fig 2b Test No1 - inside damage

Fig 3a Test No2 - outside damage

Fig 3b Test No2 - inside damage

Fig 4a Test No3 - outside damage

Fig 4b Test No3 - inside damage
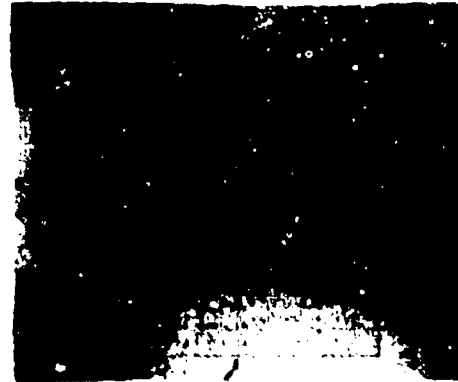
232

Fig 5a   Test No 4 – outside damage

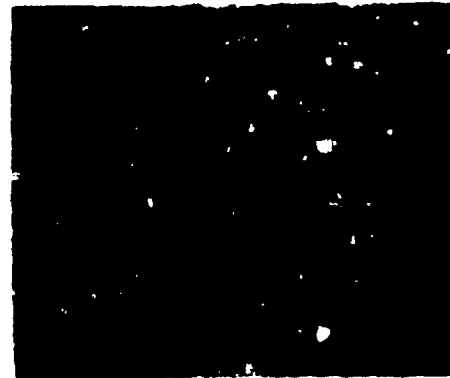Fig 5b   Test No 4 – inside damage

Fig 6a   Test No 5 – outside damage

Fig 6b   Test No 5 – inside damage

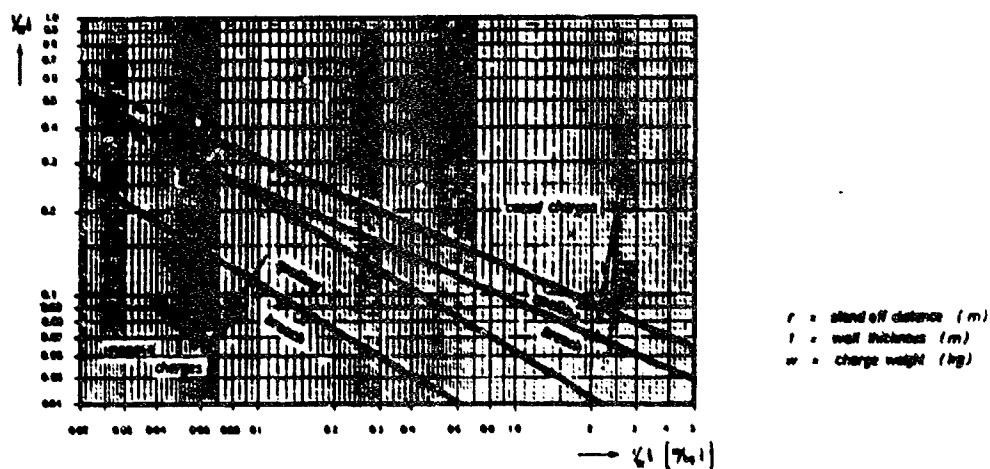Fig 7a   Test No 6 – outside damage

Fig 7b   Test No 6 – inside damage

233

Fig 8: Damage Classification (according Ref. 2)

r : stand off distance (m)
t : wall thickness (m)
w : charge weight (kg)
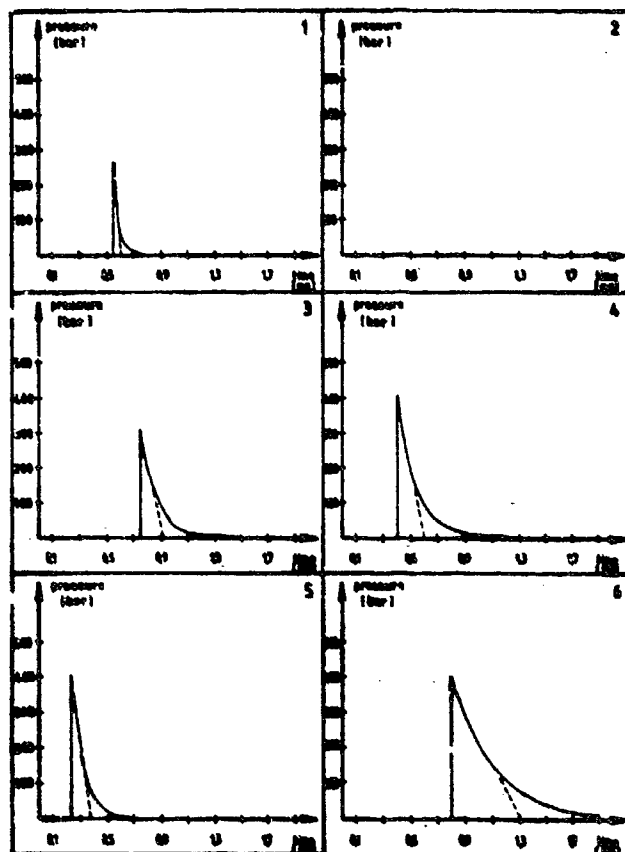
Fig 9: Pressure-Time-Histories caused by blast

BEST AVAILABLE COPY

234
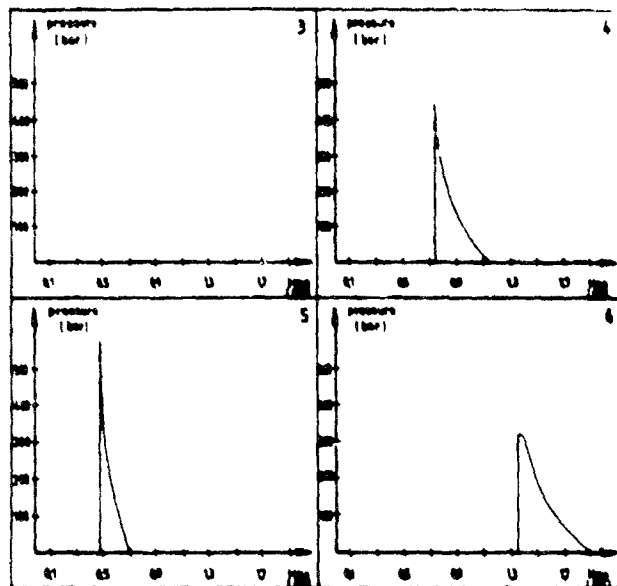
Fig 10: Pressure-Time-Histories
caused by fragmentation

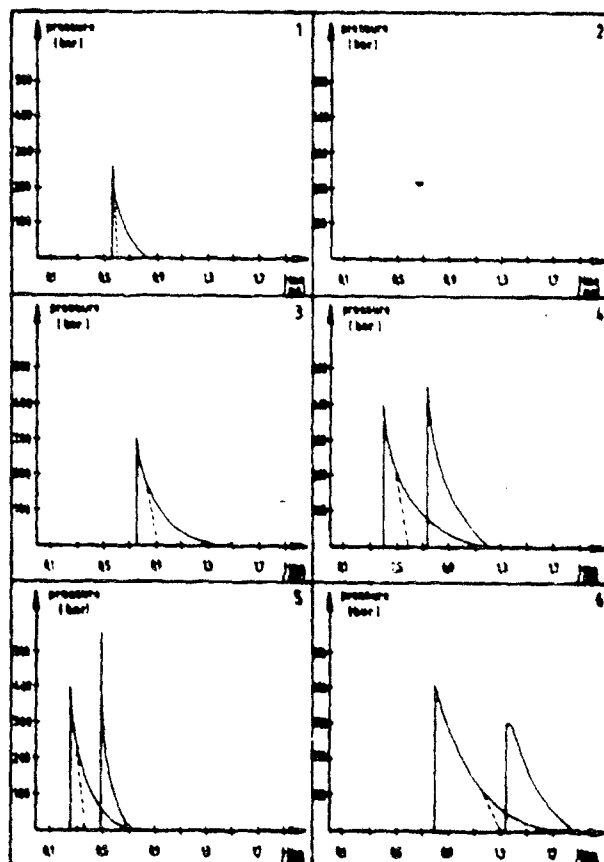Fig 11: combined Pressure-Time-Histories
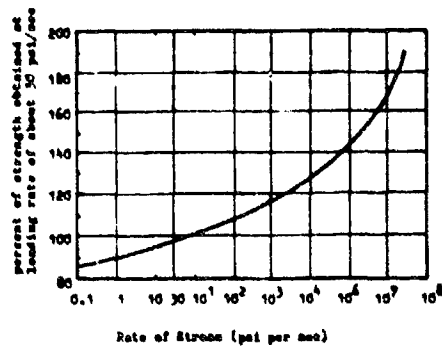caused by blast and fragmentation

235

Rate of Stress (psi per sec)

Fig 12: Effect of rate of stressing on the
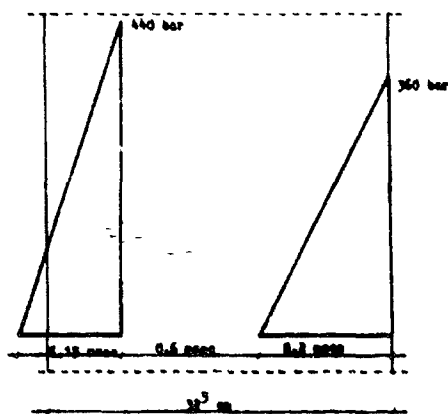compressive strength of concrete

(taken from Ref 9)

Fig 13:

Pressurewave / Structure Configuration

(e.g. Test No 4)